8-2023

Genetic Analysis Of Crossover Defective Mouse Spermatocytes Reveals Discrete Crossover Precursor Intermediates

Tolkappiyan Prem Kumar

Genetic analysis of crossover defective mouse spermatocytes reveals discrete crossover precursor intermediates

by

Prem Kumar Tolkappiyan, BTech, MTech

APPROVED:

_____
Francesca Cole, Ph.D.
Advisory Professor

_____
Richard Wood, Ph.D.

_____
Taiping Chen, Ph.D.

_____
Swathi Arur, Ph.D.

_____
Shawn Bratton, Ph.D.

APPROVED:

_____
Dean, The University of Texas
MD Anderson Cancer Center UTHealth Houston Graduate School of Biomedical Sciences

Genetic analysis of crossover defective mouse spermatocytes reveals discrete crossover precursor intermediates

A

Dissertation

Presented to the Faculty of

The University of Texas

MD Anderson Cancer Center UTHealth Houston

Graduate School of Biomedical Sciences

in Partial Fulfillment

of the Requirements

for the Degree of

Doctor of Philosophy

by

Prem Kumar Tolkappiyan BTech, MTech

Houston, Texas

August 2023

Genetic analysis of crossover defective mouse spermatocytes reveals discrete crossover precursor intermediates

by

Prem Kumar Tolkappiyan, BTech, MTech

Advisory Professor: Francesca Cole, Ph.D.

This thesis is based upon:

Genetic dissection of crossover mutants defines discrete intermediates in mouse meiosis

Tolkappiyan Premkumar[1,2], Lakshmi Paniker[1], Rhea Kang[1,2,3], Mathilde Biot[1,4], Ericka Humphrey[1,5], Honorine Destain[1,6], Isabella Ferranti[1], Iyinyeoluwa Okulate[1], Holly Nguyen[1], Vindhya Kilaru[1], Melissa Frasca[1,2], Parijat Chakraborty[1], and Francesca Cole[1,2,*].

[1]Department of Epigenetics and Molecular Carcinogenesis, The University of Texas MD Anderson Cancer Center, Houston, Texas, USA
[2]The University of Texas MD Anderson Cancer Center UTHealth Houston Graduate School of Biomedical Sciences, Program in Genetics and Epigenetics, Houston, Texas, USA
[3]Present address: Luminex Inc., Austin, Texas, USA
[4]Present address: Institut de Génétique Humaine, University Montpellier, France; Centre National de la Recherche Scientifique, University Montpellier, France
[5]Present address: The University of Texas MD Anderson Cancer Center UTHealth Houston Graduate School of Biomedical Sciences, Program in Genetics and Epigenetics, Houston, Texas, USA
[6]Present address: Committee on Development, Regeneration, and Stem Cell Biology, University of Chicago, Chicago, IL, USA.

In review, with Molecular Cell.

ACKNOWLEDGMENTS

I would like to thank my mentor Dr. Francesca Cole for the time and effort that she invested in training me. Francesca, your efforts were instrumental in my growth. It would not be an understatement to say that I gained all my science communication and critical thinking skills from training here. Additionally, thank you for allowing me to regularly attend conferences; Interactions with scientists in the field broadened my scientific view and forced me to aspire for greater goals and they were a lot of fun. There are many scientists that I respect and look up to in the meiosis community, and I was able to meet them, thanks to you. Finally, thank you for giving me the freedom to test my ideas and drive the project. Most importantly of all, thank you for being the scientist that you are.

I would like to thank Cole lab members who helped me with mouse colony maintenance and directly increased my productivity. They are April Weiss, Joanna Baird, Isabella Ferranti, Ericka Humphrey, and Julie Ontiveros. In my opinion, you took on the toughest part of my project, hence accelerating my data-producing experiments. Julie, I would like to specifically thank you for all your help during my graduating year, and for generously taking on more of my mouse work, which allowed me to focus on writing my thesis.

I would also like to thank all the other past and present members of the Cole laboratory for all their help. Maria Sandoval, Melissa Frasca, Emely Larios, Drs. Lakshmi Paniker, Rhea Kang, Holly Hamilton-Nguyen, Yunfu Lin, Parijat Chakraborty, and Aastha Pandey, thank you for all your help both inside and outside the lab. I would like to specifically thank Lakshmi Paniker and Rhea Kang for training me and for helping me get unstuck, particularly during my first year in the lab when I had about a year of failed experiments.

I would like to thank all the scientists that I had the opportunity to mentor: Honorine Destain, Melissa Frasca, Vindhya Kilaru, and Lindsey Ran. Your patience, feedback, and enthusiasm not only enhanced my people skills but also helped me grow as a communicator.

I would like to thank all my committee members for believing in me and driving me to do better. You patiently explained limitations in my skills and persistently believed that I would improve. My presentation skills improved thanks to your encouragement. Dr. Richard Wood, thank you for the recommendation letters, for checking in on me, and for providing helpful advice, especially as I was writing my thesis. Dr. Swathi Arur, thank you for the recommendation letters, for traveling over 4 hours to attend my committee meetings, and for helping me navigate the graduate program. Drs. Shawn Bratton and Taiping Chen, thank you very much for all the conversations, and advice and for helping whenever I came to you asking for it. I want to thank Drs. Blaine Bartholomew, Mark Bedford, David Johnson and Xiaobing Shi for their support during my rotations and thank Drs. David Johnson and Kevin McBride for support during my candidacy exam. I would also like to thank Dr. Sharon Dent for her support and leadership of the Epigenetics and Molecular Carcinogenesis Department. Finally, I thank the department and GSBS and especially the HEB and Cockrell Foundations for the fellowships and awards to support my graduate training.

I would like to thank Dr. Briana Dennehey and Dr. Evangelia Koutelou for helping me with proofreading the dissertation and related matters. I also want to thank Dr. Evangelia Koutelou for all her help during postdoc interviews and other career-adjacent issues.

I would like to thank all the people in the Epigenetics and Molecular Carcinogenesis Department, both those from Science Park and those in Houston. Pam Whitney and Joshua Plummer have both generously stayed long hours assisting me with my work. I would like to thank mouse facility personnel both at Science Park and the South Campus for taking care of our mouse lines.

Additionally, I would like to express my gratitude to Becky Brooks, Rebecca Deen, and Elisabeth Lindheim for their readiness to help at a moment's notice. I would like to thank Laura Denton and Lisa Shriver for helping me with a lot of things on a day-to-day basis. I would like to thank Lourdes Perez, Elisabeth Lau, Drs. Bill Mattox, and Natalie Sirisaengtaksin, for all the regular reminders on program requirements and for helping me navigate the graduation process. I would like to thank Brian Cunningham, Jennifer Crunk, and Jim Sotelo for helping me navigate MD Anderson's IT-related and computer-related issues.

Mom and Dad, thank you for allowing me to follow my own path, even when it diverged from your expectations and belief systems. I would also like to thank my friends outside my lab in particular, Aman, Kanisk, and Keshav for all their time, conversations, and help. Thank you for talking to me and helping me whenever I needed help, whether it was professional or personal.

Genetic analysis of crossover defective mouse spermatocytes reveals discrete crossover precursor intermediates

Prem kumar Tolkappiyan, B. Tech, M. Tech

Advisory Professor: Francesca Cole, Ph.D.

Abstract

In healthy, non-replicating somatic cells of diploid organisms, like humans and mice, there are two copies of each chromosome, one from each parent. However, the germ cells of these organisms, the oocytes, and the sperm, have only one copy of each chromosome, thus ensuring that when haploid oocytes and sperm fuse to form a zygote, a diploid number of chromosomes is restored. The reduction of a diploid number of chromosomes to a haploid number of chromosomes takes place during meiosis. The meiotic cell cycle consists of two rounds of cell division, Meiosis I and Meiosis II. Meiosis I create haploid gametes from diploid cells, through a reductional division that doubles the number of cells, but not the number of chromosomes.

Abnormal numbers of chromosomes, result in aneuploidy. In humans, 1-8% of spermatocytes and 10-30% of oocytes are aneuploid, contributing to ~ 5% of clinically detected pregnancies with aneuploid embryos. With few exceptions, human aneuploidies are lethal; thus, aneuploidy is the leading genetic cause of infertility and pregnancy loss. Offspring resulting from aneuploid embryos that survive to term will have other developmental defects. Most germline aneuploidy results from defective meiotic DNA repair product called a crossover. When DNA double-strand breaks are repaired as crossovers via homologous recombination, homologs exchange chromosome arms allowing sister chromatid cohesion to physically connect homologs and hence properly segregate them. Consistently, defects in human

crossover formation underlie the high incidence of human aneuploid germ cells, but the precise mechanisms leading to these defects are unknown.

Most of the mechanistic details of the mammalian meiotic crossover pathway have been extrapolated from yeast. However, accumulating evidence suggests that the DNA repair intermediates in mammals differ from those in yeast. Up to now, we have been ignorant of how many different mammalian crossover precursors exist, their length, their polymerization patterning, and their genetic requirements. To define these parameters, we analyzed mouse spermatocytes representing 13 different genetic conditions, including WT in this work. I identified two mouse crossover precursors like, but distinct from, those in yeast. The first, polymerized single-end invasion (pSEI), has ~300 bp of DNA polymerization, whereas yeast single-end invasion (SEI) lacks a polymerized strand. The second, a double Holliday Junction (dHJ), requires the MutL homolog MLH3 in a nuclease-independent manner. We suggest that the dHJ is not fully ligated in mammals, unlike in yeast, where dHJ has been shown to be ligated. Finally, our evidence suggests that MLH3's nuclease activity plays an extensive role during mismatch repair (MMR) in crossover precursors. In summary, we defined two crossover precursors and their characteristics for the first time in mammals, potentially enabling future research aimed at understanding crossover loss in humans. Our observation of genetic requirement for a dHJ formation is first in any organism. Finally, while some of the proteins identified in this work are meiosis specific, it is likely that similar DNA repair intermediates also occurs during somatic homologous recombination. Together, our work is valuable to anyone interested in mammalian meiotic recombination and the broader mammalian homologous recombination.

TABLE OF CONTENTS

TABLE OF FIGURES

TABLE OF TABLES

Introduction

Meiotic homologous recombination and human disease

Despite the many advantages of asexual reproduction, many organisms, including mammals, reproduce exclusively via sexual reproduction. Considering that sexual reproduction is typically both more complex and energy-intensive than asexual reproduction, sexual reproduction may carry a significant evolutionary advantage that offsets these costs [1]. One fundamental problem any sexually reproducing organism must solve is maintaining the proper number of chromosomes (euploidy) despite combining the genetic information from two parents. In diploid organisms like humans, the reproductive cell (gamete) must have half the parental number of chromosomes. One way to accomplish this is to reduce the ploidy of the reproductive cell from 2n (diploid) chromosome content to 1n (haploid) content. In mammals, germ cells undergo DNA replication once and segregate chromosomes twice, reducing the ploidy by half, to produce haploid gametes (**Figure 1**). This reductive cell division is termed meiosis. Maintaining genome integrity in meiosis is crucial both to generate a viable pregnancy and to prevent mutations and chromosomal aberrations that can cause genetic diseases in the short term, thus ensuring the continuation of the species in the long term.

Humans have the highest frequency of germline errors compared to most of the well-studied model organisms [2]. For example, in budding yeast (*S. cerevisiae*), meiotic errors occur at a rate of less than 1 per 10,000 meioses. In mice, meiotic errors are more common but do not exceed 1-2% of total fertilized eggs. In humans, however, up to 35% of clinically detectable natural conceptions have an aberrant number of chromosomes [2]. This is likely an underestimate, as fertilized eggs with chromosome imbalances often fail implantation, pushing the rates of aneuploidy higher in preimplantation embryos [3]. Meiotic aneuploidy is usually caused by problems in chromosome segregation during the first meiotic division [2] and is the leading genetic cause of pregnancy loss. Even if an aneuploid embryo survives through fetal development to birth, the child will often be affected by developmental deficits and mental retardation [2].

About 20-30% of oocytes from reproductive age women and 1-8% of spermatocytes carry meiosis I errors, contributing to the clinically observed aneuploidy rates [4,5]. Most of these chromosome segregation errors are caused by inadequate or improperly positioned crossovers. Crossovers are the result of specialized DNA repair by homologous recombination in which an entire chromosome arm is exchanged between parental chromosomes (homologs). DNA double-strand breaks (DSBs) are deliberately induced in early meiotic prophase I to provoke meiotic recombination and ensure formation of crossovers. To understand how meiotic recombination is interlinked with meiotic aneuploidy, it is important to understand chromosome segregation during meiosis.

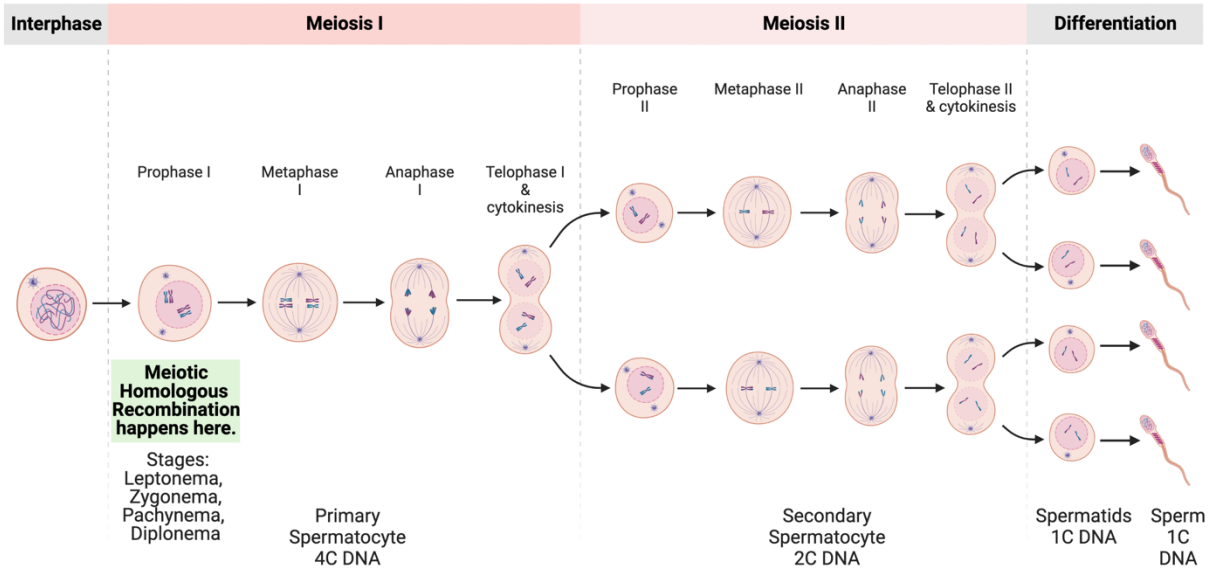

Figure 1: Meiotic Cell cycle
A brief overview of the Meiotic cell cycle is shown. During meiosis, one round of DNA replication (during interphase) is followed by two rounds of chromosome segregation (Meiosis I & II) to produce haploid gametes. By the end of Meiosis I, homologous chromosomes are segregated, and these steps require each homolog to have at least one DNA repair product, crossover. Sister chromatids are segregated during Meiosis II. Meiotic homologous recombination, the DNA repair that produces the crossovers occurs during Prophase I, and cells from this step were used for analysis in this thesis work. Prophase I is further divided into Leptonema, Zygonema, Pachynema, and Diplonema.

Reprinted with minimal edits from “Meiosis - Sperm”, by BioRender.com (2023). Retrieved from https://app.biorender.com/biorender-templates

How does homologous recombination relate to meiotic chromosome segregation?

During the meiotic cell cycle, haploid gametes are produced. In contrast to mitotic cell division in mammals and other organisms, which often preserves the chromosome content, meiotic cell division reduces the diploid set of chromosomes to a haploid set of chromosomes through two cell divisions namely, meiosis I - the reductional division step and meiosis II – a mitotic-like equational division. An important distinction between meiosis and mitosis, is that the mitotic chromosome segregation machinery cannot separate homologs or reduce ploidy. Consequently, germ cells have adapted and/or specialized the mitotic segregation machinery and make use of homologous recombination to ensure proper chromosome segregation [6]. Accurate chromosome segregation in eukaryotes has three fundamental requirements: 1) Cells need machinery that applies force and separates chromosomes; 2) Chromosomes need to be properly connected to this machinery; and 3) Chromosomes that are segregated need to be physically connected as the tension created across the chromosomes guides proper segregation. The last requirement, the physical connection needed to segregate homologs during meiosis I is enabled by the DNA repair product crossover between homologs. When crossovers are executed between homologs, they exchange chromosome arms, and hence the sister chromatid cohesion between the exchanged arm on the recombinant chromosome and its non-recombinant sister provides the necessary physical connection for the homologs (**Figure 4**).

While using recombination to connect homologs is ingenious in many aspects, it also intertwines two complicated processes: meiotic homologous recombination with proper meiotic chromosome segregation. This can be problematic as recombination errors would inevitably exacerbate problems with germline chromosome segregation. Further, while the majority of aneuploidy in oocytes is associated with advanced maternal age, it is frequently attributable to underlying meiotic recombination problems that are exacerbated with aging [7]. The work in this thesis is focused on meiotic recombination that ensures crossovers in the first meiotic cell

division. To aid in the understanding of meiosis I, a brief discussion of the important players in mitotic chromosome segregation will be discussed, followed by how they have been specialized for meiosis I.

Microtubules, the primary contributors of force

Microtubules are self-assembling polymeric single walled tubes made from heterodimers of alpha- and beta-tubulin. Microtubules are rigid and polar tubes when bound by GTP [8]. The polarity of the microtubules is such that the plus end extends away from the pole and the minus end extends toward or at the pole where the centrosome is located. Although microtubules act as tracks for cellular motor proteins, the depolymerization of one microtubule provides 10 times more energy than a motor enzyme, suggesting that the microtubule itself is the primary producer of force [9]. In support of this model, chromosome motion is not arrested when motor proteins are depleted in vertebrates [10,11]. Further, based on experiments measuring the amount of force provided by microtubule depolymerization, it is clear that microtubules are capable of providing sufficient force for chromosome segregation, estimated to require as little as 0.1 piconewtons [12-14].

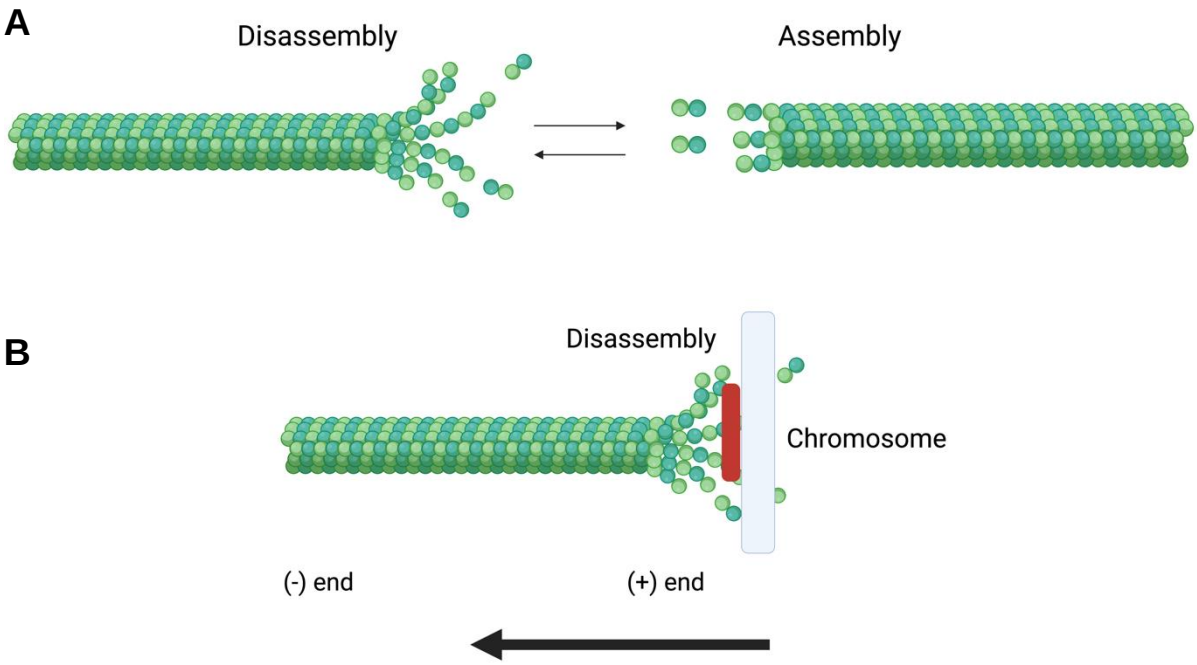

Figure 2: Schematic of chromosome movement by microtubules
(A) Microtubules are dynamic structures that can assemble and disassemble from both the (-) and the (+) end of the tubule. Microtubules bend as GTP is hydrolyzed during disassembly, and this bend stores a portion of the energy from GTP.
(B) A schematic of the microtubule applying force on the chromosome (light blue bar) via depolymerization from the (+) end. Notably, depolymerization can also occur from the (-) end but it is not shown here. The red bar depicts a kinetochore. Created with BioRender.com and based on [15]

Duro, E., and Marston, A.L. (2015). From equator to pole: splitting chromosomes in mitosis and meiosis. Genes & development *29*, 109-122. 10.1101/gad.255554.114. This figure has been recreated, with permissions from Genes and Development, under Attribution-NonCommercial 4.0 International (CC BY-NC 4.0)

Connecting Chromosomes to Microtubules

To move chromosomes inside the cells, the force must be continuously applied to the chromosomes. Consistently, the components that connect chromosomes to microtubules need to form persistent and dynamic load-bearing connections that do not break under constant force while allowing depolymerization/polymerization of microtubules (**Figure 3**). This

connection is provided by protein complexes called kinetochores that assemble on chromosome domains called centromeres. Centromeres are regions on chromosomes that are generally enriched for repeat sequences and are characterized by centromere binding proteins like CENP and a repressive chromatin environment [16]. Kinetochores, in addition to connecting chromosomes to microtubules, also play a role in regulating microtubule disassembly [17,18]. Further, in many organisms, microtubule depolymerization from the chromosome facing plus ends provides the force to move the chromosomes [9,19]. Overall, kinetochores essentially harness the energy available in microtubules to segregate the chromosomes. However, microtubules, GTP, and kinetochores are not enough to provide directionality to chromosome segregation. For directionality, tension is required, which is provided by the physical connection between sister chromatids - sister chromatid cohesion.

In S phase, in addition to DNA replication a ring-like protein complex called cohesin is laid down between sister chromatids. The cohesin protein complex acts like a glue between sister chromatids and physically connects them until they need to be separated [20]. In mammals, the components of cohesin responsible for the structural integrity of the physical connection include Structural maintenance of chromosomes subunits: SMC1 (alpha & beta), SMC3, and alpha-Kleisin subunits: RAD21 and meiosis-specific paralogs RAD21L and REC8. The Kleisin subunit behaves like a latch, therefore, when the connected chromosomes need to be separated Kleisin subunit gets cleaved, disconnecting the chromatids [20,21]. In addition to cohesins, a related family of proteins, the condensins make the chromosomes compact, giving them their characteristic rod shape and allowing proper microtubule capture and movement during chromosome segregation [22].

The kinetochores capture microtubules almost randomly, so how do the two sister kinetochores ensure bipolar attachment to microtubules from opposite sides of the cell? The cell uses tension as a readout and regulator for accurate attachment [23-25]. Tension regulates proper microtubule-kinetochore attachments by stabilizing them – meaning more tension leads to stronger microtubule-kinetochore attachments. This is clever as tension across microtubule -

sister kinetochore axis would only exist when the pull on the sister kinetochores becomes opposing (bi-oriented) and when those chromatids are connected by cohesins. This tension will reach its peak when the pull to opposing poles becomes equal [23] Therefore, microtubule-kinetochore attachments is most stable only when the force applied by microtubules on the sister kinetochores is opposing and equal (**Figure 3**).

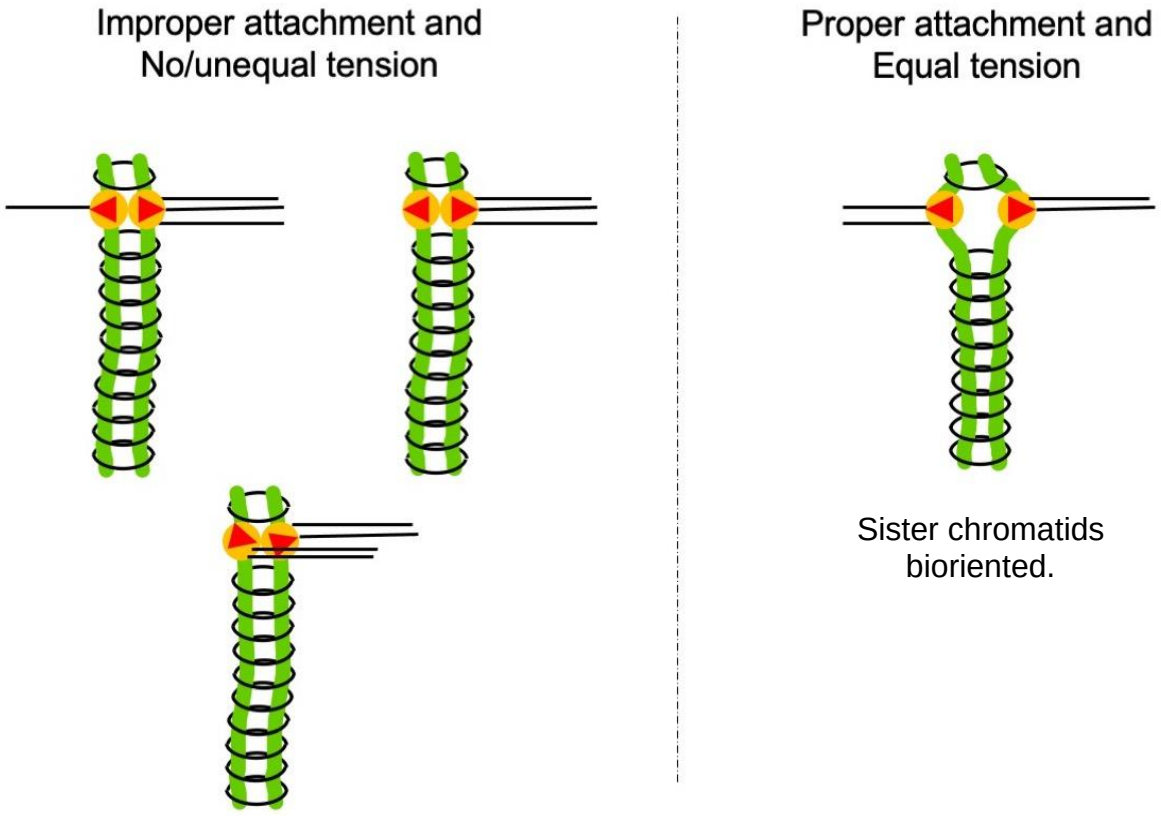

Figure 3: Role of tension in chromosome segregation
Chromosomes are depicted by green lines, kinetochores by orange circles and kinetochore orientation by red triangles. The open, black ovals show sister chromatid cohesion, which holds the sister chromatids together and provides the necessary opposing force to microtubules. Only when the microtubule attachments are proper and sister kinetochores experience equal tension across them, do the sister kinetochores pull apart (right example). Thus, equal tension stabilizes the microtubule-kinetochore interactions allowing proper chromosome segregation. Here the sister chromatids are facing the opposite sides of the cell – so the sister chromatids are bioriented here. A simple 'Embrace' model of sister cohesion shown, but this model is contested. This figure is recreated based on [15].

Tension is also used as a readout for proper chromosome attachment. Lack of tension across sister kinetochores may trigger the spindle checkpoint. The spindle checkpoint then blocks cell cycle progression in response to incorrectly attached chromosomes [26]. Lack of tension can also trigger the spindle checkpoint indirectly as when tension is absent, microtubule-kinetochore attachments are weakened or dismantled by a kinase Aurora B [27,28]. These unconnected kinetochores then trigger the spindle checkpoint [29]. Together tension plays a central role in proper chromosome segregation [26].

In addition to even and opposing tension, changes to pericentromeric chromatin initiated by loading of cohesins and condensins also favors bi-orientation [30-33]. Thus, the correct direction of segregation is regulated by a combination of pericentromeric chromatin and tension acting together, and both rely upon cohesin and condensins.

How does meiosis segregate homologs accurately?

In meiosis, after an initial round of DNA replication, homologous chromosomes are segregated during the first meiotic division and sister chromatids are segregated during the second meiotic division (**Figure 1**). The first meiotic division is intertwined with recombination and is the subject of this thesis. Accurate chromosome segregation requires several specialized steps:

1) During meiosis I, homologs are physically connected via structures called chiasmata which are formed by crossover recombination coupled with sister chromatid cohesion.
2) Sister chromatids orient in the same direction as it is the homologs that are segregated during meiosis I while sisters get segregated during meiosis II (compare sister kinetochores orientation in **Figure 3 vs 4**)

3) Cohesin complex is removed in a stepwise manner – first from the arms to separate homologs and then from the pericentromeres to separate sister chromatids.

As in mitosis, tension plays a crucial role in ensuring the correct attachment of chromosomes to the spindle; however, during meiosis I, homologs must be bioriented, which requires them to be physically connected. Therefore, to physically connect homologs, they must first undergo programmed DNA DSB formation followed by DNA repair by homologous recombination between homologs.

Homologous recombination requires that the homologs find their correct partner during DNA repair both to prevent improper DNA repair and to prevent aneuploidy. The details of DNA repair will be discussed below. Briefly, recombination starts when deliberate DNA breaks are induced along the chromosomes [34-36]. A subset of these breaks is repaired as crossovers exchanging chromosome arms. Such crossovers, combined with the existing sister chromatid cohesion together form a structure called chiasmata, which connects the homologs (**Figure 4**). The linked homolog pair can now bi-orient under tension with the interhomolog chiasma providing the necessary opposing force [37]. In most organisms, one such connection per homolog is sufficient to provide the necessary tension and allow accurate chromosome segregation [38]. Since the chiasmata is far away from the attachment point of microtubules (centromeres), the direction and the characteristics of forces on meiotic chromosomes are likely going to be different than in mitosis. It is currently unknown if chromatin near chiasmata becomes springy as it does in the mitotic pericentromeric region. It is also currently unclear if structural properties of chromosome arms changes to transfer the force from pericentromeric microtubule attachments to chiasmata. But once the chiasmata forms, the homologs can segregate accurately in anaphase I.

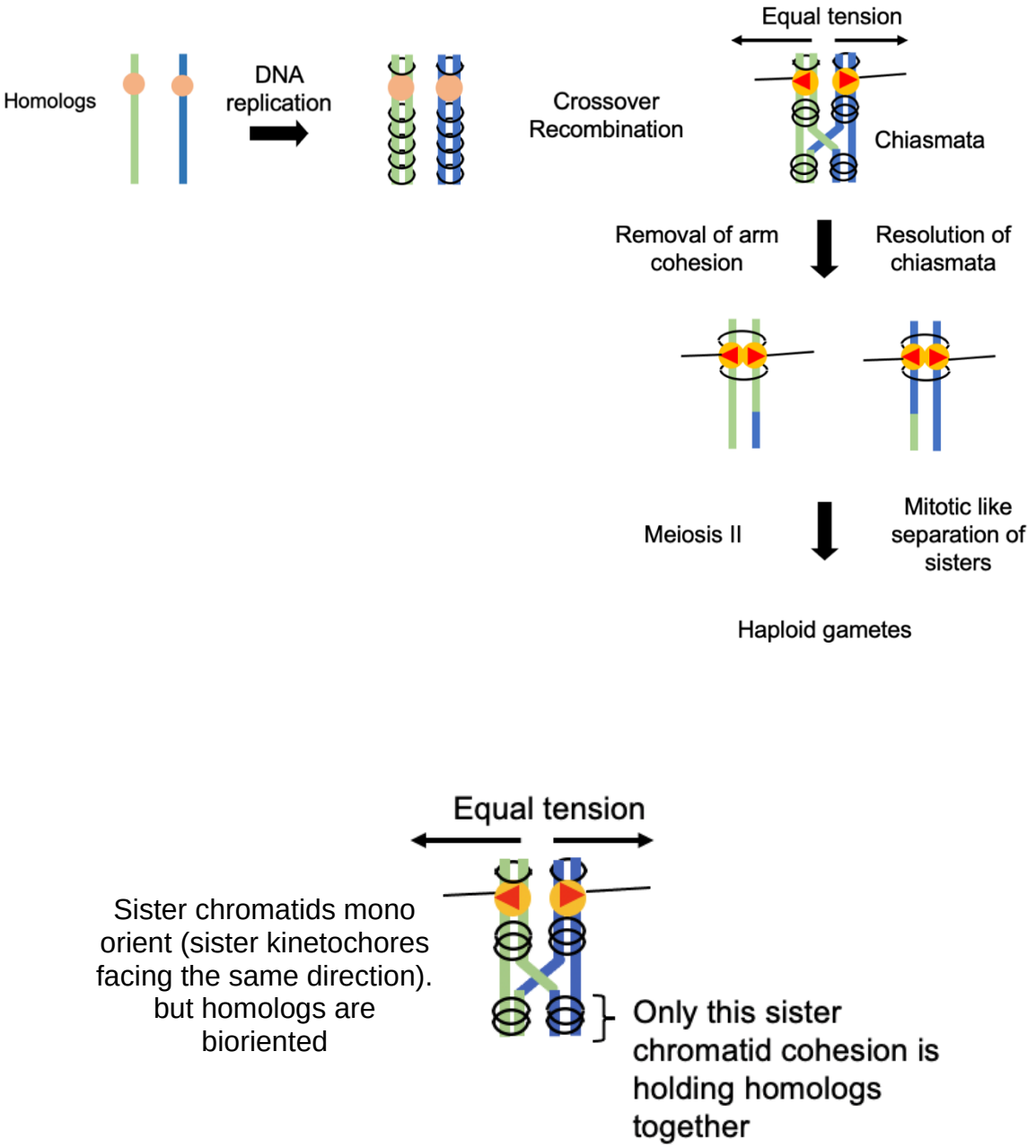

Figure 4: Chiasmata connect homologs during meiosis- I
(Top) Homologs are depicted by green and blue lines. The orange circles depict kinetochores, and their orientation is given by red arrows. The open, black ellipses depict sister chromatid cohesion. Sister chromatid cohesin is laid down during DNA replication between the sisters and holds sister chromatids together. To physically connect homologs, crossovers are introduced between homologs that exchange chromosome arms. This allows the formation of chiasmata which enables the sister chromatid cohesion to hold homologs together, allowing proper homolog segregation. A simple 'Embrace' model of sister cohesion shown, but this model is contested. This figure is based on [15].
(Bottom) It is important to note that only the sister chromatid cohesion distal to the centromere is holding the homologs together.

Duro, E., and Marston, A.L. (2015). From equator to pole: splitting chromosomes in mitosis and meiosis. Genes & development *29*, 109-122. 10.1101/gad.255554.114. With permissions from Genes and Development, under Attribution-NonCommercial 4.0 International (CC BY-NC 4.0)

Sisters need to co-segregate during meiosis I

When homologs are segregated during meiosis I, the sister chromatids must stay together. A specialization that prevents premature sister chromatid separation and, thus, promotes co-segregation is thought to be the fusing of the sister kinetochores. The evidence for such a fusion was first seen in electron microscopy observations of Drosophila melanogaster sister kinetochores, earlier in meiosis as a single two-layered hemisphere on each bivalent and later as double disks. This arrangement is different from the characteristic separation of sister kinetochores often observed in mitosis [39]. Similar evidence for co-segregation of sisters due to kinetochore fusion was observed in maize [40], budding yeast [41], fission yeast [42], and mice [43]. In budding yeast, a four-component complex, monopolin, plays crucial roles in arranging sister kinetochores such that they create a single microtubule binding unit [44-46]. In contrast to budding yeast, in fission yeast the meiosis-specific cohesin subunit Rec8 promotes mono-orientation [42]. Rec8 also plays roles in sister chromatid co-segregation in mice [43].

Stepwise removal of cohesin

Once homologs align and get bioriented, the physical connection between homologs but not sisters must be severed to allow the separation of homologs. This is accomplished by the stepwise removal of cohesin. A meiosis-specific cohesin klesin sub-unit, Rec8, plays a crucial role at this step. Phosphorylation of Rec8, which in yeast is accomplished by polo kinase Cdc5 and in mouse oocytes by activity of AURORA B/C kinases, allows it to be cleaved by separase [47-50], and this cleavage is limited to chromosome cohesin, allowing homologs to segregate [51]. At this stage, pericentromeric cohesin needs to be protected from cleavage so that sister chromatids remain attached for meiosis II. To accomplish the stepwise cleavage, and to protect pericentromeric cohesin, a protein phosphatase, PP2A, is recruited to pericentromeres, to dephosphorylate Rec8, thus protecting it from separase activity [48,52]. This

residual pericentromeric cohesin provides the necessary tension during meiosis II for proper segregation of sister chromatids into gametes (**Figure 4**).

Cell biology of aneuploidy in humans

The frequency of aneuploidy in human gametes is relatively high (1-4% in spermatocytes and at least 10% in young, to ~70% in older oocytes) [2,53-55] and in oocytes, aneuploidy increases with age (Roecker and Huether 1983). The majority of these aneuploid germ cells arise from direct or indirect errors in meiotic recombination, leading to the mis-segregation of homologous chromosomes [54,55]

One of the primary reasons for high levels of aneuploidy in young women (10%) is the loss of crossovers in oocytes due to crossover maturation inefficiency [56]. During the early steps of meiotic recombination, the precursor intermediates for crossovers are distributed, in general, proportional to the length of the chromosome axis. However, this distribution mechanism ensures that every chromosome gets at least one of these precursors by spreading them farther apart. The observation that every chromosome gets at least one of the precursors is called crossover assurance and these crossovers are termed obligate crossovers. The obligate crossover formation has been observed in many organisms including in mammals [57-59]. Comparison between human oocytes and spermatocytes reveals that the precursors for these obligate crossovers form without defect in oocytes. But in oocytes, a fraction of these precursors fail to become crossovers, and a similar defect is not seen in spermatocytes. This failure to generate a crossover from its precursor is termed “crossover maturation inefficiency” [56]. Intuitively, it is easier to realize that shorter chromosomes (e.g., chromosome 21 in humans) are at most risk as they only ever get assigned one precursor per chromosome. One might perhaps assume that the longer chromosomes that get more than one crossover precursor, owing to their length will not be at risk of aneuploidy from the crossover maturation inefficiency. Unfortunately, however, even the longer chromosomes are at risk of aneuploidy as the effects of the crossover loss worsen with maternal age. Therefore, maternal age exacerbates the loss

of crossovers from crossover maturation inefficiency leading up to a total of 70% aneuploid oocytes [55].

The above-mentioned crossover distribution machinery prevents placing two crossover precursors close together on the same chromosome [37]. Essentially, if two crossover precursors were assigned to a single chromosome, it is often assigned towards the two ends of the chromosome rather than close to the center (**Figure 5**) [56,60]. The underlying mechanism at play here will be discussed later, but relevant for this section, when a chromosome gets more than one precursor, most of these precursors are positioned towards the ends of the chromosome. As discussed earlier in **Figure 4**, only the cohesin on the exchanged arm, which is distal to the centromere provides the physical connection during meiosis I. If the chromosome receives only one crossover, then cohesins on almost half the arm of the chromosome distal to the centromere would hold the homologs together (**Figure 4**). However, if the chromosome gets assigned two crossovers, only the cohesins between the crossover location and chromosome end hold the homologs together. Thus, when chromosomes get two crossovers, the total cohesion between homologs is lower than when the chromosome gets only one crossover. While chromosomes with double crossovers also occur in spermatocytes, in oocytes a fraction of these crossovers fail to form due to crossover maturation inefficiency. Therefore, crossover maturation inefficiency-dependent crossover loss in oocytes further reduces the cohesion between homologs (**Figure 5**) [56]. Thus, when the sister chromatid cohesion loss occurs with increasing maternal age, even long chromosomes that experience crossover maturation inefficiency become increasingly aneuploid. Together, defective recombination during meiosis I underlies increased aneuploidy in humans and aggravates the age-dependent loss of cohesion in oocytes.

Earlier work from our lab suggests that the spermatocytes of juvenile male mice may also share crossover maturation inefficiency. However, given the constitutive nature of spermatogenesis, mice appear to mature out of this defect [61]. Young human fathers are also more likely to parent a child with Down syndrome compared to adult fathers [62,63]. In juvenile

mice and human spermatocytes, the number of crossover locations on chromosome axes as cytologically marked by MutL homolog 1 MLH1 protein foci was reduced, resulting in a phenotype similar to crossover maturation inefficiency in oocytes [61]. Additionally, designated crossovers are lost in juvenile mouse spermatocytes due to a failure to convert crossover precursors into crossovers, causing aneuploidy.

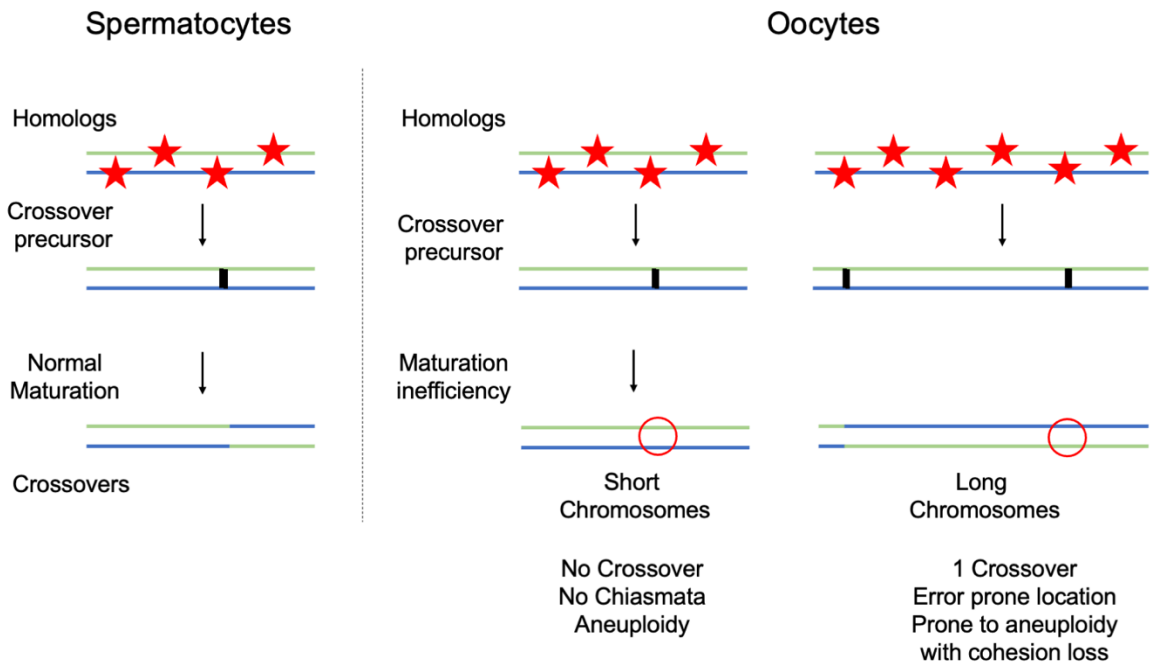

Figure 5: Crossover maturation problems underlie human germline aneuploidy

In this schematic, DNA DSBs are depicted by red stars. Homologs are shown as green and blue chromosomes. Crossover precursors are depicted by thick black lines between homologs. Crossovers are shown by the exchange of homolog arms and red circles depict the loss of potential crossovers. Oocytes show crossover maturation inefficiency when a proportion of the crossover precursors do not become crossovers. On short chromosomes, this crossover loss may directly cause aneuploidy. On longer chromosomes, crossovers may form in an error-prone position, either closer to the telomere or centromere, with little sister chromatid cohesion available to hold homologs together. Age-dependent loss of sister chromatid cohesion, therefore, increases the chances of the chromosomes with such misplaced crossovers to become aneuploid. This figure is based on [56].

Wang, S., Hassold, T., Hunt, P., White, M.A., Zickler, D., Kleckner, N., and Zhang, L. (2017). Inefficient Crossover Maturation Underlies Elevated Aneuploidy in Human Female Meiosis. Cell *168*, 977-989 e917. 10.1016/j.cell.2017.02.002

In summary, we know that human meiotic chromosomes lose crossovers, but the mechanisms that underlie crossover loss are unknown. Most of the mechanistic details of crossover formation in mammals have been extrapolated from yeast. However, mechanisms of recombination in yeast differ from mammals at many mechanistic steps. Therefore, to better understand human germline aneuploidy, it is essential to identify and define the mechanisms of recombination specific to mammals. The project that underlies this thesis addresses this problem by analyzing recombination outcomes in many crossover-defective mutant mouse spermatocytes.

What makes a meiotic recombination hotspot?

During meiotic recombination, the initiating DSBs in mice and humans occur at specific locations in the genome called hotspots. In both mice and humans, hotspot locations are determined by a zinc finger domain-containing, DNA-binding, histone methyltransferase called PR domain-containing protein 9 (PRDM9) [64-67]. PRDM9 is an epigenetic modifier with three broad domains: an N-terminal KRAB-related domain [68], a PR/SET domain [69], and a C-terminal, DNA binding, zinc finger array containing Cysteine(2) Histidine(2) or C2H2 motifs [70] (**Figure 6**).

PR/SET domains are known to have lysine methyl transferase function, and consistently mouse and human PRDM9 can catalyze mono-, di- and tri-methylation of histone H3K4 and H3K36 sites *in vitro* [71-74]. The methyltransferase activity of PRDM9 is essential *in vivo* for its hotspot designating function [75]. PRDM9 also has a KRAB-related domain in addition to an SSXRD domain (**Figure 6**). Both of these domains have been implicated in transcriptional repression, but PRDM9 does not appear to regulate transcription [76]. However, the KRAB-related domain of PRDM9 is important for PRDM9 function as N-terminal truncation alleles that alter the KRAB-like domain lead to loss of PRDM9 methyltransferase activity. This may be due to the loss of protein-protein interactions mediated via the KRAB-related domain [77,78].

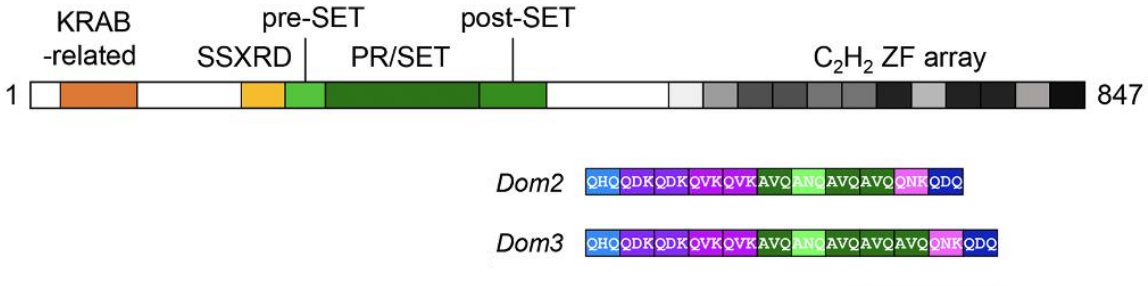

Figure 6: PRDM9 protein
(Top) A simple schematic of PRDM9 protein domains. The presence of a PR/SET domain followed by a C2H2 zinc finger array is a feature that defines PRDM family members [79-81]. Repeating zinc fingers in the C2H2 ZF arrays are indicated in the same shade of gray. (Bottom) The C2H2 zinc finger array of PRDM9 evolves rapidly and is therefore not conserved even between subspecies. PDRM9^{Dom2} (C57BL/6 mice) and PRDM9^{Dom3} (C3H mice) represent two different PDRM9 mouse alleles. These zinc finger domains show binding preference based on DNA sequence and thus each PRDM9 allele has distinct preferred DNA binding motifs, with each colored box containing three amino acids representing one zinc finger. Notably, both the C57BL/6 and DBA/2J mice used in this study have the same *Dom2* allele [75].
Reused from Grey, C., Baudat, F., and de Massy, B. (2018). PRDM9, a driver of the genetic map. PLoS Genet *14*, e1007479. 10.1371/journal.pgen.1007479 with permissions from PLOS Genetics, under Creative Commons Attribution License which permits unrestricted use, distribution, and reproduction in any medium, provided the original author and source are credited.

PRDM9 is H3K4 and H3K36 writer, and this activity depends on the PR/SET domain. PRDM9 binds to genomic locations based on the sequence specificity of its C2H2 zinc finger array (**Figure 6**). A fraction of the sites marked by PRDM9 are chosen for DSB formation and therefore PRDM9 chooses the hotspot sites across the genome during meiosis [82]. PRDM9 is not required for DSB formation as DSBs form in the absence of PRDM9 although at altered locations, primarily CpG islands. Therefore, PRDM9 marks the sites at which DSBs form but is not required for DSB formation. In mice and humans, most meiotic recombination events occur at locations marked by PRDM9 and these hotspots are usually located in genic and intergenic regions. [82-84].

Although PRDM9 marks the location of hotspots, only a small fraction of PRDM9-marked sites is used for initiating DSB formation and subsequent recombination. In mice,

PDRM9 has been mapped to roughly 15,000 different genomic binding sites [82,85-87]; but only 300-400 sites are used per cell for initiating DSBs [37]. An estimated 4700 sites are marked by PRDM9 per cell, which is many-fold higher than the actual number of DSBs that ultimately form, thus in most cases, PRDM9 protein levels and/or the number of sites marked with H3K4 and H3K36 trimethylation is sufficient for proper DSB formation and later repair progression [88].

Because the repair happens between homologs, over evolutionary time DSB sites on one homolog that bind PRDM9 strongly are replaced by sequences on the homolog through DNA repair. As such, weaker PRDM9 sites become more prevalent over time. This process is called hotspot erosion and can lead to sterility due to poor DSB formation. Therefore, hotspot erosion has been proposed to select PRDM9 that binds to newer/different sequences. Consistently, the DNA binding domains of PRDM9 show high variability within and between species, as the PRDM9 zinc finger domains are under positive selection to evolve quickly [89]. However, due to this rapid evolution of the PRDM9 zinc finger arrays and changing hotspot locations, PRDM9 marked sites may become limiting in hybrids like B6xPWD, making these hybrids sterile. B6 and PWD each carry their own PRDM9 alleles, *PRDM9*^{B6} and *PRDM9*^{PWD}, respectively. Comparisons of the sites marked by *PRDM9*^{B6}-and *PRDM9*^{PWD}-mediated H3K4 and H3K36 trimethylation showed that the majority (72%) of the marked hotspots are not the same between homologs. These hotspots where one of the homologs carry a PRDM9 mark but the homolog does not is termed asymmetric hotspots. Although a certain level of hotspot asymmetry is tolerated during both mouse and human meiosis, including the *59.5* hotspot [82,84,86,87,90], used extensively in this work, an overabundance of asymmetric hotspots will interfere with the progression of meiotic recombination. For example, spermatocytes from B6xPWD hybrid mice display both impaired meiotic DNA repair and sterility [87,91]. This sterility defect can be rescued by inserting short stretches (~27 Mb) of homology on short chromosomes that have the hardest time finding their homolog partner (pairing) to initiate DNA repair. The short stretches of homology likely introduce enough symmetric PRDM9 hotspots to alleviate the pairing defect and almost fully rescue B6xPWD hybrid sterility [91]. Together, this

suggests that PRDM9-dependent epigenetic modification likely also helps with the homologs find their partner and therefore help with downstream inter-homolog repair.

Induction of meiotic DNA DSBs

Based on chromatin immunoprecipitation followed by high-throughput sequencing (ChIP-seq) data, we know that PRDM9- trimethylatated H3K4 and H3K36 are located in immediate proximity to PRDM9-binding sites [73]. Further, chromatin accessibility increases around PRDM9-binding sites in a PRDM9-dependent manner [88]. At about the same time that PRDM9 binds to chromatin, meiotic chromosomes reorganize their higher-order structures. This results in sister chromatids being extruded out as loops in all directions from the central axis (**Figure 7**) [92-94].

Proteins required for DSB formation, including Meiotic Double-Stranded Break Formation Protein 4 (MEI4), meiotic recombination protein REC114, HORMA domain-containing protein 1 (HORMAD1), Interactor Of HORMAD1 (IHO1), and the DSB inducing type II DNA topoisomerase-like protein SPO11 and its obligate partner TopoVIBL, load onto the chromosome axis [95-98]. But PRDM9 has been shown to localize to DNA sequences in the loop that is extruded out from the axis [78,85]. So how is it that the DSBs are induced in the loops when many of the essential proteins localize to the axis? The sites marked by PRDM9 are thought to be transiently brought down to the axis, where the DSB-inducing factors MEI4, REC114, HORMAD1, and IHO1, activate SPO11 to induce DSBs [99,100]. The exact DSB sites often overlap with PRDM9-binding sites, suggesting that PRDM9 is evicted during or after the induction of DSBs [101]. SPO11 is a topoisomerase-like protein that creates a nick on the DNA strand through covalent attachment via a transesterification mechanism. As such, SPO11 acts as a dimer creating two nicks in opposite strands of DNA in close proximity [34]. However, at this point the SPO11 dimer is still bound to DNA and a DSB has not been induced yet. To induce the DSB and remove SPO11, an endonuclease involved in DNA resection, meiotic recombination 11 (MRE11), creates additional nicks releasing SPO11 and initiating DNA repair (**Figure 7**) [102]. The released SPO11 protein is still covalently bound to short oligonucleotides

that correspond to DSB sites, and can be purified and sequenced to identify DSB sites [101]. Such maps are called SPO11 oligonucleotide maps.

DSB formation initiates during the first stage of meiotic prophase I, leptonema, and is largely completed by the end of the second stage, zygonema (**Figure 8**). The number of chromosome sites capable of making a DSB far exceeds the number of DSBs that occur. The number of DSBs is negatively regulated by a serine/threonine kinase Ataxia-telangiectasia mutated (ATM) that is activated upon DSB initiation [103]. In mice, initiation of DNA repair is associated with the appearance of lateral element proteins (e.g., SYCP3) of the interhomolog higher order protein structure called the synaptonemal complex. The establishment of the synaptonemal complex between homologs requires formation of the central element components (e.g., SYCP1), which leads to removal of the DSB machinery from the chromosome axis, essentially stopping formation of additional breaks [97].

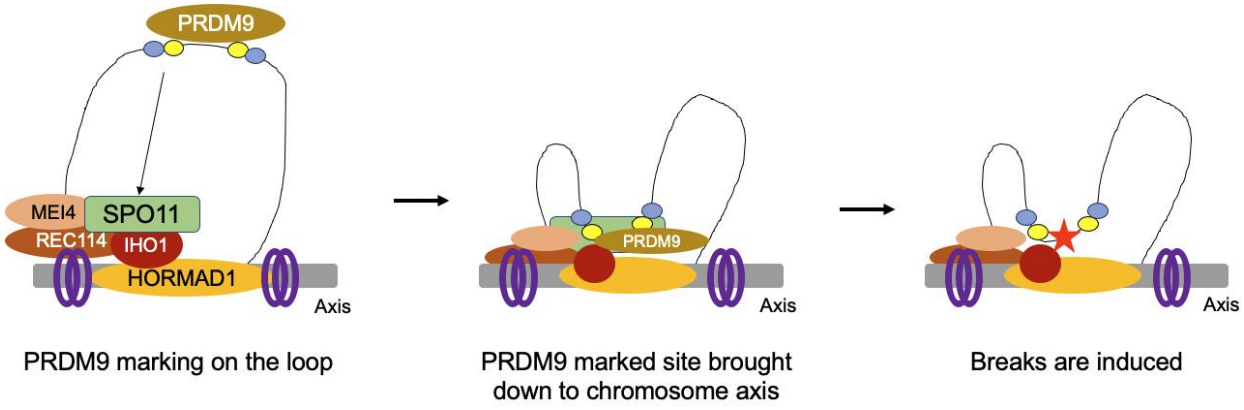

Figure 7: Current model of DSB formation
In this schematic, the grey bar represents the chromosome axis, and the purple rings depict cohesin rings. The loop extruding from the axis is shown by a hand-drawn black line. The yellow circle near PRDM9 on the loop depicts H3K4me3 and the blue circle depicts H3K36me3. For simplicity, only one sister chromatid is shown and chromatin elements on the loop are not shown. Once PRDM9 methylates histone H3, the modified site is brought down to the axis, which has the essential components of the DSB machinery. At this point, the DSB is induced by SPO11 and PRDM9 is evicted from the cut chromatid.

Figure based on Grey, C., Baudat, F., and de Massy, B. (2018). PRDM9, a driver of the genetic map. PLoS Genet *14*, e1007479. 10.1371/journal.pgen.1007479. With permission from PLOS Genetics, under Creative Commons Attribution License which permits unrestricted use, distribution, and reproduction in any medium, provided the original author and source are credited.

Temporal progression of spermatocytes in meiosis I can be tracked using immunofluorescence images of spermatocytes stained for the axial element (SYCP3) and axial element (SYCP1) of the synaptonemal complex. The synaptonemal complex can be used to study some aspects of chromosome behavior and is mechanistically intertwined with repair, the details of which are beyond the scope of this introduction [37]. However, the morphology of synaptonemal complex proteins in spermatocytes is useful for identifying the temporal progression for meiotic DNA repair as shown below (**Figure 8**).

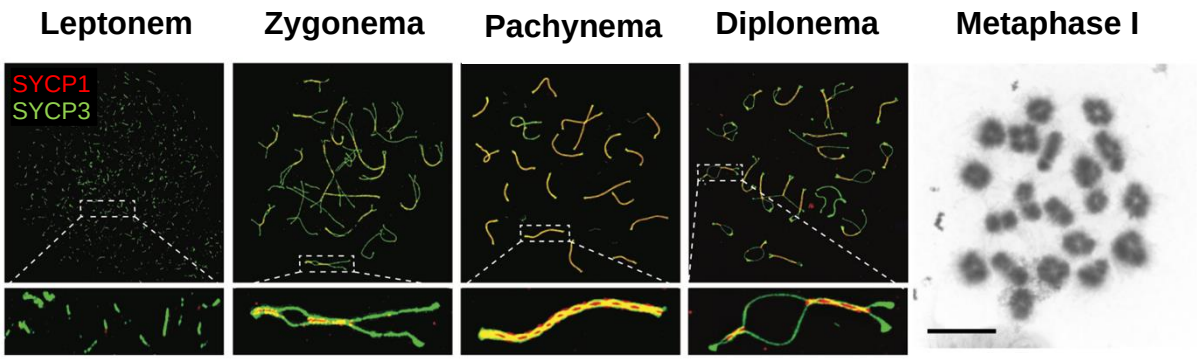

Figure 8: Stages of meiosis I spermatocytes
Top panel), immunofluorescence images of spermatocyte cells stained with SYCP1 (central element) and SYCP3 (axial element). From left to right, the first four stages of meiosis I are shown. DSB induction begins to occur in leptonema. SYCP3 axis formation is not complete and SYCP3 staining appears as grains scattered on sand. During leptonema, SYCP1 is either absent or present as rare dots. During zygonema, SYCP3 axis formation is complete and SYCP1 begins to form contiguous stretches between SYCP3 marked homologs as they begin to synapse (inset). In pachynema, synapsis is completed and both SYCP3 and SYCP1 are fully contiguous between homologs. Crossovers are produced during pachynema in wildtype (WT) spermatocytes (Rhea Kang, Francesca Cole unpublished). During diplonema, SYCP1 is removed from homologs, while SYCP3 marked chromosomes de-synapse (inset). Our lab

showed that alternative repair pathways are active in diplonema (Rhea Kang, Francesca Cole unpublished).
A bright field image of mouse metaphase I spermatocytes stained with Geimsa. Each one of the 20 objects are called bivalent or connected homologous chromosome via a crossover. Image reused from Gray, S. and P. E. Cohen (2016). "Control of Meiotic Crossovers: From Double-Strand Break Formation to Designation." Annu Rev Genet **50**: 175-210. Permissions provided by the ANNUAL reviews (Licesce ID: 1343046-1)

Strand invasion

After MRE11 nicks on either side releasing the SPO11 dimers and their oligonucleotides, recombination is initiated by 5' to 3' end resection at the DNA DSB. A 5' to 3' exonuclease, Exonuclease-1 (EXO1) is required for extended resection in yeast but not in mouse spermatocytes [104,105]. Alternative enzymes such as DNA2 with helicase BLM may therefore function to do long resection redundantly to EXO1 in mammals [106]. Nonetheless, in both yeast and mice, ~1 kb of 3' overhang is generated on both sides of the DSB site [104,105,107,108]. This 3' single-strand (ss) DNA is first bound by the single strand-binding protein RPA which is thought to facilitate the recruitment of DMC1 and RAD51 onto the 3' overhang [109-111]. DMC1 is a meiosis-specific recombinase that is necessary for the initiation of strand exchange in yeast, mice, and many other organisms [112]. RAD51 is expressed in all tissues and participates in strand exchange in both meiosis and mitosis, both in budding yeast and mice [109,113,114].

ChIP-seq data indicate that in mice, DMC1 and RAD51 co-occupy the 3' overhang with DMC1 present closer to the DSB site/free 3' end and RAD51 farther from the DSB (**Figure 9**). The DMC1-coated 3' end invades the homologous chromosome to form a D-loop. During strand invasion, RPA appears to occupy the displaced strand, likely stabilizing the D-loop (**Figure 9**) [113]. As DMC1 is recruited to the 3' overhang of the DSB, cytological estimation of the number of DMC1 foci per cell can be used as a proxy for the number of DSBs. Indeed, in my thesis project, we have used DMC1 to estimate the number of DSBs in spermatocytes carrying EXO1 mutant alleles.

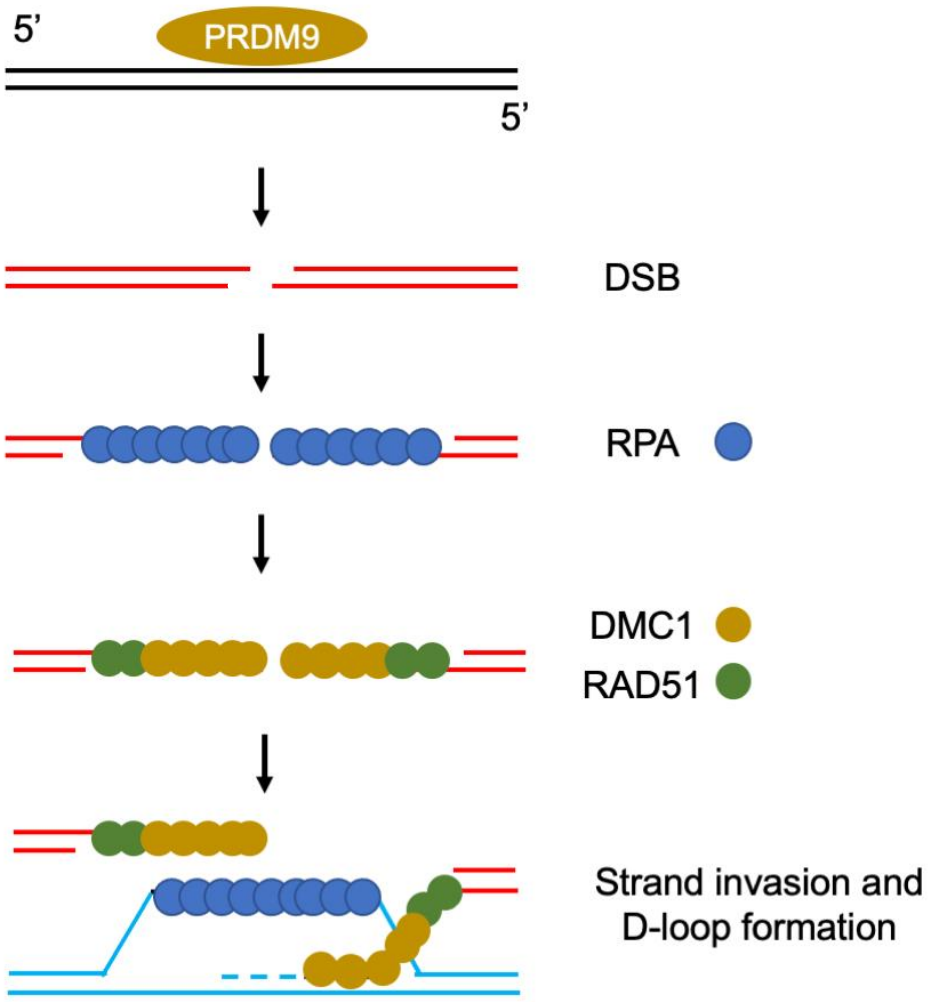

Figure 9: Schematic of strand exchange

Each line represents one of the two strands of the double-stranded DNA. Here, the cut (recipient) chromosome is shown in red, and the donor intact chromosome is shown in blue. After the DSB forms, the ends of the break undergo 5' to 3' end resection, exposing ssDNA. Initially, RPA loads onto the ssDNA before being replaced by DMC1 and RAD51. The DMC1 coated 3' end invades into the homolog to form a D-loop, and RPA stabilizes the displaced strand. The invaded strand is then extended by polymerization (shown by the dashed line).

Hinch, A.G., Becker, P.W., Li, T., Moralli, D., Zhang, G., Bycroft, C., Green, C., Keeney, S., Shi, Q., Davies, B., and Donnelly, P. (2020). The Configuration of RPA, RAD51, and DMC1 Binding in Meiosis Reveals the Nature of Critical Recombination Intermediates. Mol Cell *79*, 689-701 e610. 10.1016/j.molcel.2020.06.015.

Synthesis-dependent strand annealing (SDSA):

In mice, humans, and many other organisms, the number of initiating DSBs during meiosis is ~10 fold higher than the number of crossovers required for proper chromosome segregation [37]. Most of the DSBs in yeast, mouse, and humans are repaired as short patch-like products called non-crossovers(NCO) via synthesis-dependent strand annealing or SDSA [115]. SDSA is genetically and temporally separate from the crossover pathway in both yeast and mice [Rhea Kang, Francesca Cole unpublished [61,116,117]]. In SDSA, the cut chromosome invades the donor, is polymerized, and is then ejected from the D-loop. The newly synthesized DNA strand can either anneal back to the other end of the cut parental chromosome and complete repair or undergo template switching. During template switching, the invading strand switches back and forth between the sister and the homolog, with each template switch, the cut chromosome invades, is polymerized, and is then ejected. In budding yeast, a typical SDSA event can involve multiple rounds of template switching [118,119] (**Figure 10**); however, extensive template switching has not been observed in SDSA in mice [120-122]. Additionally, the repair tract length of SDSA products, i.e. NCOs, are longer in yeast (~1.5 - 2 kb) than in mouse spermatocytes (~30 bp) [118-121,123].

More importantly, unlike crossovers, which can be detected cytologically in mouse spermatocytes, NCOs are invisible to cytological approaches. Therefore, to detect and analyze NCOs one must analyze the genomic DNA for repair either by using a variation of Southern blotting [124,125], or via sequencing [118,119]. Further, these NCOs and other recombination outcomes can only be analyzed in an F1 hybrid, in which the recipient and donor chromosome contain different sequences (polymorphisms). Crossovers involve the exchange of the entire chromosome arm and therefore incorporate multiple polymorphisms from the donor. Therefore, crossovers are always detected in our assays. However, NCOs repaired by SDSA have been estimated to be only about ~30bp and may not always incorporate a polymorphism from the

donor as typical polymorphism density at this hotspot is ~0.8/100 bp [61,120]. Therefore, NCOs from SDSA are detected only if the products incorporate a donor polymorphism.

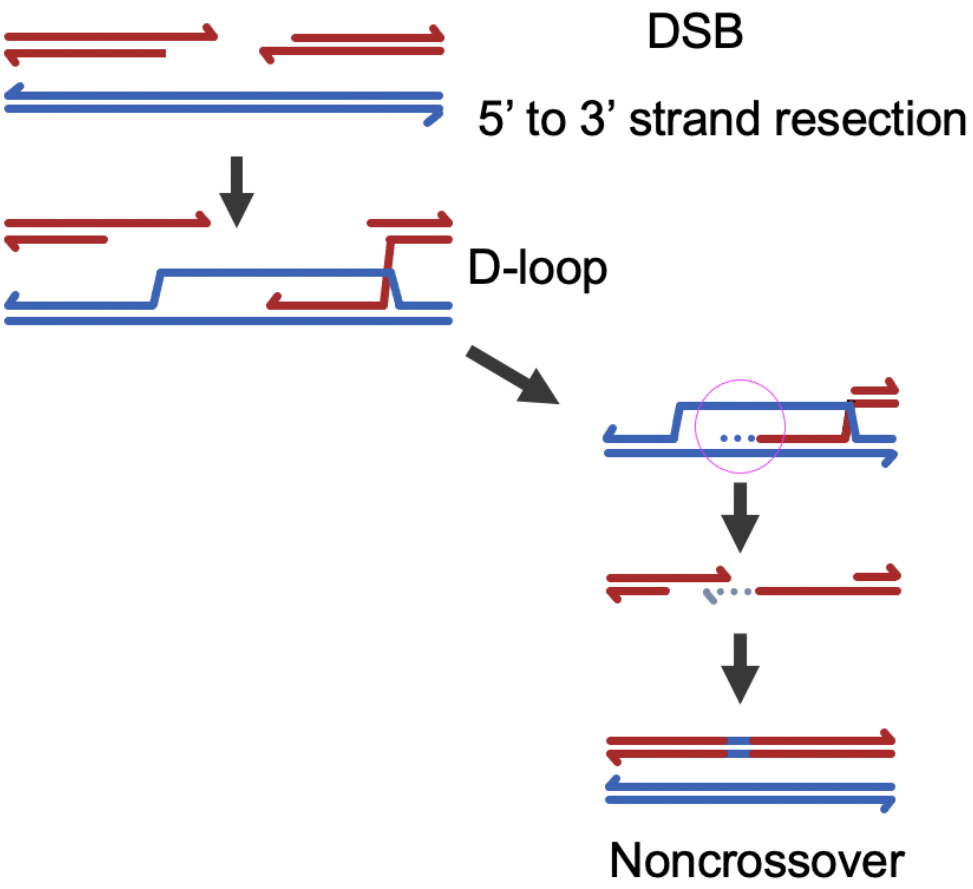

Figure 10: Schematic of SDSA
The cut chromosome is shown in red, and the donor chromosome in blue. The newly synthesized strands are shown as dashed lines and marked by the magenta circle. During SDSA, the invading strand in a D-loop is polymerized, gets displaced, and anneals back to the other end of the parent strand to complete repair.

Crossover designation

In simple terms, crossover designation is the process by which D-loops are converted into precursor intermediates for crossovers. In yeast, the first detectable intermediate in crossover repair is a single-end invasion (SEI) [126] The SEI is an asymmetrical intermediate like a stabilized D-loop with only one of the 3’ DSB ends invading the donor (**Figure 11**). The

second crossover precursor identified in yeast was the double Holliday Junction (dHJ), where the SEI captures the second 3' end of the DSB (**Figure 11**). Prior to this work, the first crossover precursor intermediate was unknown in mice or any other organism. Further, it was unclear if the second dHJ intermediate formed in mouse spermatocytes [127]. Crossovers are required for fertility and therefore, the survival of any species. However, in most organisms, the total number of crossover precursor intermediates per cell that is available to be assigned equates to the total number of homologous chromosomes. Therefore, crossover precursor intermediates must be distributed such that each homolog pair receives at least one of these precursors. Several regulatory mechanisms and proteins act to ensure that the precursors are distributed properly and ensure that every homolog in each meiotic cell gets a crossover precursor. A brief overview of the relevant regulatory mechanisms and proteins is provided below.

Crossover designation is regulated by a class of proteins called ZMM proteins, named after the Zip/Mer/Msh family of proteins first discovered in yeast [128]. These pro-crossover factors regulate both the number and distribution of crossovers across meiotic cells. Relevant members of the family include yeast Zip3 and its mouse orthologs Ring Finger Protein 212 (RNF212) and E3 ubiquitin ligase HEI10 [129,130]; yeast Mer3 and its mouse ortholog HFM1 [131]; and the yeast meiosis-specific mismatch repair-related Msh4-Msh5 MutSgamma complex, composed of orthologs MSH4 and MSH5 in mice [128,132]. The crossovers regulated by ZMM proteins are called Class-I crossovers, which show features like positioning farther apart than expected by chance (crossover interference) and crossover homeostasis where the number of crossovers is maintained despite fluctuations in early recombination intermediates. In budding yeast, the ZMM-independent crossovers, or class-II crossovers, form a significant proportion of crossovers (~40%), but it is the class-I crossovers that play roles in fidelity of chromosome segregation and spore viability [133]. This data clearly illustrates the importance of crossover distribution dictated by crossover interference in proper chromosome segregation. Yeast is an exception in terms of the number of crossovers per meiosis, as they receive many more

crossovers (~90 in budding yeast) than there are homolog pairs (16 in budding yeast). In most organisms, including mice and humans, the number of crossovers per germ cell is slightly more than the number of homologs, and most of those crossovers are ZMM-dependent (>95%) [134]. In mammals, the ZMM-dependent crossover pathway plays crucial roles in mitigating germline aneuploidy. Relevant to this thesis, there are three interrelated features of ZMM crossovers with underlying mechanisms in mice: crossover assurance, crossover interference, and crossover homeostasis.

Crossover assurance describes the observation that in a meiotic cell every homologous chromosome pair will have at least one crossover, thus named the obligate crossover. This observation has been made in all organisms that rely on crossovers to segregate chromosomes [57-59]. Since crossovers allow sister chromatid cohesion to physically connect homologs (**Figure 4**), at least one crossover per homolog is necessary for proper chromosome segregation. It is therefore reasonable to speculate that the obligate crossover requirement must have driven meiotic cells to evolve crossover interference and crossover homeostasis to work with a limited number of crossover precursors and prevent aneuploidy. Crossover interference and crossover homeostasis were discovered independently, but in many organisms including mice, these two phenomena may be two separably measured facets of the same underlying regulation.

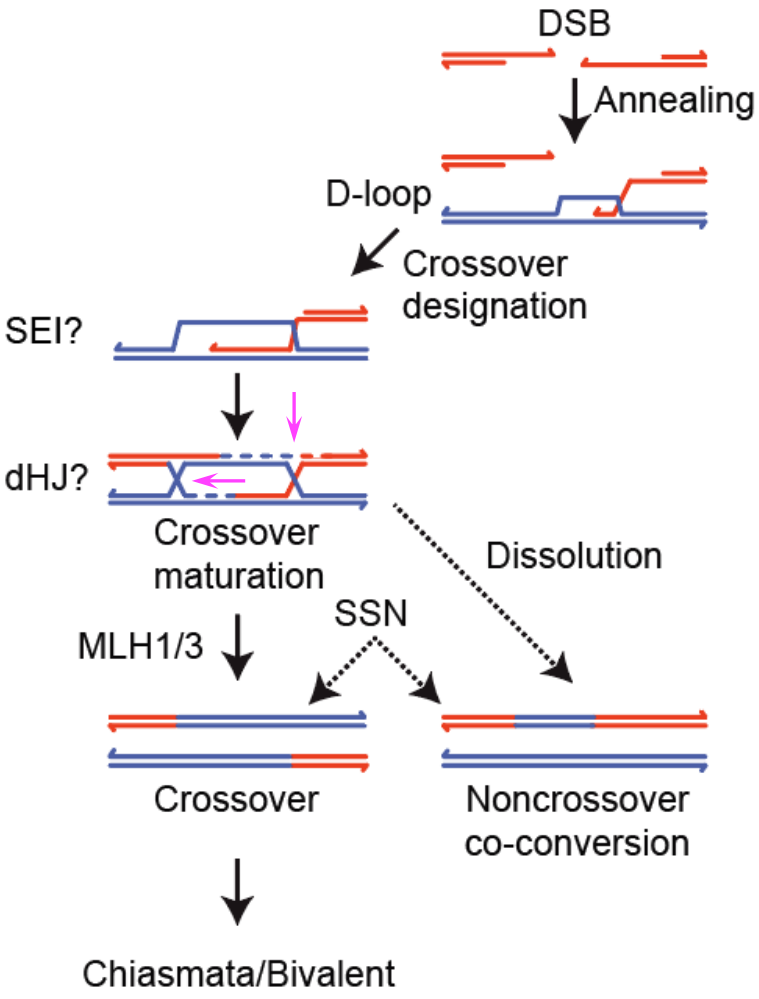

Figure 11: Schematic of crossover pathway

Schematic outline of the crossover pathway, most of which is extrapolated from budding yeast. Once DSBs are induced, the ends undergo 5' to 3' end resection to produce 3' overhangs that invade into the homolog to form a D-loop. It is thought that a small proportion of all D-loops become a single-end invasion intermediate (SEI) in a process called crossover designation. The SEI is then converted into a double Holliday Junction (dHJ), which is then converted into a crossover via a process called crossover maturation. To convert dHJ into a crossover, the intermediate has to be cut at orthogonal planes, in a coordinated manner (e.g., here inner two strands on the left and outer two stands on the right, cutting planes by arrows). A simple crossover product that has undergone mismatch repair correction is shown. SEI and dHJ are followed by a question mark '?' to denote that evidence for the existence of these intermediates has not been shown in mammals. In mice, most of the crossovers are ZMM dependent thus, they also depend on meiosis specific resolvase MLH1/3 MutLgamma complex that likely does coordinated resolution of dHJs. It has been shown that structure-selective nucleases (SSN) contribute ~5-10% of the total crossovers in mice. SSNs, unlike MLH1/3 can produce both crossovers and co-conversions from dHJs and, therefore, are less efficient than MLH1/3 for producing crossovers from dHJs. Dissolution also acts upon dHJs, converting the dHJ

exclusively into NCOs that are distinctly longer (>300 bp, on average) also called co-conversions.

Crossover interference

Once a D-loop is converted into a crossover precursor, another crossover precursor will not be designated nearby on the same chromosome (**Figure 12**). This observation and the underlying process is termed crossover interference, and the interference signal is observed to spread along the chromosome axis. The interference between crossovers is only observed for class-I ZMM-dependent crossovers and has been seen in many organisms including budding yeast, mice, and humans [57,135,136]. It has been well established from work done in yeast that crossover interference does not require synaptonemal complex formation and likely occurs in leptonema-zygonema. Observations in yeast also suggest that almost all the designated crossover precursor sites that are cytologically visible as ZMM foci eventually become crossovers [128].

In contrast, the details of crossover interference in mouse are less clear. In mice, defects in synaptonemal complex formation also disrupt both the recruitment of crossover-promoting factors to chromosomes and crossover formation [37]. Further, it is difficult to determine when the crossover precursor intermediates are designated. The amount of cytologically visible ZMM protein foci in zygonema and early pachynema far exceed the number of crossovers [129,130,137]. To explain the discrepancy between the number of early ZMM foci and crossovers in mouse spermatocytes, it has been suggested that many DSBs on chromosomes can potentially be repaired by the crossover pathway (~150 sites) but are winnowed down to only a few (~24 sites) by mid-pachynema. It is these few sites that are converted into crossovers by a process called crossover maturation.

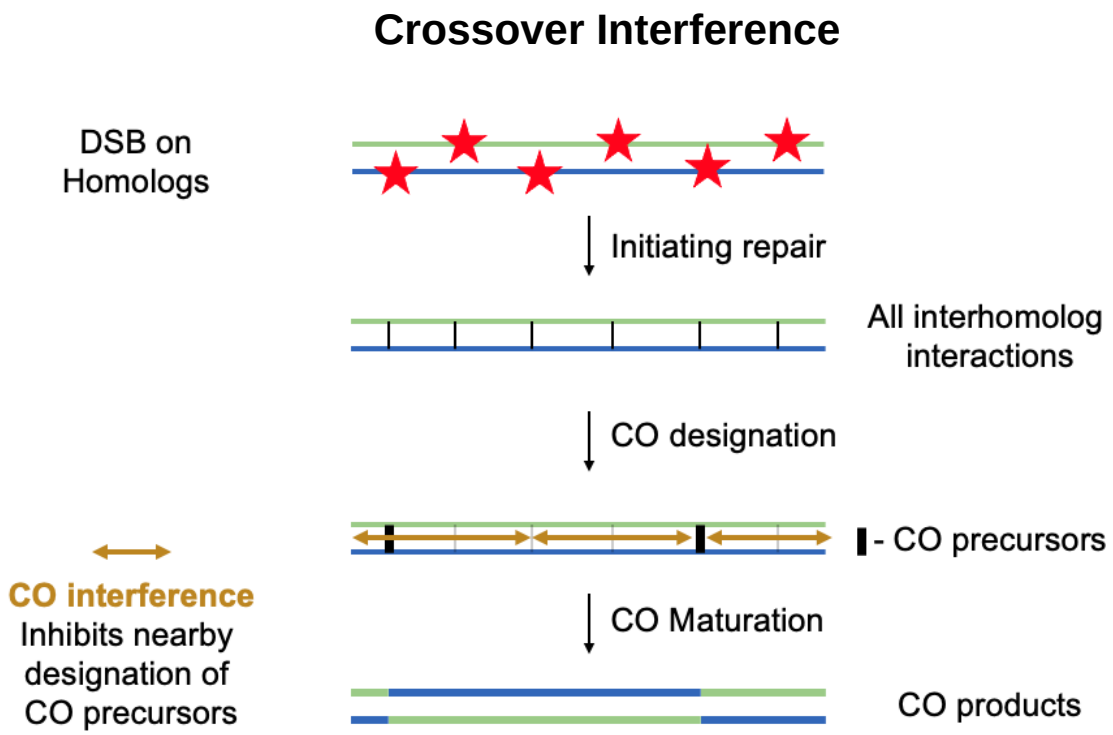

Figure 12: Schematic of crossover interference
Homologs are depicted by green and blue lines. Sister chromatids are not shown for simplicity. The DSB sites are marked by red stars. Early interhomolog interactions are marked by thin black lines between homologs. Crossover precursors are shown with thick black lines and interference is depicted with a brown two-sided arrow. Crossovers are depicted by the exchange of chromosome arms or color-switching lines in the bottom-most row.

Crossover Homeostasis

Crossover homeostasis was first observed in budding yeast and was subsequently observed in many organisms, including mice [138,139]. Crossover homeostasis is considered normal when the final number of crossovers per cell is maintained within a narrow margin, despite large fluctuations in the number of initiating DSBs [139]. The details on how crossover homeostasis is implemented are still unclear; however, it has been suggested that crossover homeostasis may depend on crossover interference, as crossover interference determines both the upper and lower limits of the number of crossovers per cell for a given chromosome axis length [140]. When crossover homeostasis is normal the changes in numbers of initiating DSBs is

buffered, likely by changing the number of SDSA events to compensate for and maintain the number of final crossovers [139]. Observations in mice have shown that crossover homeostasis, when normal and active, can buffer up to ± 30% fluctuations in early recombination intermediates without affecting the number of crossover sites, cytologically marked by MutLgamma complex proteins MLH1 and MLH3 [138].

RNF212 and HEI10

Zip3 is a RING domain protein that is thought to act as a E3 SUMO ligase. In budding yeast, Zip3 is required for crossover designation to occur. Zip3 is the earliest acting ZMM protein and is genetically upstream to all other ZMM proteins in yeast [141,142]. The mouse orthologs for Zip3 are RNF212 and HEI10, and both RNF212 and HEI10 play crucial roles in crossover formation in mouse spermatocytes [129,130,137].

RNF212 is a RING finger domain-containing protein with putative E3 SUMO ligase activity. RNF212 is cytologically visible as >100 foci along the chromosome axis during the leptonema to zygonema transition, which decrease, dropping to ~20 foci by mid-pachynema. Current reports support the model that RNF212 promotes crossover designation and the formation of crossover precursors. Consistently, when RNF212 is absent almost no connected homologs or bivalents are observed in metaphase and the mouse is sterile. Further, when RNF212 is absent, another crossover-promoting factor, MSH4, is removed from chromosome sites faster, as expected, if chromosomes lack crossover precursors [129]. The definitive evidence for the lack of crossover designation relies on recombination analysis performed using *Rnf212*$^{-/-}$ spermatocytes. When crossover designation occurs but crossovers are not matured, the designated precursors are converted into long NCOs that are long enough to incorporate multiple consecutive polymorphisms from the donor homolog in a F1 hybrid. These long NCOs arise via alternative pathways and are called co-conversions [61]. However, earlier work in our lab showed that *Rnf212*$^{-/-}$ spermatocytes neither produce crossovers nor form co-conversions. Instead, we saw a corresponding increase in SDSA-dependent NCOs that typically only incorporate one polymorphism from the donor in an F1 hybrid called singletons, indicating that

Rnf212$^{-/-}$ spermatocytes lack crossover designation completely (Rhea Kang, Francesca Cole unpublished)

HEI10 is an E3 ubiquitin ligase that has been proposed to antagonize the crossover-promoting function of RNF212. When HEI10 is absent, RNF212 foci form at a higher frequency and persist longer, along with MSH4 foci, suggesting a delay in the removal of these factors. Like spermatocytes that lack RNF212, those that lack HEI10 do not form crossovers either, as HEI10 has an additional function that is required before the conversion of crossover precursors into crossovers (crossover Maturation) [130,137,143].

HFM1

Another ZMM protein required for crossover designation in yeast is an ATP-dependent helicase Mer3, and its paralog in mouse is HFM1 [128,144,145]. HFM1 bears protein motifs commonly seen in DNA and/or RNA helicases [146]. In budding yeast, Mer3 plays a role in early recombination and has a structural role in controlling the length of all DNA repair intermediates during meiosis [144,147]. In yeast lacking Mer3, and consistent with its role as a ZMM protein, there is a slight but significant reduction of the first crossover precursor SEI and a severe reduction in the second crossover precursor dHJ [133,145,148,149]. Mice lacking HFM1 are sterile, and in spermatocytes that lack HFM1, only ~20% homologs form metaphase bivalents as compared to ~100% of homologs in wildtype (WT) spermatocytes. Consistent with the proposed role for Mer3 in early recombination in yeast, mouse spermatocytes lacking HFM1 show delayed repair of early recombination intermediates, but unlike *mer3*$^{-/-}$ yeast, spermatocytes lacking HFM1 show milder defects in synaptonemal complex formation [131,146]. More importantly, based on current evidence, it is unclear whether HFM1 is required for crossover designation in mice and whether HFM1 regulates the length of repair events. Considering that co-conversions are observable only in mutants with crossover designation, in this work, I isolated co-conversions and found that crossover designation does occur in spermatocytes lacking HFM1

Crossover maturation

Crossover maturation is the final step of the crossover pathway during which the crossover precursor is converted into a crossover. In mice, most crossovers require the MLH1/3 MutLgamma complex for the efficient conversion of crossover precursors into crossovers [150]. Proper crossover maturation thus requires all of the upstream processes of DSB formation, strand invasion, crossover designation, interference and homeostasis and their associated proteins (mentioned above, **Figure 11, 12**) to be present and functional [37].

MLH1/MLH3 MutLgamma complex

Many of the proteins involved in the crossover pathway, including MLH1 and MLH3, were co-opted from mismatch repair. In mismatch repair (MMR), MLH1 partners with PMS2 to form the MutLalpha complex, the main MMR complex [150]. The MutLgamma complex (MLH1/MLH3) acts primarily during meiotic recombination but was also seen to play a minor role in MMR in yeast [151]. During meiotic crossover formation, the MutLgamma complex (MLH1/MLH3) has been proposed to function enzymatically in a similar fashion as MMR proteins rather than by a classic endonuclease [152,153].

During pachynema, MLH1-MLH3 MutLgamma complex associates with chromosomes at putative crossover sites to form ~24-26 foci in WT mouse spermatocytes. The MutLgamma complex is an obligate heterodimer of MLH1 and MLH3, and spermatocytes lacking either MLH1 or MLH3 are infertile and defective for crossing over. In fact, the MutLgamma complex is responsible for producing almost all ZMM-dependent crossovers and is required for >90% of the crossovers in mouse [154]. Therefore, the number of MLH1-MLH3 foci present during pachynema can be used both to calculate crossover interference and to determine the number of crossover in the mutants of interest [154-158]. The endonuclease activity of MutLgamma comes entirely from MLH3 [152,153]. However, the ATPase domain of MLH1 is also required for proper crossover formation [156,159,160]. MLH3 has a metal ion binding endonuclease motif DQHA(X)2E(X)4E that is shared with PMS2 and required for its nuclease and crossover-promoting activity. This metal-binding motif is also found in PMS2 and is necessary for PMS2-

dependent MutLalpha nuclease activity [159,161]. Consistent with the importance of the metal-binding motif, a single point mutation in *MLH3* that substitutes asparagine for aspartate at amino acid 523 eliminates MLH3-dependent crossovers in budding yeast without disrupting the MLH1-MLH3 interaction [159]. A similar point mutation in mice (*Mlh3*$^{DN/DN}$) does not cause a complete loss of MLH3-dependent crossovers in mice, perhaps because *Mlh3*$^{DN/DN}$ retains residual MLH3 nuclease activity [160]. Although both MLH1 and MLH3 are needed for the MutLgamma complex to form, MLH3 is also recruited to chromosome sites prior to MLH1, suggesting that MLH3 may have roles in addition to its role in MutLgamma complex [162]

In line with additional roles for MLH3, the nuclease-deficient allele of MLH3 (*Mlh3*$^{DN/DN}$) is phenotypically different from spermatocytes lacking MLH3 for many repair intermediates. *Mlh3*$^{DN/DN}$ spermatocytes have increased numbers of early recombination intermediates, marked by RAD51, in zygonema, whereas *Mlh3*$^{-/-}$ spermatocytes have decreased numbers of early recombination intermediates compared to WT. In contrast to spermatocytes with a complete loss of MLH3 (*Mlh3*$^{-/-}$ spermatocytes), in which MLH1 foci are absent, spermatocytes bearing the *Mlh3*$^{DN/DN}$ mutant allele form both MLH1 and MLH3 foci like WT spermatocytes during pachynema. Likewise, a few other crossover-promoting factors, including HEI10 and CDK2 form WT numbers of foci in *Mlh3*$^{DN/DN}$ spermatocytes during pachynema. Whereas in *Mlh3*$^{-/-}$ spermatocytes, there is an increase in HEI10 foci and a complete lack of CDK2 foci. Together, these findings indicate that in mice, MLH3 may have a nuclease-independent role as *Mlh3*$^{DN/DN}$ retains partial MLH3 function [160].

Figure 13: MutL homolog 3 (MLH3):

A simple schematic representation of domains of MLH3. The ATPase domains are located in N-terminus while the amino acid residues responsible for nuclease activity (motif: DQHA(X)2E(X)4E) are located in c-terminus. MLH3's crossover role requires interaction with MLH1 forming MutLgamma complex and likely its nuclease activity in mice ([160] and this work). The nuclease deficient allele used in this work converts the first D to N (D1185N).

EXO1

The enzymatic function of MLH3 is stimulated by many proteins in vitro including EXO1 [152,153,163]. EXO1 is a 5' to 3' nuclease that has roles in multiple processes including MMR and homologous recombination [164]. During meiosis in budding yeast, but not in mice, Exo1's nuclease activity is required for extended resection (~1kb) of meiotic DSBs [104,105,108,165]. This loss of long resection in budding yeast does not affect either the initiation or progression of meiotic recombination, indicating that extended resection by Exo1 in yeast, plays a minimal role in these steps [104,166]. Independent of its resection role, Exo1 has a nuclease-independent role in MutLgamma-dependent crossover formation in budding yeast [167]. This role is mediated via Exo1's interaction with Mlh1 of the MutLgamma complex [104].

In mice, like yeast, EXO1's crossover function is likely nuclease-independent [104,168]. Loss of Exo1 in budding yeast leads to the loss of all MutLgamma-dependent crossovers and loss of crossover interference [104,166,167]. Consistent with this crossover-promoting role, human EXO1 stimulates the enzymatic activity of MLH3 of the MutLgamma complex *in vitro*. However, this *in vitro* stimulation only accounts for ~10% of MLH3's nuclease activity and may not explain the massive *in vivo* crossover loss seen in both yeast cells and mouse spermatocytes lacking EXO1 [104,152,153,156,169]. In budding yeast, Exo1 recruits polo kinase (Cdc5), which in turn activates MutLgamma-dependent crossovers [163]. This could explain why a lack of Exo1 leads to a disproportionate loss of MutLgamma-derived crossovers. Importantly, although budding yeast lacking EXO1 lose all MutLgamma-derived crossovers, this work shows that mouse spermatocytes lacking EXO1 only lose ~70% of the crossovers, indicating that the MutLgamma complex remains partially active in mice without EXO1.

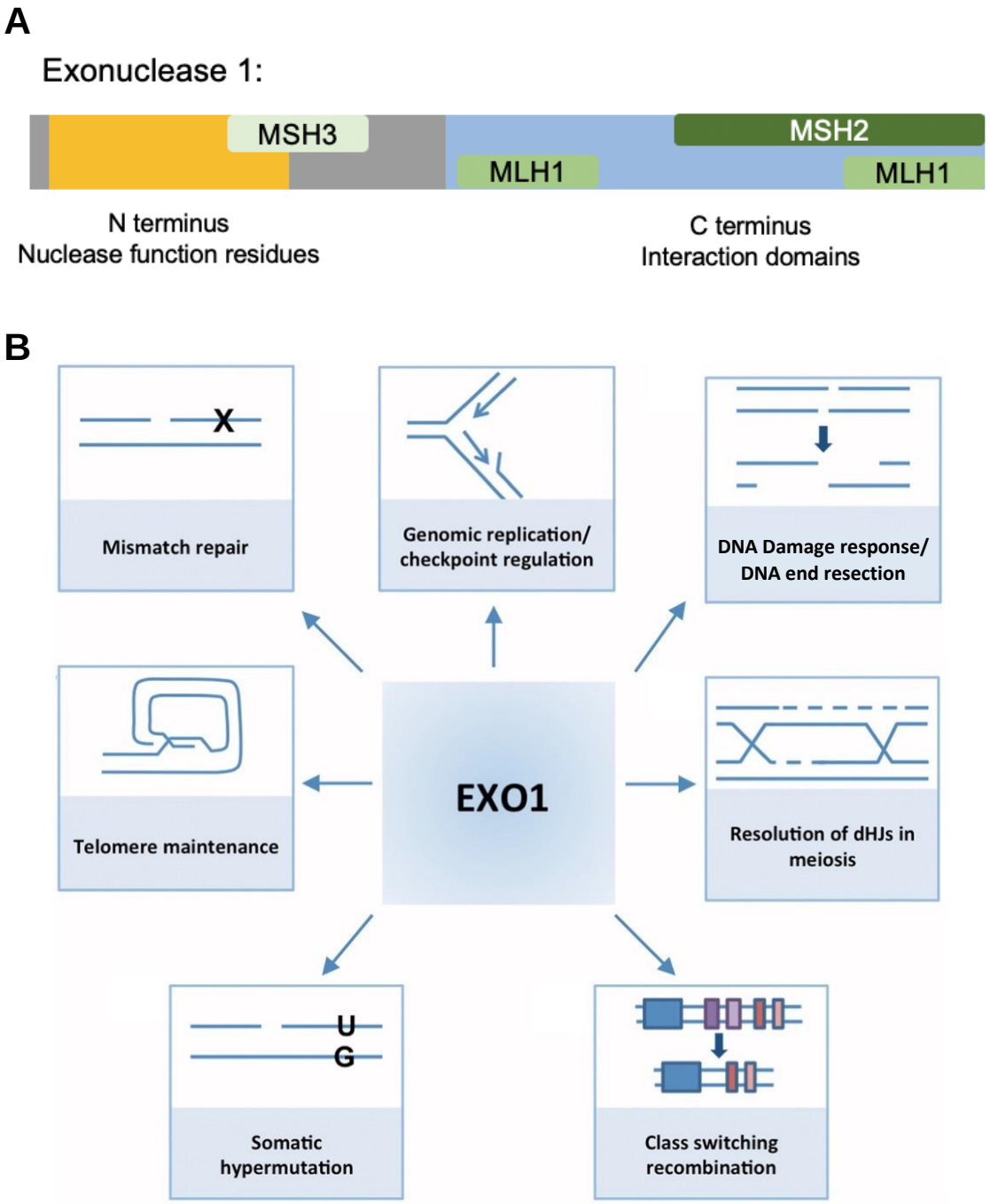

Figure 14: Exonuclease 1 (EXO1)
(A) A simple schematic of EXO1 protein. The amino acid residues important for the nuclease function of EXO1 are located in the N-terminus (orange), whereas the c-terminus of EXO1 (blue) is enriched for interaction domains. The interaction sites of EXO1 with MMR MutS homolog proteins MSH3, MSH2 and meiotic recombination protein MLH1 is marked by colored boxes. The nuclease-deficient allele of EXO1, EXO1-D173A depletes >95% of the nuclease

function of EXO1-D173A *invitro* without significantly affecting the nuclease-independent roles of EXO1. *Exo1*$^{D173A/D173A}$ is largely similar to *Exo1*$^{-/-}$ *in vivo*, when assayed for roles that that require its nuclease activity (e.g., class switch recombination) [168].EXO1 interacts with MLH1-MLH3 (MutLgamma complex) for the nuclease-independent role in recombination [104].
(B) EXO1 is a versatile enzyme that has roles in multiple processes and the processes are labelled here.
Keijzers, G., D. Liu and L. J. Rasmussen (2016). "Exonuclease 1 and its versatile roles in DNA repair." Crit Rev Biochem Mol Biol **51**(6): 440-451.

MUS81

Other than the MutLgamma complex, the only other class of enzymes capable of producing crossovers are the structure-selective endonucleases (SSNs). SSNs can convert crossover precursors into both crossovers and NCOs [37]. However, evidence for such unbiased conversion has not been seen in mouse spermatocytes *in vivo*. In mice, there are three SSNs, including MUS81 [37]. In budding yeast, almost all crossovers occurring in *mlh3*$^{-/-}$ or *exo1*$^{-/-}$ yeast (~40% of the WT crossover frequency) require Mus81 [167,170]. Similarly, MUS81 also contributes to crossovers in *Mlh3*$^{-/-}$ spermatocytes, but accounts for only 5-10% of bivalents seen in WT. This low frequency could be because ~90% of the bivalents are lost in *Mlh3*$^{-/-}$ spermatocytes compared to 50-60% crossover loss in *mlh3*$^{-/-}$ and *exo1*$^{-/-}$ yeast [134]. Although mice lacking MUS81 are fertile, *Mus81*$^{-/-}$ spermatocytes show mild defects. The defects include late appearance of chromosomal RAD51 foci in, a marker for strand exchange, suggesting the presence of unrepaired DSBs in *Mus81*$^{-/-}$ spermatocytes as compared to WT. *Mus81*$^{-/-}$ spermatocytes also show one additional MLH1 focus per cell on average, suggesting that some of the ZMM-dependent crossovers may be processed by MUS81 [134]. Therefore, in this work, I removed MUS81 alongside EXO1 to test whether the residual crossovers in *Exo1*$^{-/-}$ spermatocytes require MUS81.

Current technical and knowledge limitations in meiosis literature and our contribution from my work

Most of the details regarding DNA interactions and DNA repair intermediates during meiosis are extrapolated from yeast. Historically, yeast has been used to study meiosis due to many technical advantages. First, genetic manipulation is easy to perform in yeast; and an equivalent system i.e., cell lines for mammalian meiotic recombination do not exist. Second, two-dimensional gel electrophoresis techniques can separate crossover precursors from back by their 3D structure and were developed at least 30 years ago in yeast [126,127,171]. Third, in the yeast, hotspot used for 2D gel analysis (*HIS4 LEU2*) yields >20% crossovers, as opposed to ~0.75% at the mouse *59.5* hotspot [61,172]. Thus, in budding yeast, there is a very high signal-to-noise ratio when isolating crossover precursors using 2D gel electrophoresis [171]. Further, both SEI and dHJ intermediates in yeast are fairly long (~1.5-2 kb) compared to mouse pSEIs (~0.3 kb) (this thesis) and dHJs (~0.6 kb) [118-121,126,127,171]. The popular method for isolating these intermediates involves DNA-DNA crosslinking, thus longer intermediates allow for a greater proportion of recovered intermediates that retain the 3D structure. The smaller intermediate length and lower frequency of intermediates together make the application of 2D gel electrophoresis techniques in mice quite difficult. Fourth, mismatch defective *msh2*$^{-/-}$ yeast retain many of the mismatches between the newly synthesized strand and the parent strand during DNA repair by homologous recombination. Additionally, since yeast spores, the products of yeast meiosis, can be expanded clonally in their haploid state, the progeny from spores can be sequenced to analyze the retained mismatches and infer the progression of repair [118,119]. Spermatocytes lacking *MSH2* retain far fewer mismatches [122], making it difficult to infer recombination pathways. Finally, in this thesis, I determined that mismatch correction directed by MLH3 nuclease activity likely contributes to the removal of a large fraction of mismatches.

Nonetheless, while extrapolating DNA repair mechanisms from yeast can be helpful, it can also be problematic as there are many mechanistic distinctions between mammals and yeast. The differences between yeast and mice are outlined through this thesis as they appear,

and in the conclusion. In mouse spermatocytes and oocytes, cytological staining and analysis of proteins that localize to DNA repair intermediates have been used with great success. However, interpretation can be difficult as the steady-state number of protein foci results from a combination of both recruitment and turnover/lifespan and may not capture subtle phenotypes. Although this approach provides a great deal of information on proteins that are involved in a particular repair step, it yields little information regarding the underlying DNA repair intermediates. The cytological approach is not applicable for the study of certain repair events, for example, SDSA derived NCOs – the major repair outcome in meiosis – limiting its usefulness.

To delineate the mechanisms of meiotic recombination, an approach that directly or indirectly isolates features of DNA recombination intermediates is needed. To that end, I used a fine-scale recombination analysis - a genotyping protocol that uses polymorphism differences between parental haplotypes to track repair. This technique was originally established to study recombination in human meiotic hotspots [125] and was adapted to mice by my mentor Francesca [121,124], and can be used to track all inter-homolog repair events that incorporate a donor polymorphism.

To define the characteristics of crossover precursors, we analyzed 13 different genetic combinations – many of which fail to form crossovers at different stages of meiosis using our fine-scale recombination analysis (**Figure 46**). I infer the existence of two crossover precursors in mammals, a polymerized single-end invasion (pSEI) and a double Holliday Junction (dHJ). By genotyping all of the individual strands from alternative repair products generated when crossovers fail to form, I show evidence for dual end extension of 3' DSB ends, as is predicted in a dHJ. Finally, I provide the first evidence in any organism that MLH3 is genetically required for the formation of the dHJ.

Materials and Methods

Animals

All experimental mice were C57BL/6J x DBA/2J (BxD) F1 hybrids and were obtained from crosses: C57BL/6J (B) and DBA/2J (D). All single mutants used in this study (*Exo1*$^{-/-}$, *Hfm1*$^{-/-}$, *Hei10*$^{-/-}$, *Rnf212*$^{-/-}$, *Rmi2*$^{-/-}$, Mlh*3*$^{-/-}$, *Mlh3*$^{DN/DN}$, and *Msh2*$^{-/-}$) were maintained as heterozygotes in B and D backgrounds, independently. The double mutants (*Mlh3*$^{-/-}$ *Exo1*$^{-/-}$, *Mus81*$^{-/-}$ *Exo1*$^{-/-}$, and *Msh2*$^{-/-}$ *Exo1*$^{-/-}$) were similarly maintained as heterozygotes for both the genes involved in B and D backgrounds, independently. Expect for the *Mlh3*$^{-/DN}$ experimental cross, the *Mlh3*$^{+/-}$ parent was always from the D background and the *Mlh3*$^{+/DN}$ parent came from a B cross. *Msh2*$^{+/-}$ was generated by crossing mice with a heterozygous Msh*2.1*$^{tm2.1Rak/J/WT}$ allele to mice carrying Stra8-Cre. Subsequent *Msh2*$^{+/-}$ animals were maintained as a whole-animal heterozygotes as for all other alleles. Finally, all mice used as parents for experimental animals were backcrossed to their respective backgrounds (B or D) for at least 3 generations and homozygosity for the entirety of hotspot *59.5* was checked before experimental mating.

Spermatocyte spreads

Spermatocyte spreads were performed as described [61]. Testes were decapsulated and depending on downstream workflow, either all decapsulated tissue or only part of it (as little as half of the tissue from a mutant) was used to make spermatocyte spreads. The tissue was digested in ~2 mL of collagenase (2 mg/mL) dissolved in testis isolation medium (TIM, TIM: 104 mM NaCl, 45 mM KCl, 1.2 mM $MgSO_4$, 0.6 mM KH_2PO_4, 0.1% (w/v) glucose, 6 mM sodium lactate, 1 mM sodium pyruvate, pH 7.3). Digestions were performed in a shaker-incubator (500 rpm) for 55 mins at 32°C. Post digestion, the separated tubules were washed thrice with 15 mL of fresh TIM. At each wash, the tubules were allowed to settle before removing the wash liquid, taking care to not remove the tubules. The washed tubules were digested in ~2 mL of trypsin dissolved in TIM (0.7 mg/mL) containing DNAse I (4 μg/mL) in a shaker-incubator (500 rpm) at 32˚C for 15 minutes. During digestion, a flat moist chamber was prepared with wet paper

towels, water, and a suitable slide box. Cleaned and labeled slides were added to this box and the box was kept closed to keep the moisture in, until the later steps.

Digestions were stopped by adding trypsin inhibitor to the mix to a final concentration of 4 mg/mL. In addition, 50 μL of DNAse I (0.4 mg/mL in PBS) was added to the mix. A transfer pipette was used to separate the cells from tubules by agitation for 2 mins, before filtering through a 70-micron strainer to remove any remaining intact tubules. The resulting cells were washed twice with gentle centrifugation (1000 rpm, 5 min, Eppendorf rotor S–4–72), followed by re-suspension in fresh TIM containing DNAse I (1 μg/mL). After the two washes, the cells were harvested as described above followed by resuspension in a volume of fresh PBS containing DNAse I. About 1 mL of cells resuspended in PBS solution was harvested by centrifugation (1500 rpm, Eppendorf, Rotor FA-24x2), before resuspending in prewarmed (37 °C), hypotonic 0.1 M sucrose solution for 5 mins. In the meantime, 65 μL prewarmed (37 °C) 1% PFA (pH 9.2)/ 0.1% Triton X-100 was laid onto the glass slides in the moist chamber. The hypotonic sucrose cell suspension was then dropped onto the slides in the pool of PFA, about ~20 μL per slide. The slide boxes were closed and left undisturbed for 2.5 hours, before cracking the lid open for 30 mins, and then completely opening the lid for another 30 mins. Subsequently, the slides were washed once with water, twice with Photo Flo 200 solution (1:250 in water), and air-dried before storing at -80°C.

Immunofluorescence

Immunofluorescence imaging was done on spermatocyte spreads stained with antibodies. The entirety of the antibody staining was performed in a moist flat chamber, and care was taken to not let the slides dry during the staining process. For antibody staining, the slides were first blocked for 30 mins at 37 °C with antibody dilution buffer (ADB, ADB: 10% goat serum, 3% BSA, 0.05% Triton X-100, 1x PBS). Post blocking, the slides were incubated with ADB containing primary antibodies diluted to the recommended concentration, either at room temperature, overnight, or at 37 °C for 1 hour. After primary antibody staining, the slides were

washed once with Photo Flo diluted in PBS (1x PBS/ 0.4% Photo-Flo 200), and then once with Photo Flo solution containing Triton-X (1x PBS/ 0.4% Photo-Flo 200/ 0.01% Triton X-100). Each of these wash steps was 5 mins, and the slides were then moved back to the moist flat chamber for blocking. During the second blocking step, the slides were blocked for 10 mins, at 37°C, followed by incubation with fluorescently labeled secondary antibody solution diluted in ADB. Once the secondary antibody was added to the slides, the slides were handled in dark. After secondary antibody staining, the slides were washed again. First with Photo Flo diluted in PBS (1x PBS/ 0.4% Photo-Flo 200) for 5 mins, followed by Photo Flo solution containing Triton-X (1x PBS/ 0.4% Photo-Flo 200/ 0.01% Triton X-100) for 5 mins, and finally with Photo Flo solution (1:250 in water) for 1 min. These slides were air-dried in the dark and mounted using Prolong Gold antifade which also has DAPI.

Metaphase spreads

This protocol was done as elaborated in [61]. In short, testes were decapsulated and the entire tissue or a part of it (as little as half a testis from a mutant) was used for this protocol. The tissue thus isolated was transferred to isotonic sodium citrate (2.9% in water) solution at room temperature. Using tweezers, the tubules in the tissue were pulled apart and agitated for about 5 mins to release the cells. This turbid supernatant is then transferred to a fresh tube, with care taken to not pick the tubules. The cells were pelleted by centrifugation (1000 rpm, 5 min, Eppendorf rotor S–4–72), resuspended, and incubated in hypotonic sodium citrate solution (1% in water) for 12 mins. Cells were immediately pelleted again, and the supernatant was removed as much as possible. The cells were resuspended, tap-mixed, and incubated in the fixative (Fixative: 3 parts 200 proof ethanol, 1-part glacial acetic acid, 0.025 parts chloroform, made fresh on the during the hypotonic incubation step) for 5 mins. The cells were then pelleted by centrifugation (1500 rpm, Eppendorf, Rotor FA-24x2), the supernatant was removed, and fresh fixative was added to the tube. The cells were properly mixed and incubated in a fresh solution of fixative for another 5 mins. A small amount of this cell suspension, say 60 μL is taken and a small drop from that is allowed to fall on a pre-cleaned

slide. More of the fixative cell suspension can be dropped to get the desired cell density, onto the same slide after the initial drop has dried. The slides were then washed for 5 min in water, followed by a 5 min wash in PhotoFlo-200 solution (1:250 in water), and then air-dried. These slides were stained for Giemsa, by incubating the slides in Giemsa solution with mild shaking for 45 mins. To remove excess stain, these slides were briefly washed with water, air-dried, and checked for staining intensity with the highest available magnification with a non-oil objective. Post stain intensity test, the slides were mounted with coverslips for imaging.

Synchronization of mouse spermatogenesis

Mouse spermatocyte synchronization was performed as described earlier by [94,173]. In short, a retinoic acid inhibitor WIN 18446 was fed using pipettes to pups starting 1-3 days postpartum (dpp), for at least seven days continuously, once every 22-24 hours, at 100 μg/g body weight. The WIN treatment was continued for additional days if the pups were below 4 gm by the last day of this treatment, as the subsequent retinoic acid injection (200 μg/pup) can be toxic if the pups were below 4 gm body weight. On the 8th day, if the pups weighed more than 4 gm, then they were injected with retinoic acid (200 μg retinoic acid in 10 μL dimethyl sulfoxide) intraperitoneally. Once injected spermatocytes enter meiosis and the exact time window can be calculated based on already established spermatocyte stage timing, reviewed in [173]. Because the spermatocytes enter meiosis in periodic waves, to get adult spermatocytes one needs to wait for at least the 4th wave of spermatocytes. Spermatocytes spend a similar amount of time through each of the meiosis I stage in all the waves and a specific stage repeat about every 8 days, although the specific day for each of the stages varies slightly between mutants and between animals of the same genotype, and therefore the exact time window per stage was experimentally determined and in the Table 4. For mutants (*Hei10*$^{-/-}$, *Rnf212*$^{-/-}$, *Mlh3*$^{-/-}$, and *Exo1*$^{-/-}$), the male neonates were tailed and genotyped between 0-2 dpp to test for animals homozygous for the mutant allele before synchronization treatment.

Spermatocyte enrichment by Fluorescence assisted Cell Sorting

Spermatocytes were enriched for specific stages using FACS as described by [61,120]. A testis was decapsulated and the tissue was then digested with 10 mL collagenase solution (0.5 mg/mL in Gey's Balanced Salt Solution, GBSS) while shaking (500 rpm) at 33°C for 15 mins. Post digestion, the tubules were allowed to settle, and the supernatant was removed, and the tubules were washed once with fresh 10 mL GBSS. These washed tubules were resuspended in trypsin solution in GBSS at 0.5 mg/mL and were supplemented with 1 μg/mL DNAse I. To trypsin digest tubules, these tubules were incubated in trypsin solution for 15 mins at 33°C, shaking at 500 RPM. After 15 mins, Newborn Calf Serum (NCS) was added (5% V/V) to stop the trypsin digestion. To separate the cells, this digested tubules-NCS suspension was aspirated continuously with a transfer pipette for 3 mins, and then the suspension was passed through a 70-micron cell strainer to remove intact tubules or clumped cells that may later interfere with the sorting. To wash, these suspended cells were pelleted by centrifugation (1500 rpm, 3 min, Eppendorf rotor S–4–72) and tap-mixed before resuspending in fresh GBSS with 2% NCS and the cells were washed twice. The cells were then resuspended in about 6 m of GBSS solution containing 5% NCS, 5 μg/mL Hoechst 33342, and 2% NCS. To stain the cells with Hoechst, the cells were incubated in the above Hoechst solution for 45 min, at 33°C, while shaking (500 rpm). Since longer sorts affect the health of the cells, the amount of the Hoechst solution used was reduced in the case of mutant tissues from 6 to 3 mL. At this point, propidium iodide was added (0.2 μg/mL) to the Hoechst-cells suspension to detect inviable cells. The cells were strained through a 70-micron BD cell strainer again right before initiating the sort.

These cells were flow-sorted in a BD Aria or BD Fusion flow cytometer, with the Hoechst staining stimulated with a UV 350 nm argon laser. Hoechst stain fluoresces both in red and blue wavelengths, where the intensity on the blue wavelength approximately corresponds to DNA content and the intensity on the red wavelength approximately corresponds to

chromosome compaction. If a synchronized animal was used for fluorescence sorting, distinct cell populations appear on the scatter plot. Spermatocytes from an unsynchronized animal however form a continuous population. The later stages (Pachynema and diplonema, also called Late-4C) appear towards the tail end of the distribution along the chromosome compaction axis. The collected isolated this way was used to make spermatocyte spreads which were then used to access the purity of the isolated population. This way the gating strategy was empirically optimized. To make the spermatocyte cells from the sorted cells, about 5000-20000 cells were taken and washed with PBS by centrifugation and resuspension (1500 rpm, Eppendorf, Rotor FA-24x2). These spermatocytes in PBS were then incubated in a hypotonic sucrose solution and spread on a glass slide containing 1% PFA similar to the spermatocyte protocol described above. These slides were then stained with stage-specific antibody combinations (anti-SYPC3/anti-SYCP1 along with anti-H1t or anti-gammaH2AX) to access the proportion of cells from the different meiotic cell stages present in the sample. The rest of the isolated cells were pelleted, and the supernatant was removed, snap-frozen, and transferred to -80 °C for long-term storage.

DNA Isolation

Genomic DNA isolation from spermatocytes was performed as described earlier in [61]. The frozen spermatocyte pellets were briefly thawed and resuspended in 500 μL of 0.2x SSC, pH 7 (SSC 20x: 3M NaCl, 0.3M Citric acid trisodium salt dihydrate). To this suspension, the following were added in order: 60 μL of b-mercaptoethanol, 10 μL of 20 mg/mL Proteinase K, and 50 μL of 10% SDS. This solution was incubated at 55°C, for 30 mins while shaking at 500 rpm. Post digestion the DNA was separated from this mix by extracting the aqueous layer following Phenol/Chloroform/isoamyl alcohol extraction. DNA was then precipitated by adding two volumes of ice-cold 200-proof ethanol and centrifugation at the highest speed (>20000g) for 10 mins. To remove any residual phenol or other contaminants, the pellet was resuspended in water and reprecipitated with Ethanol as above with added Sodium acetate. The salt was

then washed off with 70% ethanol. The pellet was then air-dried for 3-5 mins and was resuspended in 5 mM Tris pH 7.4 by incubating the pellet in ~45 μL of the 5 mM Tris overnight at 4°C.

Estimating amplification efficiency for isolated genomic DNA

The amplification efficiency of isolated genomic DNA was determined as described by [124]. The estimation begins with measuring the DNA concentration via nanodrop. Assuming that this nanodrop quantification is accurate, a 24 or 48-well PCR reaction was performed with 12 pg DNA (2 diploid genome equivalents) as input per PCR well. The input DNA was then amplified for 2 rounds of PCR (27 cycles 1st round and 32 cycles 2nd round), with nested primers. The PCR conditions were identical to the NCO amplification PCR reactions with one allele-specific primer and one universal primer. Thus, calculated amplification efficiency was associated with and was only valid for that primer pair – DNA – PCR buffer. For crossover amplifications since each round of PCR amplification utilizes two allele-specific primers, 2 sets of amplification efficiency reactions were performed, one per allele-specific primer, and the lower of the two values was used as the amplification efficiency of that primer pair. Post second round of amplification, in each of the cases, amplified products were run on a gel and the number of wells without a band was quantified. The amplification efficiency of 1 genomic equivalent of DNA or amplification adjustment factor was then calculated with the formula: $(-\log_2(\text{Number of negative wells/Number of total wells}))/2$. For good reproducibility, the optimal amplification adjustment factor was kept between 0.2 and 0.8. If the amplification adjustment factor was outside these bounds, the assumed concentration was revised, and the experiment was repeated until the estimated amplification adjustment factor was between 0.2 and 0.8.

Crossover amplification

Amplification of crossover molecules was performed as described in [121,124]. The extent to which the DNA was diluted for each of the mutant and WT differed as the objective was to dilute the DNA input such that the likely hood of more than one crossover by chance in one PCR input was minimal, but the input DNA concentration was kept high enough to get a

sufficient number of crossovers for statistical analysis. In practice this amounted to higher DNA input in crossover defective mutants in *Exo1*$^{-/-}$ (~100 diploid DNA equivalents) and *Mlh3*$^{-/-}$ (~300 diploid DNA equivalents) but lower DNA input (~40) for crossover proficient mutants like *Exo1*$^{nd/nd}$ or in WT. The melting temperature of allele-specific primers was empirically determined for each batch of 11.1x buffer, and the melting temperature was chosen such that the allele-specific primer amplified the correct allele without amplifying the other allele. Empirically tested, an appropriate amount of DNA was added to the primary PCR reaction (8 μL), containing 1x buffer (10x: 450 mM Tris-HCl pH 8.8, 110 mM (NH4)2SO4, 45 mM MgCl2, 67mM Beta-mercaptoethanol, 44 μM EDTA, 10 mM each of [dATP, dTTP, dGTP, and dCTP], and 1.13 mg/mL non-acetylated BSA), 12.5 mM Tris-base, 0.2 μM of forward and reverse primers, 0.25 U of Taq, and 0.05 U of Pfu DNA polymerase. The overall PCR conditions for all following PCRs were the same: 96°C, for 1 min - initial denaturation, 20 sec - for subsequent cycles, annealing for 30 sec at optimized T_m, and final extension at 65°C for 1 min per kb. To clear the primary PCR products off of primers and incomplete PCR amplicons, 2 μL of the primary PCR product was digested with S1 nuclease (For 10 μL reaction: 0.7 U/μL S1 nuclease in 1x buffer: 20 mM sodium acetate, 1 mM Zn acetate, 0.1 M NaCl) for 20 minutes at room temperature. The reaction was stopped with 45 μL of dilution buffer (dilution buffer: 10 mM Tris-HCl pH 7.5 and 5 μg/mL sonicated salmon sperm DNA). 1.6 μL of the S1 digested primary PCR product was then used as input for secondary PCR, and the PCR conditions used were identical to the primary PCR, but with nested primers and their corresponding melting temperatures. In a crossover PCR plate, by design, most of the wells do not have a crossover, and the wells that have a crossover was identified by running a small sample (1/10 of the reaction) on an agarose gel. The PCR product from the wells that have a crossover was then used as an input for a high-volume tertiary PCR (30 μL). The overall PCR conditions for all PCRs were the same: 96°C, for 1 min - initial denaturation, 20 sec - for subsequent cycles, annealing for 30 sec at optimized T_m, and final extension at 65°C for 1 min per kb. The tertiary

PCR was performed for 30 amplification cycles, unlike the primary and secondary PCRs which were amplified for 27 cycles. PCR amplification was tested for the tertiary PCR, after which the amplicon was transferred to a positively charged nylon membrane for subsequent genotyping by southern blotting.

Amplification of NCOs

NCO products were amplified from the genomic DNA as described by [121,124]. Amplification of NCOs was largely similar to amplify crossovers but differed in a few key aspects. The primer combinations were identical to those used in amplification efficiency primers: one allele-specific primer and one universal primer that amplifies both the homologs equally. This primer combination also amplifies DNA that didn't undergo any DNA repair and therefore to keep the background to a minimum, the input DNA was kept lower than 30 genome equivalents per well across all conditions. Finally, tertiary PCR was not performed for NCOs but instead, the secondary PCR had a higher volume (30 μL) and more cycles (36 cycles) as compared to primary PCR (8 μL volume and 27 cycles). Since genomic DNA that didn't undergo meiotic recombination also amplifies in this PCR, all the wells have amplification, as the presence of the NCOs cannot be identified until after genotyping by southern blotting. Thus, entire secondary amplification is transferred to a positively charged membrane, in 96 well formats.

Genotyping by allele-specific oligo hybridization

Genotyping of recombinant amplicons (crossover/NCO) was performed as described in [121,124]. Allele-specific oligos (ASOs) were labeled with a T4 polynucleotide kinase by using ATP-containing gamma-P^{32}. ASO radiolabeling reaction per 2 blots contained the following (10 μL): 1x buffer (70 mM Tris-HCl, pH 7.5, 10 mM MgCl2, 5 mM spermidine trichloride, 2 mM dithiothreitol), 8 ng ASO, 3.5 U T4 polynucleotide kinase, 0.2 μL γ-32P-ATP (10 mCi/mL)) and water to make up the volume to 10 μL. The radiolabeling reaction mix was incubated for 45 mins to an hour at 37 °C. The reaction was stopped with 20 μL of stop solution (25 mM EDTA,

0.1% SDS, 10 μM non-radioactive ATP) and then 20 μL of unlabeled competitor ASO (8 μg/mL) of the other homolog was added to the mix.

Positively charged nylon membranes containing the amplified DNA products were first washed with 3X SSC (20x SSC: 3 M NaCl and 0.3 M citric acid trisodium salt dihydrate) before loading into the hybridization bottles. Up to 6 blots were added per bottle, with the blots separated by nylon mesh. These blots were then prehybridized in a rotisserie at 56 °C for 15 mins, with 3 mL of hybridization buffer per blot (Hybridization buffer: 3 M TMAC, 0.6% SDS, 10 mM NaPO4 pH 6.8, 1 mM EDTA, 4 μg/mL yeast RNA, in 5x Denhardt's solution; 50x Denhardt's solution: 1% (w/v) Ficoll 400, 1% (w/v) polyvinyl pyrrolidone, 1% (w/v) BSA (Fraction V)). After pre-hybridization, the buffer was replaced with fresh hybridization buffer (2.5 mL per blot), containing sonicated salmon sperm DNA at 8.4 μg/mL, and was incubated in a rotisserie at 53 °C for 10 mins. Radio-labeled ASO mix (50 μL per 2 blots) was subsequently added and the blots were incubated in the rotisserie at 53 °C for 45 mins to 1 hour. The blots were then washed thrice with wash buffer at 56 °C (Wash buffer: 3 M TMAC, 0.6% SDS, 10 mM NaPO4 pH 6.8, 1 mM EDTA; 2.5 mL per blot) in about 20 mins, about 4-6 mins per wash. The blots were then washed once more with wash buffer, at 56°C for 15 mins, but with 4 mL of wash buffer per blot. Then the blots were rinsed in 2X SSC twice to remove any TMAC and were then exposed overnight to a phosphor imager screen. While the excess SSC is blotted off before exposure, care is taken to not dry the blots and to not wet the screen during the exposure.

Cytological analysis

Immunofluorescence images were blinded before analysis and all animals used in the analysis were BXD F1 hybrids. To reduce inter-person variability the mutants and controls were analyzed by the same individual. For foci counts, only the SYCP3- axis associated foci were counted and for MLH1 foci counts, foci on XY chromosomes were excluded from the analysis.

For analysis of DMC1 foci, Zygonema cells were chosen. To choose the Zygonema, SYCP3 axis morphology was used where cells with contiguous, but un-synapsed axis were considered for analysis. Cells were classified as early mid zygonema if the cells had <50% synapsis (visually estimated) and were classified as mid-late zygonema if the cells had >50% synapsis (visually estimated). A similar number of early-mid and mid-late zygonema cells were present in WT and mutant alleles (Fisher's Exact test, two-tailed n.s). For MLH1 and MLH3 foci analysis any pachynema cell positive for foci was considered for analysis. The pachynema was identified using SYCP3 morphology – only the cells with fully synapsed SYCP3 axis were classified as pachynema.

Metaphase bivalents were analyzed after blinding the images as much as possible. To make sure the blinding is convincing, it was done between mutants with similar crossover loss (for example between *Exo1*$^{-/-}$ and *Mlh3*$^{DN/DN}$). Bivalent counts were performed by multiple authors and therefore to reduce the inter-experimentalist variation, the authors defined the rules before counting to differentiate chromosomes with crossovers versus those that do not have a crossover. Only intact nuclei, nuclei with 20-40 objects, were included in the analysis to avoid broken cells, and cells with unclear counts were excluded from the analysis. Metaphase cells that overlap with nearby cells and cells with overlapping bivalents were excluded from the analysis.

Co-efficient of Coincidence (CoC) of MLH1 foci on pachytene cells was performed as described in [60]. The DAPI-rich end of each chromosome was designated as the starting end for the distance estimates. The distance of each focus on the chromosome from the DAPI end and the length of the chromosomes were manually estimated using the free-hand function in ImageJ. The number of intervals per bivalent was taken to be 10, and it was arrived at based on the number of MLH1 foci per micron axis and the number of cells counted. After distance measurement, the mean CoC vs inter-interval distance was calculated using MATLAB as described in [60]. Axis length analysis used for WT and *Exo1*$^{-/-}$ spermatocytes was taken from the CoC dataset.

Experimental design, and statistical analysis

Cytological quantification and analysis were blinded wherever possible, and the phenotype and quantification were checked by independent experimenters to check for consistency. For crossover/NCO recombination analysis, PCR plates from different mutants were amplified and genotyped by southern blotting together to increase throughput and reduce inter-experiment variation. While the blots and plates were not blinded, the analysis was done on a per-polymorphism basis rather than a per-animal basis effectively blinding the analysis step.

All the graphs were shown as mean with standard deviation showing 95% confidence intervals. The p-value was often only shown when the difference was significant, and the p-values for comparison of the means were adjusted for multiple comparisons. We see that in our mutants the total frequency of repair at *59.5* remains mostly unaffected but the proportion of the repair products changes between mutants. Therefore, to compare changes in the proportion of a repair event (e.g., crossover) between mutants, Fisher's exact test, two-tailed was used. Since most of our cytological foci count data are not normally distributed, for comparing means, Mann-Whitney was used for pairwise comparisons, and Kruskal-Wallis followed by Dunn's multiple comparison corrections was used for one-versus many comparisons. For all the data shown, the statistical tests done were shown in figure legends, the total number of animals analyzed was depicted with 'N' and the data points were depicted with 'n'.

Results

Chapter 1: EXO1 has a nuclease-independent role promoting mammalian meiotic crossovers and is important for proper timing of crossovers. (*Exo1*^{het}, *Exo1*$^{-/-}$, and *Exo1*$^{nd/nd}$ (nuclease-deficient) alleles

Exo1$^{-/-}$ spermatocytes show reduced early recombination foci

By the end of meiosis-I, homologous chromosomes need to be physically connected to undergo proper chromosome segregation during the first meiotic division. This physical connection between homologs depends upon a DNA repair end product, the crossover that exchanges homolog arms. EXO1 is a 5' to 3' nuclease that is required during meiosis for proper crossover formation. Thus, in mouse *Exo1*$^{-/-}$ spermatocytes, crossovers fail to form properly, resulting in meiotic aneuploidy and infertility (Wei et al., 2003., Kan et al., 2008). The precise function of EXO1 in crossover formation is currently unclear. In yeast lacking EXO1, an entire class of crossovers, those enzymatically produced by the crossover-specific resolvase complex MutLgamma, is lost [104,166]. However, this does not seem to be the case in mice. Mouse spermatocytes deficient for *Exo1* (*Exo1*$^{-/-}$) have a less severe phenotype than mouse spermatocytes defective for the MutLgamma complex (e.g., *Mlh3*$^{-/-}$ spermatocytes) [156], indicating that the roles of MutLgamma complex and EXO1 are likely different in mice from in yeast. These phenotypic differences also allow the use of comparative genetic approaches to define the roles of EXO1 and MLH3 in mammalian meiotic DNA repair.

To define the roles of EXO1 in mammalian meiotic recombination, we analyzed the progression of early recombination intermediates that are marked by DMC1 foci. During mouse meiosis, the ends of the DNA DSB get resected and the resulting 3' overhang is coated with DMC1 and RAD51 to form a nucleoprotein filament. The DMC1/RAD51 nucleoprotein filament catalyzes homology search and subsequent strand invasion into the homolog to provide a repair template (donor) [37]. The average number of DMC1 foci per spermatocyte is affected by a combination of factors, including the number of DSBs, the lifespan of the DMC1 nucleoprotein

filaments, and the extent of resection. Overall, in zygonema when the bulk of the DSBs initiate repair, we found that *Exo1*$^{-/-}$ spermatocytes had fewer DMC1 foci (155.8 ± 60) than WT or *Exo1*^{het} (224.0 ± 72.2 and 196.5 ± 60.45, respectively) (**Figure 15**). While the decrease in DMC1 foci in *Exo1*$^{-/-}$ spermatocytes could be due to a reduction in DSBs, this model is less likely as budding yeast lacking EXO1, which has normal DSB levels [104,107,166,174]. In support of the idea that the number of initiating DSBs are unaffected, the homolog axis length that is proportional to DSB frequency is also unaffected in *Exo1*$^{-/-}$ spermatocytes (**Figure 16**).

Loss of EXO1, however, does lead to a mild (~10%) reduction in DSB resection [105,108]. This 10% reduction in resection is unlikely to explain the 22% - 30% (vs *Exo1*^{het} and WT, respectively) reduction in DMC1 foci, suggesting that in *Exo1*$^{-/-}$ spermatocytes, the lifespan of the DMC1 nucleoprotein filaments may also be decreased.

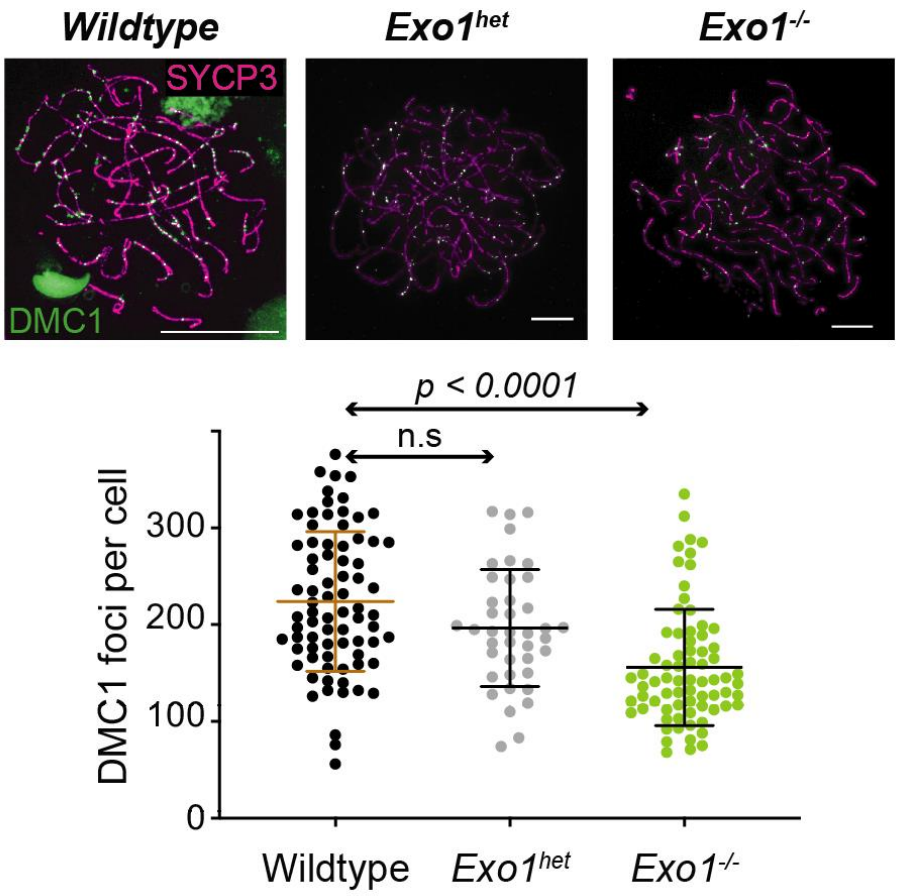

Figure 15: *Exo1*$^{-/-}$ spermatocytes have fewer DMC1 foci per cell
(Top) Representative immunofluorescence images of zygotene stage spermatocytes of the indicated genotypes stained for SYCP3 (magenta) and DMC1 (green). Scale bar (10 microns).

(Bottom, graph) Scatter plot of DMC1 foci per cell (y-axis) indicating the average number of DMC1 foci ± SD in WT (N=3, 224 ± 72.2), *Exo1*^{het} (N=2, 196.5 ± 60.45), and *Exo1*$^{-/-}$ (N=4, 155.8 ± 60). P-values were determined by the Kruskal-Wallis test with Dunn's multiple comparison correction.

Exo1$^{-/-}$ spermatocytes maintain WT-like homolog axis length

To further test whether the reduction in DMC1 foci seen in *Exo1*$^{-/-}$ spermatocytes reflect a reduction in initiating DSBs, I measured homolog axis lengths using antibodies against the axis component SYCP3. The rationale behind the experiment is that the DSB potential of a cell is mechanistically linked to the homolog axis length [175]. Therefore, a reduction in average axis length per cell in *Exo1*$^{-/-}$ spermatocytes compared to WT controls would indicate that the number of initiating DSBs is reduced in *Exo1*$^{-/-}$ spermatocytes. This analysis was performed with pachytene stage WT and *Exo1*$^{-/-}$ spermatocytes when the homolog axis formation is complete. I found that *Exo1*$^{-/-}$ spermatocytes had similar axis lengths compared to WT, further supporting the notion that initiating DSB numbers are unaffected in *Exo1*$^{-/-}$ spermatocytes.

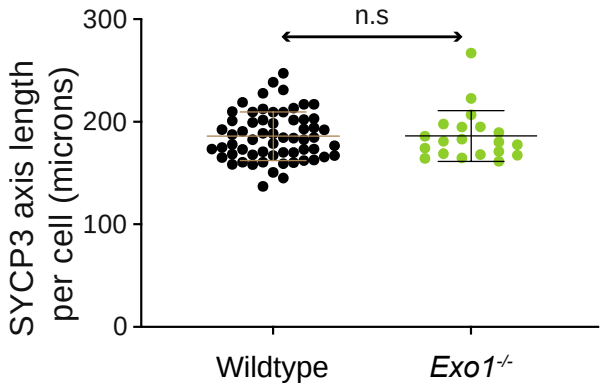

Figure 16: *Exo1*$^{-/-}$ spermatocyte inter-homolog axis (SYCP3) length
Scatter plot of the axis lengths per cell measured in microns (mean ± SD) in WT (N=3 185.8 ± 23.6) and *Exo1*$^{-/-}$ (N=2 186.0 ± 24.8) spermatocytes. The number of animals is given by (N), and the Mann-Whitney test was used for statistical analysis.

Exo1$^{-/-}$ spermatocytes show reduced MLH1 and MLH3 cytological foci

About 10% of early DSBs enter the crossover pathway and become upstream intermediates for crossovers in a process called designation. It is well established that most

crossover precursors are converted into crossovers by the MutLgamma complex, an obligate heterodimer of MLH1 and MLH3 [37]. Both MLH1 and MLH3 form cytologically visible foci at the crossover precursor sites, and these foci overlap with the homolog axis (marked by SYCP3) in pachytene spermatocytes.

Given the crucial roles that the crossovers play in chromosome segregation, the cell regulates the crossover numbers via a process called crossover homeostasis. Crossover homeostasis buffers the number of crossover precursors per cell despite large variations in early recombination intermediates [139]. Therefore, if crossover homeostasis is normal in *Exo1*$^{-/-}$ spermatocytes [138], we would not expect a change in MLH1/MLH3 foci that mark crossover precursors despite the 22-30% reduction in DMC1 foci. In contrast to this expectation, we saw a ~10% reduction in the average number of both MLH1 and MLH3 foci per cell in *Exo1*$^{-/-}$ spermatocytes compared to WT (**Figure 17**). Our observation was consistent with earlier reports from oocytes lacking EXO1 (Kan et al., 2008). Specifically, we saw, on average, 20.0 ± 3.6 MLH1 foci per cell in *Exo1*$^{-/-}$ spermatocytes compared to 22.3 ± 2.5 and 22.4 ± 2.3 in WT and *Exo1*^{het} spermatocytes, respectively. We saw a similar reduction in MLH3 foci, with 20.3 ± 3.6 foci per cell on average in *Exo1*$^{-/-}$ as compared to 22.9 ± 4.1 in *Exo1*^{het} spermatocytes.

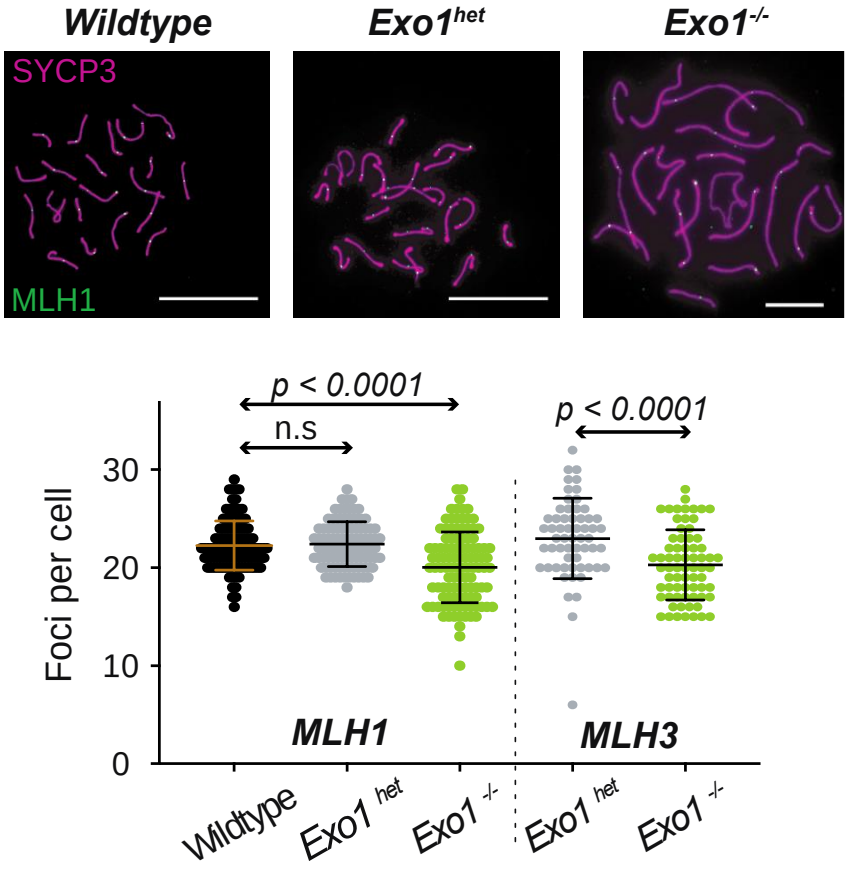

Figure 17: MLH1 and MLH3 foci in *Exo1*$^{-/-}$ spermatocytes
(Top) Representative immunofluorescence images of pachytene stage spermatocytes of the indicated genotypes stained for SYCP3 (magenta) and MLH1 (green). Cells in pachynema with bright MLH1 foci were imaged for counting. Scale bar (10 microns).
(Bottom) Scatter plot showing the number of MLH1 and MLH3 foci per cell in WT (MLH1, N=3, 22.3 ± 2.5), *Exo1*^{het} (MLH1, N=3, 22.4 ± 2.3), *Exo1*$^{-/-}$ (MLH1, N=3, 20.0 ± 3.6) and *Exo1*^{het} (MLH3, N=2, 22.9 ± 4.1), *Exo1*$^{-/-}$ (Mlh3, N=3, 20.3 ± 3.6). P-values were determined by either the Kruskal-Wallis test with Dunn's multiple comparison correction (MLH1) or the Mann-Whitney two-tailed test (MLH3).

Exo1$^{-/-}$ spermatocytes show WT crossover interference, despite the reduction in MLH1 foci

On average, WT mouse spermatocytes only have ~24 crossover precursors to distribute among 20 chromosomes. Yet, each homologous chromosome pair gets at least one MLH1 or MLH3 focus consistently, indicating a non-random distribution of crossover precursors. This non-random distribution of crossovers is termed crossover interference. Once a crossover precursor gets designated at a genomic location on a chromosome, a second

crossover precursor is prevented from getting designated nearby. The locations of MLH1 and MLH3 foci in WT spermatocytes are thought to mark the locations of actual crossover precursors, and hence their cytologically observable distribution can be used to measure crossover interference. The extent of this interference between MLH1 foci can be measured as the ratio of observed double MLH1 foci to expected double MLH1 foci per unit inter-MLH1 interval distance (microns) (**Figure 18**). This ratio (observed double MLH1 or crossovers/expected) is termed co-efficient of coincidence (CoC). Since the interference is very strong at smaller distances and weakens as farther along a chromosome, CoC increase from 0 towards 1. We can get the inter-interval distance where the CoC of that genotype reaches 0.5 to get a simple estimate of interference of that genotype. A decrease in interference as compared to WT will show reduction in inter-interval distance while an increase in interference will show longer inter-interval distance for the same 0.5 CoC value.

Because we saw a reduction in MLH1 and MLH3 foci in *Exo1*$^{-/-}$ spermatocytes, I wanted to test whether crossover interference was reduced in the absence of EXO1 as it is in budding yeast [167]. I found that in contrast to budding yeast, mouse *Exo1*$^{-/-}$ spermatocytes displayed crossover interference similar to WT spermatocytes, indicating that EXO1 likely does not play a role during the crossover designation step or in crossover interference in mouse spermatocytes.

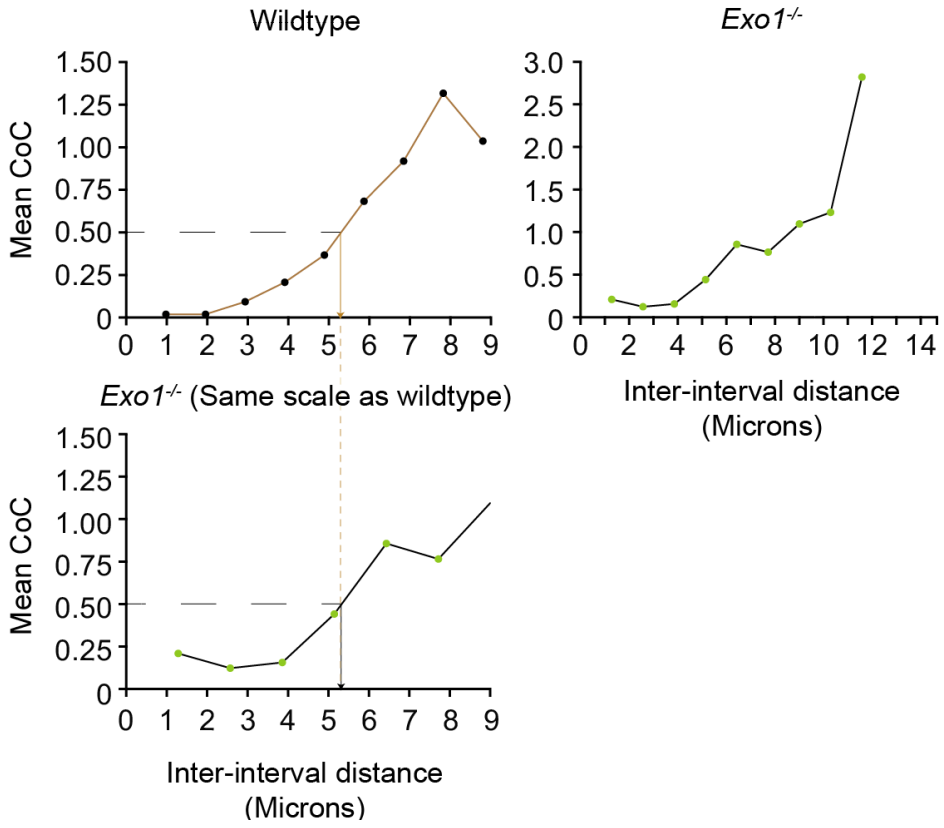

Figure 18: *Exo1*$^{-/-}$ spermatocytes show similar crossover interference as WT
A plot of the mean coefficient of coincidence (CoC) versus inter-interval distance (microns) was calculated by measuring the MLH1 focus distribution of the indicated genotypes. (Top Left) WT. (Top right and left bottom, with scale adjusted) *Exo1*$^{-/-}$ spermatocytes.

Exo1$^{-/-}$ spermatocytes show a disproportionate reduction in metaphase bivalents

During the first meiotic division (Meiosis I), homologous chromosomes are segregated, and this step requires the homologs to be physically tethered. Because crossovers result in the exchange of chromosome arms, crossovers also enable a physical connection between homologs by allowing sister chromatid cohesion to hold homologs together to form bivalents. Consequently, loss of crossovers will increase the number of unconnected homologs (univalent) which is cytologically visible during the metaphase stage of Meiosis I (**Figure 19**). Considering that there was an ~10% reduction in MLH1 and MLH3 foci and by inference a 10% reduction in crossover precursor intermediates, we next tested whether this reduction leads to a decrease in bivalents in Meiosis I metaphase cells. We found, as previously reported (Kan et al., 2008; Wei et al., 2003), that *Exo1*$^{-/-}$ spermatocytes showed a disproportionate ~70%

reduction in the number of bivalents (5.3 ± 2.0) compared to *Exo1*^{het} (19.9 ± 0.3) and WT (19.7 ± 0.5) spermatocytes (**Figure 20**). This data suggests that without EXO1, the MutLgamma complex may be unable to efficiently convert crossover precursors into crossovers.

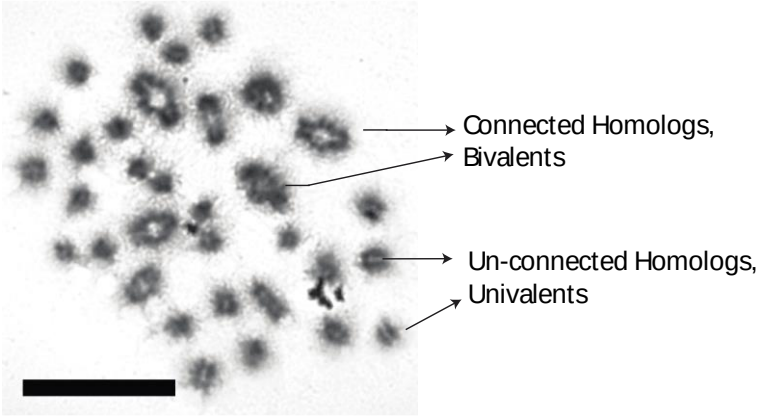

Figure 19: An example metaphase image
Metaphase spermatocyte cell from *Exo1*$^{-/-}$ mice, stained with Giemsa. Examples of connected homologs (bivalents) and unconnected homologs (univalents) are labeled.

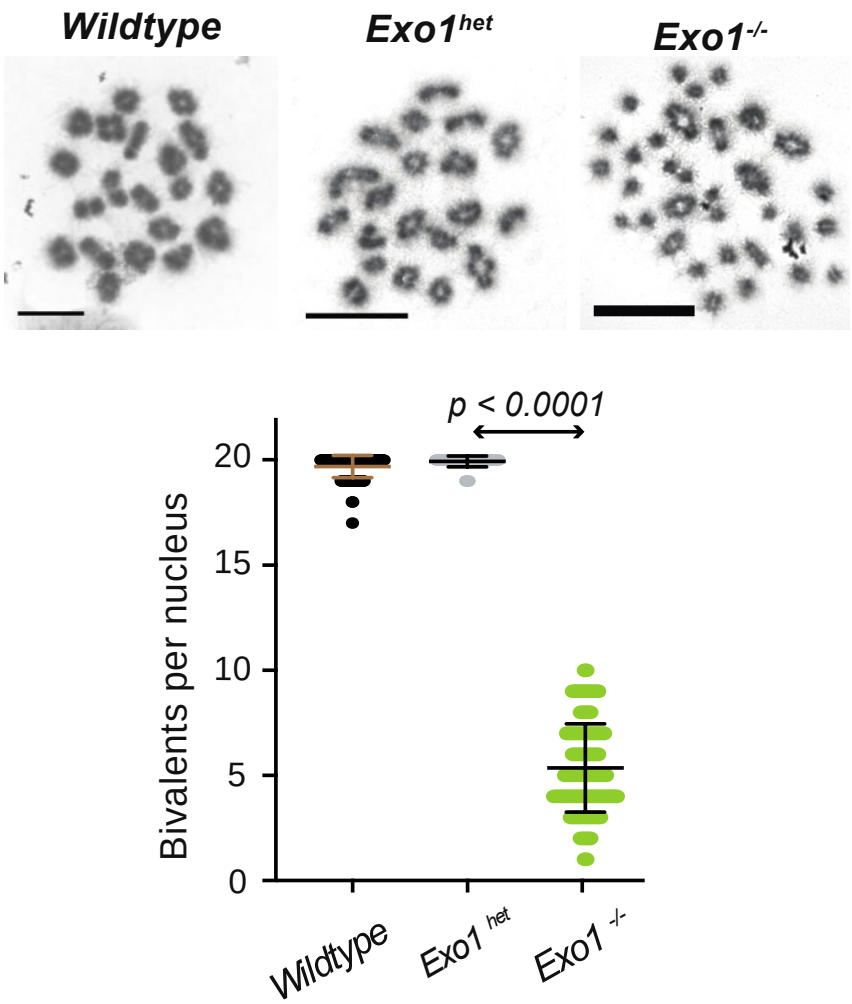

Figure 20: ***Exo1*$^{-/-}$ spermatocytes show disproportionate loss of bivalents in metaphase compared to numbers of MLH1/MLH3 foci**
(Top) Representative metaphase images of spermatocytes from the indicated genotypes stained with Giemsa. Scale bar (10 microns).
(Bottom) Scatter plot of bivalent counts per cell (y-axis) for each of the indicated genotypes (y-axis) with the mean ± SD displayed for WT (N=2, 19.7 ± 0.5), *Exo1*^{het} (N=3, 19.9 ± 0.3), *Exo1*$^{-/-}$ (N=4, 5.3 ± 2.0). P-values were determined by the Kruskal-Wallis test with Dunn's multiple comparison correction.

Rationale for isolating crossovers from diplotene spermatocytes

Although there was only a 10% reduction in the number of MLH1 and MLH3 foci in *Exo1*$^{-/-}$ spermatocytes, ~70% of homologs were not connected as bivalents in metaphase spermatocytes. To better understand the role of EXO1 in crossover formation, I analyzed the residual crossovers that formed in the absence of EXO1 at one genomic hotspot, *59.5*, on chromosome 19. Hotspot *59.5* is enriched for crossover formation and hence is suited to isolate crossovers from mutants defective for crossovers, despite their diminished frequency [61]. *Exo1*$^{-/-}$

spermatocytes fail to progress beyond metaphase I, and do not form 2˚spermatocytes or sperm, as they undergo apoptosis at metaphase [169]. Therefore, to compare *Exo1*$^{-/-}$ and WT spermatocytes directly, I performed our analysis at diplonema when all recombination is completed but the spermatocytes are still present in crossover defective mutants. I enriched for diplotene stage spermatocytes using fluorescence-activated cell sorting (FACS). The recombination outcomes observed in the WT diplotene spermatocytes were similar to those of mature sperm indicating that recombination including crossover formation have completed by diplonema (**Figure 21**, shown below).

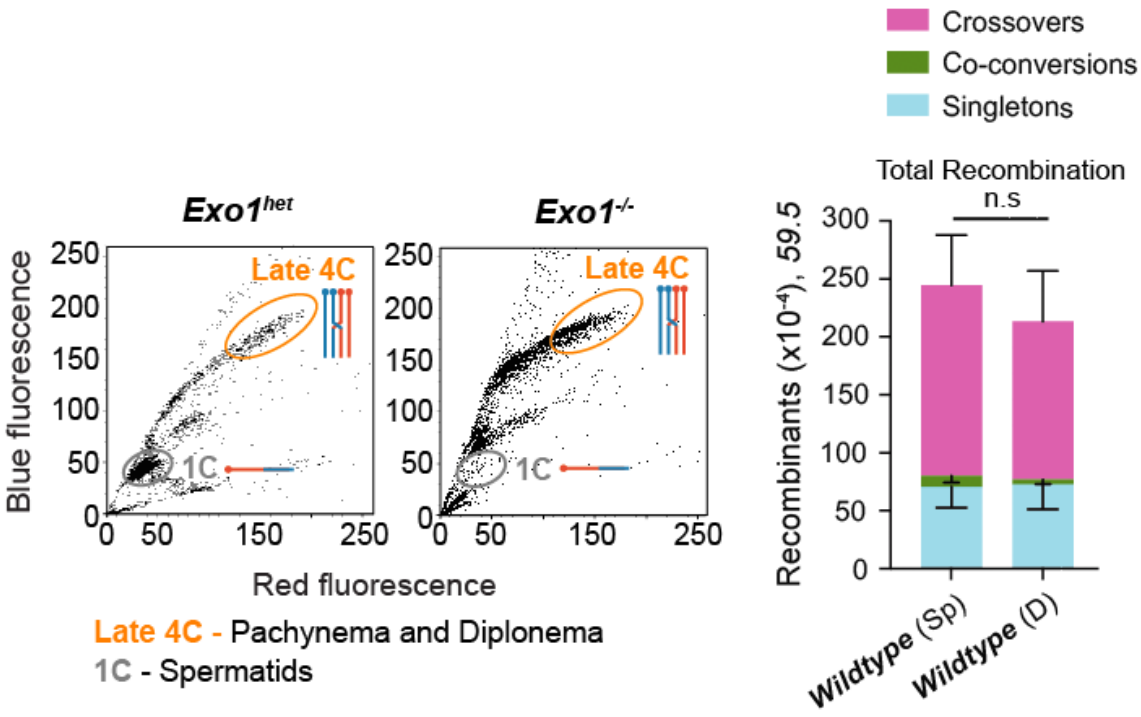

Figure 21: Isolation of late 4C cells enriched for diplonema by FACS.
(Left), Isolated live testicular cells from adult *Exo1*^{het} and *Exo1*$^{-/-}$ B x D mice were stained with Hoechst 33342 and sorted based on red (chromosome compaction) and blue (DNA content) fluorescence emission by UV-stimulated fluorescence-activated cell sorting (FACS). The orange oval shows the Late 4C population and sorting gate used to enrich for cells in diplonema. The gray oval shows the population of 1C spermatids. Sorted samples contained at least ≥70% diplonema spermatocytes (**Table 2**).
(Right) Histogram of the total recombination frequency per 10,000 haploid genome equivalents for WT sperm (SP) and diplotene stage spermatocytes (D) categorized into crossovers (pink), co-conversions (green), and singletons (blue). Total recombination frequencies were similar between WT sperm (240.8) and diplonema spermatocytes (213.4). P-values were determined by Fisher's exact test, two-tailed.

Schematic for recovering crossovers

High molecular weight DNA was isolated from late 4C cells enriched for diplotene spermatocytes. To specifically isolate crossovers, PCR reactions were performed with two allele-specific primers in a crossover configuration (C57B6/J, B forward to DBA/2J, D reverse or vice-versa, shown below). The late-4C DNA was seeded at sufficiently low concentrations to reduce the frequency of multiple events per well. This concentration was determined empirically, for example, ~20 amplifiable molecules were used for WT and *Exo1*^{het} spermatocytes and ~50 amplifiable molecules for *Exo1*$^{-/-}$ spermatocytes. Each crossover PCR reaction consisted of two consecutive rounds of PCR and cells with crossover amplification were identified by agarose gel electrophoresis. The polymorphisms in these crossovers were then genotyped using Southern blotting with allele-specific oligonucleotides.

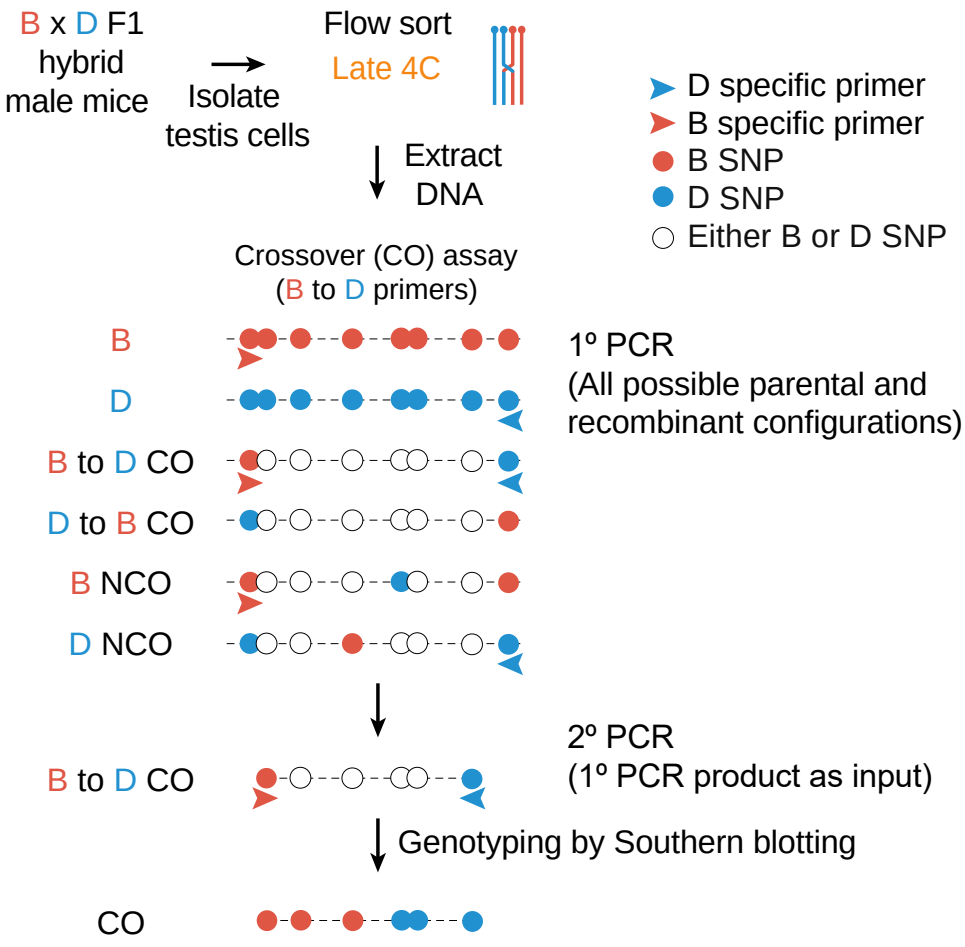

Figure 22: Schematic of crossover assay
Schematic describing the method used to recover crossover events (only B to D crossover PCR shown). High molecular weight DNA purified from B x D Late 4C spermatocytes is added at low concentration into multiple wells of a 96-well PCR plate. The DNA in these wells were amplified with two rounds of PCR with the second round being a nested PCR. To specifically isolate crossovers, two allele specific primers targeting alternating homolog was used (e.g., B forward and D reverse primers for B to D crossover, colored arrows). Amplicons were dot blotted and genotyped by Southern blotting to identify haplotype switches using labeled allele-specific oligonucleotides.

Exo1$^{-/-}$ spermatocytes show significantly fewer crossovers at *59.5*

I recovered crossovers ocurring at the *59.5* hotspot from *Exo1*$^{-/-}$ spermatocytes and compared them to crossovers isolated from *Exo1*^{het}, WT, and a nuclease deficient allele of EXO1, *Exo1*$^{nd/nd}$. It has been previously shown in yeast that Exo1 nuclease activity is not required to promote MutLgamma-dependent crossing over [104]. Similarly, *Exo1*$^{nd/nd}$ mice are fertile [168,176]. In *Exo1*$^{nd/nd}$, one of five metal binding residues (D173A) is replaced with alanine, thus reducing the nuclease activity of the resulting protein ~98% in vitro [168,177-180]. *Exo1*$^{nd/nd}$ also shows evidence for loss of nuclease acivity *in vivo* [168].

Even though *Exo1*^{het} and *Exo1*$^{nd/nd}$ mice are fertile with similar bivalents per cell as WT spermatocytes [168,176], both *Exo1*^{het} and *Exo1*$^{nd/nd}$ spermatocytes showed a ~28% reduction in crossover frequencies at *59.5* compared to WT (**Figure 23**). In line with previous reports and our bivalent analysis (**Figure 20**), *Exo1*$^{-/-}$ spermatocytes showed a severe loss of crossovers at *59.5*. Taken together, these findings suggest the crossover-promoting role of EXO1 in mice is largely nuclease-independent.

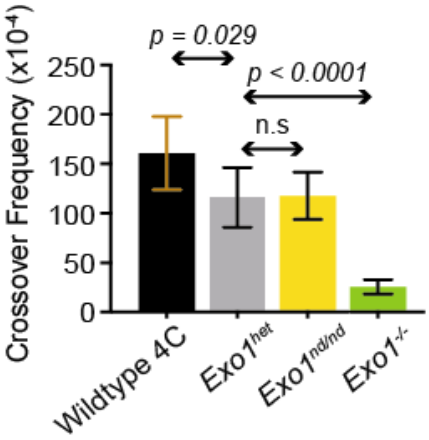

Figure 23: *Exo1*$^{-/-}$ spermatocytes have fewer crossovers at *59.5*
Histogram showing Poisson-corrected frequencies of crossovers at the *59.5* hotspot plotted per 10,000 haploid genome equivalents (y-axis) with error bars of the mean ± SD in WT (N=4, 160.8 ± 37.1), *Exo1*^{het} (N=4, 116.0 ± 30.2), *Exo1*$^{nd/nd}$ (N=4, 117.6 ± 23.9), *Exo1*$^{-/-}$ (N=6, 25.59 ± 7.32). P-values were determined by Fisher's exact test, two-tailed.

Exo1$^{-/-}$ spermatocytes show increased complex crossovers

In *Exo1*$^{-/-}$ and *Exo1*$^{nd/nd}$ spermatocytes, I saw an increase in crossovers with complex exchange points. Such crossovers with complex exchange points were rarely observed in the WT. Therefore, to analyze this phenotype, I categorized the *Exo1*$^{-/-}$ and *Exo1*$^{nd/nd}$ crossovers as simple, mixed, or complex crossovers.

Most crossovers observed in mouse spermatocytes show a single exchange point between parental haplotypes (simple crossovers). However, occasionally crossovers involve a contiguous tract that scores positive for both parental haplotypes. We refer to these as 'mixed crossovers' as the simplest interpretation is that these samples contain two independent simple crossovers that have different exchange points. We can observe complex crossovers with more than two haplotype switches that may involve tracts that are positive for both parental haplotypes (**Figure 24 B**, right schematic). These complex crossovers cannot be explained as multiple events but are likely caused by template switching or branch migration during crossover formation and/or MMR (**Figure 24 A**)

In *Exo1*$^{-/-}$ spermatocytes, I saw an increase in the number of mixed crossovers. However, the number of mixed crossovers in *Exo1*$^{-/-}$ spermatocytes was not different from the

prediction of the number of multiple independent events per well based on Poisson approximation. Therefore, mixed crossovers likely arise from PCR reactions that contained two independent crossover events with different crossover exchange points. Consequently, I combined the simple and mixed crossovers as a single group. However, in *Exo1*$^{-/-}$ spermatocytes, I observed numerous complex crossovers that could not be accounted for by multiple crossovers, thus revealing a novel biological phenotype that needs further investigation.

Complex crossovers were rare in WT spermatocytes and/or sperm (0.4 ± 0.9% and 2.5 ± 3.5%, respectively) but were more common in *Exo1*$^{-/-}$ spermatocytes (32.4 ± 24.1%). Complex crossovers could result from defective MMR, which is expected in the absence of EXO1, given its known role in excising mismatched nucleotides. EXO1-dependent mismatch correction predominantly requires EXO1's nuclease function [168,181]. I assessed *Exo1*$^{nd/nd}$ spermatocytes for complex crossovers. I observed fewer complex crossovers in *Exo1*$^{nd/nd}$ (14.4 ± 9.7%) compared to *Exo1*$^{-/-}$ spermatocytes (32.4 ± 24.1%), but many more than in WT spermatocytes, indicating that the complex crossovers observed in *Exo1*$^{-/-}$ spermatocytes require both nuclease-dependent and -independent roles of EXO1. Taken together, defective mismatch correction accounts for only ~1/2 of all complex crossovers observed in *Exo1*$^{-/-}$ spermatocytes with the remaining likely reflecting alterations in crossover precursor processing.

A

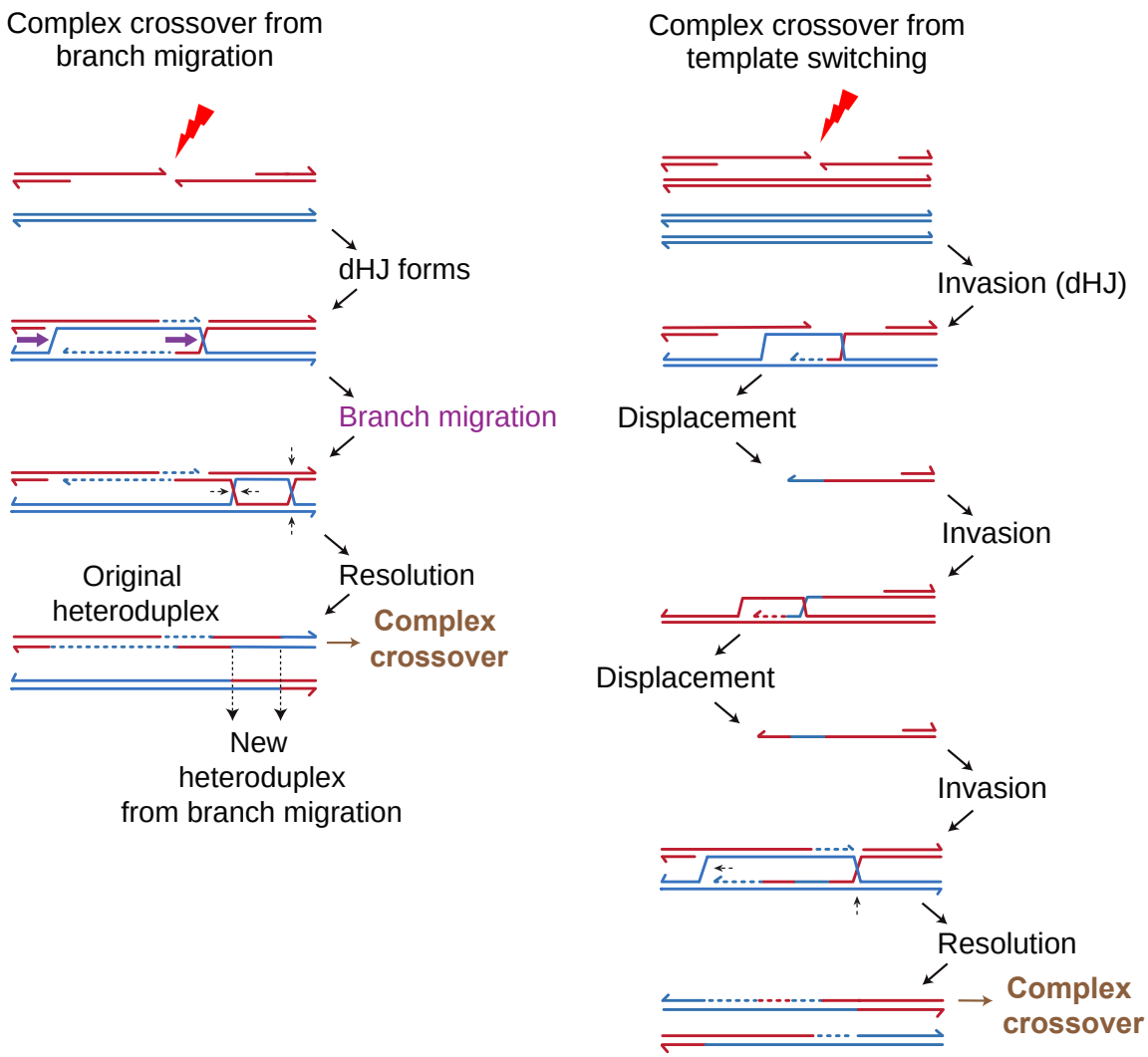
Complex crossover from branch migration
dHJ forms
Branch migration
Resolution
Original heteroduplex
Complex crossover
New heteroduplex from branch migration
Complex crossover from template switching
Invasion (dHJ)
Displacement
Invasion
Displacement
Invasion
Resolution
Complex crossover

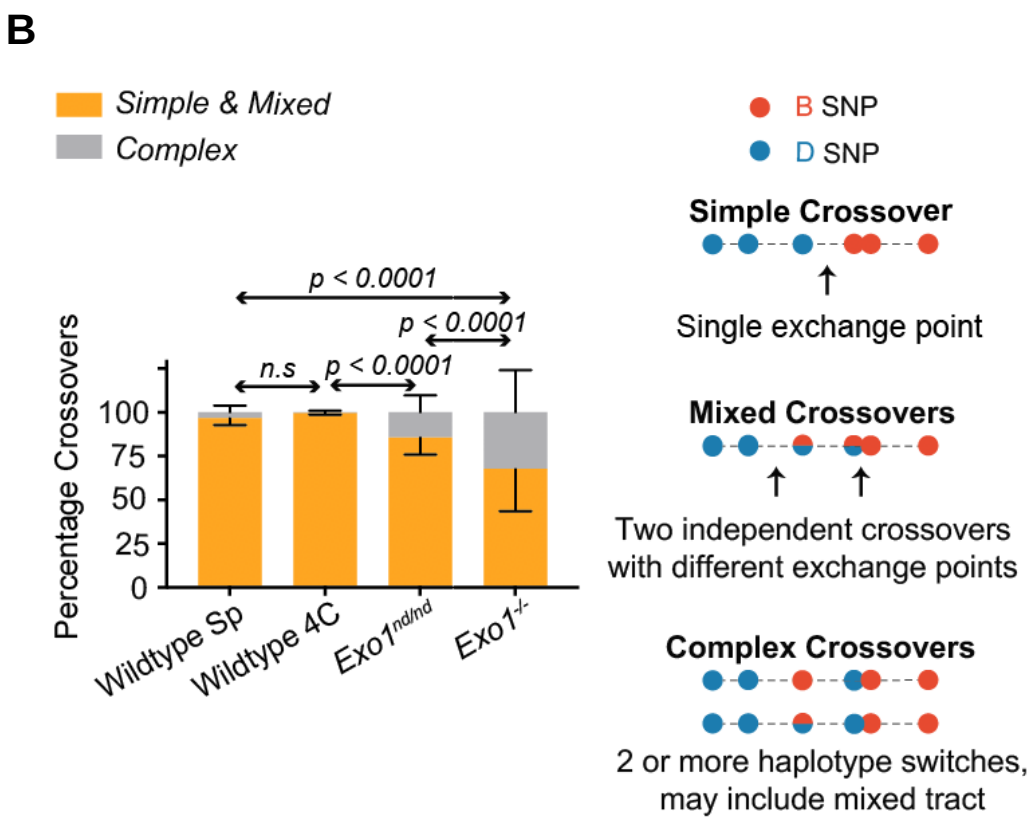

Figure 24: Branch migration and template switching and complex crossovers in *Exo1*$^{-/-}$ spermatocytes

(A) Schematic of branch migration (left) and template switching (right) is shown. For sake of simplicity, only one pattern of branch migration is shown. Similarly, in template switching example, only one of the two strands undergoing template switching is shown. More complex branch migration or template switching patterns are possible and has been observed in budding yeast [118,119]. Each example here yields one complex and one simple crossover. The DSB location is shown my red lightning on top.

(B) (Left) Histogram showing the percentages of simple and complex crossover exchange patterns (y-axis) of the indicated genotypes. Percent of complex crossovers in WT sperm (Sp) (N=6, 2.5 ± 3.5), WT Late 4C spermatocytes (N=4, 0.4 ± 0.9), *Exo1*$^{nd/nd}$ (N=4, 14.4 ± 9.7), and *Exo1*$^{-/-}$ (N=6, 32.4 ± 24.1). P-values were determined by Fisher's exact test, two-tailed. Right, schematic of simple, mixed, and complex crossovers.

Crossovers from *Exo1*$^{-/-}$ spermatocytes show altered exchange points

In addition to complex crossovers (**Figure 24 B**), I also observed that crossover exchange points in *Exo1*$^{-/-}$ spermatocytes, or the location where crossovers convert from one parental genotype to another, have shifted towards the center of the *59.5* hotspot (**Figure 25**

B). To understand the underlying mechanism, I calculated the mean exchange point for *Exo1*$^{-/-}$ spermatocytes compared to that of crossovers from *Exo1*^{het}, *Exo1*$^{nd/nd}$, and WT spermatocytes.

Crossover-dependent gene conversions result from alteration of the recipient chromosome often near the DSB, in favor of the donor. At the *59.5* hotspot, most meiotic DSBs, and by extension DSBs that become crossovers, occur on the B (recipient) chromosome. As such, in most of the crossovers at *59.5*, the genetic information of the B chromosome will be converted to that of the D (donor) chromosome around DSB sites. As a consequence, if we plot the crossover exchange points at *59.5*, the B to D exchange points and D to B exchange points cluster on opposite sides of the DSB center. This can be seen below, where the majority of B (recipient) to D (donor) crossover exchange points cluster to the left of the hotspot center (Top, red), and the majority of D to B exchange points cluster to the right (Bottom, blue) (**Figure 25**). Additionally, the distance between the midlines of the two crossover exchange point distributions reflects the average crossover-dependent gene conversion tract (**Figure 25**). This phenomenon has been observed at many hotspots in mice and humans and is termed reciprocal crossover asymmetry [61,182].

The estimated gene conversion tract length observed at *59.5* in WT sperm is ~575 bp [61], similar to the directly measured gene conversion tracts from previous work (446, 556, and 626 bp) [120]. The estimated gene conversion tract length in *Exo1*^{het} and *Exo1*$^{nd/nd}$ spermatocytes was ~400 bp, similar to that of WT [61,120]. However, I observed that *Exo1*$^{-/-}$ spermatocytes had a shorter estimated gene conversion tract length measuring only 182 bp. Given that *Exo1*$^{nd/nd}$ and *Exo1*^{het} spermatocytes have similar estimated gene conversion tract lengths, it is unlikely that defective MMR in *Exo1*$^{-/-}$ contributes to this phenotype. Further, I found that crossover exchange points in *Exo1*$^{-/-}$ spermatocytes were not clustered on either side of the breakpoint center, but rather were positioned non-stereotypically near the hotspot center (**Figure 25**). Such positioning is uncommon in WT, *Exo1*^{het}, and *Exo1*$^{nd/nd}$ spermatocytes ($p < 0.0001$, $p = 0.0005$ and 0.0416, respectively. Fishers Exact test, two-tailed) as compared to *Exo1*$^{-/-}$ spermatocytes. Therefore, I suggest that the reduced reciprocal crossover asymmetry

observed in *Exo1*$^{-/-}$ spermatocytes is driven by the non-stereotypical positioning of the crossover exchange points in *Exo1*$^{-/-}$ spermatocytes and may not reflect the crossover dependent gene conversion tract length.

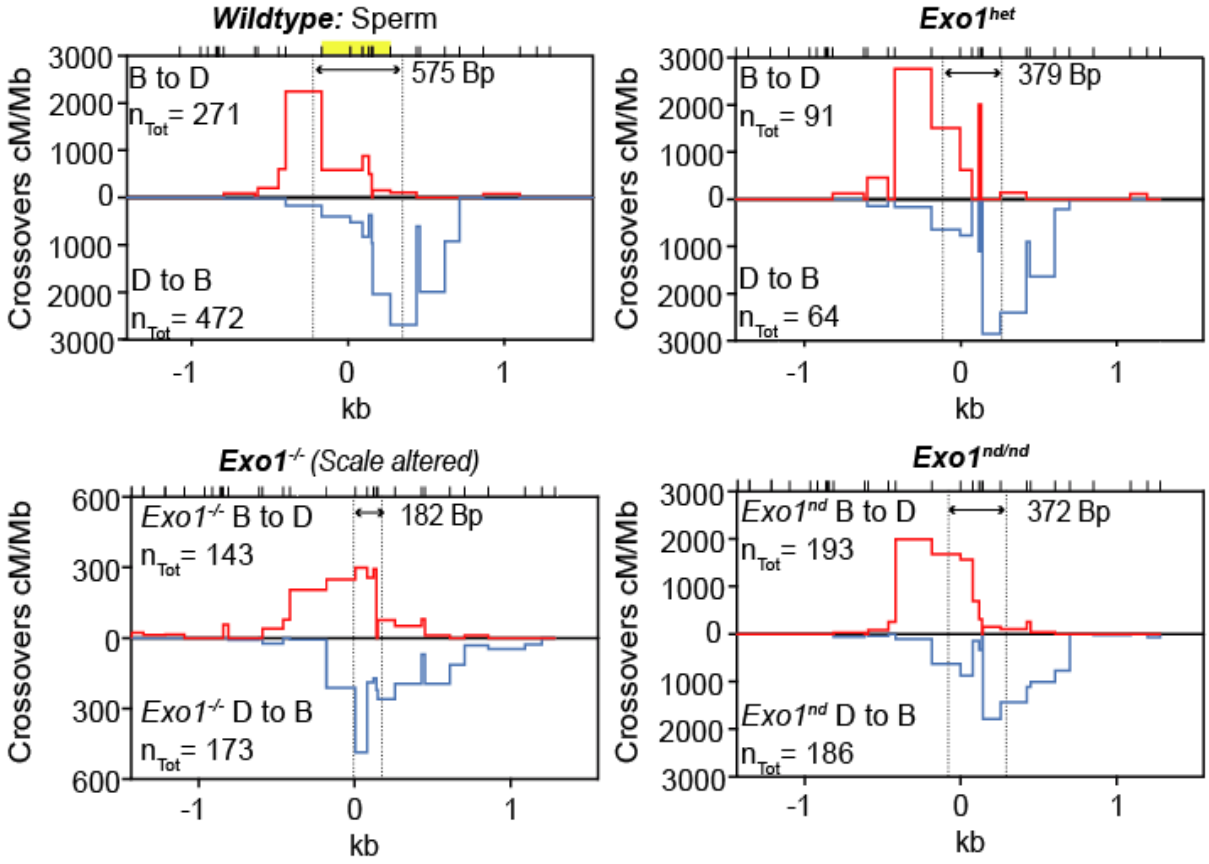

Figure 25: Crossover exchange points in *Exo1*$^{-/-}$ spermatocytes accumulate at the hotspot center

Crossover exchange point frequency in centiMorgans per Megabase (cM/Mb) is plotted on the y-axis and crossover exchange point distribution is plotted on the x-axis. The hotspot center is set at 0 kb. The area under the curve represents the total crossover frequency. Note the crossover exchange point map for B to D crossovers (in red, top) and D to B crossovers (in blue, bottom) cluster on opposite sides of the hotspot center, Vertical dotted lines mark the average location of crossover exchange points by cumulative distribution with the difference between them estimating the mean crossover-dependent gene conversion tract length. Tick marks on the top of the plot represent the locations of the genotyped polymorphisms. N_{Tot} is the total number of mapped crossovers. The yellow bar in the WT sperm plot denotes the central polymorphisms used to compare the distribution of crossover exchange points.

Crossover formation is delayed in *Exo1*$^{-/-}$ spermatocytes

Bivalent quantification and crossover analysis at *59.5* (**Figure 20, 23**) revealed that, although crossing over is defective in *Exo1*$^{-/-}$ spermatocytes compared to WT, crossovers can occur in the absence of EXO1. To better define the role of EXO1 in crossover formation, I determined whether the timing of crossover events may be altered in *Exo1* mutants. To that end, I compared synchronized cell populations at distinct meiotic stages between WT and *Exo1*$^{-/-}$ spermatocytes (**Figure 26 B** (Rhea Kang, Francesca Cole unpublished)).

To isolate spermatocytes from specific stages, spermatogenesis was synchronized following similar steps as described previously [94]. Briefly, pups were pipette fed a retinoic acid biosynthesis inhibitor, WIN 18,446, for ~7 days, starting on the second day after birth. This inhibitor depletes retinoic acid, which is required for spermatogonia to differentiate and enter meiosis. To initiate synchronized differentiation, mice were injected with retinoic acid 24 hours after the last dose of WIN 18,446, ~day 9 after birth. By waiting an empirically determined 10-50 days post injection (dpi) and flow-sorting the spermatocytes from the testis, cells from specific stages of meiosis were isolated. The purity of these populations was verified with immunofluorescence staining. A brief schematic of this protocol is shown below (**Figure 26 A**), and sample purity and the corresponding wait time (dpi) is shown in **Table 2**.

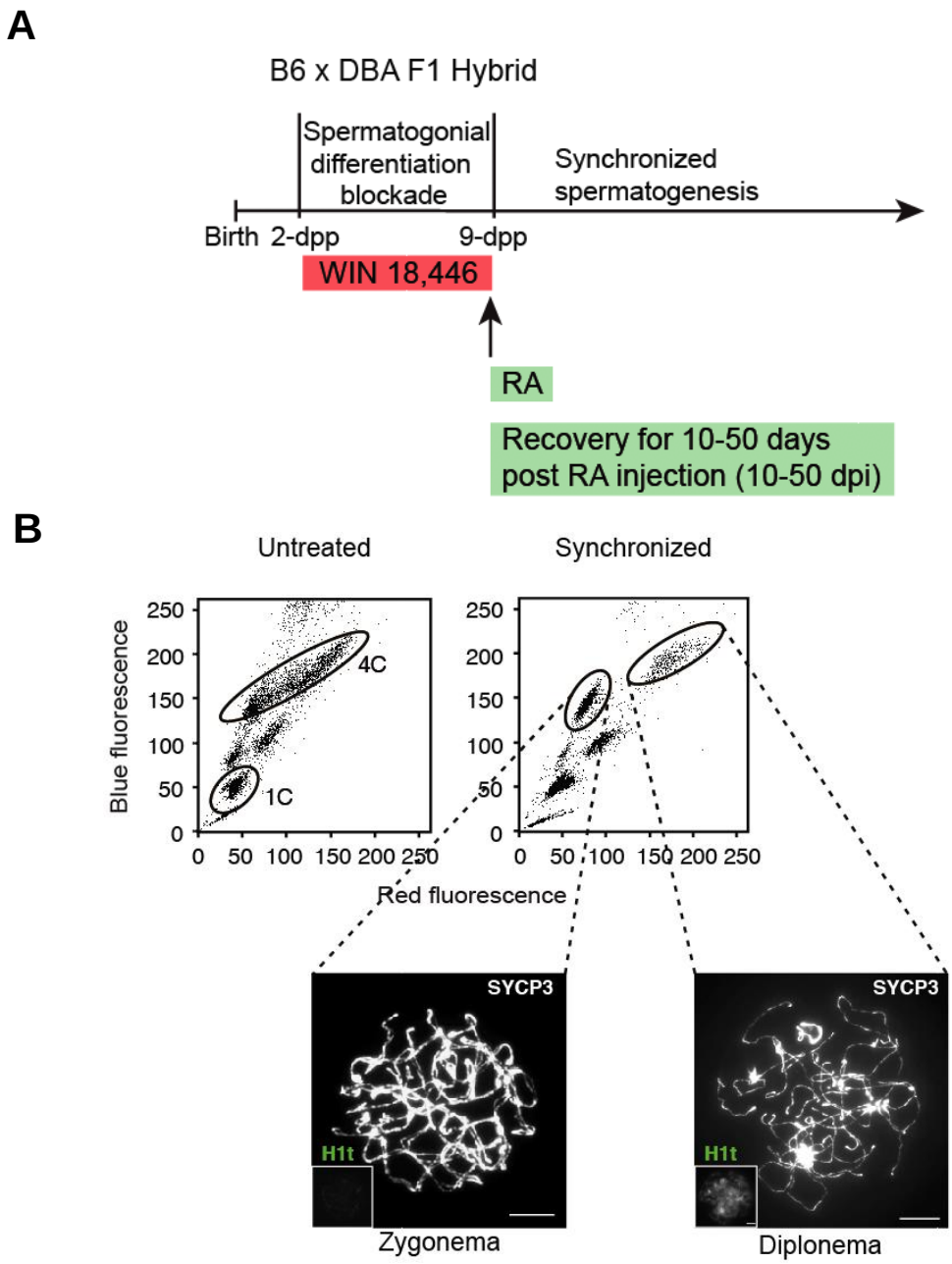

Figure 26: Synchronization of spermatocytes

(A) Schematic of the synchronization of spermatogenesis by treatment of pups 2 days postpartum (dpp) with the aldehyde dehydrogenase 1a2 inhibitor WIN 18,446. This treatment inhibits biosynthesis of retinoic acid from retinol and blocks spermatogonial differentiation. Upon injection with retinoic acid at 9-dpp, spermatogonial differentiation and subsequent spermatogenesis is synchronized well into adulthood.

(B) Top Left, isolated live testicular cells from an adult mouse stained with Hoechst 33342 and sorted for red (chromosome compaction) and blue (DNA content) emission by UV-stimulated fluorescence activated cell sorting. When Hoechst 33342 is activated at a UV wavelength, it emits at red and blue wavelength. The upper and lower oval encircle the 4C and 1C spermatid populations, respectively.

Top Right, example of a synchronized population for zygonema and diplonema. Hoechst 33342 treated testicular cells from a synchronized mouse show two discrete 4C populations. The ovals depict the sort window used to isolate zygotene (left) and diplotene (right) spermatocytes. Bottom, photomicrographs of spread cells from the sorted population that was used to confirm the stages and purity of the experiment (**Table 2**). Examples from each population are shown stained with antibodies to SYCP3 (white) and the Histone variant H1t (white, inset) that is expressed from mid-pachynema through meiotic prophase I. Scale bar (10 microns).

Our earlier temporal analysis in WT showed that there were almost no crossovers (0.65 ± 1.0 $x10^{-4}$) detected in zygonema, the second stage of meiotic prophase I, at *59.5*. However, by pachynema, the third stage of meiotic prophase I, crossovers appear (206.6 ± 21.6 $x10^{-4}$) and do not increase further in the fourth stage, diplonema (136.4 ± 43.8 $x10^{-4}$). Considering that MutLgamma is the primary crossover producing complex in WT, this data indicates that in WT spermatocytes, all MLH3-derived crossovers are detected by pachynema. In contrast, in *Exo1*$^{-/-}$ spermatocytes, only ~40% (9.0 ± 5.5 $x10^{-4}$) of crossovers were detectable in pachynema, with the rest appearing in diplonema (22.7 ± 10.8 $x10^{-4}$). Crossover frequency in *Exo1*$^{-/-}$ spermatocytes was similar between diplonema and Late 4C spermatocytes (Late 4C – at least 70% diplonema, sample purity shown in **Table 2**), consistent with the observation that all crossover recombination is completed by this stage. This analysis also shows that crossover timing is delayed in *Exo1*$^{-/-}$ spermatocytes, indicating that EXO1 is important for the proper timing of MutLgamma-dependent crossover formation (**Figure 27**).

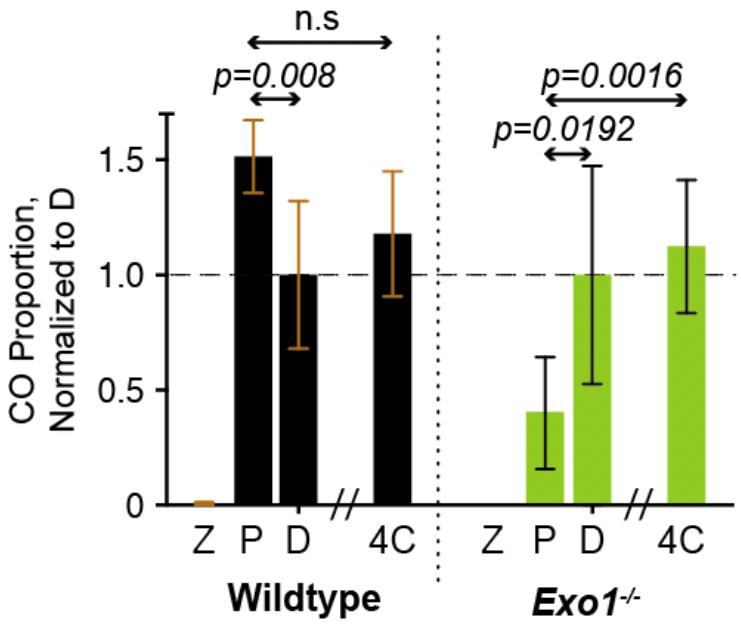

Figure 27: Crossover timing is defective in *Exo1*$^{-/-}$ spermatocytes
Histogram showing the proportion of crossovers (normalized to the diplonema frequency) found in Late 4C and enriched populations of the indicated stages of meiotic prophase I from WT, and *Exo1*$^{-/-}$ spermatocytes. P-values were determined with raw numbers by Fisher's exact test, two-tailed. Total un-normalized frequencies, from left: WT zygonema (N=3, 0.65 ± 1.0 x10^{-4}), WT pachynema (N=3, 206.6 ± 21.6 x10^{-4}), WT diplonema (N=3, 136.4 ± 43.8 x10^{-4}), and WT Late 4C (N=4, 160.8 ± 37.1 x10^{-4}). *Exo1*$^{-/-}$ spermatocytes, zygonema: not determined, *Exo1*$^{-/-}$ pachynema (N=3, 9.0 ± 5.5 x10^{-4}), *Exo1*$^{-/-}$ diplonema (N=3, 22.7 ± 10.8 x10^{-4}), and *Exo1*$^{-/-}$ Late 4C (N=6, 25.6 ± 7.32 x10^{-4}). Error bars represent the standard deviation from the mean.

Isolation of inter-homolog NCO repair products at hotspot *59.5*

Exo1$^{-/-}$ spermatocytes displayed only a ~10% reduction in MLH1/MLH3 foci (**Figure 17**) but a >70% reduction in metaphase bivalents (**Figure 20**) and crossover frequency (**Figure 23**) at the *59.5* hotspot relative to WT spermatocytes. This indicates that most *Exo1*$^{-/-}$ crossover precursors are not converted into crossovers. Previous work has shown that when crossover precursors form or 'designation' occurs but crossover formation is defective, the unrepaired precursors are repaired via alternative pathways resulting in their repair as alternative NCO products. These alternative NCOs are distinctly longer than events repaired from SDSA and often incorporate multiple consecutive polymorphisms in our F1 hybrid and are called co-conversions [61]. To determine whether *Exo1*$^{-/-}$ spermatocytes displayed an increase in co-

conversions, I performed a NCO assay at *59.5* that recovers all inter-homolog repair products, including NCOs, co-conversionss, and crossovers in an unbiased fashion.

To perform the NCO assay, I performed multiple parallel PCR reactions with ~10 amplifiable molecules of Late 4C DNA. The DNA was amplified using an allele-specific primer on the left-hand side of the hotspot (B, red) and a universal primer on the right-hand side of the hotspot (U, Black) (**Figure 28**). Universal primers amplify both parental genotypes equally. The primary PCR was followed by a second, nested PCR with similar primer configurations. Each reaction amplifies any potential crossovers (B to D) or NCOs (on the B chromosome) that were originally present (only B-U primer configuration is shown). All PCR reactions were dot-blotted and genotyped across the hotspot by Southern blotting (see methods).

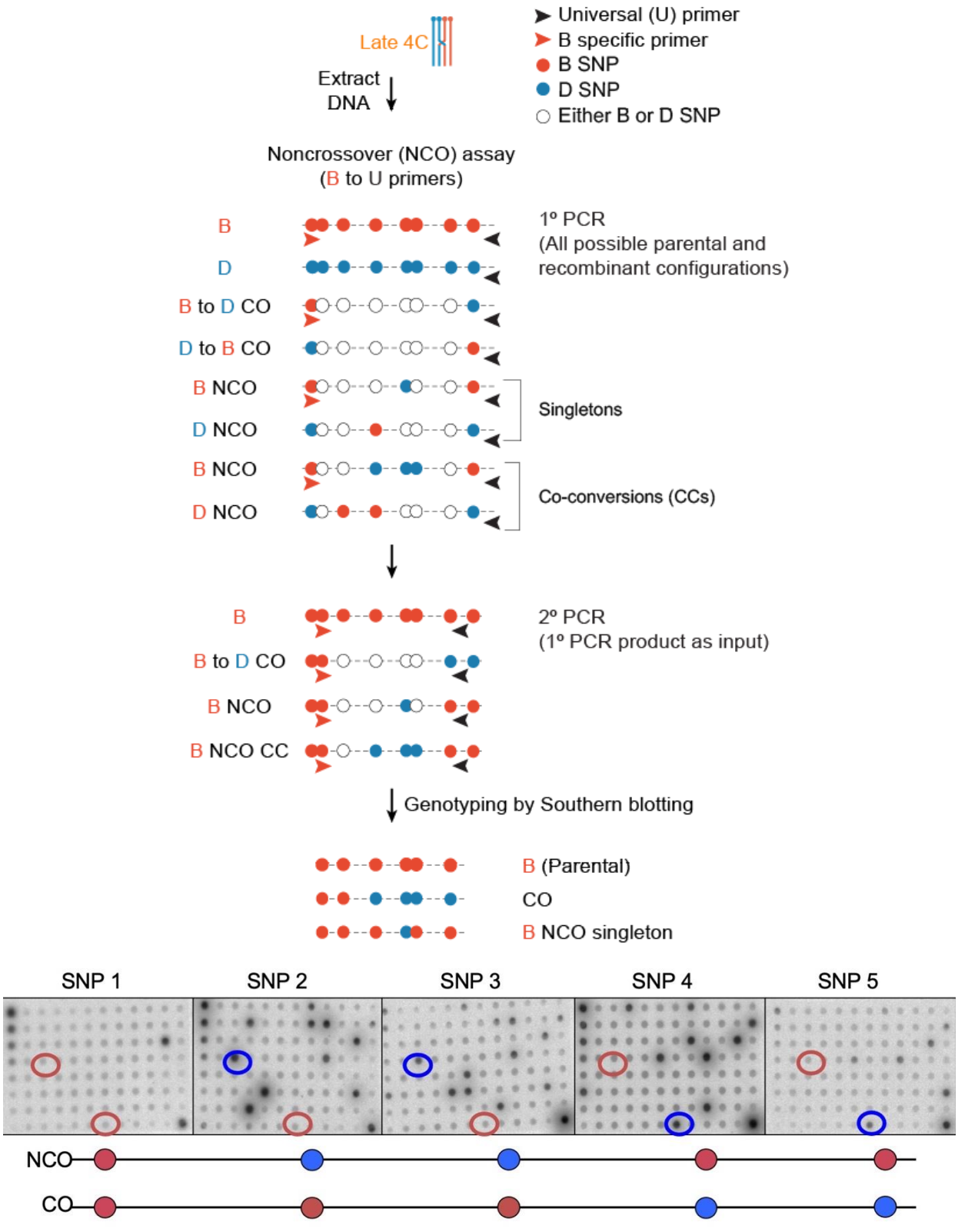

Figure 28: Schematic of NCO assay and representative blots
(Top) Schematic describing the NCO assay PCR that recovers all interhomolog recombinants present on one chromosome (here B chromosome). As in **Figure 22**, ~10 amplifiable genomes

were used as a template for two rounds of PCR using allele-specific primers, with the second PCR being nested into the first. The primers are given by (B, red arrow) on one side of the hotspot and a universal (U, black arrow) primer on the other.
(Bottom) Representative blots are used in southern blotting. Amplified products from a 96-well BU NCO PCR plate was replica-plated onto 5 positively charged nylon membrane in this example. Left most column on each blot shows positive controls used to detect positive wells. These blots were labeled with probes detecting the donor D chromosome. Examples of one NCO and one CO shown.

Exo1$^{-/-}$ spermatocytes have more singleton NCOs than WT

In mouse spermatocytes, most DSBs are repaired as short patch-like NCO products called singletons. These singleton NCO products incorporate only one polymorphism from the donor and the resulting repair product is consistent with repair via synthesis-dependent strand annealing (SDSA) [120]. During SDSA, the 3' overhang of the resected DSB invades the homolog, extends, and then gets displaced to anneal back to the parental strand to complete repair. SDSA is genetically independent of the crossover pathway, and thus it occurs in WT and crossover-defective mutants, such as *Mlh3*$^{-/-}$ [61].

To analyze the singleton NCO events, the NCO assay was performed on DNA isolated from late 4C *Exo1*$^{-/-}$, *Exo1*^{het}, *Exo1*$^{nd/nd}$, and WT late 4C spermatocytes. All *Exo1* mutants I examined (*Exo1*$^{-/-}$, *Exo1*^{het}, and *Exo1*$^{nd/nd}$) had a higher frequency of singletons than WT. While *Exo1*$^{nd/nd}$ and *Exo1*$^{-/-}$ spermatocytes had similar numbers of singletons, they were greater than *Exo1*^{het} spermatocytes (**Figure 29**). This finding suggests the increase in singletons observed in *Exo1*$^{-/-}$ spermatocytes is due to loss of the nuclease role of EXO1. Consistently, I suggest the increase in singletons is likely due to a decrease in EXO1-dependent mismatch correction of heteroduplex DNA that would normally cause reversion to the original parental genotype [178,181].

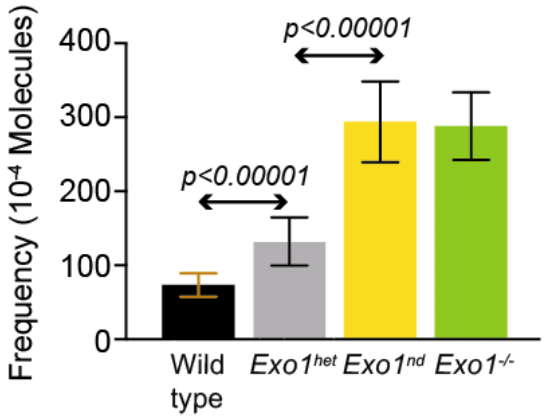

Figure 29: Singleton NCOs in *Exo1*$^{-/-}$ and *Exo1*$^{nd/nd}$ spermatocytes

Histogram showing Poisson-corrected frequencies of singletons at the *59.5* hotspot, plotted per 10,000 haploid genome equivalents (y-axis) with error bars representing the SD of the mean in WT (N=4, 73.4 ± 15.8), *Exo1*^{het} (N=4, 131.9 ± 32.6), *Exo1*$^{nd/nd}$ (N=4, 293.8 ± 54.6), *Exo1*$^{-/-}$ (N=6, 288.0 ± 54.6). P-values were determined by Fisher's exact test, two-tailed.

The alternative repair product co-conversions are longer in *Exo1*$^{-/-}$ spermatocytes

In mutants like *Mlh3*$^{-/-}$ spermatocytes, when crossover precursors form but are not converted into crossovers, long NCOs called co-conversions arise in lieu of lost crossovers. In *Mlh3*$^{-/-}$ spermatocytes, these co-conversions average ~300 bp and are likely the products of alternative repair pathway acting on the unrepaired crossover precursors [61]. To recover such alternative repair products in *Exo1*$^{-/-}$ and *Mlh3*$^{-/-}$ spermatocytes, I performed an NCO assay (**Figure 28**) using DNA from Late 4C spermatocytes (**Figure 21**). I found that the co-conversions isolated from *Exo1*$^{-/-}$ mutants averaged 692 ± 567 bp whereas *Mlh3*$^{-/-}$ mutants averaged 298 ± 231bp. Despite the difference in length, the frequency of *Exo1*$^{-/-}$ and *Mlh3*$^{-/-}$ co-conversions were similar indicating that the total number of upstream crossover precursors is unchanged between *Exo1*$^{-/-}$ and *Mlh3*$^{-/-}$ spermatocytes (Fisher's exact test, two-tailed). Together this comparison suggests the characteristics of the crossover precursors in spermatocytes may be different in the absence of EXO1 compared to MLH3.

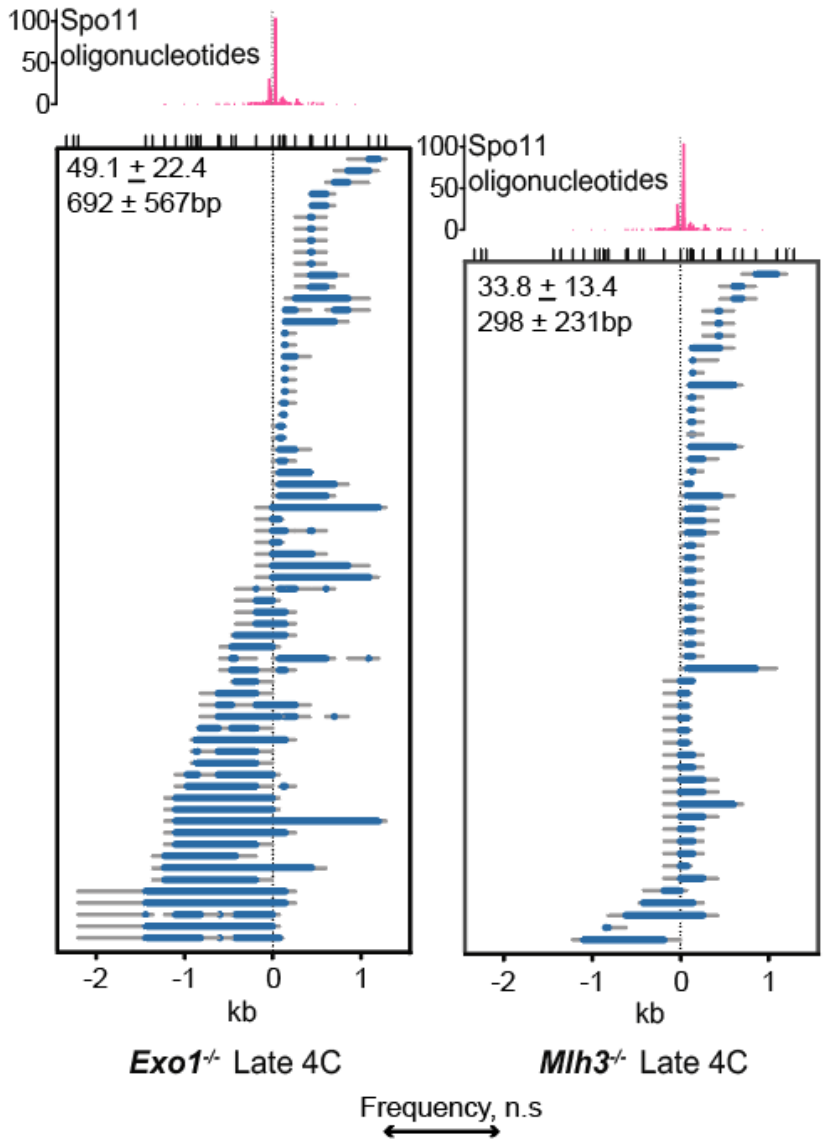

Figure 30: Co-conversions in *Exo1*$^{-/-}$ are longer than those from *Mlh3*$^{-/-}$ spermatocytes
Plot showing all co-conversions assessed in *Mlh3*$^{-/-}$ and *Exo1*$^{-/-}$ Late 4C spermatocytes. Top x-axis shows ticks marking polymorphisms used to map the repair events. Bottom, x-axis position on the genome relative to hotspot center (0 kb). Each of the repair events was plotted at the same location they would appear in the genome and relative to the center of the hotspot. For repair events, the minimum possible (blue) and maximum possible (gray) co-conversion tracts are shown. Asterisks mark discontinuous events. The upper-left corner of each plot displays the frequency per 10,000 analyzed haploid genomes followed by the average co-conversion tract length. Significance was tested by Fisher's exact test, two-tailed. Hotspot center is also extended as a dotted line through the plot.
Above the main plot on X-axis, is a second plot showing DSB locations at *59.5*. When SPO11 creates DSBs in meiosis, it gets covalently linked to the short DNA oligos at the location of the break. The magenta plot shows sequenced SPO11 oligonucleotide frequency in reads per

million [101]. The hotspot center denotes the location around which ~80% of the meiotic DSBs occur at *59.5* as estimated from sequenced SPO11 oligonucleotides.

Co-conversions are produced in diplonema in *Exo1*$^{-/-}$ spermatocytes

I saw that co-conversions in *Exo1*$^{-/-}$ spermatocytes are longer than those in *Mlh3*$^{-/-}$ spermatocytes (**Figure 30)**. I was able to observe a high frequency of these co-conversions at *59.5* in spermatocytes defective for crossover maturation, such as *Mlh3*$^{-/-}$ and *Exo1*$^{-/-}$ due to the enrichment of crossovers at *59.5* in our model organism. We have previously shown that in *Mlh3*$^{-/-}$ spermatocytes, these co-conversions likely arise via SDSA and/or dissolution of crossover-designated intermediates [61]. When the crossover precursors are dismantled by SDSA/dissolution the newly synthesized strand is contiguous from the invading strand [119]. In support of this model, I saw enrichment of co-conversions only on the B (recipient) chromosome and never on the D (donor) chromosome. Notably, the B chromosome is where most of the crossovers are assigned, based on evidence from crossover-dependent gene conversion in WT (**Figure 25,** [61]). To determine when these co-conversions form, I examined recombination in synchronized *Exo1*$^{-/-}$, WT, and *Mlh3*$^{-/-}$ spermatocytes. In WT, co-conversions formed at very low frequency in pachynema without an increase in diplonema. Like WT pachynema, *Mlh3*$^{-/-}$ and *Exo1*$^{-/-}$ spermatocytes had low frequencies of co-conversions in pachynema. However, *Mlh3*$^{-/-}$ diplonema spermatocytes had 10-fold more co-conversions and 13-fold more co-conversions than observed in WT spermatocytes at pachynema and diplonema, respectively. Similarly, *Exo1*$^{-/-}$ diplonema spermatocytes had 5-fold more co-conversions and 10-fold more co-conversions than wildtype pachynema and wildtype diplonema spermatocytes. Together, these data suggest that the co-conversions in *Exo1*$^{-/-}$ and *Mlh3*$^{-/-}$ spermatocytes likely result from backup repair pathways acting on unrepaired crossover-designated intermediates in diplonema, i.e., at a time after which crossover formation would normally have been completed in WT pachynema.

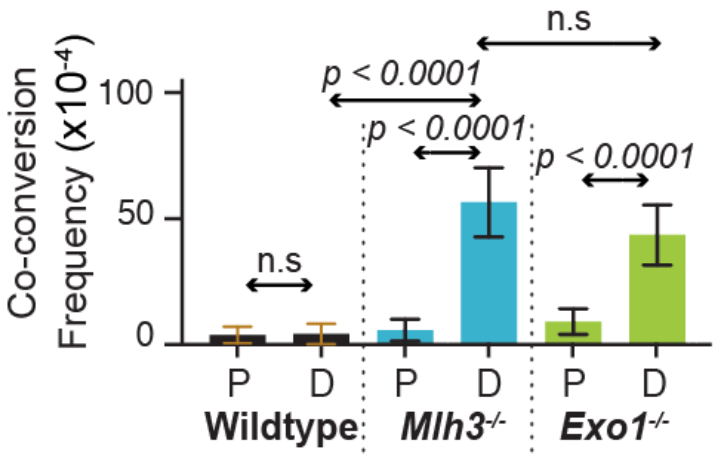

Figure 31: Timing of co-conversions in *Exo1*$^{-/-}$ spermatocytes
Histogram showing co-conversion frequency found in WT, *Mlh3*$^{-/-}$, and *Exo1*$^{-/-}$ spermatocyte populations enriched for pachynema (P) and diplonema (D). WT co-conversions in both pachynema and diplonema, 3.8 ± 3.3 (N=3, n=4 of 18079 haploid genome tested) and 4.2 ± 4 (N=3, n=5 of 15695 haploid genome tested), respectively. *Mlh3*$^{-/-}$, co-conversions in pachynema and diplonema 5.7 ± 4.3 (N=3, n=10 of 17610 haploid genome tested) and 56.5 ± 13.7 (N=3, n=62 of 11162 haploid genome tested), respectively. *Exo1*$^{-/-}$ spermatocytes, co-conversions in pachynema and diplonema 9.1 ± 5.1 (N=3, n=9 of 9952 haploid genome tested) and 40.4 ± 11.4 (N=3, n=38 of 9805 haploid genome tested), respectively. N=number of animals analyzed, n=number of events isolated. P-values were determined by Fisher's exact test, two-tailed.

Chapter 2: *Mlh3* produces residual crossovers in *Exo1*$^{-/-}$ spermatocytes, and long co-conversions in *Exo1*$^{-/-}$ spermatocytes require MLH3

MLH3 is required for bivalents observed in *Exo1*$^{-/-}$ spermatocytes

Exo1$^{-/-}$ spermatocytes showed only a ~10% reduction in MLH1/MLH3 foci (**Figure 17**) but a disproportionately large >70% reduction (**Figure 20**) in bivalents compared to WT spermatocytes. This suggests that the sites marked by MLH1/MLH3 that typically represent crossover precursors are not being converted to crossovers. Interestingly, the crossover phenotype in *Exo1*$^{-/-}$ spermatocytes is less severe than in *Mlh3*$^{-/-}$ spermatocytes, which lose over 90% of their crossovers [61]. To determine whether the residual crossovers in *Exo1*$^{-/-}$ spermatocytes require MLH3, I quantified bivalents in metaphase *Mlh3*$^{-/-}$ and *Exo1*$^{-/-}$ single and double mutant spermatocytes. I saw that *Mlh3*$^{-/-}$*Exo1*$^{-/-}$ double mutant spermatocytes had

similar average numbers of bivalents per cell, 1.2 ± 1.1, as *Mlh3*$^{-/-}$ spermatocytes (1.4 ± 1.2), but fewer than *Exo1*$^{-/-}$ spermatocytes (5.3 ± 2.0) (**Figure 32**). This data shows that *Mlh3* is epistatic to *Exo1* for formation of crossover bivalents. Additionally, the data shows that MLH3 is required for formation of the residual bivalents observed in *Exo1*$^{-/-}$ spermatocytes and that in mice, EXO1 may be only partially required for MutLgamma crossovers. In contrast, in budding yeast, EXO1 is required for all MutLgamma-derived bivalents [104].

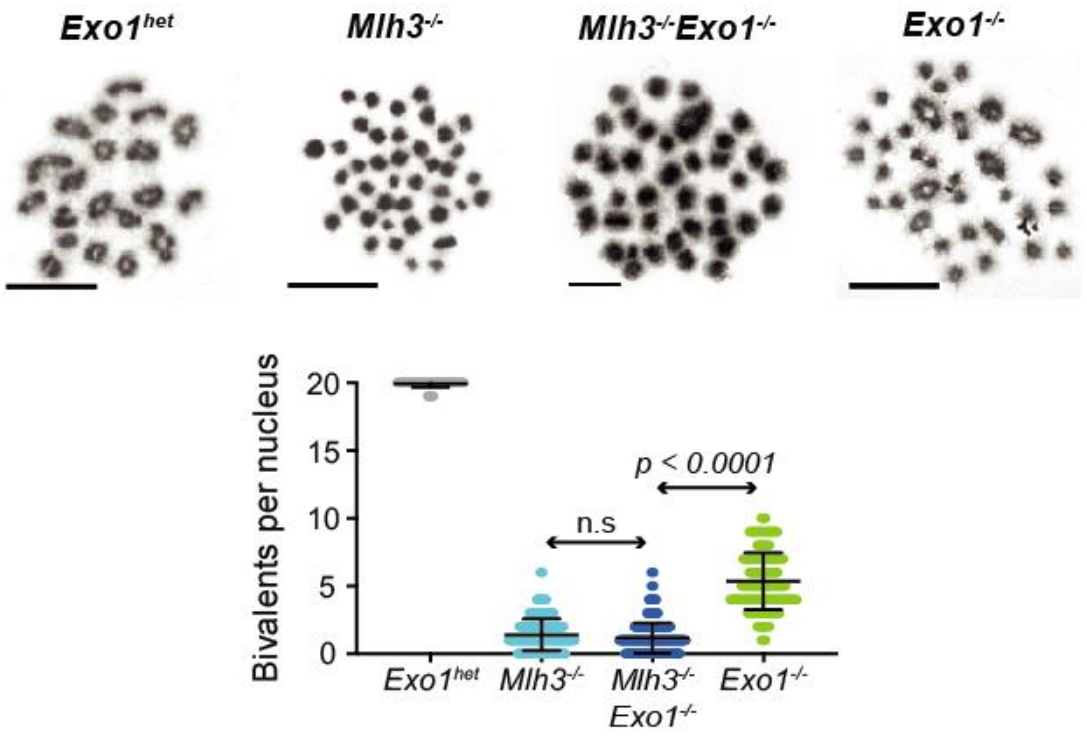

Figure 32: *Mlh3* is epistatic to *Exo1* for formation of metaphase bivalents
Top, representative metaphase images of spermatocytes from the indicated genotypes stained with Giemsa. Scale bar = 10 microns
Bottom, scatter plot of bivalent counts per cell (y-axis) showing the mean ± SD, in *Exo1*^{het} (N=3, 19.9 ± 0.3), *Mlh3*$^{-/-}$ (N=5, 1.4 ± 1.2), *Exo1*$^{-/-}$*Mlh3*$^{-/-}$ (N=4, 1.2 ± 1.1), and *Exo1*$^{-/-}$ (N=4, 5.3 ± 2.0) spermatocytes. P-values were determined by the Kruskal-Wallis test with Dunn's multiple comparison correction.

MLH3 is required for residual *Exo1*$^{-/-}$ crossovers at *59.5*

To determine whether the residual crossovers observed in *Exo1*$^{-/-}$ spermatocytes required MLH3, I examined crossover frequency in diplotene spermatocytes. Diplotene

spermatocytes were isolated as in **Figure 21** and analyzed as in **Figure 22**. I had showed earlier that there was a significant number of residual crossovers at *59.5* in *Exo1*$^{-/-}$ spermatocytes. I found that the crossover frequency in *Exo1*$^{-/-}$*Mlh3*$^{-/-}$ spermatocytes was similar to that of *Mlh3*$^{-/-}$ diplotene spermatocytes, (**Figure 33)**, indicating that MLH3 produces the residual crossovers in *Exo1*$^{-/-}$ spermatocytes similar to observations in bivalent analysis (**Figure 32)**.

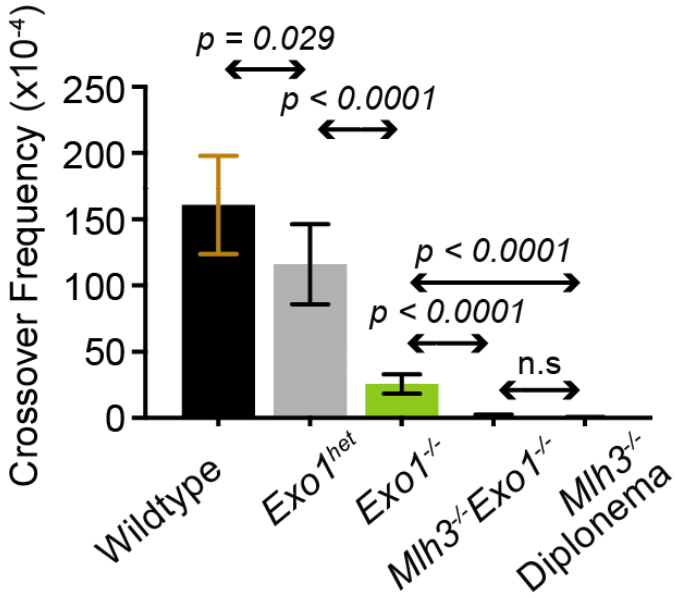

Figure 33: MLH3 is required for residual crossovers in *Exo1*$^{-/-}$ spermatocytes
Histogram showing the Poisson-corrected frequencies of crossovers at the *59.5* hotspot, plotted per 10,000 haploid genome equivalents (y-axis) for WT (N=4, n=238 crossovers), *Exo1*^{het} (N=4, n=91), *Exo1*$^{-/-}$ (N=6, n=145), *Mlh3*$^{-/-}$*Exo1*$^{-/-}$ (N=4, n=1), and *Mlh3*$^{-/-}$ Diplonema (N=3, n=11) spermatocytes. Error bars represent the SD of the mean. P-values were determined by Fisher's exact test, two-tailed. N=number of animals analyzed, n=number of events isolated also found in **Table 1**. All data in this figure are from the Late 4C population (~70% diplotene spermatocytes) except for *Mlh3*$^{-/-}$ mutants which was a sample with at least ~90% diplotene spermatocytes.

MLH3 is required for longer co-conversions observed in *Exo1*$^{-/-}$ spermatocytes

Mutants like *Mlh3*$^{-/-}$ and *Exo1*$^{-/-}$ form crossover precursors, most of which are not converted into crossover products but can instead become co-conversions [61]. These co-conversions are enriched at the *59.5* hotspot on the B chromosome, where a large fraction of meiotic DSBs are designated to form crossover precursors. Notably, co-conversions are not

enriched in mutants that fail to designate crossover precursors, for example *Rnf212*$^{-/-}$ spermatocytes (Lakshmi Paniker, Francesca Cole. unpublished data) (full names). This evidence, together with the appearance of co-conversions at the end of meiotic prophase I (**Figure 31**), suggests that the *Exo1*$^{-/-}$ co-conversions are products of backup repair, likely arising from unresolved crossover precursors. (I will stop highlighting co-conversions in the following text)

The co-conversion gene conversion tracts in *Exo1*$^{-/-}$ spermatocytes were longer than the co-conversion tracts in *Mlh3*$^{-/-}$ spermatocytes (**Figure 30**). To dissect the genetic requirements for the longer co-conversions, and to test if MLH3 is epistatic for co-conversion length, I analyzed co-conversions in *Mlh3*$^{-/-}$*Exo1*$^{-/-}$ spermatocytes. To isolate co-conversions, I performed a NCO assay as outlined in **Figure 28,** using *Mlh3*$^{-/-}$*Exo1*$^{-/-}$ spermatocytes. I saw that co-conversion tract lengths in *Exo1*$^{-/-}$*Mlh3*$^{-/-}$ spermatocytes averaged 334 ± 288 bp and were comparable in length to those of *Mlh3*$^{-/-}$ spermatocytes (298 ± 231 bp), showing that *Mlh3* is epistatic to *Exo1* for co-conversion tract lengths.

If the MMR defect were an important contributor to co-conversion length, *Exo1*$^{-/-}$ spermatocytes would be expected to have a stronger defect than *Mlh3*$^{-/-}$ mutant spermatocytes given the minor role of MLH3 in mammalian MMR [168,169,183,184]. But I instead find that *Mlh3* is epistatic to *Exo1* for longer co-conversions. This likely rules out defective MMR as a significant contributor to the elongated co-conversions seen in *Exo1*$^{-/-}$ spermatocytes.

More importantly, the average length of co-conversions in *Exo1*$^{-/-}$ spermatocytes is similar to the average estimated crossover precursor lengths measured in humans and mice [61,120,182]. Taking the similarity between length of co-conversions in *Exo1*$^{-/-}$ spermatocytes and WT crossover precursor lengths, the data suggest the longer co-conversions may reflect differences in the crossover precursors between *Mlh3*$^{-/-}$ and *Exo1*$^{-/-}$ mutant spermatocytes. In support of this model, I find that MLH3, a protein with primary roles in crossover formation is required to see longer co-conversions. Together, I suggest that crossover precursors are elongated in *Exo1*$^{-/-}$ spermatocytes, a process that requires MLH3.

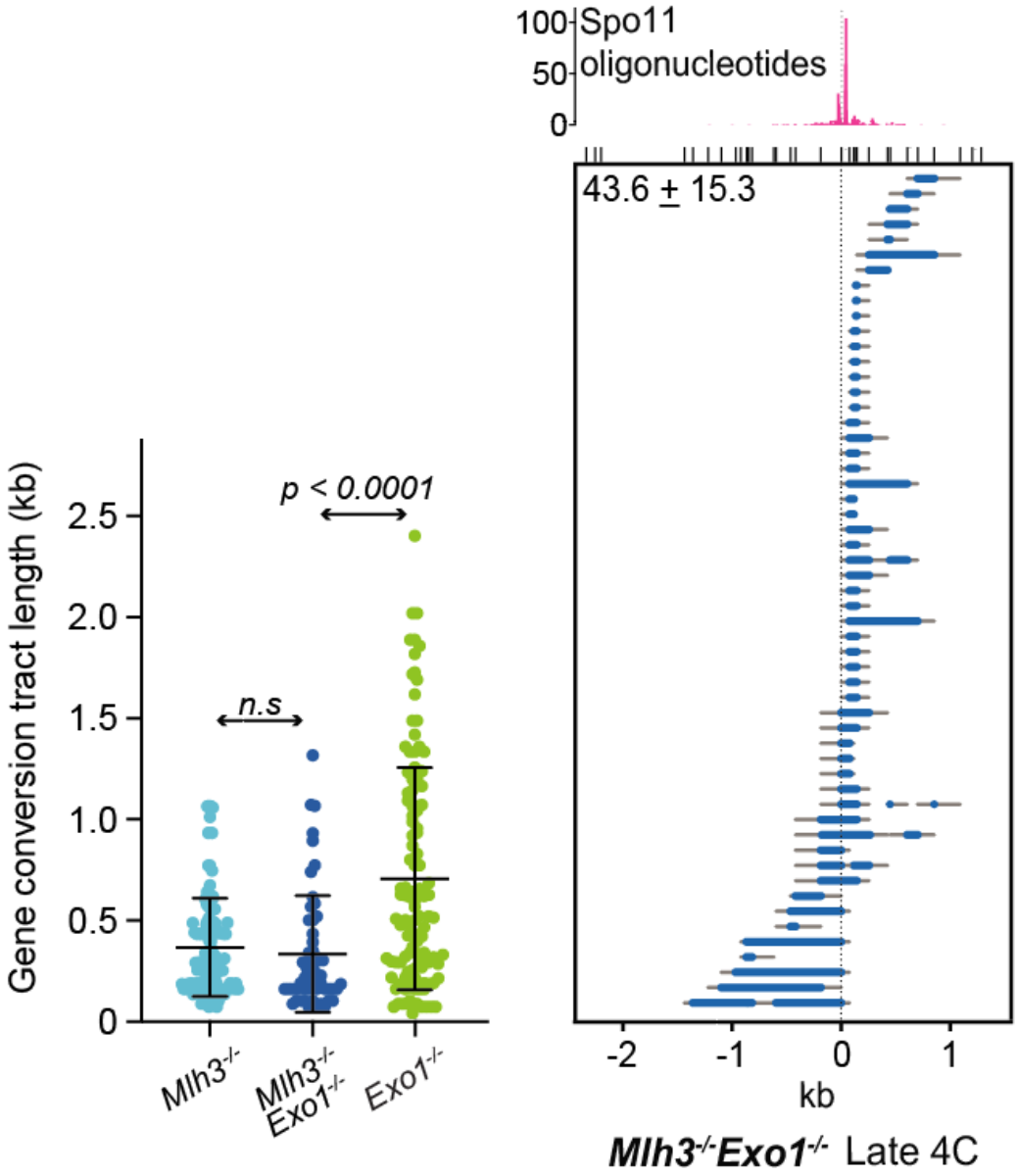

Figure 34: MLH3 is epistatic to EXO1 for co-conversion tract length

Left**,** Scatter plot showing the length of co-conversions in kb (mean ± SD) from *Mlh3*$^{-/-}$ (N=6, 298 ± 230bp), *Mlh3*$^{-/-}$ *Exo1*$^{-/-}$ (N=4, 334 ± 288bp), and *Exo1*$^{-/-}$ (N=6, 692 ± 567bp) spermatocytes. P-values are derived from the Kruskal-Wallis test with Dunn's multiple comparison correction. All samples used in this analysis were Late 4C spermatocytes (~70% enriched for diplonema). N = the number of animals analyzed.

Right**,** co-conversion tract plot. All co-conversions isolated from *Mlh3*$^{-/-}$*Exo1*$^{-/-}$ late 4C spermatocytes were plotted. The blue line plots the minimal and the gray line the maximal possible gene conversion tract. The x-axis shows ticks marking polymorphisms at the top and relative positions within the hotspot at the bottom. The total frequency ± SD (top left) of co-

conversions per 10,000 haploid genomes analyzed is shown. The center of the hotspot is marked by a vertical dotted line and plotted at 0kb.

Above the main plot on X-axis, is a second plot showing DSB locations at *59.5* [101].

Chapter 3: MLH3 has a nuclease-independent role in the formation of longer, WT-like crossover precursors.

Mlh3$^{DN/DN}$ mutant spermatocytes have residual crossover activity

Metaphase bivalent chromosome analysis of EXO1 and MLH3 single and double mutants (**Figure 32**) revealed that *Mlh3* was epistatic to *Exo1* for the loss of connected homologs (metaphase bivalents). Although MLH3's role in producing crossovers (maturation) has been established in mammals [154 Gray, 2016 #60,156,157,185], it is unclear whether maturation is dependent only on the nuclease activity of MLH3, rather than a combination of nuclease activity and a possible structural role.

An earlier report analyzing spermatocytes with a presumptive nuclease deficient allele of MLH3 (*Mlh3*$^{DN/DN}$) hinted that MLH3 may have an additional nuclease-independent function in mammals [160]. The MLH3^{DN} protein bears an asparagine residue substituted for a nuclease active site aspartate residue (D1185). This mutation has been shown to lack enzyme activity when purified enzymes were tested *in vitro* [186]. Unlike *Mlh3*$^{-/-}$ spermatocytes, *Mlh3*$^{DN/DN}$ mutants retain proper chromosome association of crossover promoting factors, including MLH1, MLH3, cyclin-dependent kinase-2 (CDK2), and the putative ubiquitin E3 ligase and Human Enhancer of Invasion-10 protein HEI10. Despite these normal protein associations, *Mlh3*$^{DN/DN}$ spermatocytes are infertile due to reduced metaphase bivalents. However, *Mlh3*$^{DN/DN}$ spermatocytes have higher numbers of residual crossovers than *Mlh3*$^{-/-}$ spermatocytes. Based upon this phenotype, some *Mlh3*$^{-/-}$ defects are mitigated in *Mlh3*$^{DN/DN}$ spermatocytes, but it is unknown whether the *Mlh3*$^{DN/DN}$ encoded protein maintains any enzymatic activity. Therefore, it remains unclear whether the higher number of residual bivalents observed in *Mlh3*$^{DN/DN}$ compared to *Mlh3*$^{-/-}$ mutants arises from residual enzymatic activity or a nuclease-independent function of MLH3.

To test whether MLH3 has a nuclease-independent function in crossover maturation, we analyzed metaphase bivalents from various combinations of single and double mutants of *Mlh3*$^{DN/-}$, *Mlh3*$^{-/-}$, and *Exo1*$^{-/-}$. *Mlh3*$^{-/DN}$ spermatocytes were included to test whether there might be a dosage-dependent effect of the allele encoding the MLH3^{DN} protein (**Figure 35**). In line with published work, *Mlh3*$^{DN/DN}$ mutant spermatocytes fail to form WT levels of bivalents [160]. *Mlh3*$^{DN/DN}$ spermatocytes had 5.5 ± 1.9 bivalents per cell on average, which was similar to *Exo1*$^{-/-}$ spermatocytes (5.3 ± 2.0). However, the *Mlh3*$^{-/DN}$ heterozygous mutant had fewer, bivalents per cell on average (3.97 ± 1.9) compared to *Mlh3*$^{DN/DN}$ homozygous spermatocytes, indicating that the bivalent phenotype is dosage sensitive. However, the dosage sensitivity can arise either because of a residual enzymatic activity or a non-enzymatic structural role for MLH3 in crossover maturation.

To definitively test whether the residual bivalents in *Mlh3*$^{DN/DN}$ spermatocytes are produced via a nuclease-dependent or -independent function of MLH3, we analyzed bivalents in *Mlh3*$^{DN/DN}$ *Exo1*$^{-/-}$ double mutants. The *Mlh3*$^{DN/DN}$ *Exo1*$^{-/-}$ double mutant was chosen because each mutant alone has similar numbers of residual bivalents and MLH3 protein is present but defective for nuclease activity. We have shown earlier that EXO1 promotes MLH3's nuclease activity (**Figure 32**). If *Mlh3*$^{DN/DN}$ retains residual nuclease activity, loss of EXO1 should show a further reduction in MLH3's nuclease activity. If instead crossover formation in *Mlh3*$^{DN/DN}$ spermatocytes is MLH3 nuclease-independent, then bivalent counts in *Mlh3*$^{DN/DN}$ *Exo1*$^{-/-}$ should be similar to *Mlh3*$^{DN/DN}$ spermatocytes. My results show that *Mlh3*$^{DN/DN}$ *Exo1*$^{-/-}$ double mutant spermatocytes had almost no bivalents on average (1.7 ± 1.3), similar to observations in *Mlh3*$^{-/-}$ spermatocytes that completely lack MLH3 nuclease activity. Together the data suggest that the higher number of residual bivalents observed in *Mlh3*$^{DN/DN}$ spermatocytes are likely a product of the residual enzymatic activity of MLH3-DN protein.

When MLH3 is absent in mouse spermatocytes, ~1 bivalent is formed per mouse spermatocyte [154,157,185]. This bivalent is likely produced by structure selective endonucleases (SSNs), such as MUS81 [134], that can resolve dHJs into both crossovers and NCOs [155,170,187]. To

test the potential contribution of MUS81 to the frequency of residual crossovers in *Exo1*$^{-/-}$ spermatocytes, I analyzed *Mus81*$^{-/-}$*Exo1*$^{-/-}$ spermatocytes. I only saw a mild reduction in the average number of bivalents per cell in *Mus81*$^{-/-}$*Exo1*$^{-/-}$ (4.1 ± 1.9) compared to *Exo1*$^{-/-}$ (5.3 ± 2.0) spermatocytes, similar to the mild reduction in chiasmata previously reported for *Mus81*$^{-/-}$ *Mlh3*$^{-/-}$ spermatocytes [134,160]. These data suggest that MUS81 is not a major contributor to residual crossover formation in Exo1 mutants, making it more likely that the residual crossovers in both *Exo1*$^{-/-}$ and *Mlh3*$^{DN/DN}$ single mutants result from diminished but not absent nuclease activity of MLH3. Further, these data indicate that EXO1 is only partially required for MutLgamma nuclease activity in mouse spermatocytes, which differs from budding yeast that requires EXO1 for all MutLgamma-dependent crossovers [104].

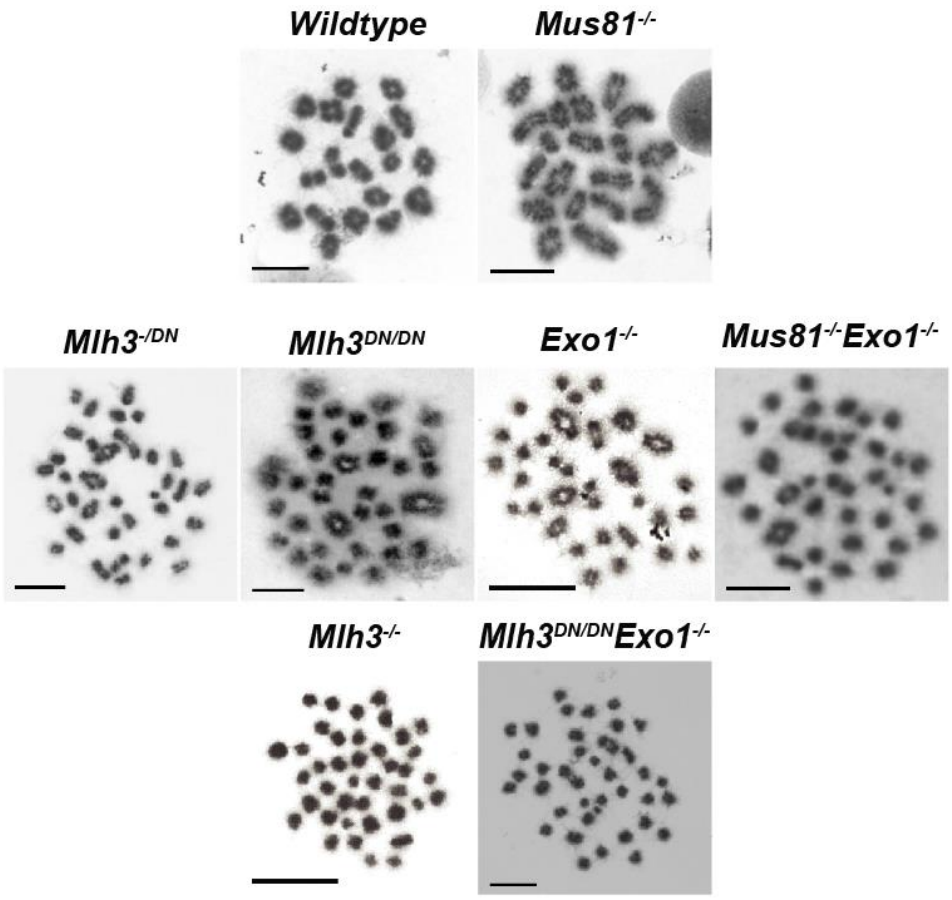
Wildtype
Mus81-/-
Mlh3-/DN
Mlh3DN/DN
Exo1-/-
Mus81-/-Exo1-/-
Mlh3-/-
Mlh3DN/DNExo1-/-

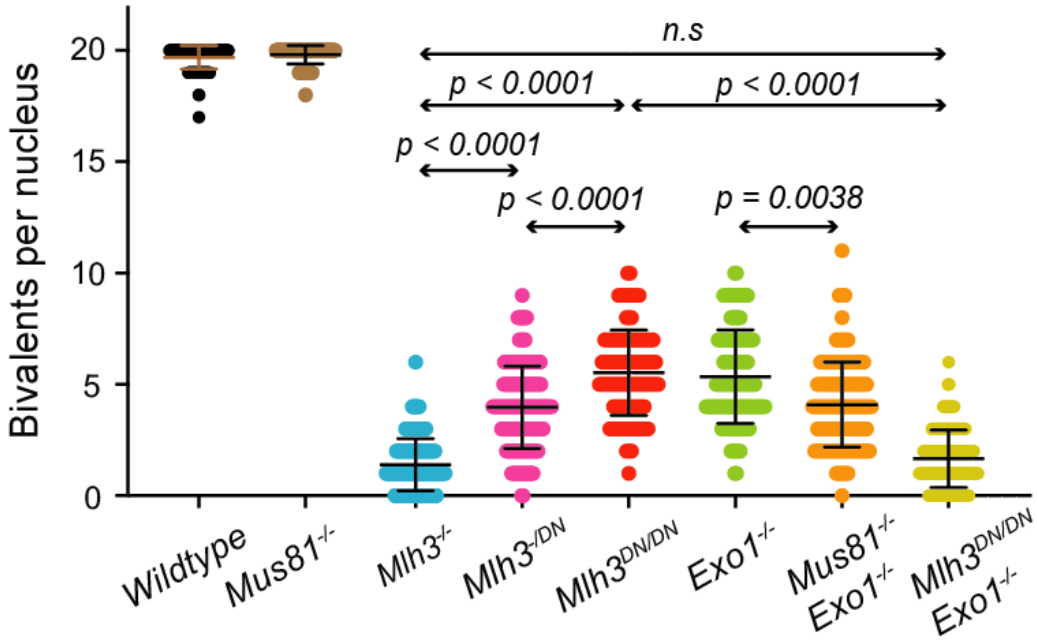
Bivalents per nucleus
20
15
10
5
0
n.s
p < 0.0001
p < 0.0001
p < 0.0001
p < 0.0001
p = 0.0038
Wildtype
Mus81-/-
Mlh3-/-
Mlh3-/DN
Mlh3DN/DN
Exo1-/-
Mus81-/- Exo1-/-
Mlh3DN/DN Exo1-/-

Figure 35: Metaphase bivalent counts in single and double mutants of *Mlh3*$^{DN/DN}$, *Exo1*$^{-/-}$ and *Mus81*$^{-/-}$ spermatocytes

(Top)**,** Representative metaphase images of spermatocytes from the indicated genotypes stained with Giemsa. The representative images are grouped by phenotype. First row: WT; second row: partial loss of bivalents; and the third row: severe loss of bivalents. Scale bar =10 microns.

(Bottom)**,** Scatter plot showing number of bivalent counts per cell (y-axis) with error bars representing the SD of the mean (central bar) in WT (N=2, 19.7 ± 0.5), *Mus81*$^{-/-}$ (N=5, 19.8 ± 0.6), *Mlh3*$^{-/-}$ (N=5, 1.4 ± 1.2), *Mlh3*$^{-/DN}$ (N=3, 3.97 ± 1.9), *Mlh3*$^{DN/DN}$ (N=3, 5.5 ± 1.9), *Exo1*$^{-/-}$ (N=4, 5.3 ± 2.0), *Mus81*$^{-/-}$*Exo1*$^{-/-}$ (N=3, 4.1 ± 1.9), and *Mlh3*$^{DN/DN}$*Exo1*$^{-/-}$ (N=2, 1.7 ± 1.3). P-values were determined by the Kruskal-Wallis test with Dunn's multiple comparison correction.

Mlh3$^{DN/DN}$*Exo1*$^{-/-}$ spermatocytes have lower crossovers at *59.5*

My cytological analysis showed that *Mlh3*$^{DN/DN}$ and *Exo1*$^{-/-}$ spermatocytes had similar numbers of bivalents to each other. In contrast, *Mlh3*$^{DN/DN}$ *Exo1*$^{-/-}$ spermatocytes had many fewer bivalents similar to *Mlh3*$^{-/-}$ spermatocytes (**Figure 35)**. To directly examine crossover formation, I analyzed recombination at the *59.5* hotspot in *Mlh3*$^{DN/DN}$*Exo1*$^{-/-}$ and *Mlh3*$^{DN/DN}$ spermatocytes. I found that, like bivalent frequencies, *Mlh3*$^{DN/DN}$ and *Exo1*$^{-/-}$ spermatocytes had similar numbers of crossovers, whereas *Mlh3*$^{DN/DN}$*Exo1*$^{-/-}$ spermatocytes had fewer. Finally, for reasons that are unclear, *Mlh3*$^{DN/DN}$*Exo1*$^{-/-}$ spermatocytes had more crossovers than *Mlh3*$^{-/-}$ spermatocytes, perhaps because the *59.5* locus is enriched for crossovers, which allows differentiation of subtle crossover phenotypes. Together, these crossover data support a model in which crossovers that occur in *Mlh3*$^{DN/DN}$ and *Exo1*$^{-/-}$ single mutant spermatocytes result from residual MLH3 nuclease activity.

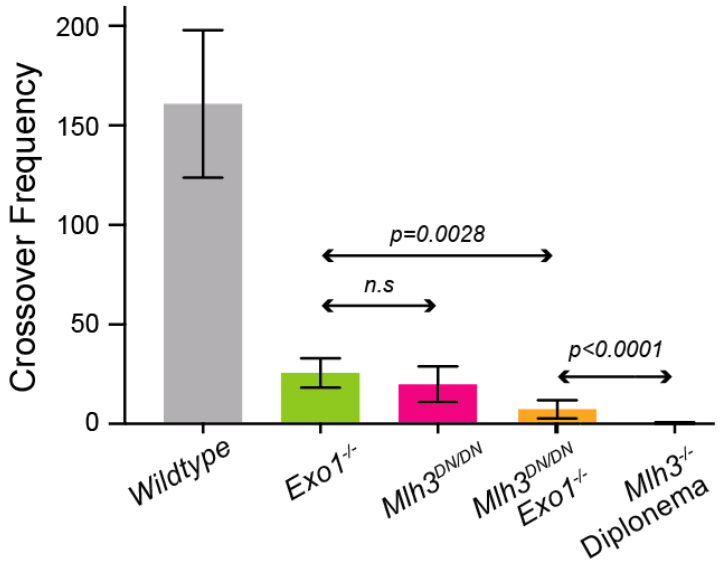

Figure 36: *Mlh3$^{DN/DN}$Exo1$^{-/-}$* have fewer crossovers than *Exo1$^{-/-}$* spermatocytes at *59.5*

Histogram showing the average Poisson-corrected frequencies of crossovers at the *59.5* hotspot in diplonema-enriched Late-4C spermatocytes, plotted per 10,000 haploid genome equivalents (y-axis) and error bars represent the standard deviation of the mean. WT (N=4, 160.8 ± 37.1), *Exo1$^{-/-}$* (N=6, 25.59 ± 7.32), *Mlh3$^{DN/DN}$* (N=2, 19.9 ± 9.0), *Mlh3$^{DN/DN}$Exo1$^{-/-}$* (N=2, 7.3 ± 4.6), and *Mlh3$^{-/-}$* (N=3, 0.28 ± 0.50). P-values were determined by Fisher's exact test, two-tailed. All genotypes shown in this figure except *Mlh3$^{-/-}$* spermatocytes are from the late-4C population (about 70% diplonema) while the *Mlh3$^{-/-}$* spermatocytes sample is more enriched, about 90% for diplonema.

Mlh3$^{DN/DN}$Exo1$^{-/-}$ double mutants have fewer MLH1 foci than *Exo1^{het}* spermatocytes

Mlh3$^{DN/DN}$Exo1$^{-/-}$ double mutant and *Mlh3$^{-/-}$* single mutant spermatocytes had only <10% of WT bivalents per cell on average. The MutLgamma complex is an obligate heterodimer of MLH1 and MLH3, thus in *Mlh3$^{-/-}$* single mutant spermatocytes, MLH1 and, by extension, MutLgamma complex do not localize to chromosome sites. Given the similarity in bivalent numbers between *Mlh3$^{DN/DN}$Exo1$^{-/-}$* double mutant and *Mlh3$^{-/-}$* single mutant spermatocytes, I quantified MLH1/MutLgamma foci formation at chromosome sites in *Mlh3$^{DN/DN}$Exo1$^{-/-}$* double mutant spermatocytes.

Importantly, both *Mlh3$^{DN/DN}$* and *Exo1$^{-/-}$* spermatocytes form MLH1 foci. *Mlh3$^{DN/DN}$* spermatocytes display WT numbers of MLH1 foci [160], while *Exo1$^{-/-}$* spermatocytes show 10%

fewer (**Figure 17**). I found fainter MLH1 foci in *Mlh3*$^{DN/DN}$*Exo1*$^{-/-}$ spermatocytes than in WT or *Exo1*^{het} spermatocytes. I hypothesized that the *Mlh1-Mlh3*$^{DN/DN}$ MutLgamma complex may have less stable recruitment when EXO1 is also simultaneously absent in *Mlh3*$^{DN/DN}$*Exo1*$^{-/-}$ spermatocytes. Therefore, to test complex formation on the axis, I performed immunofluorescence staining using an MLH1 antibody and estimated the proportion of pachytene cells containing MLH1 foci in *Mlh3*$^{DN/DN}$*Exo1*$^{-/-}$ spermatocytes. I found that the proportion of cells containing MLH1 foci in *Mlh3*$^{DN/DN}$*Exo1*$^{-/-}$ spermatocytes was significantly lower than in *Exo1*^{het} spermatocytes. Further, in the cells with foci, *Mlh3*$^{DN/DN}$*Exo1*$^{-/-}$ double mutant spermatocytes had fewer MLH1 foci than *Exo1*^{het} spermatocytes. These data show that while the *Mlh3*$^{DN/DN}$*Exo1*$^{-/-}$ spermatocytes form MLH1 foci, they are fewer in number and show less stable recruitment to chromosome sites than in *Exo1*^{het} spermatocytes.

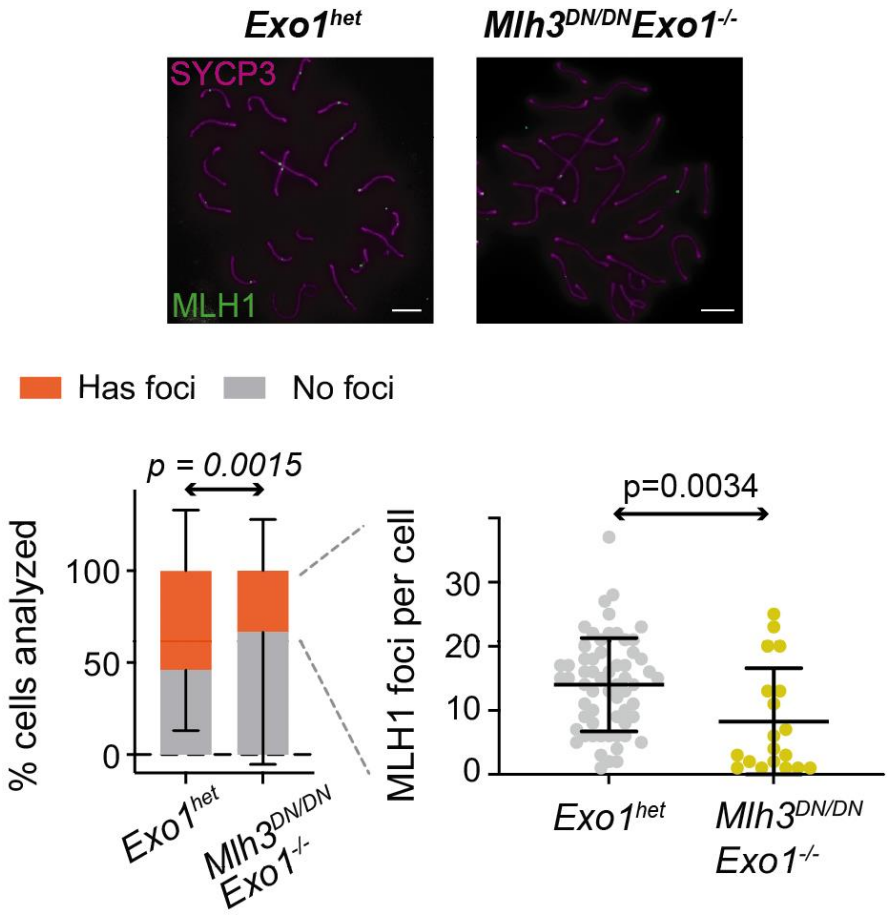

Figure 37: *Mlh3*$^{DN/DN}$*Exo1*$^{-/-}$ spermatocytes have fewer MLH1 foci than *Exo1*^{het} spermatocytes.
(Top)**,** Representative immunofluorescence images of pachytene stage spermatocytes of the indicated genotypes stained for SYCP3 (magenta) and MLH1 (green). Scale bar, 10 microns. Cells in pachynema were imaged at random without regard to MLH1 focus status prior to determine the proportion of cells bearing MLH1 foci. Qualitatively, *Mlh3*$^{DN/DN}$*Exo1*$^{-/-}$ appeared to have fewer and weaker foci that were hard to discern under the microscope.
(Bottom)**,** Left, histogram of the percent of cells with MLH1 foci in *Exo1*^{het} (N=3, n=108, 53.9% ± 33.1% cells had foci) and *Mlh3*$^{DN/DN}$*Exo1*$^{-/-}$ pachytene spermatocytes (N=2, n=64, 33.3% ± 27.9% cells had foci). P-values were determined by Fisher's exact test, two-tailed. Right, Scatter plot of MLH1 foci per positive cell in *Exo1*^{het} (N=3, n=61, 14.0 ± 7.3) and *Mlh3*$^{DN/DN}$*Exo1*$^{-/-}$ (N=2, n=19, 8.3 ± 8.3) pachytene spermatocytes. N=animals counted, n=number of cells included in corresponding analysis. P-values were determined by Mann-Whitney. N.B. The mean number of foci in *Exo1*^{het} spermatocytes was lower than in **Figure 17** because the current figure quantifies MLH1 foci in all cells with any MLH1 foci whereas in **Figure 17,** only cells with bright visible MLH1 foci were included in the analysis. These cells likely bear peak numbers of MLH1 foci.

Mlh3$^{DN/DN}$*Exo1*$^{-/-}$ spermatocytes have fewer CDK2 foci

MutLgamma is the crossover-producing complex in mammalian meiosis [37] and MLH1 foci were reduced in *Mlh3*$^{DN/DN}$*Exo1*$^{-/-}$ spermatocytes. Therefore, to determine whether the localization of another crossover-promoting factor, cyclin-dependent kinase 2 (CDK2), [188] was also affected, I isolated pachytene spermatocytes and stained them with antibodies raised against CDK2. In WT cells, CDK2 is recruited independent of crossover precursor formation to telomeres with interstitial locations associated with crossover sites in pachytene spermatocytes. In *Mlh3*$^{DN/DN}$ spermatocytes, CDK2 foci form with similar timing, frequency, and distribution as in WT [160]. However, I saw fewer cells with interstitial CDK2 foci in *Mlh3*$^{DN/DN}$*Exo1*$^{-/-}$ spermatocytes (**Figure 38**), like reduction in number of cells with MLH1 foci (**Figure 37**). Further, the number of CDK2 foci was lower compared to WT and *Exo1*^{het} samples and was lower compared to *Exo1*$^{-/-}$ spermatocytes. Together, these data suggest that crossover-promoting complexes containing CDK2 are either recruited less often or have less stable chromosome localization in *Mlh3*$^{DN/DN}$*Exo1*$^{-/-}$ as compared to *Exo1*$^{-/-}$ (**Figure 38**) or *Mlh3*$^{DN/DN}$ spermatocytes [160].

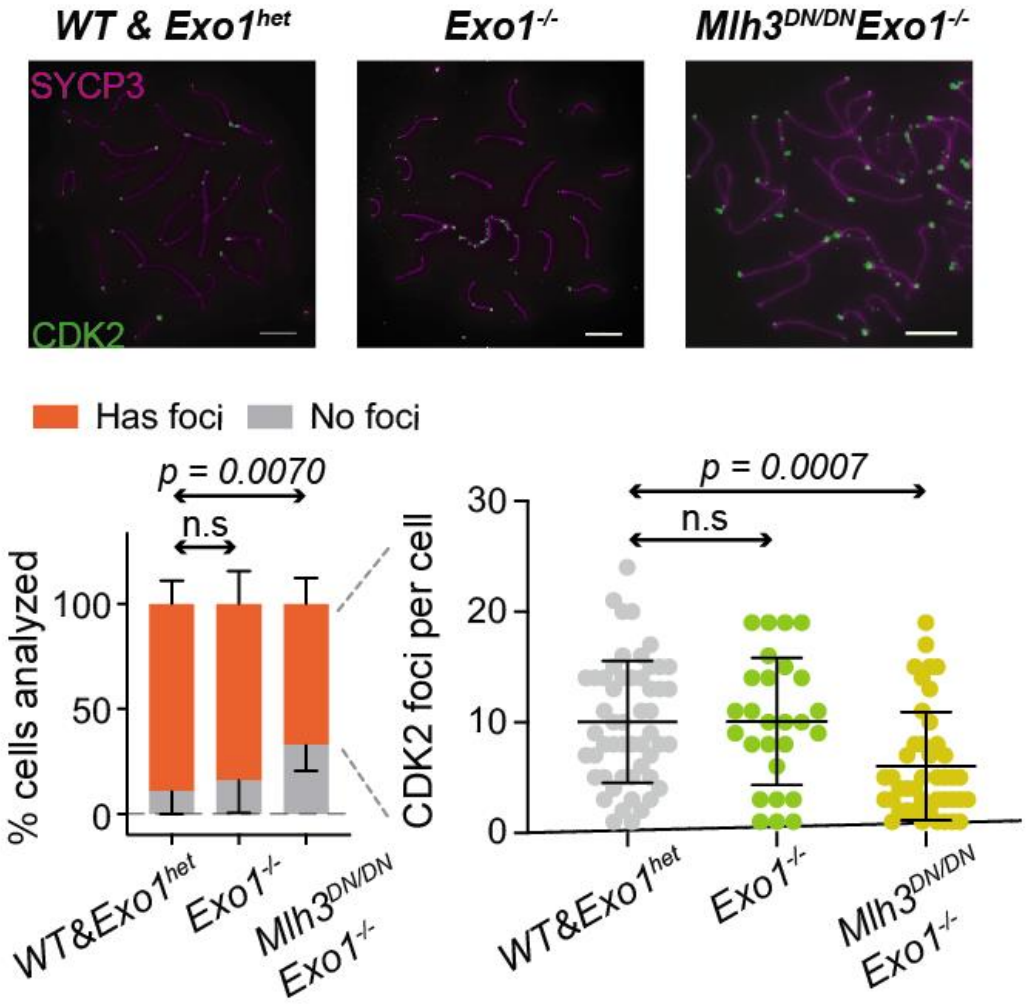

Figure 38: *Mlh3$^{DN/DN}$Exo1$^{-/-}$* have fewer CDK2 foci

(Top)**,** Representative immunofluorescence images of pachytene stage spermatocytes of the indicated genotypes stained for SYCP3 (magenta) and CDK2 (green). Scale bar =10 microns. *Mlh3$^{DN/DN}$Exo1$^{-/-}$* had fewer and weaker interstitial (non-telomeric) CDK2 foci and were scored as in **Figure 37**.

(Bottom), Left, histogram showing the percentage of cells with CDK2 foci in *WT* (N=1, n=27*) & Exo1^{het}* (N=2, n=34) together (89.1 ± 11.1 had foci), *Exo1$^{-/-}$* (N=2, n=31 , 83.9 ± 15.7 had foci), and *Mlh3$^{DN/DN}$Exo1$^{-/-}$* (N=2, n=65, 67.1 ± 12.4 had foci). N=animals counted, n=number of cells included in corresponding analysis. P-values were determined by Fisher's exact test, two-tailed. Right, Scatter plot of CDK2 foci per positive cell in *WT (N=1) & Exo1^{het}* (N=2) together (10.0 ± 5.5, n=53), *Exo1$^{-/-}$* (N=2, 10.0 ± 5.7, n=27), and *Mlh3$^{DN/DN}$Exo1$^{-/-}$* (N=2, 6.0 ± 4.9, n=43). P-values were determined by the Kruskal-Wallis test with Dunn's multiple comparison correction. While non-telomeric CDK2 foci were present in *Mlh3$^{DN/DN}$Exo1$^{-/-}$*, the percent of pachytene spermatocytes bearing interstitial CDK2 foci and their frequency were similar between *WT&Exo1^{het}* and *Exo1$^{-/-}$* and lower for *Mlh3$^{DN/DN}$Exo1$^{-/-}$*. WT N=1 & *Exo1^{het}* N=2 had similar phenotype and were combined from statistical analysis.

$Mlh3^{DN/DN}$, $Mlh3^{-/DN}$, and $Mlh3^{DN/DN}Exo1^{-/-}$, like $Exo1^{-/-}$ spermatocytes, have longer co-conversion tracts at *59.5*

$Exo1^{-/-}$ mutant spermatocytes displayed longer average co-conversion tracts than either *$Mlh3^{-/-}$* or *$Exo1^{-/-}Mlh3^{-/-}$* spermatocytes at *59.5.* These co-conversions were similar in length to those of WT crossovers (**Figure 34**) and require MLH3 for their WT-like length ([61], **Figure 31**). Given that lack of EXO1 shows more mismatch defects that lack of MLH3 [168,169,183,184], the increase in co-conversion length is likely not caused by defective MMR. I therefore inferred that the longer co-conversions in *$Exo1^{-/-}$* mutants likely arose from crossover precursors that are similar in length to WT crossover gene conversion tracts.

Although MLH3 was required for the formation of the longer co-conversion tracts in *$Exo1^{-/-}$* mutant spermatocytes (**Figure 34**), it is unclear whether the increased length of co-conversions in *$Exo1^{-/-}$* mutant spermatocytes requires the nuclease function of MLH3. Therefore, I analyzed co-conversions from *$Mlh3^{DN/DN}$*, *$Mlh3^{-/DN}$*, and *$Mlh3^{DN/DN}Exo1^{-/-}$* spermatocytes at the *59.5* hotspot by the NCO assay as shown in **Figure 28**. I saw that co-conversions from *$Mlh3^{DN/DN}$*, *$Mlh3^{-/DN}$*, and *$Mlh3^{DN/DN}Exo1^{-/-}$* spermatocytes (619 ± 422bp, 613 ± 432bp, and 898 ± 583bp, respectively) were comparable in length to co-conversions in *$Exo1^{-/-}$* spermatocytes (**Figure 39**). The similarity in co-conversion tract lengths among mutants with defective nuclease activity of MLH3 (*$Mlh3^{DN/DN}$*, *$Exo1^{-/-}$* , and *$Mlh3^{-/DN}$*) and in a mutant that lacks all or almost all nuclease activity of MLH3, *$Mlh3^{DN/DN}$ $Exo1^{-/-}$* (bivalent and crossover data, **Figure 35, 23, Table 1**) indicates that the longer co-conversions observed in *$Mlh3^{DN/DN}$*, *$Mlh3^{-/DN}$*, *$Mlh3^{DN/DN}Exo1^{-/-}$*, and *$Exo1^{-/-}$* spermatocytes are likely independent of MLH3's nuclease function.

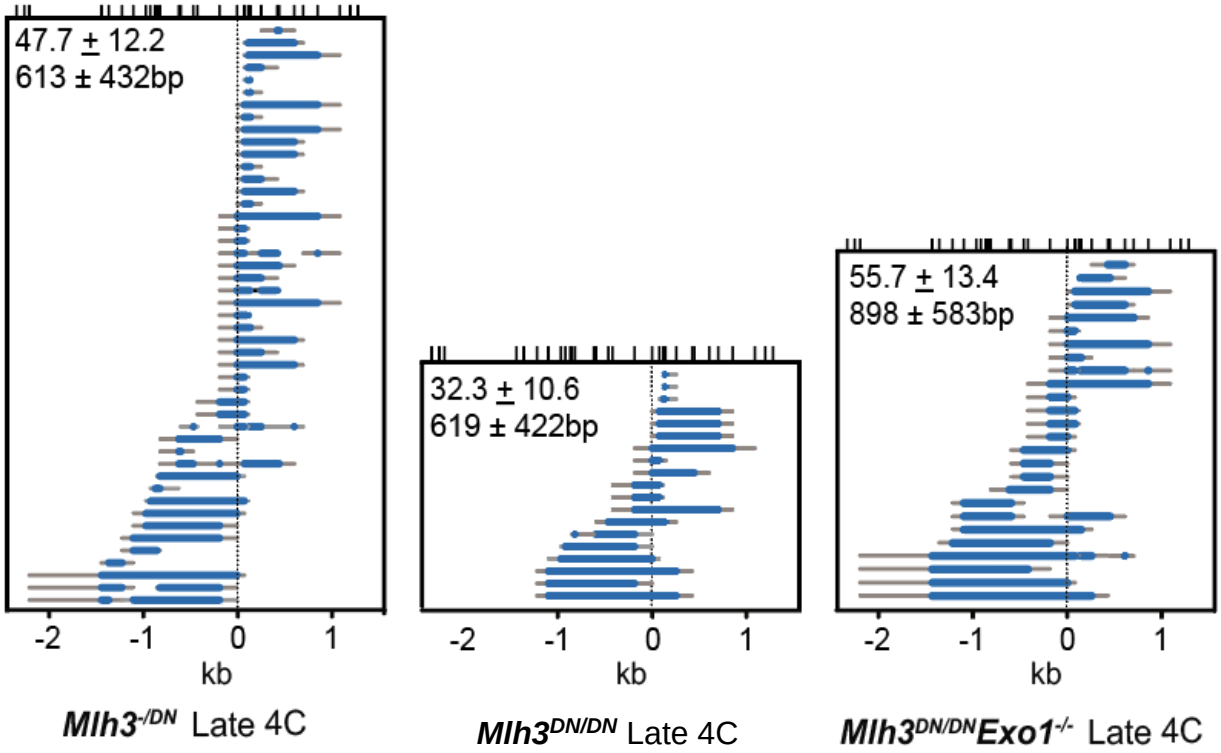
47.7 ± 12.2
613 ± 432bp
-2
-1
0
1
kb
Mlh3-/DN Late 4C
32.3 ± 10.6
619 ± 422bp
-2
-1
0
1
kb
Mlh3DN/DN Late 4C
55.7 ± 13.4
898 ± 583bp
-2
-1
0
1
kb
Mlh3DN/DNExo1-/- Late 4C

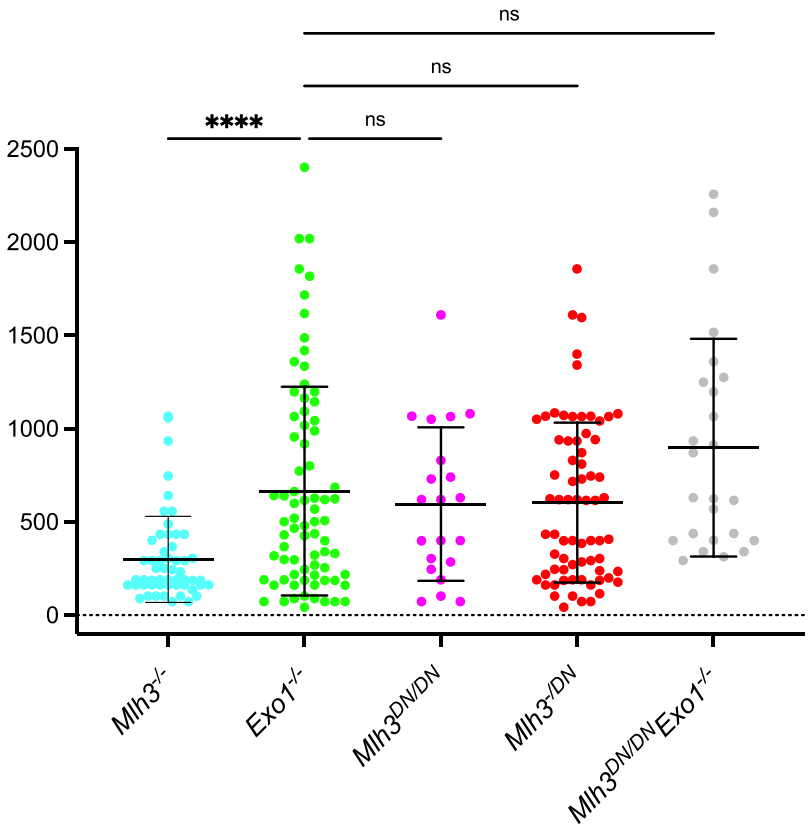
ns
ns
****
ns
2500
2000
1500
1000
500
0
Mlh3-/-
Exo1-/-
Mlh3DN/DN
Mlh3-/DN
Mlh3DN/DNExo1-/-

Figure 39: *Mlh3*$^{DN/DN}$, *Mlh3*$^{-/DN}$, and *Mlh3*$^{DN/DN}$*Exo1*$^{-/-}$ spermatocytes have longer co-conversion tract lengths

(Top)**,** Co-conversions were isolated from *Mlh3*$^{DN/DN}$, *Mlh3*$^{-/DN}$, and *Mlh3*$^{DN/DN}$*Exo1*$^{-/-}$ Late 4C spermatocytes as in **Figure 21**. The minimum (blue) and maximum (gray) possible gene co-conversion tracts are shown. The upper x-axis ticks mark the location of polymorphisms and the lower x-axis ticks mark the relative base pair positions to the center of the hotspot (0 kb). The center of the hotspot is defined as the location with maximum DSB frequency and marked by a vertical dotted line. The total frequency ± SD and average co-conversion length for the mutant are indicated in the upper-left portion of the plot. Frequency is given per 10,000 haploid genomes analyzed.

(Bottom), Scatter plot showing the length of co-conversions in kb (mean ± SD) from Late 4C spermatocytes (~70% enriched for diplonema) for *Mlh3*$^{-/-}$ (N=6, 298 ± 230bp), *Exo1*$^{-/-}$ (N=6, 692 ± 567bp), *Mlh3*$^{-/DN}$ (613 ± 432bp), *Mlh3*$^{DN/DN}$ (619 ± 422bp), and *Mlh3*$^{DN/DN}$*Exo1*$^{-/-}$ (N=2, 898 ± 583bp) spermatocytes. P-values are derived from Kruskal-Wallis test with Dunn's multiple comparison correction. N=the number of animals analyzed

Chapter 4: Characterizing co-conversions reveals that MLH3's nuclease-independent role is genetically required for formation of crossover precursor double Holliday Junction (dHJ).

Hfm1$^{-/-}$ and *Mlh3*$^{-/-}$ spermatocytes have similar, shorter (300 bp) co-conversion tract lengths

I showed that co-conversions in *Mlh3*$^{DN/DN}$ and *Exo1*$^{-/-}$ spermatocytes are longer than those in *Mlh3*$^{-/-}$ spermatocytes. I inferred that these co-conversions are likely arising from crossover precursors that are similar in length to crossover precursors found in WT (~600 bp). In budding yeast, the Mlh1-Mlh2 MutL beta complex interacts with a helicase, Mer3, and limits the gene conversion tract lengths of crossovers and NCOs. However, control over gene conversion tract length by MutL beta does not require Mer3 helicase activity, but rather requires Mer3 structurally [144]. In budding yeast, Mer3 is also required for the proper formation of crossover precursors and functions upstream of the MutLgamma complex [133,145]. However, it is unclear whether the mouse ortholog of Mer3, HFM1, has similar roles in crossover precursor formation and limiting crossover precursor length.

Mouse spermatocytes that lack HFM1 have numerous cytological defects. *Hfm1*$^{-/-}$ spermatocytes show slower turnover of early recombination foci, as quantified using the strand exchange protein RAD51. *Hfm1*$^{-/-}$ spermatocytes also lack MLH1 foci that mark crossover precursor sites and are defective for crossover formation [131]. Therefore, to examine a putative role for HFM1 in crossover precursor formation and/or controlling crossover precursor length, I analyzed the recombination outcomes in spermatocytes that lack HFM1 using the NCO assay (**Figure 28**).

At *59.5,* I found that *Hfm1*$^{-/-}$ and *Mlh3*$^{-/-}$ spermatocytes have similar CO frequencies ($0.77 \pm 1.5 \times 10^{-4}$ and $0.28 \pm 0.50 \times 10^{-4}$, respectively. Statistical test: Fishers exact test, two tailed) and similar co-conversion frequencies ($21.7 \pm 13.5 \times 10^{-4}$, and $33.8 \pm 13.4 \times 10^{-4}$, respectively, **Figure 40, Table 1**. Statistical test: Fishers exact test, two tailed). Additionally, I found *Hfm1*$^{-/-}$ and *Mlh3*$^{-/-}$ spermatocytes had similar average co-conversion lengths (237 ± 120 bp and 298 ± 230 bp, respectively) (**Figure 38**). The co-conversions found in *Mlh3*$^{-/-}$ spermatocytes are products of backup repair products acting on unrepaired crossover precursors (**Figure 28**). Based on these co-conversion frequencies and gene conversion tract lengths, I infer that *Hfm1*$^{-/-}$ and *Mlh3*$^{-/-}$ spermatocytes are similar in terms of crossover precursor formation. I thus infer that HFM1 affects neither crossover precursor formation nor the crossover precursor length in mouse spermatocytes, in contrast to its ortholog Mer3 in budding yeast.

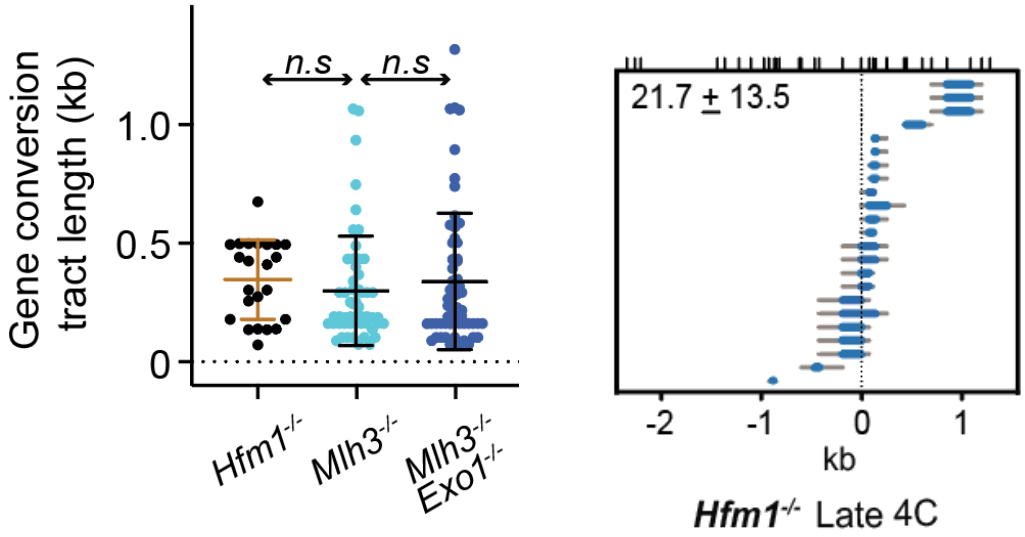

Figure 40: Co-conversions in *Hfm1*$^{-/-}$ spermatocytes
(Left), Scatter plot showing co-conversion length in kb (mean ± SD) in Late 4C from *Hfm1*$^{-/-}$ (237 ± 120 bp), *Mlh3*$^{-/-}$ (298 ± 230 bp), and *Mlh3*$^{-/-}$*Exo1*$^{-/-}$ (334 ± 288 bp) spermatocytes. P-values are derived from the Kruskal-Wallis test with Dunn's multiple comparison correction. (Right), All co-conversions isolated from *Hfm1*$^{-/-}$ Late 4C spermatocytes. The minimum (blue) and maximum (gray) possible gene co-conversion tracts are shown. The upper x-axis ticks mark the location of polymorphisms and the lower x-axis ticks mark the relative base pair positions to center of the hotspot (0 kb). The total frequency ± SD of co-conversions is shown in (top left).

Mus81$^{-/-}$*Exo1*$^{-/-}$, *Msh2*$^{-/-}$*Exo1*$^{-/-}$, and *Exo1*$^{-/-}$ spermatocytes have similarly long co-conversion tracts

Having established that most co-conversions at *59.5* in crossover maturation defective mutants likely arise from CO-designated intermediates, I sought to further investigate the source of long co-conversions. Although the overall frequency of co-conversions was similar for *Mlh3*$^{-/-}$, *Exo1*$^{-/-}$, and *Mlh3*$^{DN/DN}$ Late 4C spermatocytes, the co-conversion tracts were twice as long for *Exo1*$^{-/-}$ and *Mlh3*$^{DN/DN}$ single and *Exo1*$^{-/-}$*Mlh3*$^{DN/DN}$ double mutants compared to *Mlh3*$^{-/-}$ single mutant spermatocytes (**Figure 39**). If the co-conversion tract length reflects its precursor intermediate, then I expect that the crossover-designated precursor would be elongated in mutants with longer co-converstion tracts. However, I have not yet identified the genetic factor(s) that contributes to elongated co-conversion tracts.

In somatic cells and during yeast meiosis, MSH2 plays critical roles in MMR [179,189-192]. Defective MMR could lead to elongated recombinant products due to retained heteroduplex that is usually reverted to the parental genotype. To test if MMR contributes to co-conversion tract length, I analyzed co-conversions in *Exo1*$^{-/-}$*Msh2*$^{-/-}$ double mutant spermatocytes and found that they were not significantly different in length (1111 ± 898 bp) from *Exo1*$^{-/-}$ spermatocyte co-conversions. This indicated that MMR defects in *Exo1*$^{-/-}$ single or *Exo1*$^{-/-}$*Msh2*$^{-/-}$ double mutant spermatocytes do not contribute to co-conversion length.

SSNs like MUS81 have been suggested to resolve crossover precursors into co-conversions [155,187]. To test whether MUS81 contributes to producing longer co-conversion tracts, I analyzed co-conversions in *Mus81*$^{-/-}$*Exo1*$^{-/-}$ spermatocytes and found that co-conversion length was independent of MUS81 (**Figure 42**). My analysis of the nine crossover defective mutant combinations indicates that elongation of the designated crossover precursor takes place in *Exo1*$^{-/-}$, *Exo1*$^{-/-}$*Msh2*$^{-/-}$, *Exo1*$^{-/-}$*Mus81*$^{-/-}$, *Mlh3*$^{DN/DN}$, *Mlh3*$^{-/DN}$, and *Mlh3*$^{DN/DN}$*Exo1*$^{-/-}$ mutant spermatocytes but not in *Mlh3*$^{-/-}$, *Exo1*$^{-/-}$*Mlh3*$^{-/-}$, or *Hfm1*$^{-/-}$ spermatocytes.

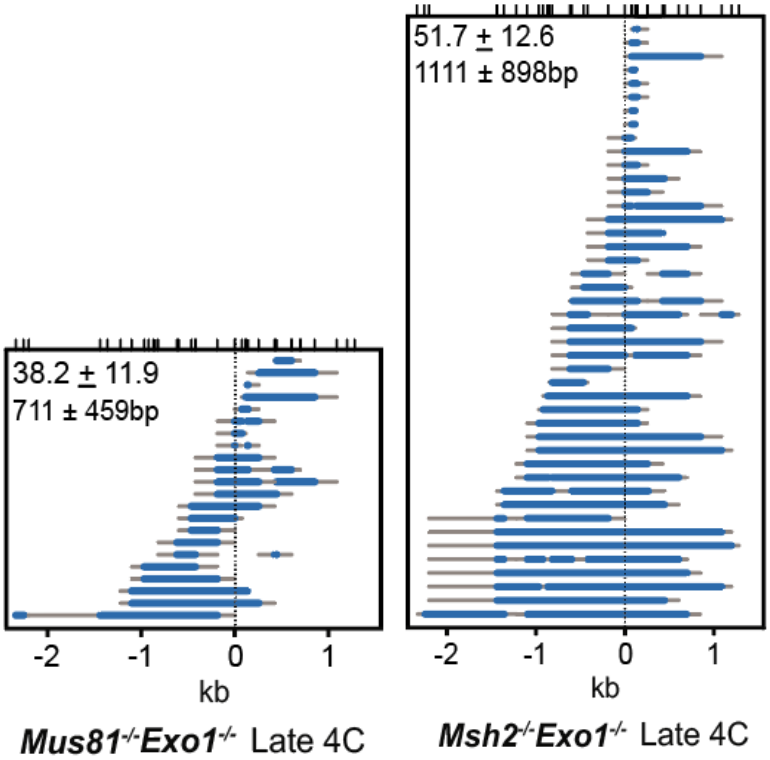

Figure 41: *Mus81*$^{-/-}$*Exo1*$^{-/-}$ *and Msh2*$^{-/-}$*Exo1*$^{-/-}$ spermatocytes have similarly long ~600 bp co-conversions

All co-conversions isolated from *Mus81*$^{-/-}$*Exo1*$^{-/-}$ *and Msh2*$^{-/-}$*Exo1*$^{-/-}$ Late 4C spermatocytes. The minimum (blue) and maximum (gray) possible gene co-conversion tracts are shown. The upper x-axis ticks mark the location of polymorphisms and the lower x-axis ticks mark the relative base pair positions to the center of the hotspot (0 kb). The center of the hotspot is defined as the location with maximum DSB frequency and is marked by a vertical dotted line. The total frequency ± SD and average co-conversion length for the mutant are indicated in the upper-left portion of the plot.

Co-conversion elongation is independent of MLH3 endonuclease activity and correlates with MutLgamma focus formation

A common feature among mutants with longer co-conversions *(Exo1*$^{-/-}$, *Exo1*$^{-/-}$*Msh2*$^{-/-}$, *Exo1*$^{-/-}$*Mus81*$^{-/-}$, *Mlh3*$^{DN/DN}$, *Mlh3*$^{-/DN}$, and *Mlh3*$^{DN/DN}$*Exo1*$^{-/-}$ spermatocytes) is the presence of the MutLgamma complex at putative crossover sites (**Figures 17, 37)** [156,160,169]. To investigate if MutLgamma focus formation correlates with longer co-conversions, I took advantage of *Hfm1*$^{-/-}$ and *Hei10*$^{-/-}$ spermatocytes. Both of these mutants express *Mlh1* and *Mlh3* but lack MutLgamma foci at putative crossover sites due to upstream roles of HFM1 and HEI10.

HEI10 is a putative E3 ubiquitin ligase, and in mouse spermatocytes, HEI10 is thought to target proteins involved in the crossover pathway for ubiquitination. This HEI10-based ubiquitination has been proposed to allow MutLgamma to be recruited to crossover precursor sites [130,137,143]. Consistently, MLH1 and MLH3 are present in *Hei10*$^{-/-}$ spermatocytes but are not visible as cytological foci at putative crossover sites. In *Hei10*$^{-/-}$ as *in Hfm1*$^{-/-}$ spermatocytes, the average co-conversion lengths (302 ± 209bp and 237 ± 120 bp, respectively) were similar to co-conversions isolated from *Mlh3*$^{-/-}$ spermatocytes (**Figure 40 and 42**).

To further test whether MutLgamma foci formation correlates with longer co-conversions, I re-examined co-conversions from single and double mutants of *Mlh3*$^{DN/DN}$ and *Exo1*$^{-/-}$ spermatocytes. *Mlh3*$^{DN/DN}$ *Exo1*$^{-/-}$ double mutant spermatocytes show diminished

MutLgamma (MLH1) focus formation but nevertheless retain the ability to form MutLgamma foci (**Figure 37**), similar to *Exo1*$^{-/-}$ and *Mlh3*$^{DN/DN}$ single mutants (**Figure 17**, [160]). Previously, I showed that co-conversion lengths from these three mutants (*Exo1*$^{-/-}$, *Mlh3*$^{DN/DN}$, and *Mlh3*$^{DN/DN}$*Exo1*$^{-/-}$) were similar (**Figure 39**). These data indicate that the longer co-conversion tract length likely correlates with MutLgamma complex formation at putative crossover sites.

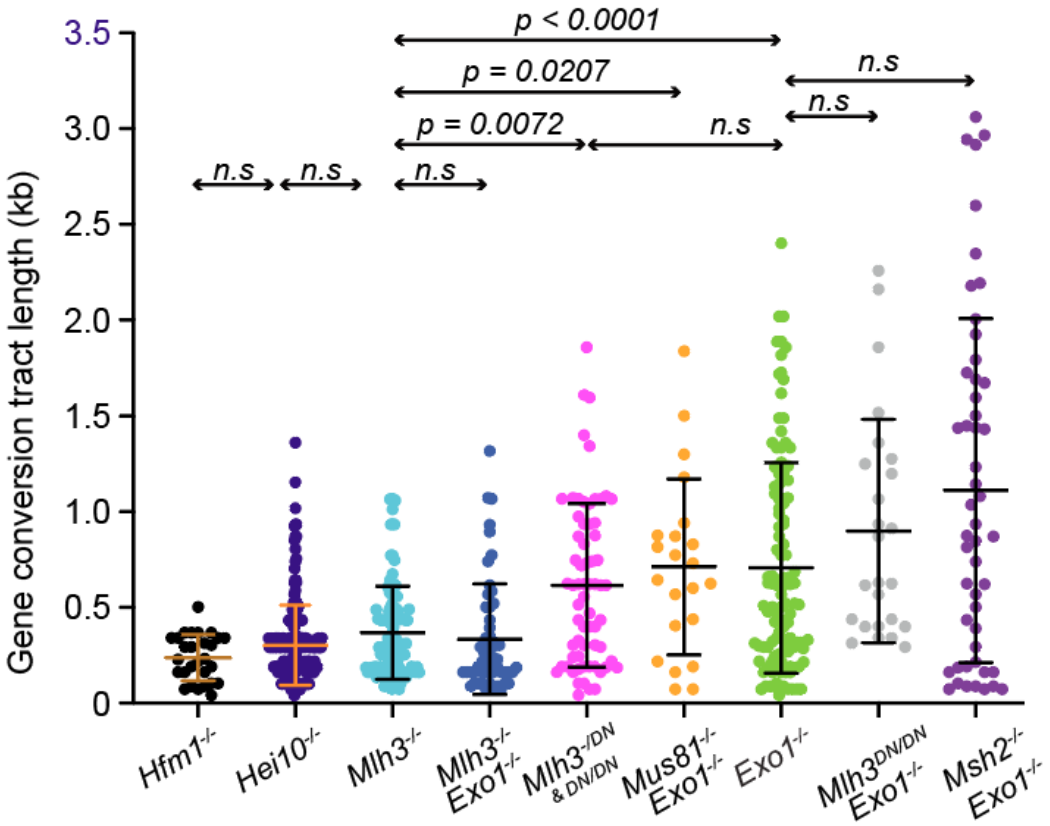

Figure 42: Co-conversion length correlates with MLH1/3 focus formation

Scatter plot showing the length (kb) of co-conversions isolated from Late 4C and diplotene samples of each genotype (mean ± SD). *Hfm1*$^{-/-}$ (237 ± 121 bp), *Hei10*$^{-/-}$ (302 ± 209bp), *Mlh3*$^{-/-}$ (367 ± 243bp), *Mlh3*$^{-/-}$*Exo1*$^{-/-}$ (334 ± 288bp), *Mlh3*$^{-/DN}$ & *Mlh3*$^{DN/DN}$ (615 ± 426bp), *Mus81*$^{-/-}$*Exo1*$^{-/-}$ (711 ± 459bp), *Exo1*$^{-/-}$ (736 ± 548bp), and *Msh2*$^{-/-}$*Exo1*$^{-/-}$ (1111 ± 898bp). N.B.., *Mlh3*$^{-/DN}$ & *Mlh3*$^{DN/DN}$ were combined to provide enough co-conversions for statistical analysis. P-values are derived from the Kruskal-Wallis test with Dunn's multiple comparison correction.

Both 3' ends of the DSB are equally likely to invade and polymerize in a crossover precursor

The inferred elongation of the designated crossover intermediate is associated with MutLgamma focus formation. Therefore, I reanalyzed the above isolated co-conversions by categorizing the mutants based on their ability to form MLH1/3 MutLgamma foci. Those that did not form MLH1 foci were categorized as *Mlh3*$^{-/-}$-like (*Hfm1*$^{-/-}$, *Hei10*$^{-/-}$, *Mlh3*$^{-/-}$, *Mlh3*$^{-/-}$*Exo1*$^{-/-}$) and those that did form MLH1 foci were catergorized as *Exo1*$^{-/-}$-like (*Exo1*$^{-/-}$, *Exo1*$^{-/-}$*Msh2*$^{-/-}$, and *Exo1*$^{-/-}$*Mus81*$^{-/-}$, *Mlh3*$^{DN/DN}$&*Mlh3*$^{-/DN}$, *Mlh3*$^{DN/DN}$*Exo1*$^{-/-}$).

To determine the features of the crossover-designated intermediate including steps in its formation, I reanalyzed the distribution of co-conversions in *Mlh3*$^{-/-}$-like and *Exo1*$^{-/-}$-like crossover maturation mutants. In our model, BxD F1 hybrid, at *59.5* large fractions of the SPO11-dependent DSBs are induced on the B chromosome and very few on the D chromosome. Further, ~80% of these DSBs are clustered within a few basepairs around the hotspot center (DSBs frequency shown as a magenta histogram in **Figure 43 A**) [101]. Consistent with the higher break frequency on the B chromosome, we see a three-fold higher frequency of singleton NCOs in WT spermatocytes on the B chromosome relative to the D chromosome. Further, reciprocal crossover asymmetry [61] occuring at 59.5 shows that most of the crossovers at *59.5* arose from DNA breaks on the B chromosome (Zelazowski et al., 2017). Because co-conversion likely arises from dissolution/SDSA, that involves displacing the newly extended strand, the polymorphisms copied from the donor during the extension identifies the invading strand [119]. Further, the sidedness of the repair is only affected by the extension from the homolog by DNA polymerization. Together with the DSB asymmetry at the *59.5* hotspot, I could analyze the distribution of co-conversions to infer invasion or extension biases that may be present during the formation of a crossover-designated intermediate.

For this analysis, I categorized co-conversions as occuring to the left, spanning, or to the right of the hotspot center (**Figure 43 B**) for all *Mlh3*$^{-/-}$-like or *Exo1*$^{-/-}$-like mutants and saw a marked enrichment for co-conversions on the "right" side of the hotspot center (**Figure 43 A**,

dotted line). For example, in *Mlh3*$^{-/-}$ mutant spermatocytes, I identified 100 co-conversions to the right and only 16 to the left (**Figure 43 B, top**). This right-sided enrichment was present in co-conversions isolated from all mutants but was particularly prevalent in mutants of the *Mlh3*$^{-/-}$-like class, which could reflect a preference for the left 3' end to invade and polymerize (**Figure 30**, quantified in **Figure 43 B**, top). However, the polymorphism density to the right of the hotspot center is higher than to the left, raising the possibility that there are more detectable events on the right side (**Figure 43 A,** 'Original polymorphism location'). To correct for the influence of polymorphism density, I included only co-conversions that postioned such that they would be detectable irrespective of whether they form to the left or to the right side of the hotspot center. To enforce the inclusion criteria, I computationally mirror-inverted the polymorphism location at the hotspot center from left to right and determined whether the original co-conversions would have been detected given the altered polymorphism map (**Figure 43 B**, **bottom magenta** 'Inverted polymorphism location').

There were four outcomes after testing co-conversions with inverted polymorphisms, and examples of each are shown in **Figure 43 A**:

Type-1) one-sided co-conversions that would not have been detected with inverted polymorphisms; This could be either because they are small or the equivalent location on the opposite side of the hotspot center lacks the polymorphism density. For example, Type-1 in Figure 43 A always falls between magenta dotted lines that depict the inverted polymorphism location. In this depiction, the blue line depicts the original detected repair event based on the actual polymorphism location (black, above)

Type-2) one-sided co-conversions that would continue to be detected with inverted polymorphisms; This is usually because the repair events are long such that the differences in polymorphism density matter less for these events.

Type-3) co-conversions that spanned the hotspot center originally, but would now be detected as one-sided with inverted polymorphisms; This is because repair on one side is shorter than the other, so upon invert testing only the long end would appear.

and finally Type-4) co-conversions that originally spanned the hotspot center and would continue to be detected as such, despite inverting the polymorphisms. This is likely because the repair events are long such that the differences in polymorphism density rarely affect the distribution of these repair events.

To counter any potential skewing of detection of sidedness, Type-1 co-conversions were removed from the analysis and Type-3 co-conversions were re-scored as one-sided (**Figure 43 B, bottom**). When I included only co-conversions that passed the inverted polymorphism test, I found that the right-sided enrichment was no longer detected, confirming my suspicion that polymorphism density was driving the apparent right-sided enrichment in *Mlh3*$^{-/-}$-like mutants.

In contrast, *Exo1*$^{-/-}$-like mutants displayed a flipped, left-sided enrichment after correcting for polymorphism density. In *Exo1*$^{-/-}$-like mutants, I did not observe a difference between left or right-sided, one-sided (Type-2) events. Instead, I found this flip in enrichment was driven by 29 of 30 events originally categorized as spanning events that were recategorized as left-sided upon enforcing our inclusion criteria (i.e. Type-3 events). Together, the data suggest that there is no invasion bias to the left or the right of the hotspot center (**Figure 43 C**, see below) in *Exo1*$^{-/-}$-like mutants and that both ends of the DSB are equally likely to engage in strand invasion at *59.5*.

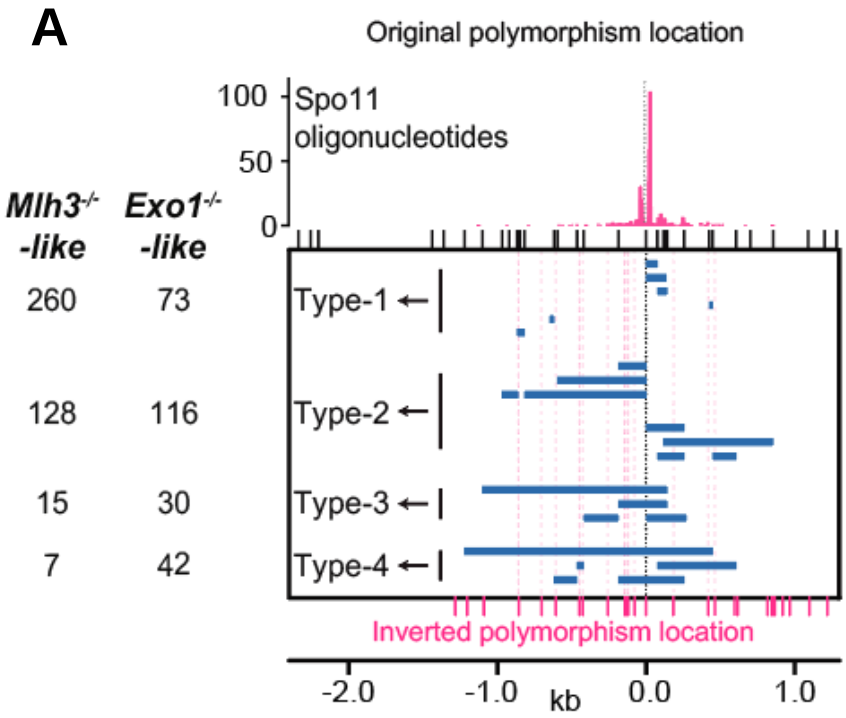
A
Original polymorphism location
100
50
0
Spo11
oligonucleotides
Mlh3-/-
-like
Exo1-/-
-like
260
73
128
116
15
30
7
42
Type-1
Type-2
Type-3
Type-4
Inverted polymorphism location
-2.0
-1.0
kb
0.0
1.0

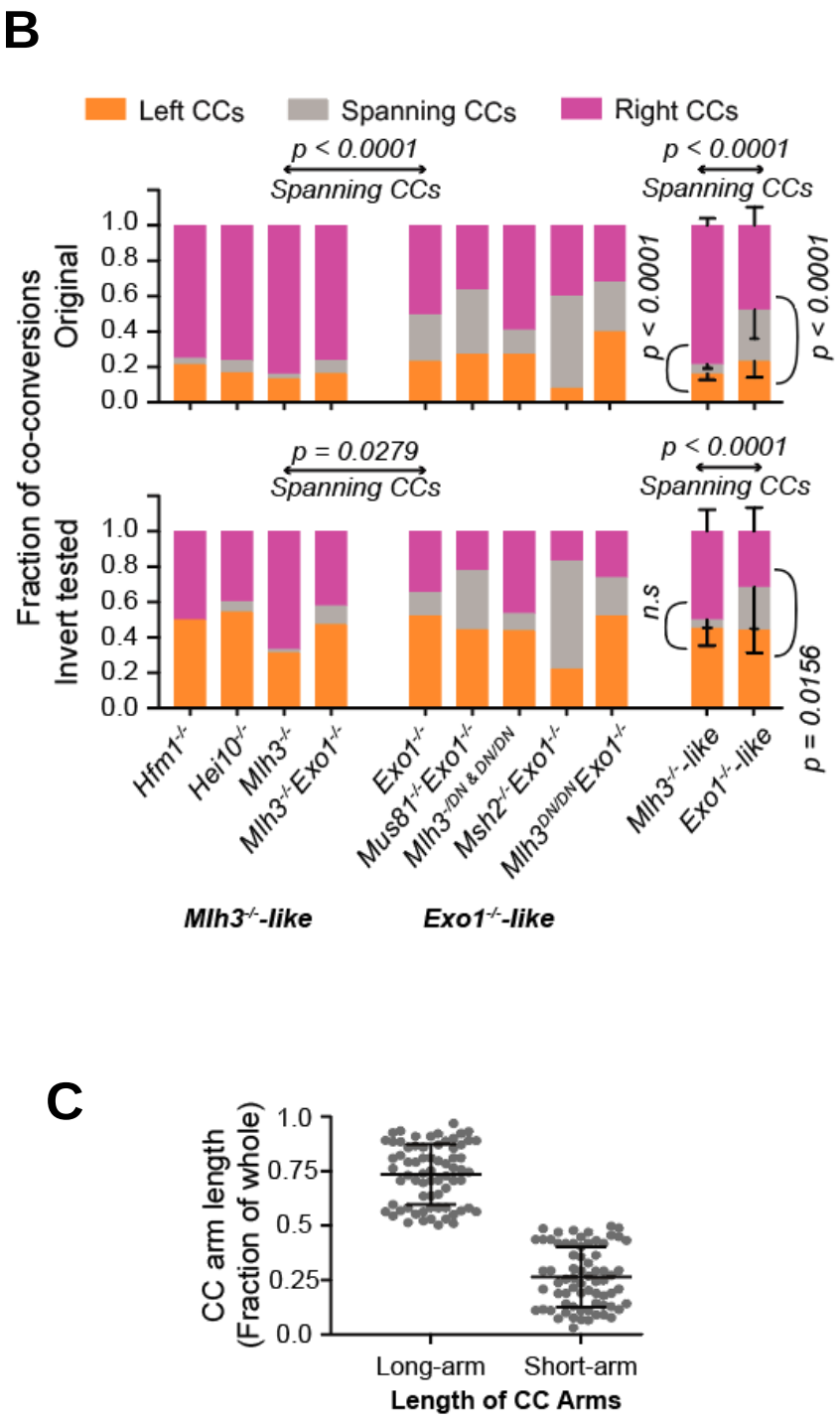

Figure 43: Co-conversion show lack of strand invasion bias in crossover precursors
(A) Representative co-conversions and their corresponding dispensation after mirror-inverting polymorphism positions. Left, the number of co-conversions mapped in each class of mutants. Bottom x-axis, relative position within the *59.5* hotspot. Black ticks (top) mark the original polymorphism locations and magenta vertical dotted lines and ticks (bottom) mark the mirror-inverted polymorphism locations. The hotspot center is indicated with a black vertical line

mapped at “0". Co-conversions were categorized into 4 groups: Type-1) one-sided co-conversions that would not have been detected following inversion of polymorphisms, Type-2) one-sided co-conversions that would still be detected after inversion, Type-3) co-conversions that originally spanned the hotspot center, but would be categorized as one-sided after polymorphism inversion, and Type-4) co-conversions that originally spanned the hotspot center and would still be categorized as spanning after inverting polymorphisms
(B) (Top)**,** Histogram showing the sidedness of the minimum gene conversion tracts of co-conversions (CC) around the hotspot center. P-values were determined by Fisher's exact test, two-tailed.
(Bottom)**,** Histogram showing the sidedness of the detectable minimum gene conversion tracts of co-conversions (CC) around the hotspot center after mirror-inverting polymorphisms. P-values were determined by Fisher's exact test, two-tailed.
(C) Scatter plot showing the fraction of each gene conversion tract contributing to either the long or short arm of the co-conversions (CC) that span the hotspot center.

Co-conversion distribution suggests step-wise polymerization of 3' invaded ends

One intriguing observation in the *Mlh3*$^{-/-}$-like class of mutants is that only 5.4% of co-conversions span the hotspot center (**Figure 43 B**). If both ends of the DSB extend via polymerization, one would expect most of these co-conversions would incorporate the hotspot center, despite their relatively short average length of ~300 bp. Therefore, I suggest that the crossover-designated intermediate in the *Mlh3*$^{-/-}$-like class of mutants is extended from only a single invaded 3' end. By contrast, in the *Exo1*$^{-/-}$-like class of mutants, 28% of events span the hotspot center, suggesting that both ends of the DSB are extended. I propose a model that upon MutLgamma loading, the second end is allowed to extend, producing the two-sided co-conversions observed in *Exo1*$^{-/-}$-like mutants **Figure 43 C**. An important caveat is that the spanning events in *Exo1*$^{-/-}$-like mutants are still fewer than would be expected, and I will describe possible reasons in the discussion section. Taken together, analysis of the co-conversions in crossover defective mutants suggests the ~300 and 600 bp crossover intermediates have distinct features and therefore, are possibly derived from independent substrates. Additionally, the shorter ~300 bp intermediate is independent of MLH3, whereas the longer ~600 bp intermediate is only seen in mutants that recruit MLH1/3 to crossover precursor sites on the chromosomes and do not correlate with nuclease function of MLH3. Together, the longer intermediate likely requires MLH3 structurally.

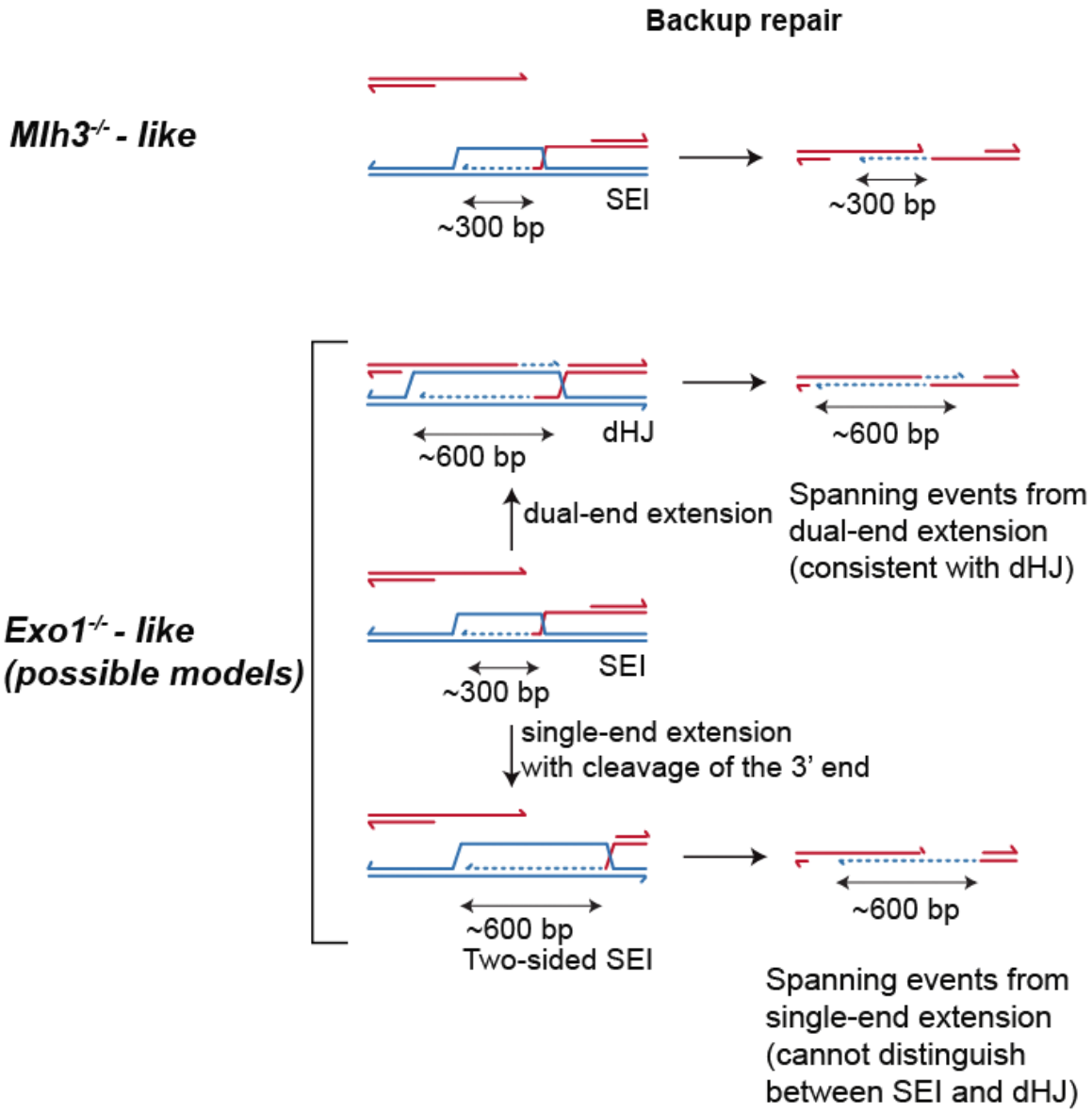

Figure 44: Possible models to explain two-sided co-conversions
Schematic of potential mechanisms that generate one- and two-sided co-conversions in the indicated mutant classes. SEI, single-end invasion. dHJ, double Holliday junction.
While I suggest that the spanning co-conversions in the *Exo1*$^{-/-}$-like mutants arise when both ends are extended (dual-end extension), the spanning co-conversions in *Exo1*$^{-/-}$-like mutants could also be derived from a single invaded end that undergoes 3' to 5' cleavage during extension. This cleavage can result from multiple causes, such as polymerase-dependent proofreading activity (possibilities shown above), [193,194]). I, therefore, used strand genotyping to differentiate between the possibilities (next section).

Msh2$^{-/-}$*Exo1*$^{-/-}$ co-conversions show trans-heteroduplex pattern consistent with double Holliday junction formation

To distinguish between dual- and single-ended extension mechanisms (**Figure 44**), I analyzed the heteroduplex pattern of co-conversions in *Exo1*$^{-/-}$ and *Msh2*$^{-/-}$*Exo1*$^{-/-}$ spermatocytes. During recombination, the 3' invading end extends from the homolog, and this newly synthesized strand anneals back to the parental chromosome to form co-conversions. The old and the new strands have differing polymorphisms, leading to mismatches between the two strands.

Therefore, it is possible to use a MMR defective mutant, for example in spermatocytes that lack MSH2, to uncover the extension pattern of the newly synthesized strand. In such a mismatch defective situation, co-conversions that derive from the extension of both DSB ends would be expected to contain a full heteroduplex tract that spans the originally detected co-conversion in a trans-heteroduplex configuration. Our NCO assay (**Figure 28**) detects the extent of co-conversion but cannot distinguish whether the co-conversion tract is contiguous (on one strand), contains heteroduplex, or is a trans-heteroduplex that spans separate strands (**Figure 45 A,** below).

To identify heteroduplex patterns, I re-amplified primary PCR wells containing co-conversions that span the hotspot center. PCR amplicons were cloned into plasmid vectors and transformed into bacteria. Multiple colonies that contained plasmids carrying the donor polymorphisms on the left side or right side of the mapped co-conversions (Asterisks in **45 B**) were picked. Plasmids were purified and sent for Sanger sequencing across the entire hotspot. In this manner, I cloned all potential strands containing converted polymorphisms. Several possible strand configurations can be distinguished with our assay (see examples, **45 A**). In the case of no heteroduplex or full heteroduplex on one contiguous strand, I expect to find only one co-conversion strand pattern, but in the cases of partial heteroduplex or full heteroduplex in trans, I expect to see two independent co-conversion strand patterns for each strand of DNA.

I found that 3 of 4 *Exo1*$^{-/-}$ co-conversions (CC1-3, in **Figure 45 B**) showed only one strand pattern that matched the mapped co-conversion tract and likely represents a mismatch corrected final product. The last co-conversion (CC4 **Figure 45 B**) showed two independent strands, with fully converted polymorphisms flanked by trans-heteroduplex. The combination of both strands matches the originally mapped co-conversion. The pattern of *Exo1*$^{-/-}$ CC4 is consistent with dual-end extension, however, the presence of extensive MMR in *Exo1*$^{-/-}$ spermatocytes limits my ability to definitively confirm either the dual- or single end extension models. Therefore, I analyzed 5 co-conversions from *Msh2*$^{-/-}$*Exo1*$^{-/-}$ spermatocytes. I found all 5 of these co-conversions had two co-conversion strand patterns in a trans heteroduplex configuration. This finding indicates that both ends of the DSB are extended in the absence of EXO1 and are consistent with the formation of a dHJ-like intermediate. Three of the five strand patterns (CC1, 3, 4) show full conversion to the donor genotype at one or more polymorphisms at the site where the retained heteroduplex switches between strands. This full conversion suggests MSH2-independent mismatch correction [195] close to the DSB site or cleavage of one or both DSB ends such as that seen in polymerase-dependent proofreading [193,194].

Taken together, the genotyping of the independent strands of co-conversions from *Exo1*$^{-/-}$ and *Msh2*$^{-/-}$*Exo1*$^{-/-}$ spermatocytes support my model that both DSB ends engage and extend from the homolog in the *Exo1*$^{-/-}$- like mutant spermatocytes. I suggest that this intermediate is a dHJ-like intermediate (**Figure 44**). Finally, in *Mlh3*$^{-/-}$ - like spermatocytes, the co-conversions are shorter. Data from previous work from our lab showed that these co-conversions have only one strand pattern [61], consistent with the model that in *Mlh3*$^{-/-}$ - like mutants, crossover repair only progresses until polymerized single end invasion (**pSEI, Figure 44**), whereas in *Exo1*$^{-/-}$- like mutant spermatocytes, pSEI is differentiated into the second crossover precursor double Holliday Junction (dHJ).

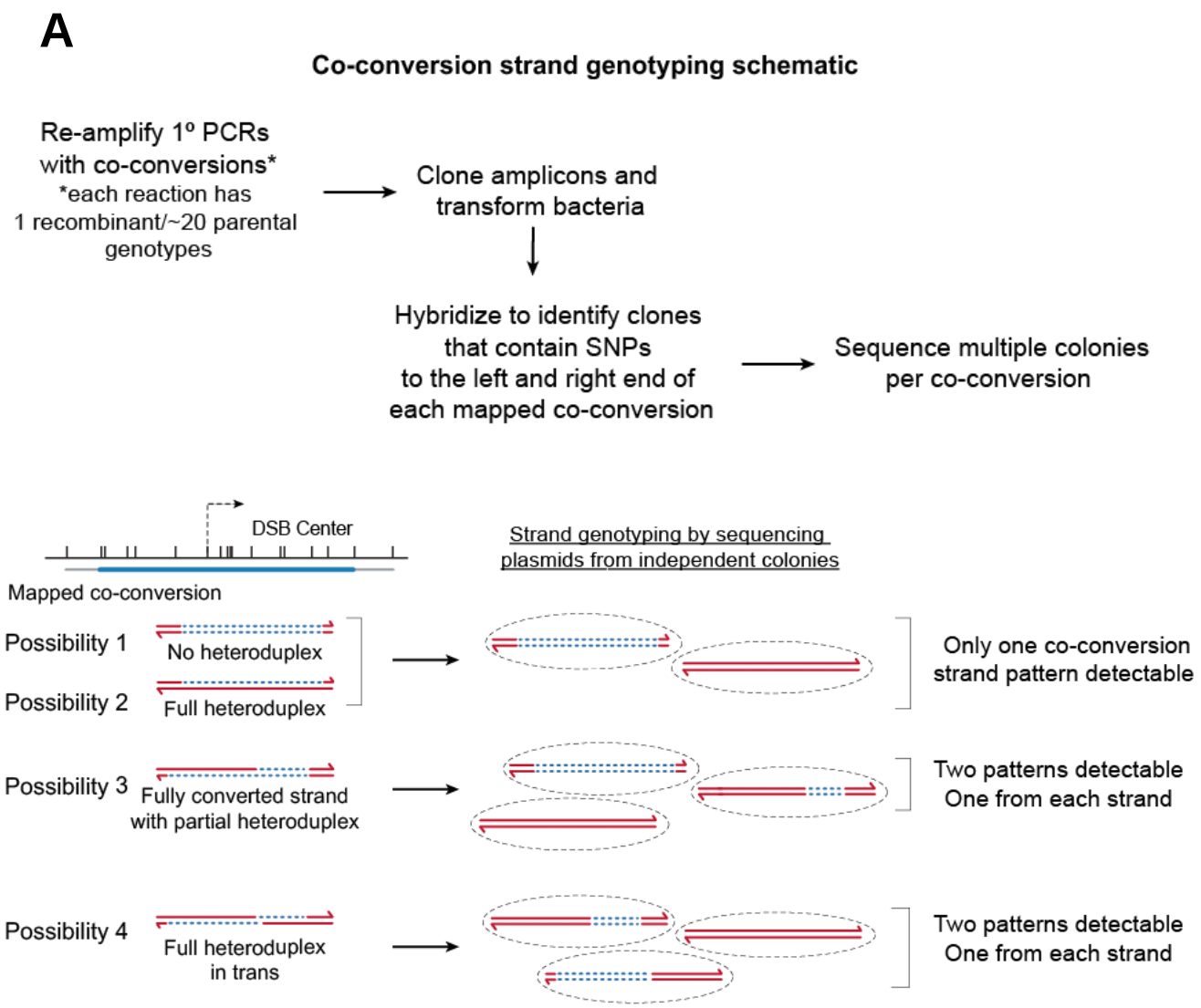
A
Co-conversion strand genotyping schematic
Re-amplify 1º PCRs
with co-conversions*
*each reaction has
1 recombinant/~20 parental
genotypes
Clone amplicons and
transform bacteria
Hybridize to identify clones
that contain SNPs
to the left and right end of
each mapped co-conversion
Sequence multiple colonies
per co-conversion
DSB Center
Mapped co-conversion
Strand genotyping by sequencing
plasmids from independent colonies
Possibility 1
No heteroduplex
Possibility 2
Full heteroduplex
Only one co-conversion
strand pattern detectable
Possibility 3
Fully converted strand
with partial heteroduplex
Two patterns detectable
One from each strand
Possibility 4
Full heteroduplex
in trans
Two patterns detectable
One from each strand

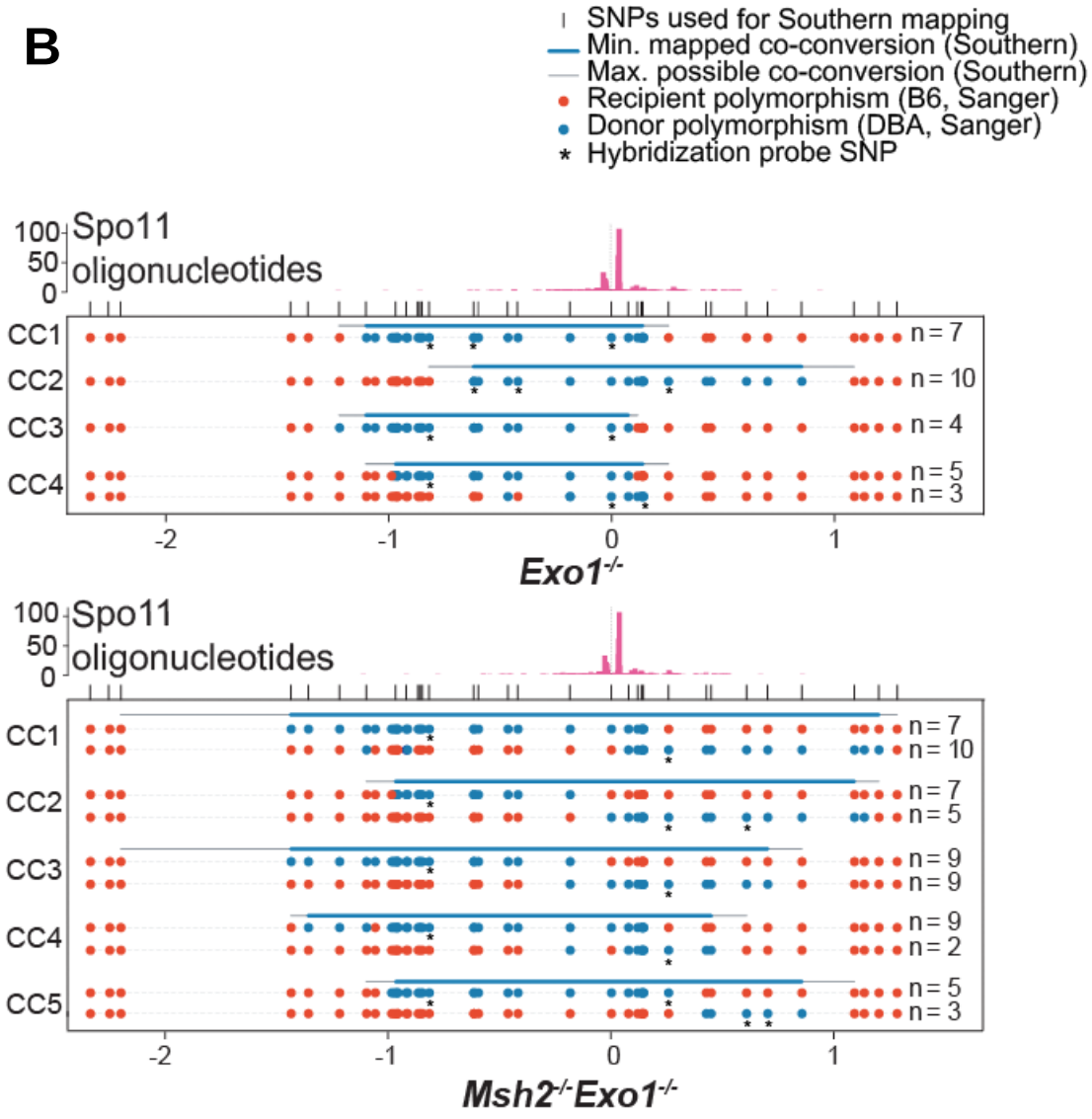

Figure 45: Genotyping independent strands of co-conversions in *Exo1*$^{-/-}$ and *Msh2*$^{-/-}$*Exo1*$^{-/-}$ show evidence for dHJ

(A) Top, cloning strategy to independently isolate both strands from the co-conversions. Bottom, Schematic of the possible strand configurations and their expected outcomes.

(B) Sanger sequencing of the independent strands from co-conversions in *Exo1*$^{-/-}$ (top) and *Msh2*$^{-/-}$*Exo1*$^{-/-}$ (bottom). Top ticks mark polymorphisms used for Southern genotyping of co-conversions. The minimum (Blue bar) and maximum (Gray line) co-conversion tracts that were cloned and sequenced are shown. Circles, the donor (Blue, DBA), and recipient (Red, B6) identity of polymorphisms in the cloned strands by Sanger sequencing. N.B. CC1-3 of *Exo1*$^{-/-}$ had only one strand sequence that made up the entire originally mapped co-conversion, whereas CC4 and all *Msh2*$^{-/-}$*Exo1*$^{-/-}$ had two independently cloned strand sequences. Numbers to the right show the number of isolated clones bearing the indicated strand sequence.

Co-conversions from *Exo1*$^{-/-}$ and *Mlh3*$^{DN/DN}$ mutant spermatocytes are frequently discontinuous

Discontinuous co-conversions are repair events with at least four switches between parental haplotypes (e.g., asterisks, **Figure 43 A**). This could result from wells that contained two independent events by chance that could be two co-conversions or one co-conversion and a singleton NCO in the same PCR. Indeed, the frequency of two independent events can be estimated using the Poisson approximation. I found that the number of discontinuous co-conversions that involved one singleton and one contiguous co-conversion were found at a frequency similar to what would be expected for two independent events, present in the same PCR by chance. Thus, these events were removed from discontinuity analysis. By contrast, the discontinuous co-conversions that involved two separate contiguous tracts (involving more than one polymorphism) were much higher in frequency than predicted by the Poisson distribution. On average, *Exo1*$^{-/-}$ spermatocytes had a 24-fold higher frequency of discontinuous co-conversions than *Mlh3*$^{-/-}$ spermatocytes (19.4 ± 23.9% and 0.8 ± 3.9%, respectively) (**Figure 46 B**). This vast difference cannot be explained by the ~2-fold longer co-conversion tract length between *Mlh3*$^{-/-}$ and *Exo1*$^{-/-}$ spermatocytes.

The discontinuity may occur due to the mild MMR defects expected in *Exo1*$^{-/-}$ spermatocytes. Consistent with this idea, *Mlh3*$^{-/-}$*Exo1*$^{-/-}$ mutant spermatocytes had a higher fraction of discontinuous co-conversions (5.3 ± 6.8%) than *Mlh3*$^{-/-}$ (0.8 ± 3.9%) but lower than *Exo1*$^{-/-}$ spermatocytes (19.4 ± 23.9%) (**Figure 46 B**), indicating that MMR defects due to EXO1 loss plays a small role. Further, levels of discontinuity do not increase further in *Msh2*$^{-/-}$ *Exo1*$^{-/-}$ (21.5 ± 11.7%) or *Mus81*$^{-/-}$*Exo1*$^{-/-}$ (18.1 ± 8.5%) spermatocytes compared to *Exo1*$^{-/-}$ spermatocytes (19.4 ± 23.9%), showing that neither the loss of MSH2-dependent canonical MMR nor the loss of MUS81 contribute much, if anything, to the discontinuity phenotype. However, co-conversions in *Mlh3*$^{-/DN}$/*Mlh3*$^{DN/DN}$ (combined for statistical power) had a high fraction of discontinuity (13.0 ± 8.1). Together, these data indicate that discontinuous co-

conversions are more frequent in *Exo1*$^{-/-}$ and *Mlh3*$^{DN/DN}$ single and double mutants, and that factors other than defective MMR are at play.

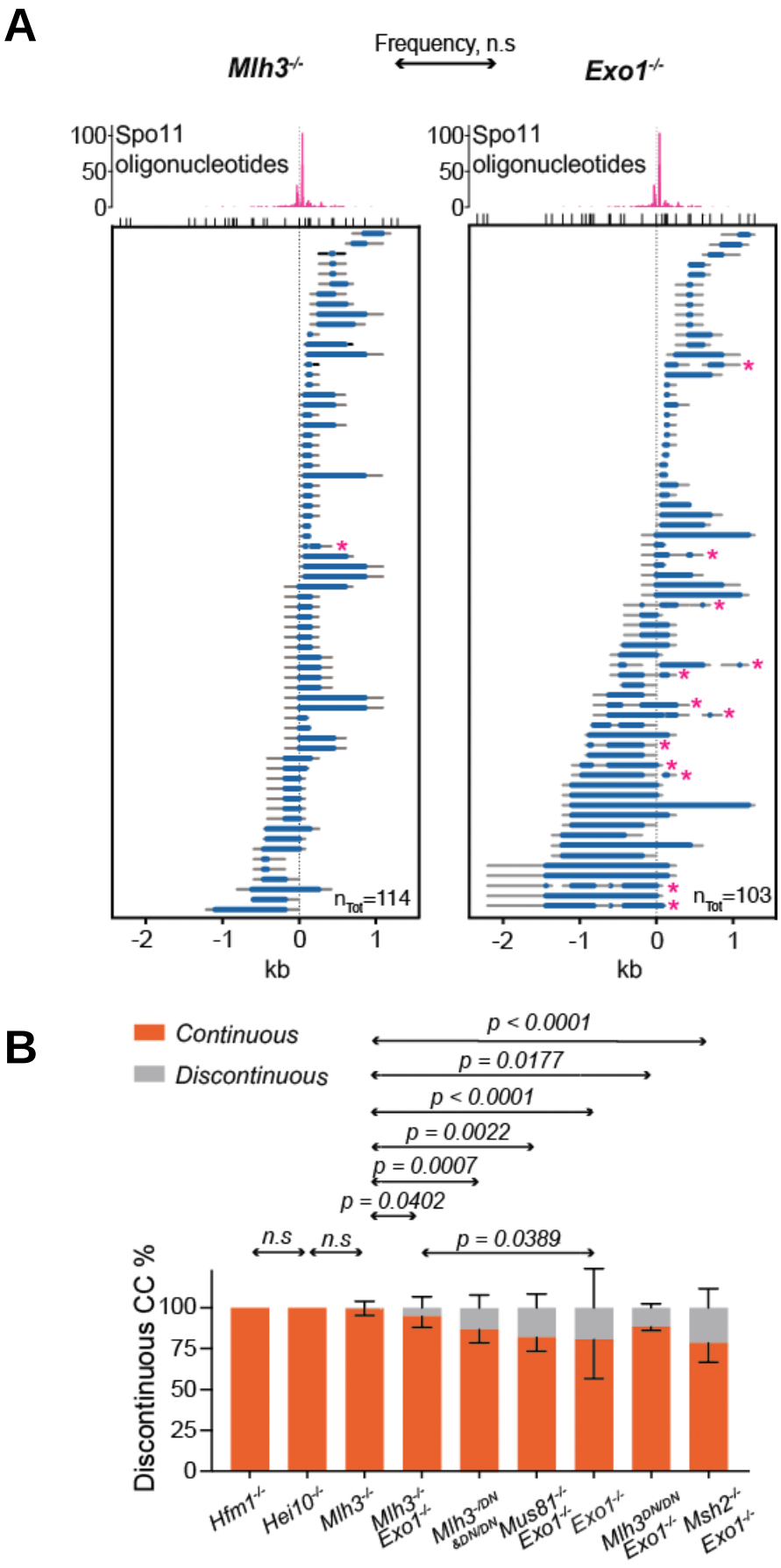
A
Frequency, n.s
Mlh3-/-
Exo1-/-
100
50
0
Spo11
oligonucleotides
nTot=114
nTot=103
-2
-1
0
1
kb
B
Continuous
Discontinuous
p < 0.0001
p = 0.0177
p < 0.0001
p = 0.0022
p = 0.0007
p = 0.0402
n.s
n.s
p = 0.0389
Discontinuous CC %
100
75
50
25
0
Hfm1-/-
Hei10-/-
Mlh3-/-
Mlh3-/- Exo1-/-
Mlh3-/DN &DN/DN
Mus81-/- Exo1-/-
Exo1-/-
Mlh3DN/DN Exo1-/-
Msh2-/- Exo1-/-

Figure 46: Co-conversion discontinuity in crossover-defective mutants

(A) The representative population of co-conversions recovered from *Mlh3*$^{-/-}$ and *Exo1*$^{-/-}$ Late 4C and diplotene spermatocytes. The blue line plots the minimal and the gray line the maximal possible gene conversion tract of the co-conversion. The x-axis shows ticks marking polymorphisms at the top and relative positions within the hotspot at the bottom. The center of the hotspot is marked by a vertical dotted line and plotted at 0kb. Above the main plot on X-axis, is a second plot showing DSB locations at *59.5*. When SPO11 creates DSB in meiosis, SPO11 gets covalently linked to the short DNA oligos at the location of the break. The Magenta plot – shows sequenced SPO11 oligonucleotide frequency map in reads per million, showing DSB sites [101]. The hotspot center denotes the location around which ~80% of the DSBs occur at *59.5* hotspot as estimated from sequenced Spo11 oligonucleotides. The total number of isolated (n_{Tot}) co-conversions is shown. Asterisks mark discontinuous events. Significance was determined by Fisher's exact test, two-tailed.

(B) Histogram showing the percent of continuous (salmon) and discontinuous (gray) co-conversions (CC) of the indicated genotypes. Discontinuity percentage: *Hfm1*$^{-/-}$ (0 ± 0%), *Hei10*$^{-/-}$ (0 ± 0%), *Mlh3*$^{-/-}$ (0.8 ± 3.9%), *Mlh3*$^{-/-}$*Exo1*$^{-/-}$ (5.3 ± 6.8%), *Mlh3*$^{-/DN}$ & *Mlh3*$^{DN/DN}$ (13.0 ± 8.1%), *Mus81*$^{-/-}$*Exo1*$^{-/-}$ (18.1 ± 8.5%), *Exo1*$^{-/-}$ (19.4 ± 23.9%), *Mlh3*$^{DN/DN}$*Exo1*$^{-/-}$ (11.7 ± 2.4%), and *Msh2*$^{-/-}$*Exo1*$^{-/-}$ (21.5 ± 11.7%). P-values were determined by Fisher's exact test, two-tailed. Co-conversions were considered discontinuous when there were two or more contiguous tracts in the same sample (Asterisks in **A**), as these were present at a higher frequency than expected by chance.

Model

I have evidence for two distinct crossover precursors, the pSEI (300 bp) and dHJ (600 bp). Both of these can be resolved as crossovers, and both can produce co-conversions of ~300 and ~600 bp in crossover-defective mutants. I favor a model that upon crossover designation, one of the two DSB ends invades into the homolog and extends by polymerization for ~300 bp to form a polymerized single-end invasion intermediate (pSEI). In mutants where MLH3 is present and able to form foci, the second end of the DSB invades the pSEI and both ends undergo a second round of extension to form a dHJ. This role of MLH3 is nuclease-independent and correlates with MutLgamma complex accumulation at the crossover precursor site. If MutLgamma/MLH3 is enzymatically proficient, the newly formed dHJ precursors are immediately and efficiently converted into crossovers. However, when MutLgamma/MLH3 is enzymatically deficient, dHJs form but the crossover function of MutLgamma is defective and the crossover precursors are instead repaired by backup enzymes into co-conversions of corresponding lengths. Finally, I find evidence for dual-end polymerization in co-conversions isolated from mismatch defective *Msh2*$^{-/-}$*Exo1*$^{-/-}$ and partially mismatch defective *Exo1*$^{-/-}$ spermatocytes. This evidence for dual-end polymerization provides strong support for my model that dHJs form in *Exo1*$^{-/-}$ -like mutant spermatocytes.

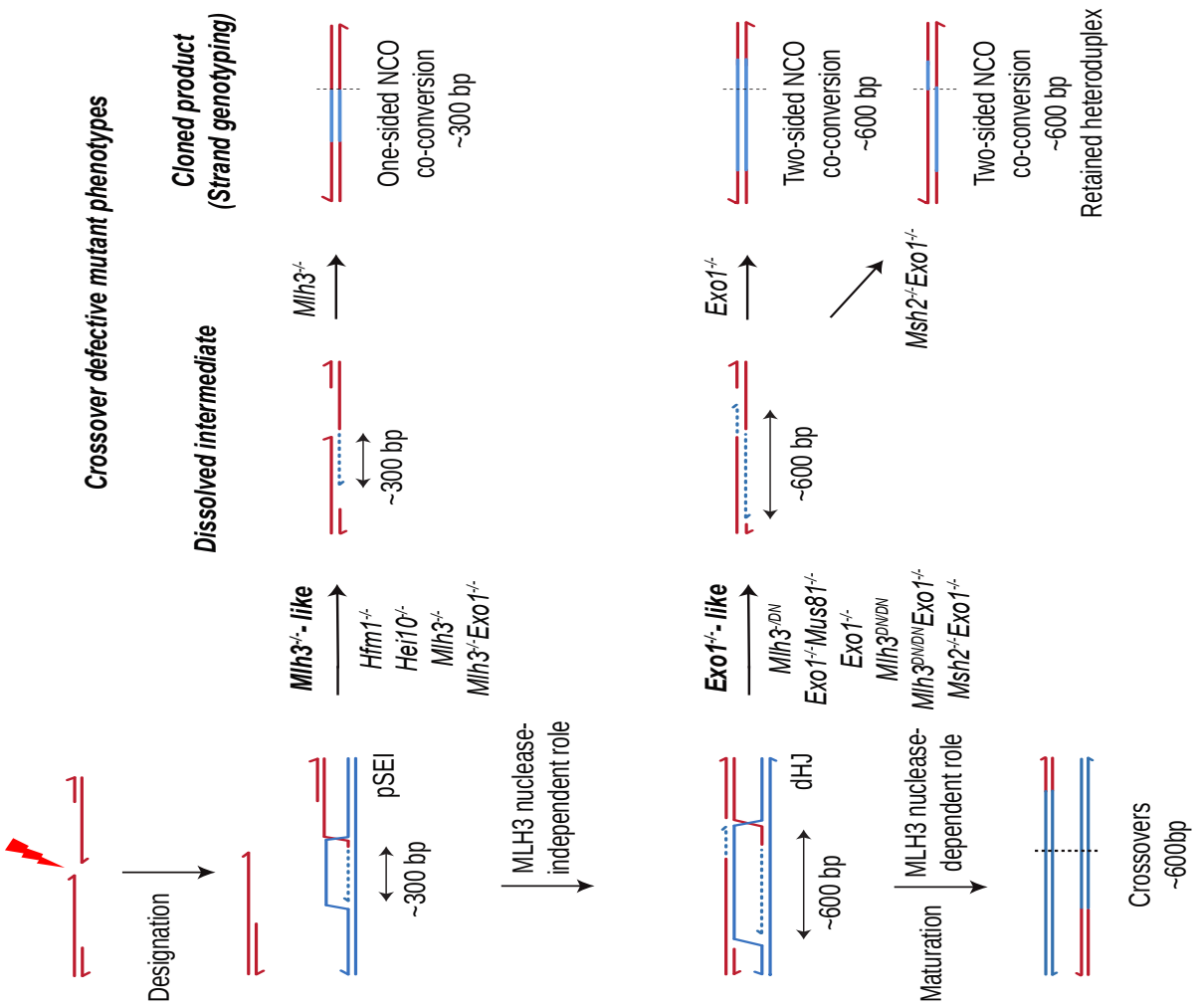

Figure 47: Model of crossover precursors in mouse spermatocytes

Upon designation, both 3' ends of the DSB are equally likely to invade. The first detected crossover precursor is a polymerized single-end invasion (pSEI) intermediate which is about 300 bp long. This first step does not require MLH3. The second step, which involves either the invasion of the second 3' end or just extension from already invaded second 3' end, requires MLH3 in a nuclease-independent manner. This MLH3-dependent second step differentiates the pSEI into a double Holliday Junction (dHJ), which is about 600 bp on average. In the presence of functional MutLgamma, these dHJs are rapidly converted into crossovers.

Strand genotyping of the co-conversions in *Mlh3*$^{-/-}$ [61], *Exo1*$^{-/-}$, and *Msh2*$^{-/-}$*Exo1*$^{-/-}$ spermatocytes (**Figure 45 B**) verified the presence of dual end polymerization in *Exo1*$^{-/-}$ -like mutants in support of my model. The vertical black dotted line in the co-conversion products shows the position of the theoretical originating DSBs.

Discussion

Lack of EXO1 affects the stability of MLH1/MLH3 MutLgamma complex

I showed that there was a reduction in early recombination intermediates, as evidenced by a marked loss of strand exchange protein DMC1's cytological foci, in *Exo1*$^{-/-}$ spermatocytes. *Exo1*$^{-/-}$ mutant spermatocytes had 21% fewer foci (155.8 ± 60) than *Exo1*^{het} mutant spermatocytes (196.5 ± 60.45) and ~30% fewer foci compared to WT (224.0 ± 72.2) spermatocytes (**Figure 15**). I expected the decrease in DMC1 marked early recombination intermediates to not affect MLH1 marked crossover site numbers. The rationale being that fully functioning crossover homeostasis mechanism has been shown to buffer up to a 30% reduction in early recombination intermediates [138]. However, I saw a 10% reduction in MLH1 and MLH3 foci in *Exo1*$^{-/-}$ spermatocytes (**Figure 17**) compared to either *Exo1*^{het} or WT spermatocytes. This reduction may suggest that EXO1 helps maintain the effectiveness of crossover homeostasis. One would predict that a partial loss of crossover homeostasis would also reduce crossover interference, which can be calculated based on the ratio of observed to expected distance between two nearby MLH1 foci [140]. However, *Exo1*$^{-/-}$ and WT spermatocytes displayed similar crossover interfence, indicating that crossover homeostasis is unaffected in *Exo1*$^{-/-}$ spermatocytes (**Figure 16**). It is possible that the number of MLH1 and MLH3 foci in *Exo1*$^{-/-}$ spermatocytes is reduced not because foci fail to form, but because the overall stability of either of these proteins themselves and/or the MutLgamma complex assembly at crossover sites is reduced. Indeed, EXO1 has been suggested to have a stabilizing structural role during MMR [189]. Further, although not a direct comparison, I noted that overall, fewer *Mlh3*$^{DN/DN}$*Exo1*$^{-/-}$ spermatocytes displayed MLH1 foci, and the *Mlh3*$^{DN/DN}$*Exo1*$^{-/-}$ spermatocytes had fewer MLH1 foci relative to either *Exo1*$^{-/-}$ or *Mlh3*$^{DN/DN}$ spermatocytes. This is consistent with EXO1 stablizing the MutLgamma complex, which may become more evident in the *Mlh3*$^{DN/DN}$ spermatocyte background. Additionally, EXO1 directly interacts with MLH1 [196] to promote the nicking activity of the MutLgamma complex *in vitro* [152,153].

Crossover exchange points in *Exo1*$^{-/-}$ spermatocytes are consistent with branch migration

Most crossovers in WT mouse spermatocytes have a single interval where haplotypes switch from one parent to another – resulting in a "simple" crossover. However, crossovers can also be "mixed" with both genotypes present at few polymorphisms between the exchange interval or "complex" with two or more haplotype switches between one parent to another (**Figure 24**). I saw that about 32% of *Exo1*$^{-/-}$ spermatocytes and 14% of *Exo1*$^{nd/nd}$ (nuclease deficient allele) spermatocytes had complex exchange points compared to WT (**Figure 24**). Considering that EXO1's role in MMR relies largely on EXO1's nuclease function [168,181], I suggest that the complex crossovers seen in *Exo1*$^{nd/nd}$ spermatocytes, and by extension, a fraction of complex crossovers in *Exo1*$^{-/-}$ spermatocytes likely arise from defective MMR.

Complex crossovers can also arise when the invading 3' ssDNA strand switches the partner between homolog and sister chromatids or by relative migration between the branches of the crossover precursor – the dHJ – during crossover formation (**Figure 24 A**). In budding yeast, template switching is commonly observed in WT crossovers [118,119]; however, similar levels of template switching have not been observed in mice. This could be because, when the MutLgamma complex is enzymatically active, its nicking activity could induce mismatch correction that erases the evidence of template switching. This mismatch correction would be independent of MSH2 and hence, would not be seen in spermatocytes that lack MSH2 alone as was previously noted [122]. Mismatch correction occurring during crossover resolution, termed crossover resolution-dependent mismatch correction, has also been observed in budding yeast [118]. Since lack of EXO1 depletes the nuclease activity of MLH3, it is likely that crossover resolution-dependent mismatch correction is also decreased in this allele to produce an observable increase in complex crossovers. Overall, this is consistent with at least 15% of the complex crossovers in *Exo1*$^{-/-}$ spermatocytes and may provide supportive evidence for template switching during crossover precursor formation/resolution.

As an alternative to template switching, the observed increase in complex crossovers could also arise through increased branch migration. Consistent with this model, I saw a decrease in reciprocal crossover asymmetry in *Exo1*$^{-/-}$ spermatocytes, due to the non-stereotypical positioning of the crossover exchange points, as would be expected for increased branch migration (**Figure 25**). Notably, increased branch migration was observed in budding yeast lacking EXO1 [119].

Crossover precursors are inaccessible to SDSA during pachynema

Having established that co-conversions arise from unrepaired crossover precursors via backup pathways, I made an interesting observation that these backup co-conversions are enriched on the B6 chromosome. These co-conversions could arise via crossover resolution from SSNs or by dissolution/SDSA of the crossover precursors. However, if these co-conversions arose via the resolution activity of SSNs, I would expect that backup co-conversions would be distributed equally between the B6 (B) and DBA (D) chromosomes (**Figure 48**, [119]). Instead, I only see co-conversion enrichment on the B or DSB receiving chromosome. Together, the data suggest that the co-conversions are likely produced via SDSA or dissolution and not via resolution. SDSA is a quite active in pachynema (Table 1), producing at least 27% of all recombination products in pachynema at *59.5*. The lack of long co-conversions in pachynema suggests that once a DSB is chosen to become a crossover precursor, the precursor become inaccessible to SDSA in pachynema and must either be resolved by MutLgamma (**Figure 27**) or repaired by backup SDSA/dissolution later in diplonema (**Figure 31**).

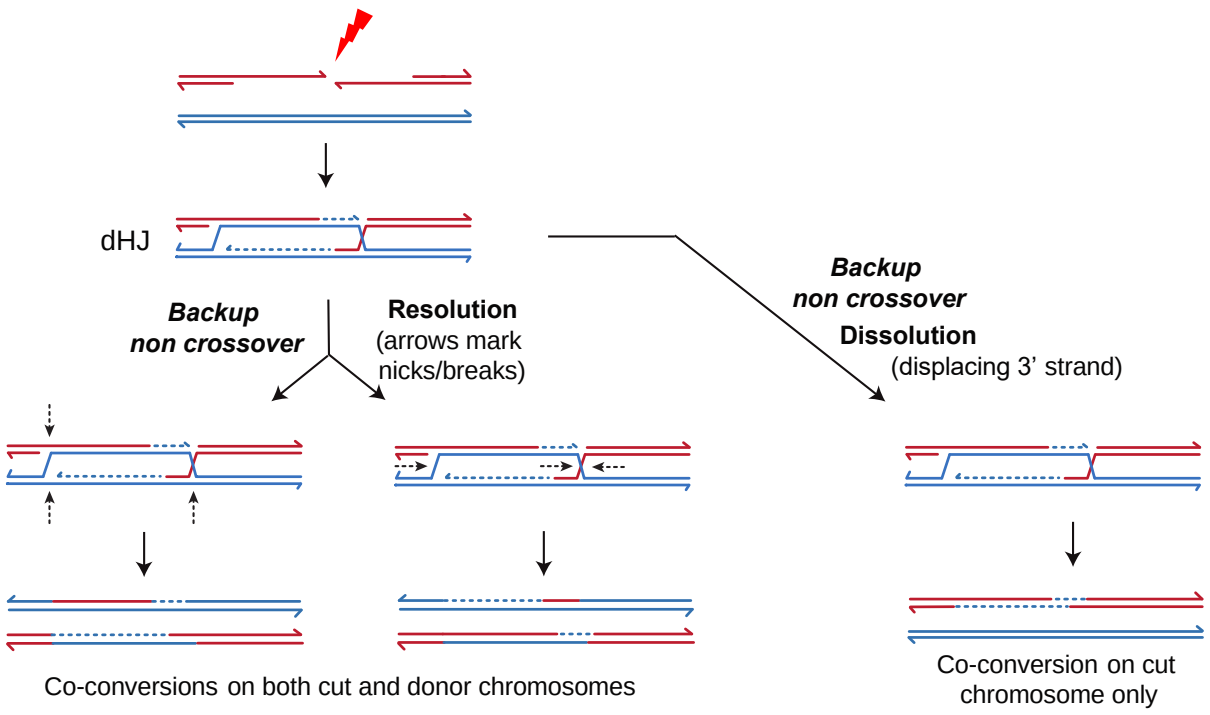

Figure 48: Co-conversions from resolution by nucleases vs by dissolution
A schematic of backup repair pathways that can produce co-conversion NCOs from dHJ. If the co-conversions are produced by nucleases via resolution of dHJ, then co-conversions should be present on both the chromosomes that got cut (B6 at *59.5*) and on donor, (DBA at *59.5*). Instead, we see co-conversions enrichment only on the cut B6 chromosome, consistent with co-conversions being produced mostly by dissolution.

Discontinuous co-conversions in *Exo1$^{-/-}$-like* mutants may provide evidence for template switching during dHJ formation

I identified two categories of mouse spermatocyte mutants based on MutLgamma foci formation and co-conversion characteristics: *Mlh3$^{-/-}$*- like mutants that lack MutLgamma cytological foci and have ~300bp co-conversions (*Hfm1$^{-/-}$*, *Hei10$^{-/-}$*, *Mlh3$^{-/-}$* and *Mlh3$^{-/-}$Exo1$^{-/-}$*); and *Exo1$^{-/-}$*- like mutants with MutLgamma foci and 600bp co-conversions (*Mlh3$^{-/DN}$* & *Mlh3$^{DN/DN}$*, *Mus81$^{-/-}$Exo1$^{-/-}$*, *Exo1$^{-/-}$*, and *Msh2$^{-/-}$Exo1$^{-/-}$*). *Exo1$^{-/-}$* - like mutants displayed a 10- (*Mlh3$^{DN/DN}$*) to 25-fold (*Msh2$^{-/-}$Exo1$^{-/-}$*) increase in discontinuous co-conversions compared to *Mlh3$^{-/-}$* spermatocytes. This increase in discontinuity cannot be accounted for by a 2-3 fold increase in co-conversion length alone, suggesting that an independent mechanism increases discontinuity in *Exo1$^{-/-}$* - like spermatocytes.

Additionally, I saw that *Mlh3*$^{-/-}$*Exo1*$^{-/-}$ mutant spermatocytes have an intermediate level of discontinuity (5.3 ± 6.8% of co-conversions), a phenotype that is stonger than *Mlh3*$^{-/-}$ mutants and weaker than *Exo1*$^{-/-}$ mutants, suggesting that *Exo1* is epistatic to *Mlh3* for this phenotype (**Figure 46**). Overall, given the role of EXO1 in MMR, discontinuity of co-conversions could arise from incomplete MMR correction. But defective MMR cannot explain why discontinuity increases in *Exo1*$^{-/-}$ versus *Mlh3*$^{-/-}$*Exo1*$^{-/-}$ spermatocytes. Additionally, the crossover pathway in *Mlh3*$^{-/-}$-like mutants only progresses until the polymerized single-end invasion (pSEI), whereas *Exo1*$^{-/-}$- like mutants progress further and form dHJs (**Figure 44, 45 and 47**). This increase could therefore reflect a process that is associated with dHJ formation, something like template switching. If MMR is active, these haplotype switches would likely be invisible owing to repair of heteroduplex strands. But as noted above, I suspect that there is an MLH3 nuclease-dependent mismatch correction that may occur during crossover formation. Therefore, I likely only see these haplotype switches in co-conversions, because of defective nuclease function of MLH3. Consistent with this idea, *Mlh3*$^{-/DN}$ & *Mlh3*$^{DN/DN}$ also show similar levels of discontinuity as *Exo1*$^{-/-}$ spermatocytes (**Figure 46**). In support of this model, template switching has been inferred to happen frequently during crossover formation in budding yeast [118]. Overall, my co-conversion data suggest that template switching is more common during the dHJ formation step rather than earlier during generation of the pSEI.

Co-conversions in *Exo1*$^{-/-}$-like mutants suggest unequal polymerization from the two invading ends of the DSB

My model predicts that, when MLH3 is physically present at crossover precursor sites, the second 3’ strand invades the homolog and extends differentiating the pSEI into a dual end polymerized, dHJ intermediate (**Figure 44 dHJ** and **Model figure 47**). If dual-end polymerization occurs in all dHJ intermediates in *Exo1*$^{-/-}$-like spermatocytes, why do only 28% of co-conversions span the hotspot center (**Figure 43 B**)? One explanation is that my analysis underestimates the number of spanning co-conversions, in part due to insufficient

polymorphism density on the left side of the hotspot center. Further, I suggest that the second 3' end extends less than the first 3' end leading to most (72%) of the spanning co-conversions having long and short conversion arms with respect to the putative DSB site or the hotspot center (**Figure 43 C**). One explanation may be that when MutLgamma loads onto a pSEI, the initially polymerized strand continues to be extended, whereas the second strand extends 3-fold shorter distance on average than the first strand. This shorter strand may often be too short to incorporate a polymorphism, making many co-conversions appear one-sided in *Exo1*$^{-/-}$-like mutants. In support of this model, in *Exo1*$^{-/-}$-like mutants, about 40 % of the spanning events are only categorized as 'spanning' because of higher polymorphism density on the right side of the hotspot (**Figure 43 A**, Type – 3 events).

Co-conversions and crossovers in crossover-defective mutants likely share the same precursor intermediate

Direct and indirect measurements of crossover gene conversion tract length in WT mouse spermatocytes, and by inference, the WT crossover precursor length, is ~600 bp [61,120,182], which is similar to co-conversion length in *Exo1*$^{-/-}$-like mutants (**Figure 42**). However, the apparent gene conversion tract length of crossovers in *Exo1*$^{-/-}$ spermatocytes calculated from reciprocal crossover asymmetry was much lower, ~ 182 bp. In WT, crossover gene conversion tract lengths estimated as a population average using reciprocal crossover asymmetry method is similar to direct measurements by mouse tetrad analysis that analyses crossovers at a single cell level [120]. So why is the reciprocal crossover asymmetry much lower than co-conversion tract length in *Exo1*$^{-/-}$ spermatocytes? Do these products arise from the same class of crossover precursors?

To test whether crossovers and co-conversions in *Exo1*$^{-/-}$ spermatocytes arise from the same class of crossover precursors (here dHJs), I plotted the ends of co-conversions as hypothetical crossover exchange points. I saw that this hypothetical crossover exchange point map reflected the observed crossover exchange point map from *Exo1*$^{-/-}$ crossovers. Therefore,

both the co-conversions and crossovers in *Exo1*$^{-/-}$ spermatocytes likely arise from a similar class of crossover intermediates, supporting the argument that the reduced reciprocal crossover asymmetry observed in *Exo1*$^{-/-}$ spermatocytes arises from non-stereotypical crossover exchange points that are positioned closer to the hotspot center rather than shorter upstream crossover intermediates (**Figure 25**). To further support the idea that co-conversions and crossovers share similar precursors, and given the shorter crossover precursors in *Mlh3*$^{-/-}$-like mutants, I tested whether there was an increase in the proportion of crossover exchange points positioned closer to the hotspot center in *Mlh3*$^{-/-}$ relative to *Exo1*$^{-/-}$ spermatocytes. Indeed, I saw that 85% (12 out of 14) of the crossovers from *Mlh3*$^{-/-}$-like mutants have exchange points in the central 500 bp of *59.5* (defined in **Figure 25**), as opposed to 54% in *Exo1*$^{-/-}$ spermatocytes and 31.4% in WT spermatocytes (p-values: =0.0398 and <0.0001 respectively. Fisher's exact test, two-tailed). Together, our data suggest that pSEIs (in *Mlh3*$^{-/-}$*-like*) and dHJs (in *Exo1*$^{-/-}$*-like*) are two distinct crossover precursors that are both capable of producing crossovers.

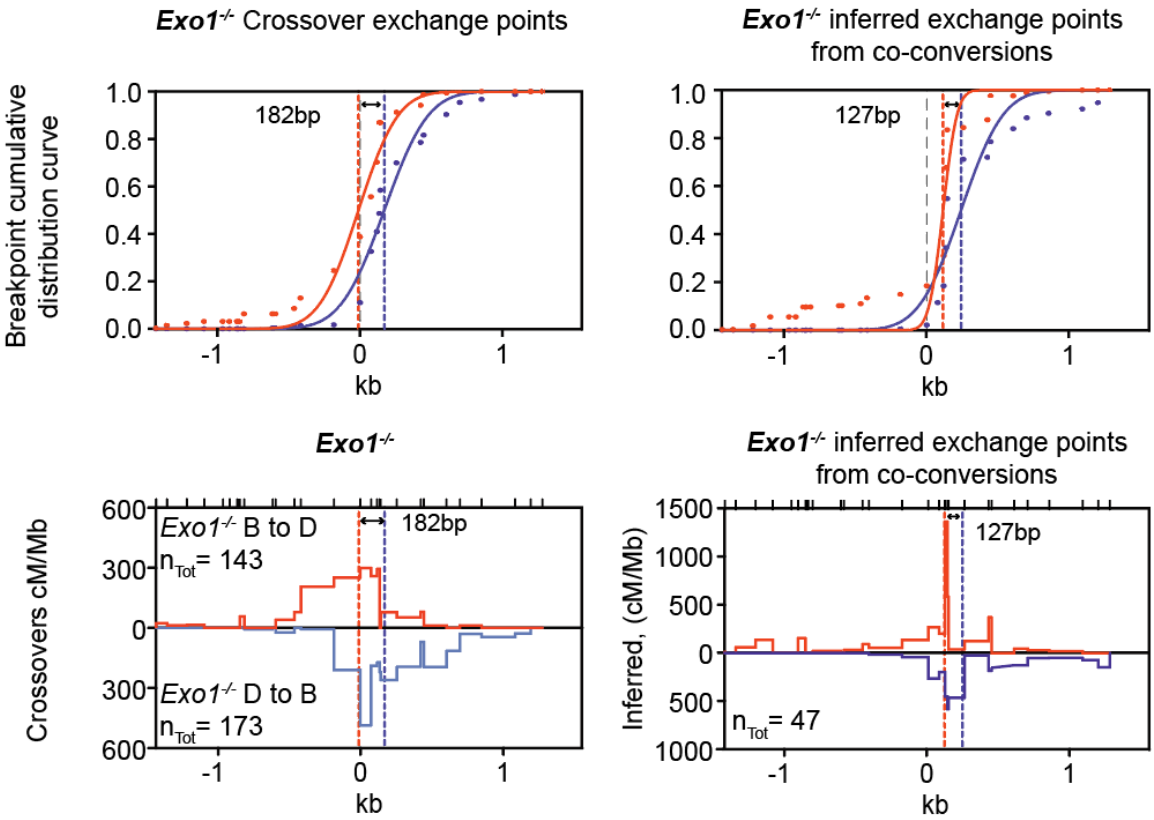

Figure 49: *Exo1*$^{-/-}$ co-conversions produce similar hypothetical inferred crossover exchange point plots as COs from the same genotype
Top, cumulative distribution curves of crossover exchange points in the B to D (red) and D to B (blue) crossovers from, *Exo1*$^{-/-}$, and inferred hypothetical exchange points from co-conversions in *Exo1*$^{-/-}$ spermatocytes. The mean of each crossover exchange point calculated from B to D or D to B distribution is indicated with a colored dotted line. The hotspot center is defined as 0kb. **Bottom**, crossover exchange point maps for *Exo1*$^{-/-}$ crossovers and inferred hypothetical exchange points using co-conversions from *Exo1*$^{-/-}$ spermatocytes in CentiMorgans/Megabase (cM/Mb). These data suggest that the reduced reciprocal crossover asymmetry in *Exo1*$^{-/-}$ co-conversions is mostly driven by non-stereotypical crossover exchange points.

Conclusions

Meiotic recombination mechanisms have been well-studied in budding yeast, and many of these mechanisms are conserved in mammals. However, there are many key differences between the two organisms, including features unique to mammals. Therefore, the establishment of recombination mechanisms in mammals is necessary. Recombination analysis at a few genomic locations (hotspots) has been performed previously in WT mouse

spermatocytes, as well as in a handful of mutant spermatocytes, namely *Msh2*$^{-/-}$, *Mlh1*$^{-/-}$, and *Mlh3*$^{-/-}$ mutants [61,117,122,197-199].

In budding yeast, MMR defective *Msh2*$^{-/-}$ mutants were used with great effectiveness to identify mechanisms of recombination [118,119,200]. But mismatch defective *Msh2*$^{-/-}$ mouse spermatocytes had comparatively less retained heteroduplex than budding yeast and are less informative to infer recombination mechanisms [122]. Further, the isolation of recombination intermediates on a gel-based DNA structure is possible in budding yeast due to large number of crossovers (signal) and less genomic DNA (background) [126,127,201]. This approach is impractical in mouse spermatocytes, as spermatocytes has orders of magnitude higher genomic DNA and far fewer crossovers. To circumvent these technical limitations, I analyzed fine-scale recombination in 12 different mutant conditions with varying degrees of defects in crossover formation, which were compared both to each other and WT controls. I performed all my recombination outcomes at a native recombination hotspot *59.5* on Chromosome 19. Overall, in this work, I analyzed over 1 million haploid genome equivalents and ~ 1300 crossovers and ~4400 NCOs.

Mechanisms conserved between yeast and mammals

Throughout the course of this study, I confirmed that many features of meiotic recombination were conserved between yeast and mice. For example, EXO1 has small MMR role in meiotic recombination, as seen in budding yeast [202]. Likewise, earlier reports determined that the EXO1's crossover-promoting role is nuclease-independent in yeast [155,167] and in mice [105,176]. Here, I determined that in mice that the crossover-promoting role of EXO1 is likely nuclease-independent.

The Single-end invasion (SEI) is the first identifiable crossover precursor intermediate in budding yeast. In yeast, the SEI is asymmetric as it involves only one invading 3' end and its formation does not require MLH3 [104,126,155,187]. Similarly, I infer that the first crossover precursor intermediate is also an SEI-like intermediate. Finally, I see evidence for template switching

based on dHJ formation in the *Exo1*$^{-/-}$-like mutants, similar to observations in budding yeast [118,119].

First observations from this work including observations unique to mammals

I provide evidence for two distinct crossover precursor intermediates in mouse spermatocytes (pSEIs and dHJs) and the specific genetic requirements for dHJ formation. In contrast to the SEI in budding yeast, which does not have any nascent polymerization [126], the inferred SEI-like intermediate in mice is likely polymerized from the first invading 3' end. Subsequent dHJ formation, via dual-end polymerization, requires MLH3, but in a nuclease-independent manner. By contrast, in budding yeast, dHJ formation does not require MLH3/MutLgamma complex [104,155,187] nor has any other protein been identified that is required for SEI to dHJ differentiation. *Exo1*$^{-/-}$ yeast have defective crossover interference [144,145,167] but *Exo1*$^{-/-}$ spermatocytes have normal crossover interference.

Finally, my observed crossover precursor phenotypes were consistent across multiple mutants, suggesting that they reflect normal, rather than aberrant, repair products. To conclude, my fine-scale recombination and cytological analyses in 12 different mutant conditions allowed me to identify recombination mechanisms specific to mammals while also expanding our overall understanding of crossover intermediate processing.

Limitations of this work

The fine-scale recombination analysis in this study was performed at *59.5* hotspot on chromosome 19. This hotspot was chosen to study crossover recombination for a few reasons, including high polymorphism density, preference for crossovers to be designated on one of the two parental homologs, and enrichment for crossover products. While I made the inferences to explain both the hotspot (local) and cytological analysis (global – cell wide) cohesively, observations at *59.5* may not hold true for other hotspots in the genome. Finally, the crossover precursors defined in this work were inferred using repair products from crossover defective mutants and were extrapolated to the WT. Therefore, future experiments that directly isolate

these precursors from WT are needed to verify the existence and characteristics of these intermediates.

Future Directions

This work, in addition to answering key questions in the field, has also opened a number of questions and venues to pursue. A few of those questions/venues are discussed below.

Examining MLH3's nuclease-independent role and *Hfm1*$^{-/-}$ crossovers

I identified that MLH3 plays a nuclease-independent role in the formation of dHJs, but my data is compatible with both direct and indirect roles of MLH3.

Testing if it is a direct role of MLH3

A direct role of MLH3 could require just the MLH3 protein or the entire MutLgamma complex at putative crossover sites. In support of the model that MLH3 can directly contribute to dHJ formation, MLH3 has been observed to localize to chromosome sites earlier than MLH1 and, by extension, earlier than the MutLgamma complex assembly [203]. To test whether MLH3's nuclease-independent role does not require the MutLgamma complex, recombination analysis can be performed in *Mlh1*$^{-/-}$ spermatocytes. In *Mlh1*$^{-/-}$ spermatocytes, MutLgamma complex does not form and crossovers are not produced, nevertheless, MLH3 is recruited to the chromosomes [203]. Therefore, for enzymatic crossover producing activity of MLH3, *Mlh1*$^{-/-}$ spermatocytes can be considered dead. So, if co-conversions in *Mlh1*$^{-/-}$ spermatocytes were consistent with the formation of a dHJ, then we can confirm that the nuclease-independent role of MLH3 is a direct role of MLH3 and does not require MutLgamma complex formation. Alternatively, however, if co-conversions from *Mlh1*$^{-/-}$ spermatocytes are consistent with the pSEI intermediate, we can verify that a full MutLgamma complex is required for dHJs to form. In the latter case, however, we cannot tell if it is a direct or indirect role of the MutLgamma complex.

Possible targets for an indirect role of MLH3/MutLgamma complex

Analysis of the nuclease-deficient allele of MLH3 (*Mlh3*$^{DN/DN}$) has shown that proper association of the crossover-promoting factor CDK2 and dissociation of HEI10 are required for MLH3 to be chromosome associated [160]. MutLgamma/MLH3's enzymatic activity is stimulated in vitro by the crossover-promoting MSH4/MSH5 (MutSgamma) complex and proteins required for polymerase processivity - replication factor C (RFC), and its loader PCNA [152,153]. MutLgamma complex likely also interacts with these factors in vivo. Any one or a combination

of these proteins may be involved in converting the pSEI into a dHJ, and this conversion step might require interaction with the MutLgamma complex. Simple removal of these factors is likely not useful as spermatocytes lacking MutSgamma do not progress to mid-pachynema and RFC and PCNA are required for viability. Therefore, an ideal approach would be to create point mutants that disrupt the interaction of these complexes with MutLgamma without disrupting their other core roles in meiosis or elsewhere. Such mutants are not available in mice and must be created and validated by *in vitro* biochemistry, yeast genetics, or cell-line studies before recombination analysis in mice.

$Hfm1^{-/-}$ crossovers

In earlier reports, spermatocytes lacking HFM1 have been shown to have more crossover bivalents (~3.5) than spermatocytes lacking MLH3 (~1.5) [131]. This result is surprising, as in mutants that lack MutLgamma complex foci, the number of bivalents is usually similar to $Mlh3^{-/-}$ spermatocytes [154,156,158]. It would therefore be interesting to identify the source of $Hfm1^{-/-}$ residual crossovers. Based on my work, I infer that dHJs do not form in $Hfm1^{-/-}$ spermatocytes. If the residual crossovers in $Hfm1^{-/-}$ spermatocytes require MLH3, we can conclude that MutLgamma is capable of converting pSEIs into crossovers. If crossovers in $Hfm1^{-/-}$ spermatocytes do not require MLH3, those crossovers must be produced by structure-selective nucleases (SSNs), the only other enzymes that can produce crossovers. If crossovers in $Hfm1^{-/-}$ spermatocytes are produced by SSNs, we can infer that HFM1 plays crucial roles in limiting access of crossover precursors to SSNs. To determine if crossovers in $Hfm1^{-/-}$ spermatocytes require MLH3, one can perform bivalent analysis in $Hfm1^{-/-}Mlh3^{-/-}$ and compare with single mutants to determine if MLH3 likely produces crossovers in $Hfm1^{-/-}$ spermatocytes.

Genome-wide analysis of meiotic recombination products

Most of the recombination analysis for this project was completed at one genomic location, the *59.5* hotspot on chromosome 19. We will uncover a lot more information from our samples for a similar amount of resources and time if we can isolate recombination products from the entire genome. Further, a whole genome approach would be invaluable to study

recombination when samples are limited – like in oocytes. The proposed whole genome approach needs to be cheap and scalable to be a practical replacement for our current recombination assay. To that end, I would like to suggest a single-cell whole genome recombination analysis approach. The protocol would start with single cell labeling of the spermatocyte cells using combinatorial indexing. The DNA from these cells would then be subjected to whole genome sequencing with long-range – pacbio or nanopore sequencing. Indeed, a similar approach was previously used to isolate mouse meiotic recombinants from the whole genome, but they recovered far fewer crossovers and almost no NCOs [204]. Briefly, these authors performed combinatorial indexing by labeling DNA in intact nuclei in random pools thrice, such that the odds of two independent nuclei getting the same three adapters in the same order is quite low. The first step of the labeling involved transposase that inserts an adapter every 0.5-1.5 kb and breaks the DNA in the process. The second and third adapters are simply ligated to the first label. Then the nuclei were lysed, and DNA was isolated, amplified, and sequenced

I hypothesize that we can increase the recovery of the recombinant products by changing at least two of the steps [204]. Considering that the hotspots are at least ~2kb long, the transposase chosen needs to insert and cut DNA with less frequency, for example once in 5 or 6kb. An alternative approach would be to use a restriction endonuclease with an average cut length of ~6 kb to create breaks and ligate adapters on the first step. If restriction endonucleases are used, multiple enzymes can ensure coverage of most hotspots. The second change would be to use long-range sequencing to read through the entire ~6 kb DNA strands as a single sequence. Despite the error rate, nanopore may still be usable for this approach since we are genotyping known polymorphisms rather than discovering new polymorphisms. However, I have not tried any proof-of-concept experiments for this protocol, so I believe a lot more changes to the original protocol by [204] will be needed to recover most, if not all, recombinant products from the entire genome as we currently do at specific hotspots.

Genome-wide isolation of pSEI and dHJ

In this work, I inferred the existence of two crossover precursors, the pSEI and dHJ from crossover-defective mutants (**Chapter 4**). While I am confident that these intermediates also form in WT, we will make a more convincing argument if we isolate those intermediates from WT mice. We think that these precursors are likely not ligated until they become a crossover or a co-conversion, as we were unable to isolate them with our PCR primers that amplify the entire hotspot. We would have isolated these intermediates, if the newly synthesized strands were contiguous across the hotspot. Therefore, we think that the newly synthesized strands are not ligated as shown in **Figure 50**.

Therefore, to isolate the precursor intermediates, we need to isolate and sequence the newly synthesized 3' ssDNA that is specifically produced in a repair intermediate during recombination. To identify these nascent DNA strands, we will need to isolate the sequence information of all 3’ ends and filter for evidence of polymerization-dependent extension of 3’ end. We can identify polymerization-dependent extension in a repair intermediate if the haplotype of the 3’ end switches from cut chromosome to donor chromosome in 5’ to 3’ direction, which is the same direction as polymerization, and should overlap with hotspot locations. These nascent synthesized strands in a pSEI and dHJ may become single-stranded or exist as gaps with single-strand – double strand junctions. Therefore, the protocol needs to be efficient at 3’ ssDNA adapter ligation. Finally, because the two nascent polymerized ends of a dHJ are on independent strands, single-cell information should be maintained to reconstruct these intermediates *in silico*.

It has been shown that TACS (full name?) ligation is efficient at 3’ ssDNA adapter ligation [205]. Therefore, TACS ligation needs to be performed in isolated, perforated nuclei to label any and all 3’ DNA ends. TACS ligation was developed to increase the yield of whole genome bisulfite sequencing data and, therefore, could be adapted to in nuclei labelling and whole genome recovery of newly synthesized 3' ssDNA ends. These nuclei would then be labelled with combinatorial indexing to retain single-cell information prior to DNA isolation. At

this point the DNA can be isolated, and the 3’ labelled ends can be isolated by primers against that adapter. This process would thereby enrich for 3' ends of the DNA that were most likely from DNA repair intermediates.

TACS ligation protocol was developed to be performed on isolated DNA, and hotspots are nucleosome free [89]. So, I would expect TACS ligation to work in isolated nuclei. If 3’ end labelling with TACS ligation does not work with perforated nuclei, other more tedious approaches to maintain single-cell identity have to be employed. We could manually pipette single cells into 96 well plates. Here, however, DNA must be isolated with care so as not to create new nicks or breaks on the DNA strands. A similar protocol to isolate ssDNA ends exists [107], and we could perform our DNA isolation based on those protocols to limit DNA shearing. 3' end labeling of ssDNA would then be performed after the DNA was isolated from single cells as described [205].

I have performed proof-of-concept test of just the TACS ligation step with purified DNA. While the protocol worked, I lost >80% of the DNA in the process, so much optimization is needed. However, steps in this protocol can be broken down into smaller steps. These smaller steps may still produce informative data while sacrificing throughput. Thus, a researcher can work up to a whole genome protocol, while starting with a low throughput approach to isolate these intermediates.

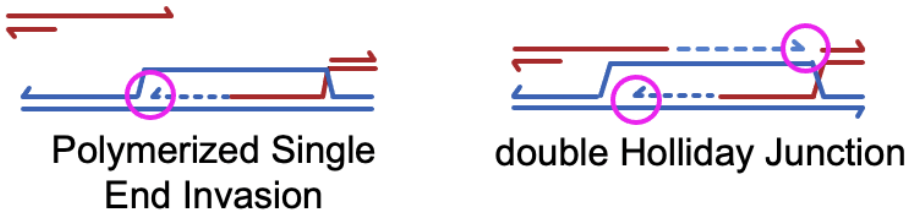

Figure 50: Schematic marking the newly synthesized strand ends of the crossover precursor intermediate

Schematic of polymerized Single End Invasion and double Holliday junctions. The cut chromosome and therefore the invading 3' end is shown in red. The donor chromosome is shown in blue. The newly synthesized strands are shown with dotted blue lines. The magenta

circle marks the 3' end that needs to be selectively ligated to an adapter to isolate the newly synthesized strands from these intermediates.

Table 1: All frequencies

Stage	Genotype (N)[a]	Singleton (molecules tested)	Singleton Frequency $x10^{-4}$ ± SD[b] (CI, 95%) [c]	Co-conversion (molecules tested)	Co-conversion Frequency $x10^{-4}$ ± SD (CI, 95%)	COs (molecules tested)	CO Frequency $x10^{-4}$ ± SD (CI, 95%)
[d]D	WT (3)	94 (15,695)	72.7 ± 21.5 (51.2 to 94.2)	5 (15,695)	4.2 ± 4 (0.2 to 8.2)	190 (15,695)	136.4 ± 43.8 (92.6 to 180.2)
[e]Late 4C	WT (4)	104 (16,721)	73.2 ± 15.8 (57.4 to 89)	9 (16,721)	6.8 ± 4.6 (2.2 to 11.4)	238 (16,721)	160.8 ± 37.1 (123.7 to 197.9)
[f]SP	WT (6)	126 (22,099)	70.8 ± 18.3 (52.5 to 89.1)	16 (22,099)	9.5 ± 6.0 (3.5 to 15.5)	311 (22,099)	164.3 ± 43.4 (120.9 to 207.7)
D	*Mlh3*$^{-/-}$ (3)	152 (11,162)	137.9 ± 23.2 (114.7 to 161.1)	62 (11,162)	56.5 ± 13.7 (42.8 to 70.2)	11 (353,598)	0.28 ± 0.50 (-0.22 to 0.78)
D	Hei10$^{-/-}$ (4)	224 (18,298)	124.7 ± 20.2 (104.5 to 144.9)	150 (18,298)	85.3 ± 15.0 (70.3 to 100.3)	3 (18,298)	1.6 ± 1.4 (0.2 to 3.0)
Late 4C	Hei10$^{-/-}$ (4)	172 (18,621)	93.8 ± 16.4 (77.4 to 110.2)	60 (18,621)	31.7 ± 9.2 (22.5 to 40.9)	0 (18,621)	0
D	*Exo1*$^{-/-}$ (3)	123 (9,805)	130.6 ± 22.1 (108.5 to 152.7)	38 (9,805)	40.4 ± 11.4 (31.6 to 55.4)	22 (9,805)	22.7 ± 10.8 (11.9 to 33.5)
Late 4C	*Exo1*^{het} (4)	101 (8,370)	131.9 ± 32.6 (99.3 to 164.5)	7 (8,370)	9.31 ± 9.4 (6.6 to 12.4)	91 (8,370)	116.0 ± 30.2 (85.8 to 146.2)
Late 4C	*Exo1*nd (4)	256 (9,301)	293.8 ± 54.6 (239.2 to 348.4)	12 (9,301)	13.8 ± 11.8 (2 to 25.6)	193 (18,026)	117.6 ± 23.9 (93.7 to 141.5)
Late 4C	*Exo1*$^{-/-}$ (6)	409 (14,683)	288.0 ± 45.6 (242.4 to 333.6)	65 (14,683)	49.1 ± 22.4 (30.8 to 77.2)	145 (59,769)	25.59 ± 7.32 (18.27 to 32.91)
Late 4C	*Exo1*$^{-/-}$ *Mlh3*$^{-/-}$ (4)	391 (12,909)	310.0 ± 43.1 (266.9 to 353.1)	55 (12,909)	43.6 ± 15.3 (31 to 62.4)	1 (12,909)	0.77 ± 1.56 (0 to 2.33)
Late 4C	*Exo1*$^{-/-}$ *Mus81*$^{-/-}$ (2)	64 (5,949)	111.2 ± 21.6 (89.6 to 132.8)	22 (5,949)	38.2 ± 11.9 (29.2 to 54)	12 (5,949)	20.3 ± 9.2 (11.1 to 29.5)
Late 4C	*Exo1*$^{-/-}$ *Msh2*$^{-/-}$ (3)	142 (10,331)	146.8 ± 23.1 (123.7 to 169.9)	50 (10,331)	51.7 ± 12.6 (41.8 to 67.8)	23 (10,331)	22.6 ± 9.0 (13.6 to 31.6)
Late 4C	*Mlh3*$^{-/DN}$ (3)	99 (10,259)	100.4 ± 18.3 (82.1 to 118.7)	47 (10,259)	47.7 ± 12.2 (37.2 to 62)	15 (10,259)	14.7 ± 6.9 (7.8 to 21.6)
Late 4C	*Mlh3*$^{DN/DN}$ (2)	59 (6,075)	100.7 ± 20.0 (80.7 to 120.7)	19 (6,075)	32.3 ± 10.6 (24.5 to 46.7)	12 (6,075)	19.9 ± 9.0 (10.9 to 28.9)

Late 4C	*Hfm1*$^{-/-}$ (4)	276 (13,018)	215.2 ± 41.4 (173.8 to 256.6)	28 (13,018)	21.7 ± 13.5 (8.2 to 35.2)	1 (13,018)	0.77 ± 1.5 (0 to 2.27)
Late 4C	*Mlh3*$^{-/-}$ (6)	419 (16,487)	258.3 ± 41.1 (217.2 to 299.4)	54 (16,487)	33.8 ± 13.4 (21.3 to 48.7)	0 (16,487)	0
Late 4C	*Mlh3*$^{DN/DN}$ *Exo1*$^{-/-}$ (2)	38 (6901)	55.7 ± 13.4 (69.1 to 42.3)	25 (6901)	36.3 ± 10.7 (47 to 25.6)	5 (6901)	7.3 ± 4.6 (11.9 to 2.7)

59.5 BU. [a]N, number of animals tested. [b]SD, standard deviation. [c]CI, confidence interval. [d]D, diplonema. [e]Late 4C, diplonema and metaphase. [f]SP, sperm.

Table 2: Sample purity

WT pachynema post sort (raw count)								
Sample	Target stage	Pre-Leptonema	Leptonema	Zygonema	Pachynema	Diplonema	Metaphase	2° spermatocytes & spermatids
#1 28 dpi	Pachynema	0	0	5	**66**	9*	0	8
#2 30 dpi	Pachynema	0	0	1	**78**	24*	0	0
#3 37 dpi	Pachynema	0	0	3	**162**	38*	0	0
Purity	76.8±2.6 %*							
Pre-sort (raw count)								
#1 28 dpi	Pachynema	0	0	4	**156**	0	0	0
#2 30 dpi	Pachynema	ND	ND	ND	ND	ND	ND	ND
#3 37 dpi	Pachynema	0	0	7	**93**	0	0	0
Purity	95.3±3.2 %							

WT diplonema post sort (raw count)								
Sample	Target stage	Pre-Leptonema	Leptonema	Zygonema	Pachynema	Diplonema	Metaphase	2° spermatocytes & spermatids
#1 43 dpi	Diplonema	0	0	0	1	**98**	14	6
#2 17 dpi	Diplonema	0	0	7	0	**64**	5	0
#3 33 dpi	Diplonema	0	0	0	0	**82**	21	2
Purity	81.6±3.1 %							
Pre-sort (raw count)								
#1 43 dpi	Diplonema	ND	ND	ND	ND	**ND**	ND	ND
#2 17 dpi	Diplonema	0	4	96	13	**36**	6	5
#3 33 dpi	Diplonema	0	0	97	0	**60**	3	0
Purity	30±10.6 %							

WT Late 4C (diplonema & metaphase) post sort (raw count)

Sample	Target stage	Pre-Leptonema	Leptonema	Zygonema	Pachynema	Diplonema	Metaphase	2º spermatocytes & spermatids
H	Late-4C	0	0	2	15	**80**	**3**	0
I	Late-4C	0	0	3	15	**67**	**3**	0
J	Late-4C	0	0	7	0	**43**	**1**	0
K	Late-4C	ND	ND	ND	ND	ND	ND	ND
Purity	82.9±3.3 %							

Mlh3$^{-/-}$ pachynema post sort (raw count) (Rhea Kang, Francesca Cole unpublished)								
Sample	Target stage	Pre-Leptonema	Leptonema	Zygonema	Pachynema	Diplonema	Metaphase	2º spermatocytes & spermatids
#1 29 dpi	Pachynema	0	4	0	**80**	16*	0	0
#2 20 dpi	Pachynema	0	4	0	**59**	37*	0	0
#3 46 dpi	Pachynema	0	4	0	**32**	64*	0	0
Purity	57.0±24.1 %*							
Pre-sort (raw count)								
#1 29 dpi	Pachynema	0	0	0	**163**	0	0	0
#2 20 dpi	Pachynema	0	0	0	**159**	2	0	0
#3 46 dpi	Pachynema	0	2	0	**160**	0	0	0
Purity	99.2±0.7 %							

Mlh3$^{-/-}$ diplonema post sort (raw count) (Rhea Kang, Francesca Cole unpublished)								
Sample	Target stage	Pre-Leptonema	Leptonema	Zygonema	Pachynema	Diplonema	Metaphase	2º spermatocytes & spermatids
#1 23 dpi	Diplonema	0	0	0	0	**100**	0	0
#2 40 dpi	Diplonema	0	0	0	0	**98**	2	0
#3 49 dpi	Diplonema	0	0	0	0	**97**	3	0
Purity	98.3±1.5 %							
Pre-sort (raw count)								
#1 23 dpi	Diplonema	0	1	0	22	**139**	0	0

#2 40 dpi	Diplonema	0	2	56	2	**100**	0	0
#3 49 dpi	Diplonema	0	10	62	0	**39**	0	0
Purity	61.1±25.3%							

Mlh3$^{-/-}$ Late 4C (diplonema & metaphase) post sort (raw count)								
Sample	Target stage	Pre-Leptonema	Leptonema	Zygonema	Pachynema	Diplonema	Metaphase	2^{o} spermatocytes & spermatids
ID 3125	Late-4C	0	0	0	0	**38**	**2**	0
ID 3126	Late-4C	0	0	0	0	**43**	**2**	0
ID 3123	Late-4C	0	0	0	0	**38**	**6**	0
ID 159	Late-4C	0	0	0	0	**39**	**1**	0
ID 189	Late-4C	0	0	0	1	**39**	**0**	0
ID 842	Late-4C	0	0	0	1	**49**	**2**	0
Purity	99.3±1.1%							

Exo1$^{-/-}$ pachynema post sort (raw count)								
Sample	Target stage	Pre-Leptonema	Leptonema	Zygonema	Pachynema	Diplonema	Metaphase	2^{o} spermatocytes & spermatids
#1 37 dpi	Pachynema	0	0	0	**46**	0	0	0
#2 37 dpi	Pachynema	0	0	0	**40**	0	0	0
#3 37 dpi	Pachynema	0	0	0	**48**	0	0	0
Purity	100.0±0.0%							
Pre-sort (raw count)								
#1 37 dpi	Pachynema	0	0	0	**71**	2	0	0
#2 37 dpi	Pachynema	0	0	2	**39**	0	0	0
#3 37 dpi	Pachynema	0	0	0	**56**	0	1	0
Purity	96.9±1.6%							

Exo1$^{-/-}$ diplonema post sort (raw count)								
Sample	Target stage	Pre-Leptonema	Leptonema	Zygonema	Pachynema	Diplonema	Metaphase	2^{o} spermatocy

								tes & spermatids
#1 41 dpi	Diplonema	0	0	0	0	**66**	4	0
#2 41 dpi	Diplonema	0	0	0	0	**42**	0	0
#3 41 dpi	Diplonema	0	0	0	0	**47**	1	0
Purity	97.4±2.9 %							
Pre-sort (raw count)								
#1 41 dpi	Diplonema	0	0	13	0	**36**	1	0
#2 41 dpi	Diplonema	0	0	17	0	**32**	0	0
#3 41 dpi	Diplonema	0	2	16	0	**38**	2	0
Purity	67.6±3.8 %							

Exo1$^{-/-}$ Late 4C (diplonema & metaphase) post sort (raw count)								
Sample	Target stage	Pre-Leptonema	Leptonema	Zygonema	Pachynema	Diplonema	Metaphase	2º spermatocytes & spermatids
ID 2501	Late-4C	0	0	0	0	**40**	**3**	0
ID 2325	Late-4C	0	0	0	6	**50**	**2**	0
ID 2263	Late-4C	0	0	1	12	**45**	**5**	0
ID 2089	Late-4C	0	0	0	0	**50**	**3**	0
ID 2088	Late-4C	0	0	0	3	**50**	**5**	0
ID 2104	Late-4C	0	0	0	4	**54**	**2**	0
ID 2105	Late-4C	0	0	0	0	**56**	**1**	0
ID 2078	Late-4C	0	0	0	0	**47**	**3**	0
Purity	94.6±7.3 %							

Exo1^{het} Late 4C (diplonema & metaphase) post sort (raw count)								
Sample	Target stage	Pre-Leptonema	Leptonema	Zygonema	Pachynema	Diplonema	Metaphase	2º spermatocytes & spermatids
ID 2077	Late-4C	0	0	0	5	**45**	**2**	0
ID 2087	Late-4C	0	0	0	2	**37**	**2**	0
ID 2437	Late-4C	0	3	0	2	**36**	**0**	0

ID 2319	Late-4C	0	1	0	0	**44**	**1**	0
Purity	92.8±4.5 %							

Mlh3$^{-/-}$*Exo1*$^{-/-}$ Late 4C (diplonema & metaphase) post sort (raw count)								
Sample	Target stage	Pre-Leptonema	Leptonema	Zygonema	Pachynema	Diplonema	Metaphase	2º spermatocytes & spermatids
ID 2620	Late-4C	0	0	0	1	**42**	**4**	0
ID 2801	Late-4C	0	0	0	1	**52**	**2**	0
ID 3400	Late-4C	0	0	1	0	**60**	**1**	0
ID 3298	Late-4C	0	0	0	0	**45**	**3**	0
Purity	98.6±0.9 %							

Mus81$^{-/-}$*Exo1*$^{-/-}$ Late 4C (diplonema & metaphase) post sort (raw count)								
Sample	Target stage	Pre-Leptonema	Leptonema	Zygonema	Pachynema	Diplonema	Metaphase	2º spermatocytes & spermatids
ID 442	Late-4C	0	0	0	0	**40**	**5**	0
ID 1660	Late-4C	0	0	4	8	**36**	**3**	0
Purity	88.2±16.6%							

Msh2$^{-/-}$*Exo1*$^{-/-}$ Late 4C (diplonema & metaphase) post sort (raw count)								
Sample	Target stage	Pre-Leptonema	Leptonema	Zygonema	Pachynema	Diplonema	Metaphase	2º spermatocytes & spermatids
ID 2488	Late-4C	0	0	0	0	**40**	**2**	0
ID 2489	Late-4C	0	0	0	1	**40**	**0**	0
ID 2290	Late-4C	0	0	1	0	**40**	**0**	0
Purity	98.3±1.4 %							

Mlh3$^{-/DN}$ Late 4C (diplonema & metaphase) post sort (raw count)								
Sample	Target stage	Pre-Leptonema	Leptonema	Zygonema	Pachynema	Diplonema	Metaphase	2º spermatocytes & spermatids
ID 32	Late-4C	0	0	0	1	**37**	**3**	0

ID 88	Late-4C	0	0	0	1	**39**	**3**	0
ID 90	Late-4C	0	0	0	1	**38**	**1**	0
Purity	97.6±0.08%							

Mlh3$^{DN/DN}$ Late 4C (diplonema & metaphase) post sort (raw count)								
Sample	Target stage	Pre-Leptonema	Leptonema	Zygonema	Pachynema	Diplonema	Metaphase	2º spermatocytes & spermatids
ID 445	Late-4C	0	0	0	0	**43**	**1**	0
ID 409	Late-4C	0	0	0	0	**35**	**7**	0
Purity	100.0±0.0%							

Hfm1$^{-/-}$ Late 4C (diplonema & metaphase) post sort (raw count)								
Sample	Target stage	Pre-Leptonema	Leptonema	Zygonema	Pachynema	Diplonema	Metaphase	2º spermatocytes & spermatids
ID 441	Late-4C	0	0	0	0	**43**	**1**	0
ID 443	Late-4C	ND	ND	ND	ND	ND	ND	ND
ID 514	Late-4C	0	0	0	0	**38**	**3**	0
ID 504	Late-4C	0	0	0	0	**43**	**6**	0
Purity	100.0±0.0%							

Exo1$^{nd/nd}$ Late 4C (diplonema & metaphase) post sort (raw count)								
Sample	Target stage	Pre-Leptonema	Leptonema	Zygonema	Pachynema	Diplonema	Metaphase	2º spermatocytes & spermatids
ID 161	Late-4C	0	0	0	0	**36**	**5**	0
ID 120	Late-4C	0	0	0	1	**34**	**5**	0
ID 254	Late-4C	0	0	0	2	**40**	**2**	0
ID 301	Late-4C	0	0	0	0	**42**	**0**	0
Purity	100.0±0.0%							

Hei10$^{-/-}$ Late 4C (diplonema & metaphase) post sort (raw count)

Sample	Target stage	Pre-Leptonema	Leptonema	Zygonema	Pachynema	Diplonema	Metaphase	2º spermatocytes & spermatids
KO A	Late-4C	0	0	7	0	**34**	**4**	0
KO B	Late-4C	0	0	10	0	**37**	**1**	0
KO C	Late-4C	0	0	9	21	**13**	**1**	0
KO D	Late-4C	0	0	6	0	**39**	**1**	0
Purity	70.6±26.1%							

Hei10$^{-/-}$ diplonema post sort (raw count)								
Sample	Target stage	Pre-Leptonema	Leptonema	Zygonema	Pachynema	Diplonema	Metaphase	2º spermatocytes & spermatids
ID 92	Late-4C	0	0	0	0	**92**	14	0
ID 94	Late-4C	0	0	0	1	**71**	31	0
ID 198	Late-4C	0	0	0	1	**97**	0	0
ID 462	Late-4C	0	0	6	1	**76**	19	0
Purity	82.3±13.3%							
Pre-sort (raw count)								
Sample	Target stage	Pre-Leptonema	Leptonema	Zygonema	Pachynema	Diplonema	Metaphase	2º spermatocytes & spermatids
ID 92	Late-4C	ND	ND	ND	ND	ND	ND	ND
ID 94	Late-4C	0	1	50	12	**48**	10	0
ID 198	Late-4C	ND	ND	ND	ND	ND	ND	ND
ID 462	Late-4C	0	0	21	0	**62**	14	0
Purity	51.8±17.1%							

*In our original chromosome spread analysis, post-sort pachytene spermatocytes occasionally show slight splaying of the axis termini. These were scored as diplonema, however, based upon pre-sort purity, the co-existing populations within the testis (e.g., zygonema from the subsequent wave of spermatogenesis are always found in conjunction with diplonema), and the disparate distribution of recombination outcomes these cells are likely pachynema. In subsequent experiments, we verified that these splayed ends retain SYCP1 staining.

ASP	Primer sequence (5'->3')	5' location (GRCm39)	EVA RefSNP release 3
Bf14590.1	TGTTTCTGAAGCACGGGA	19:59428515	rs50050489
Caf14590.1	TGTTTCTGAAGCACGGGG		
Bf14913.1	CAAGACCCGGTCAGAACC	19:59428838	rs51436899
Caf14913.1	CAAGACCCGGTCAGAACA		
Br 19630.1	CTGGCTGACTCCATAAAGA	19:59433590	rs37215264
Car19630.1	CTGGCTGACTCCATAAAGG		
Br19683	GCACTGGGGATGTAATAGG	19:59433643	rs51754290
Car19683	GCACTGGGGATGTAATAGT		
Universal Primers			
59.5Uf15721	CTGTGTACTATCATTCCTGGC	19:59429643	
59.5Uf16055	TGGGACTCACATGGTAAAGTG	19:59429977	
59.5Ur18935	CAACGAGAACACATCTGTGCCC	19:59432898	
59.5Ur19001	CCGCTGTGAACTGGGCGC	19:59432960	

Table 3: Primer list

Allele-specific primers (ASPs) used to amplify recombinants at *59.5*

Genotyping primers used to test genotype alleles

Allele	**Primer name, sequence (5'->3')**	**T_m**	**Bands**	**Multiplex**
HFM1^{Gt} (OST347241)Lex	F1: GCTGTCCAGTACTTTTATACAAC	60°C, 35 cycles	WT 340bp, MT 270bp	Yes
	R1: GGTACAAGCTTATAGTTCAGC			
	R2: ATAAACCCTCTTGCAGTTGCATC			
HEI10^{mei4}	mHei10 atg Forward: ATGTCTTTGTGTGAAGACATGCTGCT			No
	mei4Genotype Reverse WT: CCCAGCCCCTAGGCACTCAC	WT: 57°C, 35x	WT 300bp	
	mei4GenotypeReverse Mut: CCCAGCCCCTAGGCACTCAA	MT: 54°C, 35x	MT 300bp	
MLH3^{tm1Lpkn} (null allele)	P1: CGGTTTCCCACCTTCTCTACATCGTCCGTC	60°C, 35 cycles	WT 250bp, MT 196bp	Yes

	P2: TTGGGTAACGCCAGGGTTTTCCCA			
	P3: TCAGAGAAGGAAGCCAGTGTCTGCCAC			
Exo1^{tm2Wed} (null allele)	P1: CTCTTGTCTGGGCTGATATGC	60^{o}C, 35 cycles	WT 280bp, MT 300bp	Yes
	P2: AGGAGTAGAAGTGGCGCGCGAAGG			
	P3: ATGGCGTGCGTGATGTTGATA			
Msh2.1$^{tm2.1Rak/J}$	12839(184F): TACTGATGCGGGTTGAAGG	56^{o}C, 35 cycles	WT 211bp, MT 340bp	Yes
	12840(184R): AACCAGAGCCTCAACTAGC			
	165R: GGCAAACTCCTCAAATCACG			
Exo1^{DA} (nuclease dead allele)	Exo1173D InF: CAGGCTGTCATCACAGAGGACTCCGA	60^{o}C, 35 cycles	WT 611bp, 266bp MT 611bp, 399bp	Yes
	Exo1173A InR: ACCTTCTTACAGCCAAATGCGAGGAAGG			
	Exo1 DA OF: GGACTCTCCTTGCTGACCTTCCATTGTG			
	Exo1 DA OR: CAGCACCCAAAAAAATCAAACCAAACCA			
Mus81^{tm1Chmg}	P1: GGTGTGGCCCTGATGGAAGAG	60^{o}C, 35 cycles	WT 400Bp, MT 370Bp	Yes
	P2: GGAGCTAAGGCCTAGCGAGTACAG			
	P3: CTAGCCGCTTGCGTTCCACAATGT			
FVB-Tg (Stra8-cre)$^{1Reb/LguJ}$	oIMR7338 Internal control For: CTAGGCCACAGAATTGAAAGATCT	60^{o}C, 35 cycles	Internal control 324bp Transgene 179bp	Yes
	oIMR7339 Internal control Rev: GTAGGTGGAAATTCTAGCATCATCC			
	oIMR8773 Transgene For: GTGCAAGCTGAACAACAGGA			
	oIMR8774 Transgene Rev: AGGGACACAGCATTGGAGTC			
MLH3^{D1185N} (nuclease dead allele)	For: AAGCCAAGTCTGCATGAGTA	58^{o}C, 36 cycles		N/A
	Rev: TAAATGTGCCACTGACTAAAT			

Restriction Digest	Enzyme: Sau96I, at least 4 hours	37°C	WT 439bp, 263 bp MT 702 bp	
59.5 PCR	19HS59.5f16255: GAAAGACGGAAGAGAGCTTCC	60°C, 36 cycles		N/A
	19HS59.5r16825: GGAAGAATAGATGCTTGGTGG			
Restriction Digest	Enzyme: BclI, at least 4 hours	50°C	C57BL/6J 377bp, 234bp DBA/2J 616bp	

Table 4: Allele-specific oligonucleotides (ASOs), *59.5*

ASO	sequence (5'->3')	ASO	sequence (5'->3')	GRCm39	central polymorphism
	AAAAAATTAAA		AAAAAATTTTT		
B15102	AAAAAAAAAG	Ca15102	TTAAAAAAAG	19:59429036	rs241448997
	AAATGTAACGT		AAATGTAATGT		
B15185	AGGATAAAA	Ca15185	AGGATAAAA	19:59429119	rs51399465
	AATGAGGCAGA		AATGAGGTAGA		
B15239	GGTTGTT	Ca15239	GGTTGTT	19:59429174	rs48315502
	TGTACTTTCTG		TGTACTTGCTG		
B16003	CCTAGTC	Ca16003	CCTAGTC	19:59429938	rs47029339
	TACTATCAGTC		TACTATCAATC		
B16080	AATCAATC	Ca16080	AATCAATC	19:59430014	rs45707443
	CCATCAATTCC		CCATCAATCCC		
B16220	AAGGAAG	Ca16220	AAGGAAG	19:59430154	rs51260902
	TCCAATTTCTA		TCCAATTTCTG		
B16341	CCGACTG	Ca16341	TCTACCG	19:59430277	rs250557647
	CATATAAACAT		CGTATAAATGT		
B16473	TTTGCTGT	Ca16473	TTTGCTGT	19:59430414	rs46140223
	AGTCCAGGCTG		AGCCCAGACTG		
B16520	GTTTCAA	Ca16520	GTTTCAA	19:59430460	rs47627339
	GAACTACCAAT		GAACTACCAGT		
B16573	CTTCCTG	Ca16573	CTTCCTG	19:59430506	rs51468461
	TCTTCCTGCCT		TCTTCCTGTCT		
B16582	CTACCTC	Ca16582	CTACCTC	19:59430516	rs50736308
	CTACCTCCTAA		CTACCTCTTAA		
B16592	ATGCTGG	Ca16592	ATGCTGG	19:59430527	rs47233626
	ACCTCTATGAC		ACCTCTACGAC		
B16623	CAGCTTG	Ca16623	CAGCTTG	19:59430558	rs52052658
	TCCTGGGCTCC		TCCTGGGAGCC		
B16823	ACCAAG	Ca16823	ACCAAG	19:59430758	rs47310242
	TATTCTTCCTA		TATTCTTTCTA		
B16844	CTGAGAC	Ca16844	CTGAGAC	19:59430779	rs48231668
	AAGACATATCT		AAGACATGTCT		
B16976	CTCCCAA	Ca16976	CTCCCAA	19:59430911	rs50999333
	ACGTGTCCCAT		ACGTGTCTCAT		
B17021	ACTTGAC	Ca17021	ACTTGAC	19:59430956	rs51999729
	CCACAGATGCA		CCACAGAGGCA		
B17255	AGCTGCT	Ca17255	AGCTGCT	19:59431190	rs38558460
	TGGGACACCAG		TGGGACATCAG		
B17440	AAGGTAC	Ca17440	AAGGTAC	19:59431375	rs46966686
	TCCCACCTATG		TCCCACCCATG		
B17517	TCCCCA	Ca17517	TCCCCA	19:59431452	rs51412323
	AGAAAGTACTC		AGAAAGTGCTC		
B17558	ATATGACA	Ca17558	ATATGACA	19:59431493	rs39149559
	TGACAGTTTGG		TGACAGTTTGG		
B17576	CGGTTGG	Ca17576	TGGATGG	19:59431507	rs49523813
	TGGACGGATTG		TGGGCAGATTG		
B17583	GCCAGA	Ca17583	GCCAGA	19:59431522	rs216052936
	ATATATGTGTG		ATATATGTTTG		
B17697	ATGTAGTC	Ca17697	ATGTAGTC	19:59431631	rs36601719

	AATGGCTGAAC		AATGGCTAAAC		
B17866	TGTTGTAG	Ca17866	TGTTGTAG	19:59431801	rs30563970
	GACCTACTCTA		GACCTACCCTA		
B17888	ACTCTGG	Ca17888	ACTCTGG	19:59431823	rs30719850
	ATCTCTTTCCC		ATCTCTTCCCC		
B18047	TTTGAGG	Ca18047	TTTGAGG	19:59431982	rs48970885
	AGTGTAGCGGA		AGTGTAGTGGA		
B18142	GCACATC	Ca18142	GCACATC	19:59432077	rs51608210
	TTATAGGTCTC		TTATAGGCCTC		
B18295	ACTATCCA	Ca18295	ACTATCCA	19:59432230	rs37419451
	CTTCACATTGA		CTTCACATCGA		
B18531	CTCTTCCA	Ca18531	CTCTTCCA	19:59432466	rs30364053
	TTACATGTATC		TTACATGTGTC		
B18641	TCAGAACT	Ca18641	TCAGAACT	19:59432575	rs31137226
	ACTGCAGGTGG		ACTGCAGTTGG		
B18723	GGTGGA	Ca18723	GGTGGA	19:59432658	rs30661467

For strand Genotyping	Sanger sequencing primers from 5’ end to 3’ end of the *59.5* hotspot
	GGTTGGGATGCTTGACCATG
	CTGTGTAGACCAGGCTGGTC
	GCCAAGACCCAGAGTTTATT
	GAATGCCAGGCAAGAACTCTACC
	GGCTTCTACACCTGCCACAA
	GAAGCTGTCTGGCAAGGTGAG
	GGTGACATGGTGACATCCTTC

References

1. Crow, J.F. (1994). Advantages of sexual reproduction. Dev Genet *15*, 205-213. 10.1002/dvg.1020150303.

2. Hassold, T., and Hunt, P. (2001). To err (meiotically) is human: the genesis of human aneuploidy. Nat Rev Genet *2*, 280-291. 10.1038/35066065.

3. Capalbo, A., Poli, M., Jalas, C., Forman, E.J., and Treff, N.R. (2022). On the reproductive capabilities of aneuploid human preimplantation embryos. Am J Hum Genet *109*, 1572-1581. 10.1016/j.ajhg.2022.07.009.

4. Wang, J., Fan, H.C., Behr, B., and Quake, S.R. (2012). Genome-wide single-cell analysis of recombination activity and de novo mutation rates in human sperm. Cell *150*, 402-412. 10.1016/j.cell.2012.06.030.

5. Lu, S., Zong, C., Fan, W., Yang, M., Li, J., Chapman, A.R., Zhu, P., Hu, X., Xu, L., Yan, L., et al. (2012). Probing meiotic recombination and aneuploidy of single sperm cells by whole-genome sequencing. Science *338*, 1627-1630. 10.1126/science.1229112.

6. Lee, B., and Amon, A. (2001). Meiosis: how to create a specialized cell cycle. Curr Opin Cell Biol *13*, 770-777. 10.1016/s0955-0674(00)00282-9.

7. Wang, S., Shang, Y., Liu, Y., Zhai, B., Yang, X., and Zhang, L. (2021). Crossover patterns under meiotic chromosome program. Asian J Androl *23*, 562-571. 10.4103/aja.aja_86_20.

8. Desai, A., and Mitchison, T.J. (1997). Microtubule polymerization dynamics. Annu Rev Cell Dev Biol *13*, 83-117. 10.1146/annurev.cellbio.13.1.83.

9. Inoue, S., and Salmon, E.D. (1995). Force generation by microtubule assembly/disassembly in mitosis and related movements. Mol Biol Cell *6*, 1619-1640. 10.1091/mbc.6.12.1619.

10. Yang, Z., Tulu, U.S., Wadsworth, P., and Rieder, C.L. (2007). Kinetochore dynein is required for chromosome motion and congression independent of the spindle checkpoint. Curr Biol *17*, 973-980. 10.1016/j.cub.2007.04.056.

11. Kapoor, T.M., Lampson, M.A., Hergert, P., Cameron, L., Cimini, D., Salmon, E.D., McEwen, B.F., and Khodjakov, A. (2006). Chromosomes can congress to the metaphase plate before biorientation. Science *311*, 388-391. 10.1126/science.1122142.

12. Ferraro-Gideon, J., Sheykhani, R., Zhu, Q., Duquette, M.L., Berns, M.W., and Forer, A. (2013). Measurements of forces produced by the mitotic spindle using optical tweezers. Mol Biol Cell *24*, 1375-1386. 10.1091/mbc.E12-12-0901.

13. Grishchuk, E.L., Molodtsov, M.I., Ataullakhanov, F.I., and McIntosh, J.R. (2005). Force production by disassembling microtubules. Nature *438*, 384-388. 10.1038/nature04132.

14. Nicklas, R.B. (1965). Chromosome Velocity during Mitosis as a Function of Chromosome Size and Position. J Cell Biol *25*, SUPPL:119-135. 10.1083/jcb.25.1.119.

15. Duro, E., and Marston, A.L. (2015). From equator to pole: splitting chromosomes in mitosis and meiosis. Genes & development *29*, 109-122. 10.1101/gad.255554.114.

16. Barra, V., and Fachinetti, D. (2018). The dark side of centromeres: types, causes and consequences of structural abnormalities implicating centromeric DNA. Nat Commun *9*, 4340. 10.1038/s41467-018-06545-y.

17. Akiyoshi, B., Sarangapani, K.K., Powers, A.F., Nelson, C.R., Reichow, S.L., Arellano-Santoyo, H., Gonen, T., Ranish, J.A., Asbury, C.L., and Biggins, S. (2010). Tension directly stabilizes reconstituted kinetochore-microtubule attachments. Nature *468*, 576-579. 10.1038/nature09594.

18. Umbreit, N.T., Gestaut, D.R., Tien, J.F., Vollmar, B.S., Gonen, T., Asbury, C.L., and Davis, T.N. (2012). The Ndc80 kinetochore complex directly modulates microtubule dynamics. Proc Natl Acad Sci U S A *109*, 16113-16118. 10.1073/pnas.1209615109.

19. Gorbsky, G.J., Sammak, P.J., and Borisy, G.G. (1987). Chromosomes move poleward in anaphase along stationary microtubules that coordinately disassemble from their kinetochore ends. J Cell Biol *104*, 9-18. 10.1083/jcb.104.1.9.

20. Marston, A.L. (2014). Chromosome segregation in budding yeast: sister chromatid cohesion and related mechanisms. Genetics *196*, 31-63. 10.1534/genetics.112.145144.

21. Singh, V.P., and Gerton, J.L. (2015). Cohesin and human disease: lessons from mouse models. Curr Opin Cell Biol *37*, 9-17. 10.1016/j.ceb.2015.08.003.

22. Hirano, T. (2012). Condensins: universal organizers of chromosomes with diverse functions. Genes & development *26*, 1659-1678. 10.1101/gad.194746.112.

23. Nicklas, R.B., Ward, S.C., and Gorbsky, G.J. (1995). Kinetochore chemistry is sensitive to tension and may link mitotic forces to a cell cycle checkpoint. J Cell Biol *130*, 929-939. 10.1083/jcb.130.4.929.

24. Nicklas, R.B. (1997). How cells get the right chromosomes. Science *275*, 632-637. 10.1126/science.275.5300.632.

25. Li, X., and Nicklas, R.B. (1995). Mitotic forces control a cell-cycle checkpoint. Nature *373*, 630-632. 10.1038/373630a0.

26. May, K.M., and Hardwick, K.G. (2006). The spindle checkpoint. J Cell Sci *119*, 4139-4142. 10.1242/jcs.03165.

27. Sarangapani, K.K., Akiyoshi, B., Duggan, N.M., Biggins, S., and Asbury, C.L. (2013). Phosphoregulation promotes release of kinetochores from dynamic microtubules via multiple mechanisms. Proc Natl Acad Sci U S A *110*, 7282-7287. 10.1073/pnas.1220700110.

28. Lampson, M.A., and Kapoor, T.M. (2005). The human mitotic checkpoint protein BubR1 regulates chromosome-spindle attachments. Nat Cell Biol *7*, 93-98. 10.1038/ncb1208.

29. Rieder, C.L., Cole, R.W., Khodjakov, A., and Sluder, G. (1995). The checkpoint delaying anaphase in response to chromosome monoorientation is mediated by an inhibitory signal produced by unattached kinetochores. J Cell Biol *130*, 941-948. 10.1083/jcb.130.4.941.

30. Ng, T.M., Waples, W.G., Lavoie, B.D., and Biggins, S. (2009). Pericentromeric sister chromatid cohesion promotes kinetochore biorientation. Mol Biol Cell *20*, 3818-3827. 10.1091/mbc.e09-04-0330.

31. Verzijlbergen, K.F., Nerusheva, O.O., Kelly, D., Kerr, A., Clift, D., de Lima Alves, F., Rappsilber, J., and Marston, A.L. (2014). Shugoshin biases chromosomes for biorientation through condensin recruitment to the pericentromere. Elife *3*, e01374. 10.7554/eLife.01374.

32. Indjeian, V.B., and Murray, A.W. (2007). Budding yeast mitotic chromosomes have an intrinsic bias to biorient on the spindle. Curr Biol *17*, 1837-1846. 10.1016/j.cub.2007.09.056.

33. Peplowska, K., Wallek, A.U., and Storchova, Z. (2014). Sgo1 regulates both condensin and Ipl1/Aurora B to promote chromosome biorientation. PLoS Genet *10*, e1004411. 10.1371/journal.pgen.1004411.

34. Keeney, S., Giroux, C.N., and Kleckner, N. (1997). Meiosis-specific DNA double-strand breaks are catalyzed by Spo11, a member of a widely conserved protein family. Cell *88*, 375-384. 10.1016/s0092-8674(00)81876-0.

35. Keeney, S., Baudat, F., Angeles, M., Zhou, Z.H., Copeland, N.G., Jenkins, N.A., Manova, K., and Jasin, M. (1999). A mouse homolog of the Saccharomyces cerevisiae meiotic recombination DNA transesterase Spo11p. Genomics *61*, 170-182. 10.1006/geno.1999.5956.

36. Romanienko, P.J., and Camerini-Otero, R.D. (1999). Cloning, characterization, and localization of mouse and human SPO11. Genomics *61*, 156-169. 10.1006/geno.1999.5955.

37. Gray, S., and Cohen, P.E. (2016). Control of Meiotic Crossovers: From Double-Strand Break Formation to Designation. Annu Rev Genet *50*, 175-210. 10.1146/annurev-genet-120215-035111.

38. Hillers, K.J., and Villeneuve, A.M. (2003). Chromosome-wide control of meiotic crossing over in C. elegans. Curr Biol *13*, 1641-1647. 10.1016/j.cub.2003.08.026.

39. Goldstein, L.S. (1981). Kinetochore structure and its role in chromosome orientation during the first meiotic division in male D. melanogaster. Cell *25*, 591-602. 10.1016/0092-8674(81)90167-7.

40. Li, X., and Dawe, R.K. (2009). Fused sister kinetochores initiate the reductional division in meiosis I. Nat Cell Biol *11*, 1103-1108. 10.1038/ncb1923.

41. Winey, M., Morgan, G.P., Straight, P.D., Giddings, T.H., Jr., and Mastronarde, D.N. (2005). Three-dimensional ultrastructure of Saccharomyces cerevisiae meiotic spindles. Mol Biol Cell *16*, 1178-1188. 10.1091/mbc.e04-09-0765.

42. Sakuno, T., Tada, K., and Watanabe, Y. (2009). Kinetochore geometry defined by cohesion within the centromere. Nature *458*, 852-858. 10.1038/nature07876.

43. Parra, M.T., Viera, A., Gomez, R., Page, J., Benavente, R., Santos, J.L., Rufas, J.S., and Suja, J.A. (2004). Involvement of the cohesin Rad21 and SCP3 in monopolar

attachment of sister kinetochores during mouse meiosis I. J Cell Sci *117*, 1221-1234. 10.1242/jcs.00947.

44. Petronczki, M., Matos, J., Mori, S., Gregan, J., Bogdanova, A., Schwickart, M., Mechtler, K., Shirahige, K., Zachariae, W., and Nasmyth, K. (2006). Monopolar attachment of sister kinetochores at meiosis I requires casein kinase 1. Cell *126*, 1049-1064. 10.1016/j.cell.2006.07.029.

45. Rabitsch, K.P., Petronczki, M., Javerzat, J.P., Genier, S., Chwalla, B., Schleiffer, A., Tanaka, T.U., and Nasmyth, K. (2003). Kinetochore recruitment of two nucleolar proteins is required for homolog segregation in meiosis I. Developmental cell *4*, 535-548. 10.1016/s1534-5807(03)00086-8.

46. Toth, A., Rabitsch, K.P., Galova, M., Schleiffer, A., Buonomo, S.B., and Nasmyth, K. (2000). Functional genomics identifies monopolin: a kinetochore protein required for segregation of homologs during meiosis i. Cell *103*, 1155-1168. 10.1016/s0092-8674(00)00217-8.

47. Brar, G.A., Kiburz, B.M., Zhang, Y., Kim, J.E., White, F., and Amon, A. (2006). Rec8 phosphorylation and recombination promote the step-wise loss of cohesins in meiosis. Nature *441*, 532-536. 10.1038/nature04794.

48. Ishiguro, T., Tanaka, K., Sakuno, T., and Watanabe, Y. (2010). Shugoshin-PP2A counteracts casein-kinase-1-dependent cleavage of Rec8 by separase. Nat Cell Biol *12*, 500-506. 10.1038/ncb2052.

49. Attner, M.A., Miller, M.P., Ee, L.S., Elkin, S.K., and Amon, A. (2013). Polo kinase Cdc5 is a central regulator of meiosis I. Proc Natl Acad Sci U S A *110*, 14278-14283. 10.1073/pnas.1311845110.

50. Nikalayevich, E., El Jailani, S., Dupre, A., Cladiere, D., Gryaznova, Y., Fosse, C., Buffin, E., Touati, S.A., and Wassmann, K. (2022). Aurora B/C-dependent phosphorylation promotes Rec8 cleavage in mammalian oocytes. Curr Biol *32*, 2281-2290 e2284. 10.1016/j.cub.2022.03.041.

51. Kudo, N.R., Wassmann, K., Anger, M., Schuh, M., Wirth, K.G., Xu, H., Helmhart, W., Kudo, H., McKay, M., Maro, B., et al. (2006). Resolution of chiasmata in oocytes requires separase-mediated proteolysis. Cell *126*, 135-146. 10.1016/j.cell.2006.05.033.

52. Kitajima, T.S., Sakuno, T., Ishiguro, K., Iemura, S., Natsume, T., Kawashima, S.A., and Watanabe, Y. (2006). Shugoshin collaborates with protein phosphatase 2A to protect cohesin. Nature *441*, 46-52. 10.1038/nature04663.

53. Franasiak, J.M., Forman, E.J., Hong, K.H., Werner, M.D., Upham, K.M., Treff, N.R., and Scott, R.T. (2014). Aneuploidy across individual chromosomes at the embryonic level in trophectoderm biopsies: changes with patient age and chromosome structure. J Assist Reprod Genet *31*, 1501-1509. 10.1007/s10815-014-0333-x.

54. Gruhn, J.R., Zielinska, A.P., Shukla, V., Blanshard, R., Capalbo, A., Cimadomo, D., Nikiforov, D., Chan, A.C., Newnham, L.J., Vogel, I., et al. (2019). Chromosome errors in human eggs shape natural fertility over reproductive life span. Science *365*, 1466-1469. 10.1126/science.aav7321.

55. Nagaoka, S.I., Hassold, T.J., and Hunt, P.A. (2012). Human aneuploidy: mechanisms and new insights into an age-old problem. Nat Rev Genet *13*, 493-504. 10.1038/nrg3245.

56. Wang, S., Hassold, T., Hunt, P., White, M.A., Zickler, D., Kleckner, N., and Zhang, L. (2017). Inefficient Crossover Maturation Underlies Elevated Aneuploidy in Human Female Meiosis. Cell *168*, 977-989 e917. 10.1016/j.cell.2017.02.002.

57. Broman, K.W., Rowe, L.B., Churchill, G.A., and Paigen, K. (2002). Crossover interference in the mouse. Genetics *160*, 1123-1131. 10.1093/genetics/160.3.1123.

58. Jones, G.H. (1984). The control of chiasma distribution. Symp Soc Exp Biol *38*, 293-320.

59. Jones, G.H., and Franklin, F.C. (2006). Meiotic crossing-over: obligation and interference. Cell *126*, 246-248. 10.1016/j.cell.2006.07.010.

60. White, M.A., Wang, S., Zhang, L., and Kleckner, N. (2017). Quantitative Modeling and Automated Analysis of Meiotic Recombination. Methods Mol Biol *1471*, 305-323. 10.1007/978-1-4939-6340-9_18.

61. Zelazowski, M.J., Sandoval, M., Paniker, L., Hamilton, H.M., Han, J., Gribbell, M.A., Kang, R., and Cole, F. (2017). Age-Dependent Alterations in Meiotic Recombination Cause Chromosome Segregation Errors in Spermatocytes. Cell *171*, 601-614 e613. 10.1016/j.cell.2017.08.042.

62. Roecker, G.O., and Huether, C.A. (1983). An analysis for paternal-age effect in Ohio's Down syndrome births, 1970-1980. Am J Hum Genet *35*, 1297-1306.

63. Steiner, B., Masood, R., Rufibach, K., Niedrist, D., Kundert, O., Riegel, M., and Schinzel, A. (2015). An unexpected finding: younger fathers have a higher risk for offspring with chromosomal aneuploidies. Eur J Hum Genet *23*, 466-472. 10.1038/ejhg.2014.122.

64. Baudat, F., Buard, J., Grey, C., Fledel-Alon, A., Ober, C., Przeworski, M., Coop, G., and de Massy, B. (2010). PRDM9 is a major determinant of meiotic recombination hotspots in humans and mice. Science *327*, 836-840. science.1183439 [pii] 10.1126/science.1183439.

65. Myers, S., Bowden, R., Tumian, A., Bontrop, R.E., Freeman, C., Macfie, T.S., McVean, G., and Donnelly, P. (2010). Drive Against Hotspot Motifs in Primates Implicates the PRDM9 Gene in Meiotic Recombination. Science *327*, 876-879.

66. Paigen, K., and Petkov, P.M. (2018). PRDM9 and Its Role in Genetic Recombination. Trends Genet *34*, 291-300. 10.1016/j.tig.2017.12.017.

67. Parvanov, E.D., Petkov, P.M., and Paigen, K. (2010). Prdm9 controls activation of Mammalian recombination hotspots. Science *327*, 835.

68. Birtle, Z., and Ponting, C.P. (2006). Meisetz and the birth of the KRAB motif. Bioinformatics *22*, 2841-2845. 10.1093/bioinformatics/btl498.

69. Dillon, S.C., Zhang, X., Trievel, R.C., and Cheng, X. (2005). The SET-domain protein superfamily: protein lysine methyltransferases. Genome Biol *6*, 227. 10.1186/gb-2005-6-8-227.

70. Fumasoni, I., Meani, N., Rambaldi, D., Scafetta, G., Alcalay, M., and Ciccarelli, F.D. (2007). Family expansion and gene rearrangements contributed to the functional specialization of PRDM genes in vertebrates. BMC Evol Biol *7*, 187. 10.1186/1471-2148-7-187.

71. Eram, M.S., Bustos, S.P., Lima-Fernandes, E., Siarheyeva, A., Senisterra, G., Hajian, T., Chau, I., Duan, S., Wu, H., Dombrovski, L., et al. (2014). Trimethylation of histone H3 lysine 36 by human methyltransferase PRDM9 protein. J Biol Chem *289*, 12177-12188. 10.1074/jbc.M113.523183.

72. Koh-Stenta, X., Joy, J., Poulsen, A., Li, R., Tan, Y., Shim, Y., Min, J.H., Wu, L., Ngo, A., Peng, J., et al. (2014). Characterization of the histone methyltransferase PRDM9 using biochemical, biophysical and chemical biology techniques. Biochem J *461*, 323-334. 10.1042/BJ20140374.

73. Powers, N.R., Parvanov, E.D., Baker, C.L., Walker, M., Petkov, P.M., and Paigen, K. (2016). The Meiotic Recombination Activator PRDM9 Trimethylates Both H3K36 and H3K4 at Recombination Hotspots In Vivo. PLoS Genet *12*, e1006146. 10.1371/journal.pgen.1006146.

74. Wu, H., Mathioudakis, N., Diagouraga, B., Dong, A., Dombrovski, L., Baudat, F., Cusack, S., de Massy, B., and Kadlec, J. (2013). Molecular basis for the regulation of

the H3K4 methyltransferase activity of PRDM9. Cell Rep *5*, 13-20. 10.1016/j.celrep.2013.08.035.

75. Diagouraga, B., Clement, J.A.J., Duret, L., Kadlec, J., de Massy, B., and Baudat, F. (2018). PRDM9 Methyltransferase Activity Is Essential for Meiotic DNA Double-Strand Break Formation at Its Binding Sites. Mol Cell *69*, 853-865 e856. 10.1016/j.molcel.2018.01.033.

76. Born, N., Thiesen, H.J., and Lorenz, P. (2014). The B-subdomain of the Xenopus laevis XFIN KRAB-AB domain is responsible for its weaker transcriptional repressor activity compared to human ZNF10/Kox1. PLoS One *9*, e87609. 10.1371/journal.pone.0087609.

77. Imai, Y., Baudat, F., Taillepierre, M., Stanzione, M., Toth, A., and de Massy, B. (2017). The PRDM9 KRAB domain is required for meiosis and involved in protein interactions. Chromosoma *126*, 681-695. 10.1007/s00412-017-0631-z.

78. Parvanov, E.D., Tian, H., Billings, T., Saxl, R.L., Spruce, C., Aithal, R., Krejci, L., Paigen, K., and Petkov, P.M. (2017). PRDM9 interactions with other proteins provide a link between recombination hotspots and the chromosomal axis in meiosis. Mol Biol Cell *28*, 488-499. 10.1091/mbc.E16-09-0686.

79. Fog, C.K., Galli, G.G., and Lund, A.H. (2012). PRDM proteins: important players in differentiation and disease. Bioessays *34*, 50-60. 10.1002/bies.201100107.

80. Hohenauer, T., and Moore, A.W. (2012). The Prdm family: expanding roles in stem cells and development. Development *139*, 2267-2282. 10.1242/dev.070110.

81. Vervoort, M., Meulemeester, D., Behague, J., and Kerner, P. (2016). Evolution of Prdm Genes in Animals: Insights from Comparative Genomics. Mol Biol Evol *33*, 679-696. 10.1093/molbev/msv260.

82. Brick, K., Smagulova, F., Khil, P., Camerini-Otero, R.D., and Petukhova, G.V. (2012). Genetic recombination is directed away from functional genomic elements in mice. Nature *485*, 642-645. 10.1038/nature11089.

83. Hinch, A.G., Altemose, N., Noor, N., Donnelly, P., and Myers, S.R. (2014). Recombination in the human Pseudoautosomal region PAR1. PLoS Genet *10*, e1004503. 10.1371/journal.pgen.1004503.

84. Pratto, F., Brick, K., Khil, P., Smagulova, F., Petukhova, G.V., and Camerini-Otero, R.D. (2014). DNA recombination. Recombination initiation maps of individual human genomes. Science *346*, 1256442. 10.1126/science.1256442.

85. Grey, C., Clement, J.A., Buard, J., Leblanc, B., Gut, I., Gut, M., Duret, L., and de Massy, B. (2017). In vivo binding of PRDM9 reveals interactions with noncanonical genomic sites. Genome Res *27*, 580-590. 10.1101/gr.217240.116.

86. Smagulova, F., Gregoretti, I.V., Brick, K., Khil, P., Camerini-Otero, R.D., and Petukhova, G.V. (2011). Genome-wide analysis reveals novel molecular features of mouse recombination hotspots. Nature *472*, 375-378. 10.1038/nature09869.

87. Davies, B., Hatton, E., Altemose, N., Hussin, J.G., Pratto, F., Zhang, G., Hinch, A.G., Moralli, D., Biggs, D., Diaz, R., et al. (2016). Re-engineering the zinc fingers of PRDM9 reverses hybrid sterility in mice. Nature *530*, 171-176. 10.1038/nature16931.

88. Baker, C.L., Walker, M., Kajita, S., Petkov, P.M., and Paigen, K. (2014). PRDM9 binding organizes hotspot nucleosomes and limits Holliday junction migration. Genome Res *24*, 724-732. 10.1101/gr.170167.113.

89. Grey, C., Baudat, F., and de Massy, B. (2018). PRDM9, a driver of the genetic map. PLoS Genet *14*, e1007479. 10.1371/journal.pgen.1007479.

90. Baker, C.L., Kajita, S., Walker, M., Saxl, R.L., Raghupathy, N., Choi, K., Petkov, P.M., and Paigen, K. (2015). PRDM9 drives evolutionary erosion of hotspots in Mus musculus through haplotype-specific initiation of meiotic recombination. PLoS Genet *11*, e1004916. 10.1371/journal.pgen.1004916.

91. Gregorova, S., Gergelits, V., Chvatalova, I., Bhattacharyya, T., Valiskova, B., Fotopulosova, V., Jansa, P., Wiatrowska, D., and Forejt, J. (2018). Modulation of Prdm9-controlled meiotic chromosome asynapsis overrides hybrid sterility in mice. Elife *7*. 10.7554/eLife.34282.

92. Zickler, D., and Kleckner, N. (1999). Meiotic chromosomes: integrating structure and function. Annu Rev Genet *33*, 603-754. 10.1146/annurev.genet.33.1.603.

93. Kleckner, N. (2006). Chiasma formation: chromatin/axis interplay and the role(s) of the synaptonemal complex. Chromosoma *115*, 175-194. 10.1007/s00412-006-0055-7.

94. Patel, L., Kang, R., Rosenberg, S.C., Qiu, Y., Raviram, R., Chee, S., Hu, R., Ren, B., Cole, F., and Corbett, K.D. (2019). Dynamic reorganization of the genome shapes the recombination landscape in meiotic prophase. Nat Struct Mol Biol *26*, 164-174. 10.1038/s41594-019-0187-0.

95. Kumar, R., Bourbon, H.M., and de Massy, B. (2010). Functional conservation of Mei4 for meiotic DNA double-strand break formation from yeasts to mice. Genes & development *24*, 1266-1280. 10.1101/gad.571710.

96. Kumar, R., Ghyselinck, N., Ishiguro, K., Watanabe, Y., Kouznetsova, A., Hoog, C., Strong, E., Schimenti, J., Daniel, K., Toth, A., and de Massy, B. (2015). MEI4 - a central player in the regulation of meiotic DNA double-strand break formation in the mouse. J Cell Sci *128*, 1800-1811. 10.1242/jcs.165464.

97. Stanzione, M., Baumann, M., Papanikos, F., Dereli, I., Lange, J., Ramlal, A., Trankner, D., Shibuya, H., de Massy, B., Watanabe, Y., et al. (2016). Meiotic DNA break formation requires the unsynapsed chromosome axis-binding protein IHO1 (CCDC36) in mice. Nat Cell Biol *18*, 1208-1220. 10.1038/ncb3417.

98. Robert, T., Nore, A., Brun, C., Maffre, C., Crimi, B., Bourbon, H.M., and de Massy, B. (2016). The TopoVIB-Like protein family is required for meiotic DNA double-strand break formation. Science *351*, 943-949. 10.1126/science.aad5309.

99. Blat, Y., Protacio, R.U., Hunter, N., and Kleckner, N. (2002). Physical and functional interactions among basic chromosome organizational features govern early steps of meiotic chiasma formation. Cell *111*, 791-802. 10.1016/s0092-8674(02)01167-4.

100. Panizza, S., Mendoza, M.A., Berlinger, M., Huang, L., Nicolas, A., Shirahige, K., and Klein, F. (2011). Spo11-accessory proteins link double-strand break sites to the chromosome axis in early meiotic recombination. Cell *146*, 372-383. 10.1016/j.cell.2011.07.003.

101. Lange, J., Yamada, S., Tischfield, S.E., Pan, J., Kim, S., Zhu, X., Socci, N.D., Jasin, M., and Keeney, S. (2016). The Landscape of Mouse Meiotic Double-Strand Break Formation, Processing, and Repair. Cell *167*, 695-708 e616. 10.1016/j.cell.2016.09.035.

102. Neale, M.J., Pan, J., and Keeney, S. (2005). Endonucleolytic processing of covalent protein-linked DNA double-strand breaks. Nature *436*, 1053-1057. 10.1038/nature03872.

103. Lange, J., Pan, J., Cole, F., Thelen, M.P., Jasin, M., and Keeney, S. (2011). ATM controls meiotic double-strand-break formation. Nature *479*, 237-240. 10.1038/nature10508.

104. Zakharyevich, K., Ma, Y., Tang, S., Hwang, P.Y., Boiteux, S., and Hunter, N. (2010). Temporally and biochemically distinct activities of Exo1 during meiosis: double-strand break resection and resolution of double Holliday junctions. Mol Cell *40*, 1001-1015. 10.1016/j.molcel.2010.11.032.

105. Yamada, S., Hinch, A.G., Kamido, H., Zhang, Y., Edelmann, W., and Keeney, S. (2020). Molecular structures and mechanisms of DNA break processing in mouse meiosis. Genes & development *34*, 806-818. 10.1101/gad.336032.119.

106. Cejka, P., and Symington, L.S. (2021). DNA End Resection: Mechanism and Control. Annu Rev Genet *55*, 285-307. 10.1146/annurev-genet-071719-020312.

107. Mimitou, E.P., and Keeney, S. (2018). S1-seq Assay for Mapping Processed DNA Ends. Methods Enzymol *601*, 309-330. 10.1016/bs.mie.2017.11.031.

108. Paiano, J., Wu, W., Yamada, S., Sciascia, N., Callen, E., Paola Cotrim, A., Deshpande, R.A., Maman, Y., Day, A., Paull, T.T., and Nussenzweig, A. (2020). ATM and PRDM9 regulate SPO11-bound recombination intermediates during meiosis. Nat Commun *11*, 857. 10.1038/s41467-020-14654-w.

109. Brown, M.S., and Bishop, D.K. (2014). DNA strand exchange and RecA homologs in meiosis. Cold Spring Harb Perspect Biol *7*, a016659. 10.1101/cshperspect.a016659.

110. Crickard, J.B., and Greene, E.C. (2018). Biochemical attributes of mitotic and meiotic presynaptic complexes. DNA Repair (Amst) *71*, 148-157. 10.1016/j.dnarep.2018.08.018.

111. Pacheco, S., Maldonado-Linares, A., Marcet-Ortega, M., Rojas, C., Martinez-Marchal, A., Fuentes-Lazaro, J., Lange, J., Jasin, M., Keeney, S., Fernandez-Capetillo, O., et al. (2018). ATR is required to complete meiotic recombination in mice. Nat Commun *9*, 2622. 10.1038/s41467-018-04851-z.

112. Bannister, L.A., and Schimenti, J.C. (2004). Homologous recombinational repair proteins in mouse meiosis. Cytogenet Genome Res *107*, 191-200. 10.1159/000080597.

113. Hinch, A.G., Becker, P.W., Li, T., Moralli, D., Zhang, G., Bycroft, C., Green, C., Keeney, S., Shi, Q., Davies, B., and Donnelly, P. (2020). The Configuration of RPA, RAD51, and DMC1 Binding in Meiosis Reveals the Nature of Critical Recombination Intermediates. Mol Cell *79*, 689-701 e610. 10.1016/j.molcel.2020.06.015.

114. Dai, J., Voloshin, O., Potapova, S., and Camerini-Otero, R.D. (2017). Meiotic Knockdown and Complementation Reveals Essential Role of RAD51 in Mouse Spermatogenesis. Cell Rep *18*, 1383-1394. 10.1016/j.celrep.2017.01.024.

115. Nassif, N., Penney, J., Pal, S., Engels, W.R., and Gloor, G.B. (1994). Efficient copying of nonhomologous sequences from ectopic sites via P-element-induced gap repair. Mol Cell Biol *14*, 1613-1625. 10.1128/mcb.14.3.1613-1625.1994.

116. Allers, T., and Lichten, M. (2001). Differential timing and control of noncrossover and crossover recombination during meiosis. Cell *106*, 47-57.

117. Guillon, H., Baudat, F., Grey, C., Liskay, R.M., and de Massy, B. (2005). Crossover and noncrossover pathways in mouse meiosis. Mol Cell *20*, 563-573. 10.1016/j.molcel.2005.09.021.

118. Ahuja, J.S., Harvey, C.S., Wheeler, D.L., and Lichten, M. (2021). Repeated strand invasion and extensive branch migration are hallmarks of meiotic recombination. Mol Cell *81*, 4258-4270 e4254. 10.1016/j.molcel.2021.08.003.

119. Marsolier-Kergoat, M.C., Khan, M.M., Schott, J., Zhu, X., and Llorente, B. (2018). Mechanistic View and Genetic Control of DNA Recombination during Meiosis. Mol Cell *70*, 9-20 e26. 10.1016/j.molcel.2018.02.032.

120. Cole, F., Baudat, F., Grey, C., Keeney, S., de Massy, B., and Jasin, M. (2014). Mouse tetrad analysis provides insights into recombination mechanisms and hotspot evolutionary dynamics. Nature genetics *46*, 1072-1080. 10.1038/ng.3068.

121. Cole, F., Keeney, S., and Jasin, M. (2010). Comprehensive, fine-scale dissection of homologous recombination outcomes at a hot spot in mouse meiosis. Mol Cell *39*, 700-710. S1097-2765(10)00627-1 [pii]
10.1016/j.molcel.2010.08.017.

122. Peterson, S.E., Keeney, S., and Jasin, M. (2020). Mechanistic Insight into Crossing over during Mouse Meiosis. Mol Cell *78*, 1252-1263 e1253. 10.1016/j.molcel.2020.04.009.

123. Mancera, E., Bourgon, R., Brozzi, A., Huber, W., and Steinmetz, L.M. (2008). High-resolution mapping of meiotic crossovers and non-crossovers in yeast. Nature *454*, 479-485. 10.1038/nature07135.

124. Cole, F., and Jasin, M. (2011). Isolation of meiotic recombinants from mouse sperm. Methods Mol Biol *745*, 251-282. 10.1007/978-1-61779-129-1_15.

125. Jeffreys, A.J., and Neumann, R. (2005). Factors influencing recombination frequency and distribution in a human meiotic crossover hotspot. Human molecular genetics *14*, 2277-2287. 10.1093/hmg/ddi232.

126. Hunter, N., and Kleckner, N. (2001). The single-end invasion: an asymmetric intermediate at the double-strand break to double-holliday junction transition of meiotic recombination. Cell *106*, 59-70.

127. Schwacha, A., and Kleckner, N. (1995). Identification of double Holliday junctions as intermediates in meiotic recombination. Cell *83*, 783-791. 10.1016/0092-8674(95)90191-4.

128. Lynn, A., Soucek, R., and Borner, G.V. (2007). ZMM proteins during meiosis: crossover artists at work. Chromosome Res *15*, 591-605. 10.1007/s10577-007-1150-1.

129. Reynolds, A., Qiao, H., Yang, Y., Chen, J.K., Jackson, N., Biswas, K., Holloway, J.K., Baudat, F., de Massy, B., Wang, J., et al. (2013). RNF212 is a dosage-sensitive regulator of crossing-over during mammalian meiosis. Nature genetics *45*, 269-278. 10.1038/ng.2541.

130. Qiao, H., Prasada Rao, H.B., Yang, Y., Fong, J.H., Cloutier, J.M., Deacon, D.C., Nagel, K.E., Swartz, R.K., Strong, E., Holloway, J.K., et al. (2014). Antagonistic roles of ubiquitin ligase HEI10 and SUMO ligase RNF212 regulate meiotic recombination. Nature genetics *46*, 194-199. 10.1038/ng.2858.

131. Guiraldelli, M.F., Eyster, C., Wilkerson, J.L., Dresser, M.E., and Pezza, R.J. (2013). Mouse HFM1/Mer3 is required for crossover formation and complete synapsis of homologous chromosomes during meiosis. PLoS Genet *9*, e1003383. 10.1371/journal.pgen.1003383.

132. Hollingsworth, N.M., Ponte, L., and Halsey, C. (1995). MSH5, a novel MutS homolog, facilitates meiotic reciprocal recombination between homologs in Saccharomyces cerevisiae but not mismatch repair. Genes & development *9*, 1728-1739. 10.1101/gad.9.14.1728.

133. Borner, G.V., Kleckner, N., and Hunter, N. (2004). Crossover/noncrossover differentiation, synaptonemal complex formation, and regulatory surveillance at the leptotene/zygotene transition of meiosis. Cell *117*, 29-45. S0092867404002922 [pii].

134. Holloway, J.K., Booth, J., Edelmann, W., McGowan, C.H., and Cohen, P.E. (2008). MUS81 generates a subset of MLH1-MLH3-independent crossovers in mammalian meiosis. PLoS Genet *4*, e1000186. 10.1371/journal.pgen.1000186.

135. Rasmussen, S.W., and Holm, P.B. (1984). The synaptonemal complex, recombination nodules and chiasmata in human spermatocytes. Symp Soc Exp Biol *38*, 271-292.

136. Zickler, D., and Kleckner, N. (2016). A few of our favorite things: Pairing, the bouquet, crossover interference and evolution of meiosis. Semin Cell Dev Biol *54*, 135-148. 10.1016/j.semcdb.2016.02.024.

137. Rao, H.B., Qiao, H., Bhatt, S.K., Bailey, L.R., Tran, H.D., Bourne, S.L., Qiu, W., Deshpande, A., Sharma, A.N., Beebout, C.J., et al. (2017). A SUMO-ubiquitin relay recruits proteasomes to chromosome axes to regulate meiotic recombination. Science *355*, 403-407. 10.1126/science.aaf6407.

138. Cole, F., Kauppi, L., Lange, J., Roig, I., Wang, R., Keeney, S., and Jasin, M. (2012). Homeostatic control of recombination is implemented progressively in mouse meiosis. Nat Cell Biol *14*, 424-430. 10.1038/ncb2451.

139. Martini, E., Diaz, R.L., Hunter, N., and Keeney, S. (2006). Crossover homeostasis in yeast meiosis. Cell *126*, 285-295. 10.1016/j.cell.2006.05.044.

140. Wang, S., Zickler, D., Kleckner, N., and Zhang, L. (2015). Meiotic crossover patterns: obligatory crossover, interference and homeostasis in a single process. Cell Cycle *14*, 305-314. 10.4161/15384101.2014.991185.

141. Agarwal, S., and Roeder, G.S. (2000). Zip3 provides a link between recombination enzymes and synaptonemal complex proteins. Cell *102*, 245-255. 10.1016/s0092-8674(00)00029-5.

142. Shinohara, M., Oh, S.D., Hunter, N., and Shinohara, A. (2008). Crossover assurance and crossover interference are distinctly regulated by the ZMM proteins during yeast meiosis. Nature genetics *40*, 299-309. 10.1038/ng.83.

143. Ward, J.O., Reinholdt, L.G., Motley, W.W., Niswander, L.M., Deacon, D.C., Griffin, L.B., Langlais, K.K., Backus, V.L., Schimenti, K.J., O'Brien, M.J., et al. (2007). Mutation in mouse hei10, an e3 ubiquitin ligase, disrupts meiotic crossing over. PLoS Genet *3*, e139. 10.1371/journal.pgen.0030139.

144. Duroc, Y., Kumar, R., Ranjha, L., Adam, C., Guerois, R., Md Muntaz, K., Marsolier-Kergoat, M.C., Dingli, F., Laureau, R., Loew, D., et al. (2017). Concerted action of the MutLbeta heterodimer and Mer3 helicase regulates the global extent of meiotic gene conversion. Elife *6*. 10.7554/eLife.21900.

145. Nakagawa, T., and Ogawa, H. (1999). The Saccharomyces cerevisiae MER3 gene, encoding a novel helicase-like protein, is required for crossover control in meiosis. Embo J *18*, 5714-5723. 10.1093/emboj/18.20.5714.

146. Tanaka, K., Miyamoto, N., Shouguchi-Miyata, J., and Ikeda, J.E. (2006). HFM1, the human homologue of yeast Mer3, encodes a putative DNA helicase expressed specifically in germ-line cells. DNA Seq *17*, 242-246. 10.1080/10425170600805433.

147. Mazina, O.M., Mazin, A.V., Nakagawa, T., Kolodner, R.D., and Kowalczykowski, S.C. (2004). Saccharomyces cerevisiae Mer3 helicase stimulates 3'-5' heteroduplex extension by Rad51; implications for crossover control in meiotic recombination. Cell *117*, 47-56. 10.1016/s0092-8674(04)00294-6.

148. Jessop, L., Rockmill, B., Roeder, G.S., and Lichten, M. (2006). Meiotic chromosome synapsis-promoting proteins antagonize the anti-crossover activity of sgs1. PLoS Genet *2*, e155. 10.1371/journal.pgen.0020155.

149. Nakagawa, T., and Kolodner, R.D. (2002). Saccharomyces cerevisiae Mer3 is a DNA helicase involved in meiotic crossing over. Mol Cell Biol *22*, 3281-3291. 10.1128/MCB.22.10.3281-3291.2002.

150. Manhart, C.M., and Alani, E. (2016). Roles for mismatch repair family proteins in promoting meiotic crossing over. DNA Repair (Amst) *38*, 84-93. 10.1016/j.dnarep.2015.11.024.

151. Flores-Rozas, H., and Kolodner, R.D. (1998). The Saccharomyces cerevisiae MLH3 gene functions in MSH3-dependent suppression of frameshift mutations. Proc Natl Acad Sci U S A *95*, 12404-12409. 10.1073/pnas.95.21.12404.

152. Cannavo, E., Sanchez, A., Anand, R., Ranjha, L., Hugener, J., Adam, C., Acharya, A., Weyland, N., Aran-Guiu, X., Charbonnier, J.B., et al. (2020). Regulation of the MLH1-MLH3 endonuclease in meiosis. Nature *586*, 618-622. 10.1038/s41586-020-2592-2.

153. Kulkarni, D.S., Owens, S.N., Honda, M., Ito, M., Yang, Y., Corrigan, M.W., Chen, L., Quan, A.L., and Hunter, N. (2020). PCNA activates the MutLgamma endonuclease to promote meiotic crossing over. Nature *586*, 623-627. 10.1038/s41586-020-2645-6.

154. Lipkin, S.M., Moens, P.B., Wang, V., Lenzi, M., Shanmugarajah, D., Gilgeous, A., Thomas, J., Cheng, J., Touchman, J.W., Green, E.D., et al. (2002). Meiotic arrest and aneuploidy in MLH3-deficient mice. Nature genetics *31*, 385-390. 10.1038/ng931.

155. Zakharyevich, K., Tang, S., Ma, Y., and Hunter, N. (2012). Delineation of joint molecule resolution pathways in meiosis identifies a crossover-specific resolvase. Cell *149*, 334-347. 10.1016/j.cell.2012.03.023.

156. Kan, R., Sun, X., Kolas, N.K., Avdievich, E., Kneitz, B., Edelmann, W., and Cohen, P.E. (2008). Comparative analysis of meiotic progression in female mice bearing mutations in genes of the DNA mismatch repair pathway. Biol Reprod *78*, 462-471. 10.1095/biolreprod.107.065771.

157. Baker, S.M., Plug, A.W., Prolla, T.A., Bronner, C.E., Harris, A.C., Yao, X., Christie, D.M., Monell, C., Arnheim, N., Bradley, A., et al. (1996). Involvement of mouse Mlh1 in DNA mismatch repair and meiotic crossing over. Nature genetics *13*, 336-342. 10.1038/ng0796-336.

158. Marcon, E., and Moens, P. (2003). MLH1p and MLH3p localize to precociously induced chiasmata of okadaic-acid-treated mouse spermatocytes. Genetics *165*, 2283-2287. 10.1093/genetics/165.4.2283.

159. Nishant, K.T., Plys, A.J., and Alani, E. (2008). A mutation in the putative MLH3 endonuclease domain confers a defect in both mismatch repair and meiosis in Saccharomyces cerevisiae. Genetics *179*, 747-755. 10.1534/genetics.108.086645.

160. Toledo, M., Sun, X., Brieno-Enriquez, M.A., Raghavan, V., Gray, S., Pea, J., Milano, C.R., Venkatesh, A., Patel, L., Borst, P.L., et al. (2019). A mutation in the endonuclease domain of mouse MLH3 reveals novel roles for MutLgamma during crossover formation in meiotic prophase I. PLoS Genet *15*, e1008177. 10.1371/journal.pgen.1008177.

161. Kadyrov, F.A., Dzantiev, L., Constantin, N., and Modrich, P. (2006). Endonucleolytic function of MutLalpha in human mismatch repair. Cell *126*, 297-308. 10.1016/j.cell.2006.05.039.

162. Moens, P.B., Kolas, N.K., Tarsounas, M., Marcon, E., Cohen, P.E., and Spyropoulos, B. (2002). The time course and chromosomal localization of recombination-related proteins at meiosis in the mouse are compatible with models that can resolve the early DNA-DNA interactions without reciprocal recombination. J Cell Sci *115*, 1611-1622. 10.1242/jcs.115.8.1611.

163. Sanchez, A., Adam, C., Rauh, F., Duroc, Y., Ranjha, L., Lombard, B., Mu, X., Wintrebert, M., Loew, D., Guarne, A., et al. (2020). Exo1 recruits Cdc5 polo kinase to MutLgamma to ensure efficient meiotic crossover formation. Proc Natl Acad Sci U S A *117*, 30577-30588. 10.1073/pnas.2013012117.

164. Keijzers, G., Liu, D., and Rasmussen, L.J. (2016). Exonuclease 1 and its versatile roles in DNA repair. Crit Rev Biochem Mol Biol *51*, 440-451. 10.1080/10409238.2016.1215407.

165. Mimitou, E.P., Yamada, S., and Keeney, S. (2017). A global view of meiotic double-strand break end resection. Science *355*, 40-45. 10.1126/science.aak9704.

166. Keelagher, R.E., Cotton, V.E., Goldman, A.S., and Borts, R.H. (2011). Separable roles for Exonuclease I in meiotic DNA double-strand break repair. DNA Repair (Amst) *10*, 126-137. 10.1016/j.dnarep.2010.09.024.

167. Gioia, M., Payero, L., Pannafino, G., Chen, J.J., Salim, S., Fajith, G., Farnaz, A.F., Momoh, S., Scotland, M., Raghavan, V., et al. (2021). Exo1-protected DNA nicks direct crossover formation in meiosis. bioRxiv, 2021.2008.2029.458102. 10.1101/2021.08.29.458102.

168. Wang, S., Lee, K., Gray, S., Zhang, Y., Tang, C., Morrish, R.B., Tosti, E., van Oers, J., Amin, M.R., Cohen, P.E., et al. (2022). Role of EXO1 nuclease activity in genome maintenance, the immune response and tumor suppression in Exo1D173A mice. Nucleic Acids Res. 10.1093/nar/gkac616.

169. Wei, K., Clark, A.B., Wong, E., Kane, M.F., Mazur, D.J., Parris, T., Kolas, N.K., Russell, R., Hou, H., Jr., Kneitz, B., et al. (2003). Inactivation of Exonuclease 1 in mice results in DNA mismatch repair defects, increased cancer susceptibility, and male and female sterility. Genes & development *17*, 603-614. 10.1101/gad.1060603.

170. Argueso, J.L., Wanat, J., Gemici, Z., and Alani, E. (2004). Competing crossover pathways act during meiosis in Saccharomyces cerevisiae. Genetics *168*, 1805-1816. 10.1534/genetics.104.032912.

171. Schwacha, A., and Kleckner, N. (1994). Identification of joint molecules that form frequently between homologs but rarely between sister chromatids during yeast meiosis. Cell *76*, 51-63. 10.1016/0092-8674(94)90172-4.

172. Cao, L., Alani, E., and Kleckner, N. (1990). A pathway for generation and processing of double-strand breaks during meiotic recombination in S. cerevisiae. Cell *61*, 1089-1101. 10.1016/0092-8674(90)90072-m.

173. Hogarth, C.A., Evanoff, R., Mitchell, D., Kent, T., Small, C., Amory, J.K., and Griswold, M.D. (2013). Turning a spermatogenic wave into a tsunami: synchronizing murine spermatogenesis using WIN 18,446. Biol Reprod *88*, 40. 10.1095/biolreprod.112.105346.

174. Garcia, V., Phelps, S.E., Gray, S., and Neale, M.J. (2011). Bidirectional resection of DNA double-strand breaks by Mre11 and Exo1. Nature *479*, 241-244. 10.1038/nature10515.

175. Keeney, S., Lange, J., and Mohibullah, N. (2014). Self-organization of meiotic recombination initiation: general principles and molecular pathways. Annu Rev Genet *48*, 187-214. 10.1146/annurev-genet-120213-092304.

176. Zhao, X., Zhang, Y., Wilkins, K., Edelmann, W., and Usdin, K. (2018). MutLgamma promotes repeat expansion in a Fragile X mouse model while EXO1 is protective. PLoS Genet *14*, e1007719. 10.1371/journal.pgen.1007719.

177. Myler, L.R., Gallardo, I.F., Zhou, Y., Gong, F., Yang, S.H., Wold, M.S., Miller, K.M., Paull, T.T., and Finkelstein, I.J. (2016). Single-molecule imaging reveals the mechanism

of Exo1 regulation by single-stranded DNA binding proteins. Proc Natl Acad Sci U S A *113*, E1170-1179. 10.1073/pnas.1516674113.

178. Shao, H., Baitinger, C., Soderblom, E.J., Burdett, V., and Modrich, P. (2014). Hydrolytic function of Exo1 in mammalian mismatch repair. Nucleic Acids Res *42*, 7104-7112. 10.1093/nar/gku420.

179. Sokolsky, T., and Alani, E. (2000). EXO1 and MSH6 are high-copy suppressors of conditional mutations in the MSH2 mismatch repair gene of Saccharomyces cerevisiae. Genetics *155*, 589-599. 10.1093/genetics/155.2.589.

180. Tran, P.T., Erdeniz, N., Dudley, S., and Liskay, R.M. (2002). Characterization of nuclease-dependent functions of Exo1p in Saccharomyces cerevisiae. DNA Repair (Amst) *1*, 895-912. 10.1016/s1568-7864(02)00114-3.

181. Goellner, E.M., Putnam, C.D., and Kolodner, R.D. (2015). Exonuclease 1-dependent and independent mismatch repair. DNA Repair (Amst) *32*, 24-32. 10.1016/j.dnarep.2015.04.010.

182. Jeffreys, A.J., and Neumann, R. (2002). Reciprocal crossover asymmetry and meiotic drive in a human recombination hot spot. Nature genetics *31*, 267-271.

183. Furman, C.M., Elbashir, R., and Alani, E. (2021). Expanded roles for the MutL family of DNA mismatch repair proteins. Yeast *38*, 39-53. 10.1002/yea.3512.

184. Chen, P.C., Dudley, S., Hagen, W., Dizon, D., Paxton, L., Reichow, D., Yoon, S.R., Yang, K., Arnheim, N., Liskay, R.M., and Lipkin, S.M. (2005). Contributions by MutL

homologues Mlh3 and Pms2 to DNA mismatch repair and tumor suppression in the mouse. Cancer Res *65*, 8662-8670. 10.1158/0008-5472.CAN-05-0742.

185. Edelmann, W., Cohen, P.E., Kane, M., Lau, K., Morrow, B., Bennett, S., Umar, A., Kunkel, T., Cattoretti, G., Chaganti, R., et al. (1996). Meiotic pachytene arrest in MLH1-deficient mice. Cell *85*, 1125-1134. 10.1016/s0092-8674(00)81312-4.

186. Raghavan, V. (2019). Incompatibilities in Mismatch Repair Genes MLH1-PMS1 Contribute to a Wide Range of Mutation Rates in Human Isolates of Baker's Yeast. Ph.D. (Cornell University).

187. De Muyt, A., Jessop, L., Kolar, E., Sourirajan, A., Chen, J., Dayani, Y., and Lichten, M. (2012). BLM helicase ortholog Sgs1 is a central regulator of meiotic recombination intermediate metabolism. Mol Cell *46*, 43-53. 10.1016/j.molcel.2012.02.020.

188. Ashley, T., Walpita, D., and de Rooij, D.G. (2001). Localization of two mammalian cyclin dependent kinases during mammalian meiosis. J Cell Sci *114*, 685-693. 10.1242/jcs.114.4.685.

189. Amin, N.S., Nguyen, M.N., Oh, S., and Kolodner, R.D. (2001). exo1-Dependent mutator mutations: model system for studying functional interactions in mismatch repair. Mol Cell Biol *21*, 5142-5155. 10.1128/MCB.21.15.5142-5155.2001.

190. de Wind, N., Dekker, M., Berns, A., Radman, M., and te Riele, H. (1995). Inactivation of the mouse Msh2 gene results in mismatch repair deficiency, methylation tolerance, hyperrecombination, and predisposition to cancer. Cell *82*, 321-330. 10.1016/0092-8674(95)90319-4.

191. Elliott, B., and Jasin, M. (2001). Repair of double-strand breaks by homologous recombination in mismatch repair-defective mammalian cells. Mol Cell Biol *21*, 2671-2682. 10.1128/MCB.21.8.2671-2682.2001.

192. Spies, M., and Fishel, R. (2015). Mismatch repair during homologous and homeologous recombination. Cold Spring Harb Perspect Biol *7*, a022657. 10.1101/cshperspect.a022657.

193. Anand, R., Beach, A., Li, K., and Haber, J. (2017). Rad51-mediated double-strand break repair and mismatch correction of divergent substrates. Nature *544*, 377-380. 10.1038/nature22046.

194. Guo, X., Hum, Y.F., Lehner, K., and Jinks-Robertson, S. (2017). Regulation of hetDNA Length during Mitotic Double-Strand Break Repair in Yeast. Mol Cell *67*, 539-549 e534. 10.1016/j.molcel.2017.07.009.

195. Crown, K.N., McMahan, S., and Sekelsky, J. (2014). Eliminating both canonical and short-patch mismatch repair in Drosophila melanogaster suggests a new meiotic recombination model. PLoS Genet *10*, e1004583. 10.1371/journal.pgen.1004583.

196. Tran, P.T., Simon, J.A., and Liskay, R.M. (2001). Interactions of Exo1p with components of MutLalpha in Saccharomyces cerevisiae. Proc Natl Acad Sci U S A *98*, 9760-9765. 10.1073/pnas.161175998.

197. Baudat, F., and de Massy, B. (2007). Cis- and trans-acting elements regulate the mouse Psmb9 meiotic recombination hotspot. PLoS Genet *3*, e100.

198. Guillon, H., and de Massy, B. (2002). An initiation site for meiotic crossing-over and gene conversion in the mouse. Nature genetics *32*, 296-299. 10.1038/ng990.

199. Svetlanov, A., Baudat, F., Cohen, P.E., and de Massy, B. (2008). Distinct functions of MLH3 at recombination hot spots in the mouse. Genetics *178*, 1937-1945. 10.1534/genetics.107.084798.

200. Martini, E., Borde, V., Legendre, M., Audic, S., Regnault, B., Soubigou, G., Dujon, B., and Llorente, B. (2011). Genome-wide analysis of heteroduplex DNA in mismatch repair-deficient yeast cells reveals novel properties of meiotic recombination pathways. PLoS Genet *7*, e1002305. 10.1371/journal.pgen.1002305
PGENETICS-D-11-00881 [pii].

201. Cromie, G.A., Hyppa, R.W., Taylor, A.F., Zakharyevich, K., Hunter, N., and Smith, G.R. (2006). Single Holliday junctions are intermediates of meiotic recombination. Cell *127*, 1167-1178. 10.1016/j.cell.2006.09.050.

202. Kirkpatrick, D.T., Ferguson, J.R., Petes, T.D., and Symington, L.S. (2000). Decreased meiotic intergenic recombination and increased meiosis I nondisjunction in exo1 mutants of Saccharomyces cerevisiae. Genetics *156*, 1549-1557. 10.1093/genetics/156.4.1549.

203. Kolas, N.K., Svetlanov, A., Lenzi, M.L., Macaluso, F.P., Lipkin, S.M., Liskay, R.M., Greally, J., Edelmann, W., and Cohen, P.E. (2005). Localization of MMR proteins on meiotic chromosomes in mice indicates distinct functions during prophase I. J Cell Biol *171*, 447-458. 10.1083/jcb.200506170.

204. Yin, Y., Jiang, Y., Lam, K.G., Berletch, J.B., Disteche, C.M., Noble, W.S., Steemers, F.J., Camerini-Otero, R.D., Adey, A.C., and Shendure, J. (2019). High-Throughput Single-Cell Sequencing with Linear Amplification. Mol Cell *76*, 676-690 e610. 10.1016/j.molcel.2019.08.002.

205. Miura, F., Shibata, Y., Miura, M., Sangatsuda, Y., Hisano, O., Araki, H., and Ito, T. (2019). Highly efficient single-stranded DNA ligation technique improves low-input whole-genome bisulfite sequencing by post-bisulfite adaptor tagging. Nucleic Acids Res *47*, e85. 10.1093/nar/gkz435.

I, Tolkappiyan Prem Kumar is the son of Prem Kumar and Eswari Prem, PhD. I received my BTech and MTech degrees in biotechnology from IIT Madras, Chennai, India in May, 2015. In August of 2015 I entered The University of Texas MD Anderson Cancer Center UTHealth Graduate School of Biomedical Sciences and did my graduate training with Francesca Cole, PhD. I will next start my postdoctoral training with SaraH Zanders PhD at Stowers, Kansas City.

Email: premkumartolkappiyan@gmail.com